Search for Dark Matter with Liquid Argon Detectors

Centrum Astronomiczne im. Mikołaja Kopernika

Polskiej Akademii Nauk

&

Université Paris Cité

Théo Hugues

Advisors:

dr hab. Marcin Kuźniak (CAMK PAN)

dr Davide Franco (APC Paris)

September 30, 2023

Abstract

The quest to understand the elusive nature of dark matter, a substantial constituent of the universe, continues to be a fundamental challenge in modern physics and cosmology. This thesis delves into the intricate world of dark matter search, with a specific focus on two intriguing aspects: inelastic boosted dark matter (iBDM) and low-mass dark matter, particularly low-mass Weakly Interacting Massive Particles (WIMPs). Cutting-edge liquid argon detectors offer a unique and sensitive platform for the detection of these elusive particles.

The prevailing cosmological evidence for dark matter's existence, combined with its substantial gravitational influence on galaxies and galaxy clusters, suggests a non-baryonic nature. One of the leading candidates for dark matter is WIMPs, hypothesized to be weakly interacting, electrically neutral particles with a mass potentially spanning a wide range.

Low mass WIMPs, characterized by masses in the sub-GeV to GeV range, have gained significant attention in recent years due to their potential to address several outstanding issues while constituting a new frontier ready to be explore by experiments. To detect low-mass dark matter and iBDM, this thesis leverages the unique capabilities of two liquid argon detectors, DEAP-3600 and DarkSide-50.

Liquid argon, due to its low energy threshold, background mitigation potential and scalability, offers an ideal medium for the detection of low-energy recoils produced by interactions between dark matter particles and atomic nuclei or electrons. The thesis explores operation of these detectors in detail, highlighting their capacity to capture rare and low-energy events.

One of the central components of this research lays in the challenges and intricacies associated with low-mass dark matter detection, such as mitigating background noise. It explores novel analysis techniques and statistical approaches to enhance the sensitivity of the liquid argon detectors for low-mass WIMP searches. We have successfully investigated the energy range reaching a threshold as low as 0.04 keV, which is the lowest yet examined in an annual search for dark matter modulation. No modulation signal was identified in any of the analysed intervals. The level of significance associated with this outcome is inadequate to definitively validate or dismiss the DAMA/LIBRA finding. Nonetheless it proves liquid argon efficiency in this endeavor, and provided with sufficiently long data taking and stability, the potential for future detectors to achieve leading sensitivity.

In addition to low mass WIMPs, the thesis investigates inelastic boosted dark matter as a novel and less explored candidate. Inelastic dark matter models propose particles with mass splitting between their ground state and excited state, enabling them to kinetically access higher-energy interactions. This unique property may have profound implications for both cosmology and particle physics. The study discusses the potential astrophysical signatures

and detection strategies for inelastic boosted dark matter, emphasizing their distinctive features compared to standard WIMP scenarios.

In conclusion, this thesis provides a broad overview of dark matter phenomena, with a primary focus on low mass WIMPs and inelastic boosted dark matter. Through a blend of theoretical discussions and experimental prospects, it underscores the role of these candidates in unraveling the mysteries of the dark universe. The quest to understand dark matter remains a vibrant and evolving field, offering exciting opportunities to further our comprehension of the fundamental constituents of the Universe.

Streszczenie

Dążenie do zrozumienia nieuchwytnej natury ciemnej materii, istotnego składnika Wszechświata, w dalszym ciągu stanowi podstawowe wyzwanie współczesnej fizyki i kosmologii. Niniejsza praca doktorska zagłębia się w zawiły świat poszukiwań ciemnej materii, ze szczególnym naciskiem na dwa intrygujące aspekty: nieelastyczną pchniętą (ang. boosted) ciemną materię (iBDM) i ciemną materię o niskiej masie, w szczególności niskomasowe słabo oddziałujące masywne cząstki (WIMP). Najnowocześniejsze detektory ciekło-argonowe oferują wyjątkową i czułą platformę do wykrywania tych nieuchwytnych cząstek.

Przeważające dowody kosmologiczne na istnienie ciemnej materii, w połączeniu z jej znaczącym wpływem grawitacyjnym na galaktyki i gromady galaktyk, sugerują jej niebarionową naturę. Jednym z wiodących kandydatów na ciemną materię są WIMP, hipotetyczne słabo oddziałujące, elektrycznie obojętne cząstki o masach potencjalnie obejmujących szeroki zakres.

WIMPy o niskiej masie, charakteryzujące się masami w zakresie od poniżej GeV do GeV, przyciągnęły w ostatnich latach sporo uwagi ze względu na ich potencjał do rozwiązania kilku nierozstrzygniętych problemów, stanowiąc jednocześnie nową granicę dostępną do eksperymentalnego zbadania. Aby wykryć ciemną materię o małej masie i iBDM, w niniejszej pracy wykorzystano unikalne możliwości dwóch detektorów ciekło-argonowych: DEAP-3600 i DarkSide-50.

Ciekły argon, dzięki niskiemu progowi energetycznemu, potencjałowi do redukcji tła i skalowalności, stanowi idealne medium do wykrywania niskoenergetycznych odrzutów powstających w wyniku oddziaływań pomiędzy cząstkami ciemnej materii a jądrami atomowymi lub elektronami. W pracy szczegółowo zbadano działanie tych detektorów, podkreślając ich zdolność do zaobserwowania rzadkich i niskoenergetycznych zdarzeń.

Jednym z głównych elementów tych badań są wyzwania i zawiłości związane z wykrywaniem ciemnej materii o małej masie, takie jak ograniczenie wpływu tła. Nowe techniki analizy i podejścia statystyczne zostały wykorzystane do zwiększenia czułości detektorów ciekło-argonowych w poszukiwaniach lekkich WIMPów. Z powodzeniem zbadaliśmy zakres energii osiągający próg 0.04 keV, który jest najniższym dotychchczas osiągniętym w poszukiwaniu ciemnej materii za pośrednictwem sygnatury rocznej modulacji sygnału. W żadnym z analizowanych przedziałów nie stwierdzono obecności modulacji. Poziom istotności związany z tym wynikiem nie jest wystarczający, aby ostatecznie potwierdzić lub odrzucić wyniki eksperymentu DAMA/LIBRA. Niemniej jednak jest dowodem skuteczności ciekłego argonu do tego zastosowania, a przy wystarczająco długim zbieraniu danych i stabilności ma potencjał, aby przyszły detektor mógł osiągnąć wiodącą czułość.

Oprócz WIMP o niskiej masie, doktorat rozważa również nieelastyczną pchniętą ciemną

materię jako nowego i mniej zbadanego kandydata. Nieelastyczne modele ciemnej materii proponują cząstki z różnicą masy pomiędzy stanem podstawowym a stanem wzbudzonym, umożliwiając im kinetyczny dostęp do interakcji o wyższej energii. Ta wyjątkowa właściwość może mieć głębokie implikacje zarówno dla kosmologii, jak i fizyki cząstek elementarnych. W dysertacji omówiono potencjalne sygnatury astrofizyczne i strategie wykrywania nieelastycznej pchniętej Lorentzowsko ciemnej materii, podkreślając ich charakterystyczne cechy w porównaniu ze standardowymi scenariuszami WIMP.

Podsumowując, niniejsza praca zapewnia kompleksowy przegląd zjawisk ciemnej materii, ze szczególnym naciskiem na WIMPy o małej masie i nieelastyczną pchniętą ciemną materię. Poprzez połączenie dyskusji teoretycznej i perspektyw eksperymentalnych podkreśla kluczową rolę tych kandydatów w odkrywaniu tajemnic ciemnego wszechświata. Dążenie do zrozumienia ciemnej materii pozostaje tętniącą życiem i ewoluującą dziedziną, oferując ekscytujące możliwości dalszego zrozumienia podstawowych składników kosmosu i ich wpływu na strukturę i ewolucję Wszechświata.

Résumé

La quête pour comprendre la nature insaisissable de la matière noire, un constituant essentiel de l'univers, continue de constituer un défi fondamental pour la physique et la cosmologie modernes. Cette thèse se penche sur le monde complexe de la recherche de matière noire, avec un accent particulier sur deux aspects : la Inelastic Boosted Dark Matter (iBDM) et la matière noire de faible masse, en particulier les Weakly interacting Massives Particles (WIMP) de faible masse. L'étude utilise des détecteurs à argon liquide , offrant une plate-forme unique et sensible pour la détection de ces particules insaisissables. Les preuves cosmologiques de l'existence de la matière noire, combinées à son influence gravitationnelle substantielle sur les galaxies et les amas de galaxies, suggèrent une nature non baryonique. L'un des principaux candidats à la matière noire est le WIMP, supposées être des particules électriquement neutres à interaction faible et dont la masse s'étend potentiellement sur une large gamme.

Les WIMP de faible masses, caractérisés par des masses comprises entre le sub-GeV et le GeV, ont retenu l'attention ces dernières années en raison de leur potentiel à résoudre plusieurs problèmes en suspens tout en constituant une nouvelle frontière prête à être explorée par des expériences. Pour détecter la matière noire de faible masse et l'iBDM, cette thèse exploite les capacités uniques de deux détecteurs à argon liquide, DEAP-3600 et DarkSide-50.

L'argon liquide, en raison de son excellente résolution énergétique, de son atténuation du bruit de fond et de son évolutivité, offre un milieu idéal pour la détection des reculs de faible énergie produits par les interactions entre les particules de matière noire et les noyaux atomiques ou les électrons. Cette thèse explore en détail le fonctionnement de ces détecteurs, mettant en évidence leur capacité à capturer des événements rares et de faible énergie.

L'un des éléments centraux de cette recherche réside dans les défis et les subtilités associés à la détection de matière noire de faible masse, comme l'atténuation du bruit de fond. Il explore de nouvelles techniques d'analyse et des approches statistiques pour améliorer la sensibilité des détecteurs à argon liquide pour les recherches de WIMP de faible masse. Nous avons étudié avec succès la plage d'énergie atteignant un seuil de 0.04 keV, qui est le plus bas jamais examiné dans le cadre d'une recherche de modulation annuelle de la matière noire.

Aucune modulation n'a été identifié dans les intervalles analysés. Le niveau de signification associé à ce résultat est insuffisant pour valider ou rejeter définitivement les résultats de DAMA/LIBRA. Néanmoins, il prouve l'efficacité de l'argon liquide dans cette entreprise et, avec une prise de données suffisamment longue et une stabilité suffisante, le potentiel de futur détecteur pour atteindre une sensibilité de pointe.

En plus des WIMP de faible masse, la thèse étudie la Inelastic Boosted Dark Matter en tant que candidat nouveau et moins exploré. Les modèles de matière noire inélastique

proposent des particules dont la masse se divise entre leur état fondamental et leur état excité, leur permettant d'accéder cinétiquement à des interactions de plus haute énergie. L'étude discute des signatures astrophysiques potentielles et des stratégies de détection de la matière noire inélastique boostée, en soulignant leurs caractéristiques distinctives par rapport aux scénarios WIMP standards.

En conclusion, cette thèse fournit un aperçu complet des phénomènes de matière noire, avec un accent principal sur les WIMP de faible masse et la Inelastic Boosted Dark Matter. À travers un mélange de discussions théoriques et de perspectives expérimentales, il souligne le rôle de ces candidats dans la percée des mystères de l'univers. La quête pour comprendre la matière noire est un domaine dynamique et en évolution, offrant des opportunités passionnantes pour approfondir notre compréhension des constituants fondamentaux de l'Univers.

Contents

Acknowledgements

I would like to express my earnest gratitude to the many individuals and institutions that have played a pivotal role in the completion of this thesis.

First and foremost, my sincere appreciation to my Ph.D. advisors, Dr hab. Marcin Kuźniak and Dr. Davide Franco. Your guidance, mentorship, and unwavering commitment to my academic and personal growth have been indispensable. Your deep knowledge in the field, patience, and motivation helped me overcome many challenges. I am grateful for the trust you placed in me and for the opportunities to learn and grow under your mentorship.

I would also like to acknowledge my fellow colleagues, whose camaraderie, discussions, and collaboration have enriched the research experience. In particular thanks to Dr. Masato Kimura, whose collaboration and invaluable insights have significantly enriched this research endeavor.

Je suis profondément redevable au soutien de ma famille, de mes parents et de mes sœurs. Votre confiance inébranlable en mes capacités et vos encouragements pendant les hauts et les bas de ce parcours académique ont été une source constante de force. Merci pour tout l'amour que vous m'avez apporté. Merci à mes amis pour tout ces moments de joies et ces longues discussions que j'affectionne tant (particulièrement quand elles sont accompagnées d'une bière). Merci à toi Joséphine, durant presque 4 ans tu auras été une source quasi inépuisable de réconfort et d'amour.

I extend my thanks to the staff of AstroCeNT, CAMK and APC whose guidance and administrative support have facilitated the progression of this research.

This work has been supported by the International Research Agenda Programme AstroCeNT (MAB/2018/7) funded by the Foundation for Polish Science from the European Regional Development Fund (ERDF), the Polish National Agency for Academic Exchange NAWA (PHC Polonium 2020 project no. PPN/BFR/2019/1/00041), and the European Union's Horizon 2020 research and innovation programme under grant agreement No 952480 (DarkWave project).

List of Acronyms

ΛCDM	Lambda Cold Dark Matter Model
AAr	Atmospheric argon
ALP	Axion-like particle
AP	After-pulsing
BAO	Baryon Acoustic Oscillation
BBN	Big Bang Nucleosynthesis
BSM	Beyond the Standard Model
BAU	Baryon Asymmetry of the Universe
CEνNS	Coherent Elastic Neutrino-Nucleus Scattering
CMB	Cosmic Microwave Background
CP	Charge conjugation (C) and parity (P) symmetries
DAQ	Data acquisition system
DC	Dark count
DEAP	Dark matter Experiment with Argon Pulse-shape discrimination
DM	Dark Matter
ER	Electron recoil
EDM	electric dipole moment
FAP	False Alarm Probability
GADMC	Global Argon Dark Matter Collabration
iBDM	inelastic Boosted Dark Matter
LAr	Liquid argon
LHC	Large Hadron Collider
LNGS	Laboratori Nazionali del Gran SassoLSLomb-Scargle
LSV	Liquid Scintillator Veto
MACHO	MAssive Compact Halo Objects
MOND	MOdified Newtonian Dynamics
MSSM	Minimal Supersymmetric Standard Model
NR	Nuclear recoil
NQ	No quenching fluctuation
PE	Photoelectron
PQ	Peccei-Quinn
PMT	Photomultiplier Tube
PBH	Primordial black hole
PSD	Pulse shape discrimination
QCD	Quantum chromodynamics

QE	Quantum efficiency
QF	Quenching fluctuation
RoI	Region of Interest
SE	Spurious electron
SHM	Standard Halo Model
SiPMs	Silicon Photo-multipliers
SLC	SLow Control variable
SM	Standard Model
TPB	Tetraphenyl butadiene
TPC	Time Projection Chamber
UAr	Underground argon
UV	Ultra-violet
WCD	Water Cherenkov Detector
WIMP	Weakly Interacting Massive Particle
WMAP	Wilkinson Microwave Anisotropy Probe

Chapter 1

Introduction

Dark matter, a mysterious and invisible component of our universe, continues to be one of the most intriguing enigmas in modern cosmology and astrophysics. This thesis embarks on an exploration of dark matter, with a comprehensive focus on various aspects, from its cosmological significance to the experimental pursuit of its elusive nature. To guide our journey, we have structured this thesis into several key chapters, each dedicated to distinct facets of dark matter research.

Chapter 2, "Dark Matter", serves as our introductory chapter, offering a foundational understanding of the topic. It begins by elucidating the cosmological and astrophysical observations that underline the existence and relevance of dark matter in our Universe. These observations encompass the influence of dark matter on galaxies and galaxy clusters, and its connection to the cosmic microwave background and big bang nucleosynthesis. Most of the knowledge acquired to write this chapter I gained during the Les Houches 2021 summer school, with fascinating lectures from renowned lecturers.

In Sec. 2.2, we delve into the diverse range of candidates proposed to explain the nature of dark matter. This section explores intriguing theories such as new theories of gravity, the existence of MACHOs and primordial black holes, sterile neutrinos, axions and axion-like particles, as well as the prominent weakly interacting massive particles and the concept of hidden sectors.

Sec. 2.3, titled "Dark Matter Detection", takes us into the world of experimental endeavors aimed at detecting dark matter particles. It encompasses three primary detection methods: particle accelerator experiments, indirect detection through cosmic signals, and direct detection through the interaction of dark matter with target materials.

Chapter 3, "Liquid Argon Detectors", shifts our focus to the technological aspects of dark matter detection. We delve into the properties of liquid argon as a medium for such experiments, with an emphasis on its scintillation process and the use of underground argon. Due to its scintillation and ionization properties, as well as its excellent pulseshape discrimination potential liquid argon is an excellent choice for dark matter detection experiments, as it possesses incredible power to discriminate between signal and background events. Furthermore thanks to its scaleability and cost effectiveness what is already a very efficient target, will be at the forefront and lead our quest to find dark matter.

Sec. 3.2 and Sec. 3.3 introduce two significant experiments, DarkSide-50 and DEAP-3600, both utilizing liquid argon detectors. Understanding these experimental setups is vital to appreciating the results presented in subsequent chapters.

Chapter 4, "Sensitivity to inelastic boosted dark matter with DEAP-3600", introduces a specific dark matter scenario known as inelastic boosted dark matter. We examine iBDM models, focusing on upscattering off electrons, and their potential implications for experiments like DEAP-3600. We dedicated particular attention to the development of a comprehensive signal model of expected interactions within DEAP-3600. This chapter provides insights into the sensitivity of DEAP-3600.

Chapter 5, "Search for dark matter annual modulation with DarkSide-50", presents the concept of annual modulation as a method for detecting dark matter particles. We explore the reasons behind studying annual modulation, including its relevance to model-independent and standard WIMP models. Detailed analyses of DarkSide-50, including stability measurements and the Lomb-Scargle periodogram analysis, offer a comprehensive view of the experimental efforts aimed at unveiling this phenomenon.

In Sec. 5.2, "DarkSide-50 Lowmass analysis strategy", the focus shifts to the analytical strategy employed in the DarkSide-50 experiment to investigate low-mass dark matter candidates. This section discusses various factors that can affect the analysis, such as long-lived isotopes, short-lived isotopes like ^{37}Ar, and the potential influence of spurious electrons.

Section 5.3 introduces the Lomb-Scargle periodogram, a powerful statistical tool for identifying periodic variations in data. It explains key concepts such as the pseudo-Nyquist limit and white noise, which are important considerations in the context of annual modulation studies.

The chapter also addresses the stability of DarkSide-50 in Sec. 5.4, examining parameters related to the Time Projection Chamber and the Slow Control Variable. It explores correlations between Slow Control Variable and data, delayed correlations, and the Lomb-Scargle analysis in specific energy ranges.

Ultimately, this chapter lays the groundwork for the detailed annual modulation analysis with DarkSide-50, presenting our results and discussing the significance of these findings. It concludes with insights into Monte Carlo simulations and the process of setting upper limits, providing a comprehensive overview of the experimental efforts and statistical techniques employed to explore annual modulation as a potential signature of dark matter interactions within the DarkSide-50 experiment.

My role in this analysis was centered around everything related to the Lomb-Scargle analysis of the detector data as well as the slow control variables, with setting the upper limit results, as well as the stability analysis linked to correlation coefficients. I established the methodology for the time series treatment and participated in ^{37}Ar analysis.

This analysis lead to the publication of two papers: one on the results of the annual modulation search [1] and another one on the DarkSide-50 stability, with the latter currently under final review by the collaboration [2].

Chapter 2

Dark Matter

The concept of dark matter is of utmost importance to our understanding of how the Universe has developed through time. An element which is everywhere yet largely unexplained, begs to be comprehended on a deeper level. In this section, we will go over what is currently known about the dark matter puzzle, the limitations that cosmology and astrophysics impose on the features of dark matter, the role that it plays in theories that go beyond the Standard Model and an overview of the current techniques and results used to look for dark matter particles.

2.1 The Puzzle: cosmological and astrophysical observations

2.1.1 Standard cosmological model

The current understanding of dark matter is largely owed to the development of the so called standard model of cosmology, the lambda cold dark matter model (ΛCDM) and its success to predict the existence of the baryon acoustic oscillation (BAO) feature, the statistics of weak gravitational lensing, and the polarization of the Cosmic Microwave Background (CMB). Nevertheless, the lack of direct detection of cold dark matter as well as a number of other challenges have arisen over the years (for more details see Green [3]).

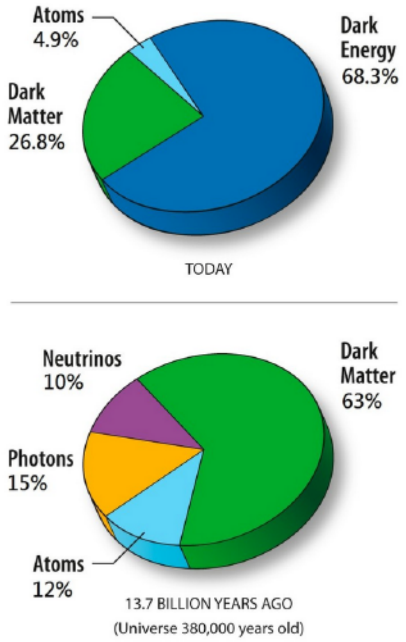

Figure 2.1: Content of the Universe, 380 000 years after the Big Bang and now, given by Eq. (2.2). *Taken from NASA website after Planck update [4].*

Using the Hubble parameter, the Friedmann equation tells us how the Universe expands, in relation to its contents: energy density, ρ, the cosmological constant[1], Λ, and its geometry k. $a(t)$ is the scale factor, which parameterizes the expansion of the Universe, usually normalized to unity today; G is the Newton's gravitational constant and c=1:

$$H^2 \equiv \left(\frac{\dot{a}}{a}\right)^2 = \frac{8\pi G}{3}\rho - \frac{k}{a^2} + \frac{\Lambda}{3}. \tag{2.1}$$

One of the strongest critiques comes from, what is commonly referred to as "the Hubble tension": h dimensionless constant parametrizing the uncertainty for the present day value of the Hubble parameter, $H_0 = 100$ km s^{-1} Mpc^{-1}. It is acknowledged to be a potential major problem for the ΛCDM model as the discrepancy observed in the results from different methods focusing on "late Universe" measurements (with calibrated distance ladder techniques) and "early Universe" techniques (using measurements of the CMB) have converged around $h = 0.73 \pm 0.02$ and $h = 0.677 \pm 0.0052$. This discrepancy can be explained using numerous hypothesis [5] categorized in modified gravity, late-time model and early-time model classes.

Furthermore other ‘small scale challenges’ [6] emerge due to the apparent differences between the observations on sub-galactic scales and numerical simulations:

- Cusp-core: Simulations with only dark matter, produce halos with an inner cuspy density profile ($\rho(r) \propto r^{-\gamma}$ with $\gamma \approx 1$) but observed galaxies, especially dwarfs galaxies, show shallower profiles, or even cored ($\gamma \sim 0$).

---

[1] Albert Einstein temporarily added this constant to his General relativity's field equation. He removed it after Edwin Hubble's observation showed an expanding Universe and not a static one.

Much later, in 1998, it was revived as observations hinted at an accelerated expanding Universe, and reinterpreted as the energy density of space, or vacuum energy arising in quantum mechanics. The notion of dark energy has become intimately linked with it.

- Missing satellites: Simulations of Milky Way-size halos contain thousands of sub-halos with dwarf galaxy size, but few of them have been observed: $\sim$ 50 (at this stage observations are incomplete).
- 'Too-big-to-fail': Observations of medium size galaxies ($M_{dm} \sim 10^{10} M_{\odot}$) is lower than expected.

It has to be noted that to this day these challenges are not absolute evidence that we need to go beyond the standard model of cosmology [3]; they can be explained by fine tuning or other ΛCDM-related explanations, and no alternative model achieved the same success. They nonetheless show the complexity that cosmology faces nowadays and the diversity of solutions that have to be consider to enhance our understanding of the Universe.

The evolution of the Universe is obtained after rewriting Eq. (2.1), ordering the terms according to the current density, radiation, matter (known+dark matter), curvature and cosmological constant (possibly Dark Energy):

$$H^2 = H_0^2 \left[\Omega_{r,0}(1+z)^4 + \Omega_{m,0}(1+z)^3 + \Omega_{k,0}(1+z)^2 + \Omega_{\Lambda,0} \right] , \tag{2.2}$$

where $\Omega_{i,0} = \frac{\rho}{\rho_c}$, ρ is given by the fluid equation: $\dot{\rho} = -3H(\rho + p)$, p is the equation of state $p = w\rho$. w is the equation of state parameter: $w = 1/3$ for photons and lights neutrinos, $w = 0$ for non-relativistic particles (usual and cold dark matter) and $w = -1$ for a fluid description of the cosmological constant (Dark Energy or other dominant fluids will lead to an accelerated expansion for $w < -1/3$). ρ_c, the critical density, is a time dependent value of the energy density, $\rho_c = \frac{3H^2}{8\pi G}$ assuming a flat Universe, $k = 0$ [3], redshift $a = \frac{1}{1+z}$. We only gave a brief summary to introduce general idea behind the ΛCDM model (Fig. 2.1 and Fig. 2.2), more complete explanation can be found in a Les Houches lecture from Green [3].

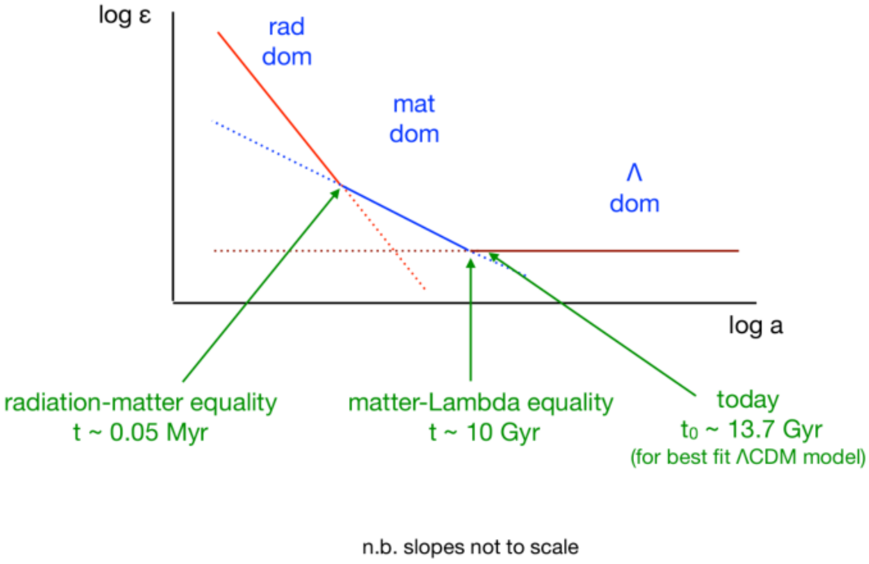

Figure 2.2: Simplified evolution of the logarithm of the Universe's density, versus the logarithm of the scale factor, $a(t)$. *Taken from [3].*

2.1.2 Galaxies and galaxy clusters

Galaxies

During the 20th century, astronomers began utilizing dynamics and their knowledge of gravity in order to calculate the overall mass of galaxies and galaxy clusters. They could calculate the mass-to-light ratio by comparing the overall mass of the system to the quantity of luminous matter it contained. The pioneer work done by Rubin and Ford [7], estimated spiral galaxies' circular velocity using the Doppler shift of the Hydrogen 21 cm line.

Objects at the periphery of spiral galaxies orbit around the galaxy's centre at a certain circular velocity, denoted as v_c. In accordance with Newton's shell theorem: The gravitational force exerted on the outside of a spherical shell of matter is equivalent to that which would be experienced if all the matter within the shell were concentrated into a single point located at its centre and Newton's law of gravity , this is described by:

$$v_c = \sqrt{\frac{GM(<r)}{r}}, \tag{2.3}$$

in which $M(<r)$ refers to the amount of mass that is contained at a given distance from the galactic centre and G denotes the gravitational constant. In this discussion, we have made the assumption that the distribution of mass is spherically symmetric, denoted by the notation $M(<r) = \int_0^r 4\pi r^2 \rho(r)\, dr$, where $\rho(r)$ refers to the matter density. In order to construct what is known as a rotation curve, astronomers evaluated the velocity of objects located at varying distances.

This gave them the ability to deduce the mass distributions of a particular galaxy. The rotation curve is essentially flat, $v_c(r) = \text{constant}$, over vast distances, much beyond the area where the majority of stars dwell, as shown in Fig. 2.3. This was observed in a number of different galaxies, and it was seen far beyond the region where the majority of stars reside. This suggests that the mass distributions do not have a bright analogue, either in gaseous or in stellar matter. It has to be noted that not all rotation curves are completely flat [8].

The advent of N-body simulations provided more support for the hypothesis that galaxies had the form of a vast symmetrical structure. They demonstrated that revolving spiral galaxies, on their own, are inherently unstable and need the presence of a dark matter halo [9].

This provided some more justification for the assumption of spherical symmetry that was used in the derivation of Eq. (2.3), which, to a first approximation, is still the one that is widely accepted. It was becoming abundantly evident that these galaxies had a significant quantity of matter that did not emit light. The precise amount of this element was unknown; nevertheless, several mass-to-light ratios were reported to be between 3 and 10 [10].

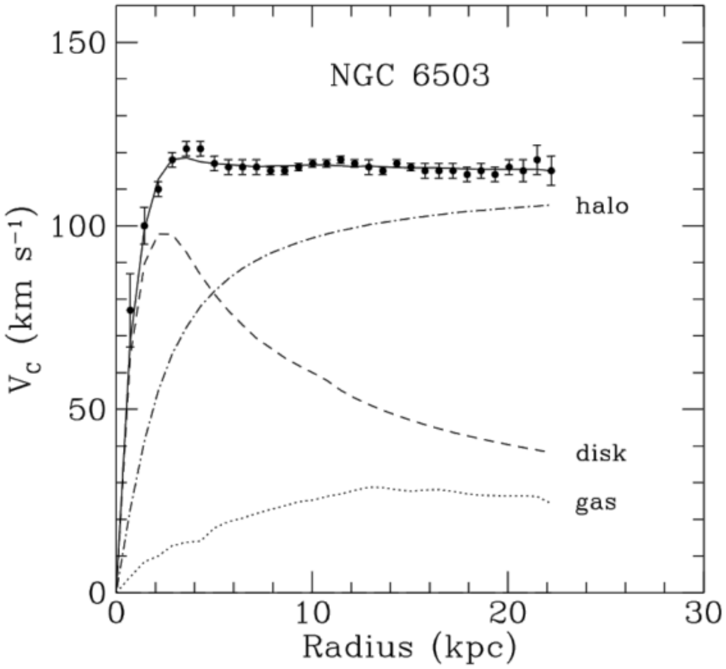

Figure 2.3: NGC 6503 rotation curve, with the predicted rotation curve from different components of the galaxy. *Taken from [11].*

Galaxy clusters

Galaxy clusters consist of numerous galaxies and are accompanied by the presence of high-temperature X-ray emitting gas. Galaxy clusters represent the most substantial entities in the Universe that are held together by gravitational forces, making them potentially representative of the overall composition of the Universe. Three types of observations are utilized to provide evidence and information regarding dark matter.

1) The virial theorem establishes a relationship between potential energy (V) and the kinetic energy (T) in a self-gravitating system, expressed as $2T + V = 0$ ([3]). It is first necessary to establish a connection between the potential and kinetic energies with measurable quantities. The mean square velocity is expressed as:

$$\langle v^2 \rangle = \frac{\sum_i m_i v_i^2}{\sum_i m_i} = \frac{2T}{M}. \tag{2.4}$$

The total mass, denoted as $M = \sum_i m_i$, and we can expressed the potential energy as follows:

$$V = -\frac{1}{2} \sum_i \sum_{j \neq i} \frac{G m_i m_j}{r_{ij}}. \tag{2.5}$$

The gravitational radius, denoted as R_G, can be defined:

$$R_G = 2 \left(\sum m_i \right)^2 \left(\sum_i \sum_{j \neq i} \frac{m_i m_j}{r_{ij}} \right)^{-1}. \tag{2.6}$$

The equation for the potential energy V can be expressed as $V = -GM^2/R_G$. Additionally, M, the total mass, is expressed with the gravitational radius, R_G, and the mean square velocity, $\langle v^2 \rangle$ as $M = R_G \langle v^2 \rangle / G$. Galaxies mean square velocity is determined by measuring their speeds using the Doppler effect.

Additionally, the gravitational radius can be estimated by observing their projected positions. These measurements enable us to estimate the total mass, which was first done by Zwicky [12] in 1933, and even if his results were almost 2 orders of magnitude higher than the current estimate, due to large uncertainty on the Hubble constant and other parameters, he was the first to use the term "dunkle Materie". This generally yields a ratio of mass to luminosity:

$$\frac{M}{L} \sim 400 \frac{M_\odot}{L_\odot}, \tag{2.7}$$

with $L_\odot$ and $M_\odot$ representing the Solar luminosity and mass, respectively. This can be approximated as a mass density parameter $\Omega_m \sim 0.3$ [13].

2) The baryon[2] fraction derived from the X-ray gas, denoted as f_b, represents the proportion of baryonic matter, M_b, to the total mass, M_{tot}, of a galaxy cluster.

If galaxy clusters are representative of the entire Universe, the baryon fraction is defined as the ratio of the baryon density parameter Ω_b to the matter density parameter, Ω_m: $f_b = \Omega_b/\Omega_m$. Assuming spherical symmetry and hydrostatic equilibrium, where gravity and the pressure gradient force are balanced,

$$\frac{1}{\rho}\frac{dP}{dr} = -\frac{GM(< r)}{r^2}. \tag{2.8}$$

Employing the ideal gas law, $P = k_B \rho T / \mu m_p$, we can then express it as:

$$\frac{k_b T}{\mu m_p}\left(\frac{d\ln T}{d\ln r} + \frac{d\ln \rho}{d\ln r}\right) = -\frac{GM(< r)}{r}. \tag{2.9}$$

The first component on the left-hand side bracket can be ascertained through the utilization of X-ray spectra, whilst the subsequent term can be determined by employing X-ray surface brightness measurements. The outcome is an estimated baryon fraction, approximately equal to 0.144 ± 0.005 [14]. Systematic errors may arise in the determination of this value due to factors such as variations from hydrostatic equilibrium as well as uncertainties in the temperature-mass relationship.

3) Gravitational lensing is the phenomenon in which the trajectory of light is altered by gravity, causing it to deviate from its original path while travelling from the emitter to the observer. Strong lensing refers to a phenomenon where the deflection of light is significant, resulting in the formation of multiple images, or a so-called Einstein ring, when the observer, lens, and source are aligned (see [15]).

---

[2] In astronomy the term Baryonic Matter is often wrongfully used to define not only composite particles with uneven number of quarks (mostly proton and neutron) but also other non-relativistic particles such as electrons.

This is due to historical reasons and the fact that the vast majority of the mass is coming from protons and neutrons.

The properties of the images, such as their number, positions, and fluxes, are contingent upon the distribution of mass. Substructure in the form of dark matter subhalos can be investigated using flux ratios and gravitational imaging.

Microlensing refers to the phenomenon that arises when the angular separation between images is of such little magnitude that it cannot be discerned, typically on the order of micro arc seconds, resulting in a temporary increase in brightness of the source [16].

Microlensing is an effective method for studying compact dark matter, such as Primordial Black Holes (Sec. 2.2.2). Weak lensing refers to a phenomenon where the deflection is of small magnitude [17]. Cosmic shear, which refers to the slight deformation of distant galaxy images caused by weak gravitational lensing, enables the mapping of matter distribution and the determination of Ω_m.

When examining cluster mergers, one encounters a particularly interesting case for the cold dark matter paradigm. The most well-known of them is called the Bullet Cluster, and it was caused by the collision of two galaxy clusters, which resulted in the production of a shock front in the gas component. Weak lensing is able to provide information about the mass distribution, distributed around the galaxies in the subcluster and cluster, whereas X-ray astronomy is able to produce information about the gaseous matter that interacts and collides in the predicted manner.

We can notice the difference between the two distibutions by looking at Fig. 2.4. Weak lensing demonstrates that the two clusters did not collide but rather merely went through one another, yet X-ray imagery depict a dramatic collision taking place.

Over the course of the years, more of these mergers have been examined [18], resulting in procedures that are very challenging to reconcile with theory focused on modifying gravity. However, according to the particle interpretation, this only places a constraint on the magnitude of the self-interaction that occurs inside the dark sector. The self-interaction strength is constrained to [19]

$$\frac{\sigma_{self}}{m_{DM}} < 1cm^2g^{-1}, \tag{2.10}$$

where σ_{self} is the interaction cross section for dark matter, self scattering, and m_{DM} is the mass of dark matter.

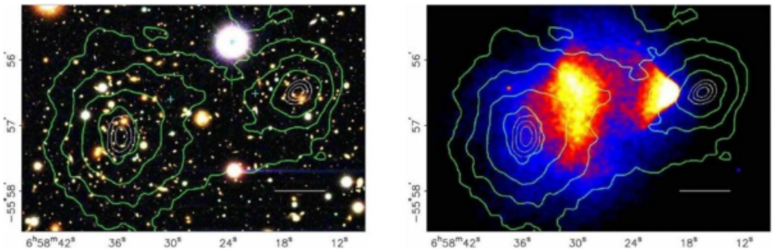

Figure 2.4: The provided image depicts the collision of the bullet cluster. The green contours on both sides depict the inferred matter density through gravitational lensing. Stellar matter is also depicted on the left. The colour grading on the right represents the distribution of hot gas as observed through X-ray observations. The majority of mass in the clusters moves past each other without being affected. *Taken from [18].*

2.1.3 Cosmic Microwave Background and Big Bang Nucleosynthesis

After the discovery of Hubble-Lemaître's law[3] and the Cosmic Microwave Background (CMB)[4], scientists began their quest to comprehend how the Universe transitioned from a hot, dense plasma to the state in which it is now found.

Galaxies were no longer required to simply exist in a stable state; rather, new galaxies had to be produced. Cosmic inflation occurred during the very early phases of the Universe and had the effect of reducing the curvature of the space-time metric to zero [3]. This phenomenon was caused by the acceleration of the expansion of the Universe during the Big Bang.

The process of converting the energy gained from the fast expansion into hot SM particles happens during the reheating phase, which comes after the inflation phase.

Nucleosynthesis

The Big Bang Nucleosynthesis refers to the formation of light element nuclei, including Helium-3 (^{3}He), Deuterium (D), Helium-4 (^{4}He), and Lithium-7 (^{7}Li), during the early stages of the Universe, specifically within a time frame ranging from seconds to minutes after the Big Bang[5].

Prior to $t \sim 1$ second (where $k_BT \sim 1$ MeV), the thermal equilibrium between protons and neutrons is maintained through weak interactions,

$$\begin{aligned} &n + \nu_e \leftrightarrow p + e^- \\ &n + e^+ \leftrightarrow p + \bar{\nu}_e. \end{aligned} \tag{2.11}$$

We can use Maxwell-Boltzmann distribution as protons and neutrons are non-relativistic ($k_BT << m_p$), their relative number densities can be determined accordingly:

$$\frac{N_n}{N_p} = \left(\frac{m_n}{m_p}\right)^{3/2} \frac{e^{-m_n/(k_BT)}}{e^{-m_p/(k_BT)}} \approx e^{-\frac{(m_n - m_p)}{k_BT}}. \tag{2.12}$$

When $k_BT >> m_n - m_p = 1.3MeV$, the number of neutrons, N_n is approximately equal to the number of protons, N_p. Nevertheless, when the thermal energy decreases below the rest mass energies difference, the number of neutrons becomes less than the number of protons.

Upon performing a comprehensive calculation, it is determined that when $k_BT \sim 0.8MeV$, the temporal scale at which weak reactions occur surpasses the age of the Universe. Consequently, the process of converting protons to neutrons, or vice versa, comes to a halt, commonly referred to as 'freeze-out'. Currently, the ratio of N_n to N_p is approximately 0.2.

---

[3] The further a galaxy is the faster it mooves away from Earth

[4] The remnant of the first light that could travel freely, see Sec. 2.1.3

[5] As for a lot of discussions in this chapter a more extensive overview can be found in Review of Particle Physics [20] from PDG (Particle Data Group), for example the chapter from Molaro, Sarkar and Fields present this subject in details.

The following synthesis of light elements' nuclei takes place through a series of chain reactions,

$$\begin{aligned} &p + n \to \mathrm{D} \\ &\mathrm{D} + p \to {}^{3}\mathrm{He} \\ &\mathrm{D} + \mathrm{D} \to {}^{4}\mathrm{He}, etc... \end{aligned} \tag{2.13}$$

At temperatures below the nuclear temperature, the majority of the remaining neutrons undergo fusion to form ^{4}He, which is the most stable light nucleus.

Additionally, small quantities of heavier nuclei are also produced. Each isotope mass fractions are as follows: $Y_{^4\mathrm{He}}$ ranges from 0.23 to 0.24, Y_{D} is approximately 10^{-4}, $Y_{^3\mathrm{He}}$ is 10^{-5}, and $Y_{^7\mathrm{Li}}$ is 10^{-10}. The precise abundances are contingent upon the ratio of photons to baryons, or alternatively, the abundance of baryons as the photon number density can be derived from the CMB temperature.

Hence, through the comparison of theoretical predictions with empirical observations, specifically the analysis of Deuterium abundance obtained from the absorption of light emitted by quasars and intercepted by primordial gas clouds, it is possible to ascertain the baryon density parameter within the range of $0.021 \leq \Omega_b h^2 \leq 0.024$ [21].

This statement aligns with the findings derived from the anisotropies observed in the CMB, the level of precision in this determination is comparatively lower.

Cosmic microwave background

Satellites such as the Wilkinson Microwave Anisotropy Probe (WMAP) have played a crucial role in understanding the early Universe and its composition. The WMAP and more recently Planck satellite have measured the CMB radiation anisotropies.

The cosmic microwave background is the afterglow of recombination, around $t \sim 0.25$ Myr while $k_B T \sim 0.32$ eV, a process that occurred around 380,000 years after the Big Bang but before the CMB. Recombination takes place, much like BBN, after the Universe has cooled down to the point where it can host composite particles; however, in this case, the particles in question are neutral atoms. When this takes place, there is no obstacles in the path of photons, and the Universe seems transparent, this process is called decoupling, and happened around $t \sim 0.37$ Myr as $k_B T \sim 0.26$ eV.

Before that time, Thomson scattering between photons and ions formed a plasma fluid by keeping baryonic matter and radiation firmly coupled. The photons that were released during this time period may still be seen today, and since there was a previous phase of inflation, the temperature distribution over the sky is astonishingly consistent, the resulting CMB has a black body spectrum with present day temperature measured at $T_0 = 2.7255 \pm 0.0006$ K [22]. Importantly, there are little variations in temperature that provide an incredible amount of information about the structure of the early Universe.

At the time of the Big Bang, density disturbances were present on all scales, but they were driven out of causal touch by inflation, which occurred on super horizon sizes. While they are above the horizon scale, disturbances are halted in their progression and will neither expand nor contract. When radiation enters the picture, disturbances start to appear on the horizon. They start to contract due to the force of gravity and then expand due to the pressure of radiation, which results in baryon acoustic oscillations (BAO).

By expanding in spherical harmonic, $Y_l^m(\theta,\Phi)$, the fluctuations of the temperature are analyzed:

$$\frac{\Delta T(\theta,\Phi)}{\bar{T}} \equiv \frac{T(\theta,\Phi)-\bar{T}}{\bar{T}} = \sum_{l=1}^{\inf} \sum_{m=-l}^{l} a_{lm} Y_l^m(\theta,\Phi). \tag{2.14}$$

$T(\theta,\Phi)$ is the temperature for a given direction, $\bar{T}$ is the average temperature, a_{lm} are coefficients of the expansion. C_l, the angular power spectrum, is obtained averaging the coefficients:

$$C_l = \langle |a_{lm}|^2 \rangle. \tag{2.15}$$

On the other hand, a disturbance caused by pure dark matter will not result in BAOs but rather will gradually expand. Because the pattern of the CMB is viewed on a two-dimensional surface, its analysis is often performed using the angular power spectrum, which allows the multipole order, l, to be connected to angular size. The disturbances that, at the moment of recombination, have just reached an extreme are what create the oscillation modes that give the biggest changes in temperature. The amount of time that passes before one compression takes place is directly proportional to the magnitude of the first peak in the power spectrum.

Because the speed of BAOs and the time it takes for recombination are both known, it is possible to anticipate the multipole order of this peak. When this value is converted to an angular size, similar to what is seen on the CMB today, the only factor that affects the outcome is the overall energy density. WMAP was the first project to measure the peak, and their findings revealed a flat curvature [23].

Measuring the peaks that come after the first one is necessary in order to get information about the components of the Universe. When looking at dark matter in particular, it is sufficient to look at the first three peaks of the CMB. This is due to the fact that one is able to differentiate between various impacts based on the relative heights of the peaks.

Lower values of the multipole moment, are generally associated with significant angular separations, while higher values tend to match smaller angular separations. Three distinct regions with specific characteristics exist Fig. 2.5.

- The low l region is commonly referred to as the 'Sachs-Wolfe' plateau. The temperature fluctuations in this system are a result of fluctuations in the gravitational potential.
- The intermediate values of l are associated with the acoustic (or Doppler) peaks. The aforementioned phenomena arise as a result of oscillations occurring within the photon-baryon fluid, which can be attributed to the interplay between gravitational forces and pressure. This pressure, in turn, emerges from the interactions between photons and electrons.
- At high l, Silk damping tail. The damping of temperature fluctuations on small scales occurs as a result of the diffusion of photons during the recombination process.

Through accurate experimental measurements, Planck was able to establish the most strict limitations on the total density of dark matter, $\Omega_{DM}h^2 = 0.1199 \pm 0.0027$ [24] Both the observations of the baryon density Ω_b emanating from the CMB and the measurements of the deuterium abundance are consistent with one another. This suggests that baryons were a significant component of matter in the cosmos even at very early periods, when the

Universe was very young. Indicating that the particle physics Standard Model (SM)[6] is lacking some kind of new basic particle, such as dark matter.

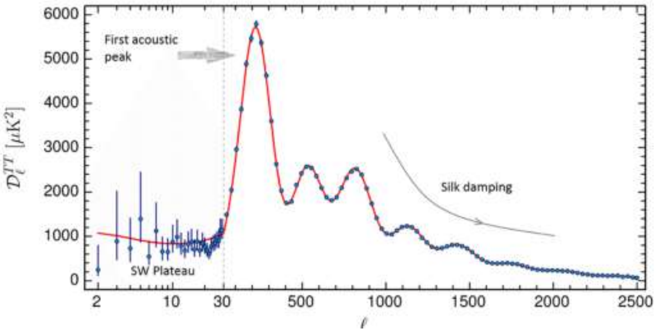

Figure 2.5: CMB angular power spectrum temperature (Planck collaboration [24]). $D_l^{TT} \equiv l(l+1)C_l/(2\pi)$; the solid line (red) represents the standard cosmological (ΛCDM) model and the bars (blue) the cosmic variance

2.2 Solutions: a variety of candidates

Numerous theoretical and experimental efforts have been dedicated to identifying potential dark matter candidates and understanding their properties. In this chapter, we delve into the diverse array of dark matter candidates and explore the wide range of mass values they could possess.

Throughout this chapter, we will investigate dark matter candidates, examining their theoretical underpinnings and the astrophysical and cosmological evidence that supports their candidacy. There is a wide range of mass values associated with these candidates, which may extend from fractions of an electronvolt to several times the mass of the sun. Understanding this diverse landscape of dark matter candidates and their mass range is essential for guiding our experimental and observational efforts in the ongoing pursuit of dark matter's secrets.

2.2.1 New Theory of Gravity

Often simplified to Milgrom's Modified Newtonian Dynamics (MOND) [26] the study of Modified Gravity is actually a thriving field of research with numerous theories that could be tested in the near future (Burrage [27]). MOND is a hypothesis based on the assumption that Newton's law do not apply to low acceleration object such as galaxies:

$$F_N = m\mu\left(\frac{a}{a_0}\right)a, \tag{2.16}$$

where a is the acceleration and $\mu(x)$ is the interpolating function that need to respect: $\mu(x) \rightarrow 1$ for $x >> 1$ and $\mu(x) \rightarrow x$ for $x << 1$ in order to agree with Newtonian physics

---

[6] The Standard Model is the description of the most basic components of our world that is derived from quantum field theory. It explains particle interactions by using local gauge symmetries and offers some of the most accurate agreement between experiment and theory in any field.

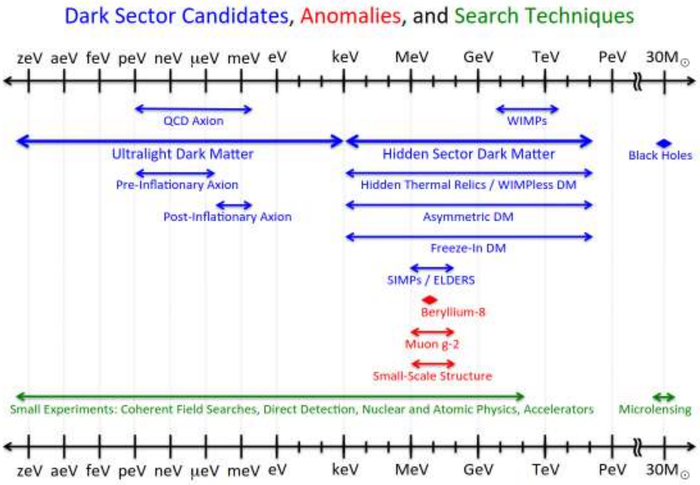

Figure 2.6: Particle dark matter candidates in blue, spanning almost a 100 orders of magnitude in mass, with detection methods in green and interesting anomalies in red. Battaglieri et al. [25]

at high acceleration and the observation of galaxy rotation curve at low a. The simplest interpolating function, $\mu\left(\frac{a}{a_0}\right) = \frac{1}{1+\frac{a_0}{a}}$ rewrite Eq. (2.16) into:

$$F_N = m\,\frac{a^2}{a_0} \quad (a << a_0). \tag{2.17}$$

Observational evidences, mostly from Dwarf Galaxies present close agreement with MOND prediction. But notorious challenges arise with the observation of galaxy clusters showing residual mass discrepancy (some considered 2 eV neutrinos as a solution) and more significantly with pair of colliding galaxy observations (Sec. 2.1.2), where MOND prediction expect the "unknown mass" to be centered centered regions where $a < a_0$.

After being presented in the beginning as a phenomenological model, a significant amount of effort has been put into a more basic theoretical framework, some notable one are scalar–tensor theories of gravity and TeVeS, which stands for tensor-vector-scalar gravity (Clifton et al. [28]).

The incorporation of modified gravity theories inherently requires the introduction of supplementary fields, broken symmetries, or extra dimensions. The consideration of whether these deviations are observed in the background cosmology or solely at the perturbations level is of utmost importance. In order to incorporate dark energy or address the cosmological constant problem through modified gravity, it is necessary for these deviations to be solutions of the Friedmann equations Eq. (2.2). However, it is crucial that these deviations do not compromise the accurate predictions made by the standard cosmology, including the abundance of light elements (Sec. 2.1.3), the positions of peaks in the cosmic microwave background acoustic spectrum (Sec. 2.1.3), or the predictions regarding baryon acoustic oscillations.

Furthermore, cosmic data has the potential to not only suggest the existence of novel physics within the gravitational sector but also impose limitations and exclude alternative theories. At present, a multitude of experiments are being devised and implemented throughout the world, indicating that we find ourselves at a pivotal moment towards comprehending gravity. The European Space Agency (ESA) is now evaluating the satellite mission Euclid [29], which has the potential to extensively survey expansive areas of space and investigate the growth rate and morphology of large-scale structures. The Square Kilometre Array (SKA) [30] is now in a development phase, wherein path finders are being constructed on two continents. These path finders aim to generate a comprehensive survey of approximately one billion radio galaxies, allowing for the mapping of the evolution of structure up to extremely high redshifts.

2.2.2 MACHOs and Primordial Black Holes

MACHOs

A population of faint astrophysical objects, like brown dwarfs for example, might provide an explanation for both the Bullet Cluster and the galaxy rotation curves. These objects are often referred to as massive astronomical compact halo objects, or MACHOs, and they were the focus of two experimental investigations that looked for instances at micro-lensing. The EROS and MACHO collaborations determined that MACHOs with masses between 10^{-7} and $1 M_\odot$ must account for only a fraction of the total mass of dark matter halos [31].

Primordial Black Holes

One of the most notable predictions from the theory of general relativity is that when a mass M is confined within its Schwarzschild radius $R_S \equiv 2GM/c^2$, it gives rise to a black hole, which is characterised by an intense gravitational field that prevents the escape of even light. Black holes have the potential to exist across a broad spectrum of mass scales. Apart from known and observed Black Holes (e.g. Intermediate Mass Black Holes ($\sim 100 M_\odot$) and Supermassive Black Holes (from $10^6 M_\odot$ to $10^{10} M_\odot$) a class of yet undetected Black Holes could have formed in the early Universe, hence the term "primordial". At a time t after the Big Bang we get the cosmological density $\rho \sim 1/Gt^2$, after expressing the Schwarzschild radius as its largest possible value from an input density before forming a black hole $R_S = \sqrt{3c^2/8\pi G\rho}$, we get the density needed for a region with a mass M to fall within R_S, $\rho \sim c^6/G^3M^2$. We then obtain the horizon mass a primordial black holes would originally form:

$$M \sim \frac{c^3 t}{G} \sim 10^{15} \left(\frac{t}{10^{-23} s} \right) g. \tag{2.18}$$

It yields a gigantic PBHs mass range depending on the time of formation, from the Planck mass, $M_{Pl} \sim 10^{-5} g$ at $t \sim 10^{-43} s$; $1 M_\odot$ at the QCD epoch $t \sim 10^{-5} s$ to $10^5 M_\odot$ (and beyond) for a formation at $t \sim 1 s$ (and after).

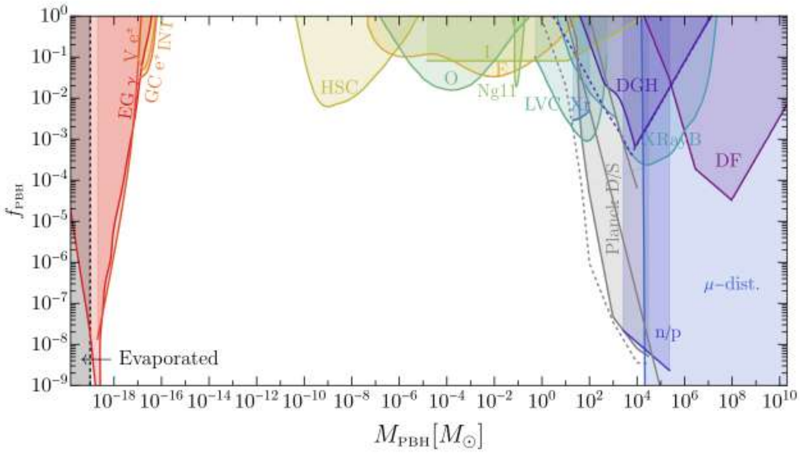

Figure 2.7: Monochromatic PBH abundance constraints for PBHs with mass M_{PBH}. The shaded zone in the leftmost section of the plot represents PBHs that undergo evaporation within a period that is less than the age of the Universe. These PBHs are not considered as a plausible candidate for dark matter. $f_{PBH} = \Omega_{PBH}/\Omega_{DM}$. *Taken from [32]*

The idea of PBHs is more than 50 years old being first mention by Zeldovich-Novikov, but really took root after Hawking and Carr showed that they couldn't grow as fast as the horizon (Carr and Kühnel [33]). Understanding the mass range of PBHs pushed Hawking to study their quantum properties. Leading to his famous discovery of thermal radiation [34]:

$$T = \frac{\hbar c^3}{8\pi G M k} \approx 10^{-7} \left(\frac{M}{M_\odot}\right)^{-1} K, \tag{2.19}$$

giving an evaporation on a timescale:

$$\tau(M) \approx \frac{\hbar c^5}{G^2 M^3} \approx 10^{64} \left(\frac{M}{M_\odot}\right)^{3} yr. \tag{2.20}$$

Only primordial black holes formed after 10^{-23} s and larger than $M \sim 10^{15}$ g (an approximate size of a proton) would have not evaporated by now as seen in Fig. 2.7

The study of Primordial Black Holes (PBHs) offers a distinctive opportunity to investigate four distinct domains of physics: (1) the primordial stages of the Universe when the mass is less than 10^{15} g; (2) the process of gravitational collapse when the mass exceeds 10^{15} g; (3) the realm of high energy physics when the mass is approximately 10^{15} g; and (4) the realm of quantum gravity when the mass is approximately 10^{-5} g.

Primordial black holes have the potential to make significant contributions to various astrophysical phenomena, including the cosmological and Galactic γ-ray backgrounds, the presence of antiprotons and positrons in cosmic rays, gamma-ray bursts, and the emission of annihilation-line radiation originating from the centre of the Galaxy.

2.2.3 Sterile neutrinos

The neutrino is perhaps one of the particle with the most fitting name in the Standard Model of Particle Physics since it is so small (-ino), neutral, and so light that its mass has never been determined. The most prevalent massive particles in the Universe are neutrinos. Neutrinos are created whenever atomic nuclei combine (like in the Sun) or disintegrate (as in a nuclear reactor).

These phantom particles nearly never interact with other matter after being created. You cannot feel the tens of billions of solar neutrinos that pass through your body every second.

Although the neutrino's existence was predicted by Pauli in 1930, it took experimenters 26 years to actually find the particle. The mass of the neutrino, how it interacts with matter, and whether or not it is its own antiparticle particle with the same mass but the opposite electric and magnetic properties are all now being investigated.

Since 1957 and Wu's discovery of the parity violation from the weak interaction, only left-handed leptons, hence neutrino (and right-handed antineutrino), have been observed. This sparkled interest for the so called sterile neutrino; according to current research, sterile neutrinos with masses exceeding keV possess the necessary characteristics to explain the existence of dark matter in the Universe.

These particles are electrically neutral and become non-relativistic early on, thus making them cold dark matter. Additionally, their weak interactions with other particles (provided their mixing angles are small) contribute to their viability as dark matter candidates. Furthermore, these particles remain stable over cosmological time scales.

One critical question for any dark matter candidate is how its abundance is determined. In the case of sterile neutrinos, the Dodelson-Widrow mechanism [35] provides a minimal explanation, there was no sterile neutrinos at the beginning of the Universe.

They were produced by active-to-sterile ($\nu_a \to \nu_s$) neutrino oscillations, a $\nu_a - \nu_s$ superposition forms relatively fast for $\mathcal{O}$ (keV) masses as the oscillation length (or oscillation time) scale $L^{osc} = 4\pi E/\Delta m^2$ is very tiny.

Even if the decay rate of dark matter candidate sterile neutrino is small, X-ray telescope might observe detectable signal from galaxy cluster. Only small mixing angles $\sin^2 2\theta \lesssim 10^{-11}$ are allowed with a limited parameter space. Nonetheless an excess from the XMM-Newton data [36] appeared in 2014, with an unidentified X-ray line around 3.55 keV.

It has been hypothesised that radiative decay of $\sim$7 keV sterile neutrino could caused such excess. There is a current debate on these observations and we will have to wait for future X-ray telescopes with better energy resolution to discriminate between atomic physics effects and dark matter origins.

Even if the constraints are not as stringent as for Primordial Black Holes, sterile neutrino has some difficulties solving the full dark matter puzzle on its own but could be part of a rich Dark Sector and would be exciting new Physics to discover (a more detailled overview can be found in Kopp [37]).

2.2.4 Axions and Axions-Like-Particles

Axion is a hypothetical elementary particle that was proposed to solve the strong CP problem. The strong CP problem arises from the observation that the strong nuclear force, described by the theory of Quantum Chromodynamics (QCD), should violate certain symmetries known as charge conjugation (C) and parity (P) symmetries. However, experimental measurements have shown no evidence of violation of these symmetries, particularly in the electric dipole moment (EDM) of the neutron (a more detailled dicussion can be found in Irastorza [38]).

The phenomenology associated with axions exhibits significant similarities with other light bosons that emerge from the spontaneous breaking of symmetries at a high energy scale. Axion-like particles (ALPs) are not typically associated with the Peccei-Quinn mechanism. As a result, their mass (m_a) and couplings ($g_{a\gamma}$, g_{ae}, etc.) do not necessarily adhere to the relationship with the axion's decay constant f_a.

In general, it is possible for ALPs to be located at any point within the plot depicted in Fig. 2.8, rather than being restricted solely to the red band. For instance, it is widely acknowledged that string theory generally postulates the presence of a substantial quantity of axion-like particles, in addition to the axion itself (e.g. [39]).

Hence, it is crucial to take into account that the majority of axion experiments will possess sensitivity towards axion-like particles as well. In order to discern between a QCD axion and an alternative type of ALP through experimental means (including, among others, super-conduction, X-ray optics and astronomy, high-field magnets, low radioactivity techniques, radiofrequency techniques, atomic physics, low background detection, quantum sensors, etc...), one must depend on the connections between couplings and mass.

It is probable that multiple experimental outcomes will be necessary to validate the identification of a QCD axion.

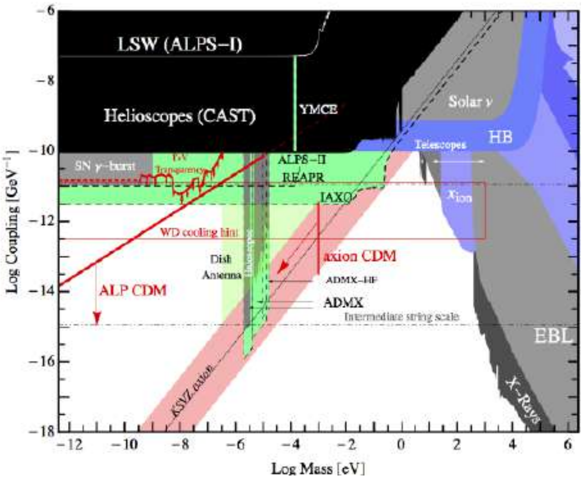

Figure 2.8: Overall panorama of axion and ALP exclusion region in the $g_{a\gamma} - m_a$ plane (coupling to photon), *Taken from Irastorza and Redondo [40].*

2.2.5 WIMPs

As shown in previous chapters, the dark matter puzzle led to a plethora of solutions to consider. There is one we did not mention yet, although it is one of the most investigated, the WIMPs (see Feng [41] for an extensive presentation). Weakly-interacting massive particles (WIMPs) can have a slightly different definition depending on the author, for simplicity we will consider WIMPs to be in a mass range between few GeV and 10 TeV interacting through the SM weak interactions.

Only a tiny portion of the available mass range is covered by the WIMP mass range, as seen in Fig. 2.6. Despite this, WIMPs have captured a significant portion of experimentalists' and theorists' interest in recent years, and the WIMP paradigm is a prerequisite for practically any discussion about DM. Two mains points encapsulate the reason it is so:

- Complementarity of dark matter. WIMP dark matter has wide-ranging effects on a variety of search experiments. Fig. 2.11 is an illustration of this. A 4-point interaction, DM-DM-SM-SM, is usually present if WIMPs are created in the early Universe via thermal freezeout. This leads to the possibility of detecting WIMP dark matter through direct detection, indirect detection, and collider searches, as current dark matter could scatter off normal matter, annihilate, and we could potentially create dark matter in the collisions of SM particles. Dark matter complementarity refers to the notion that dark matter may be found in so many fascinating and connected ways. This presents interesting targets for a wide range of studies.
- The WIMP miracle. In essence, particle theorists, cosmologists and experimentalists have remarkably fortuitous motivations to consider WIMPs. Particle theory has many models beyond the Standard Model (BSM) to explain issues in particle physics at the weak scale. WIMPs are formed with the proper relic density assuming a straightforward production process of thermal freezeout as demonstrated below.

During the 1930s, the Fermi constant, G_F, was introduced in the field of nuclear beta decay research. G_F introduced a new energy scale, known as the weak scale, which has a value approximately equal to $1.2 \times 10^5 \mathrm{GeV}^{-2}$.

The weak scale, represented by m_{weak}, is approximately 100 GeV. The origin of this scale remains elusive, as current knowledge has not provided a comprehensive understanding of the underlying reasons for its significant disparity in comparison to the Planck mass. There exist three fundamental constants: Planck's constant represented by h, the speed of light denoted as c, and Newton's gravitational constant referred to as G_N. A combination of them with the dimension of mass is known as the Planck mass and denoted as $M_{Pl} \equiv \sqrt{hc/G_N} \simeq 1.2 \times 10^{19}$. However, all attempts to comprehend the presence of this scale have consistently resulted in the introduction of novel particles possessing masses in the vicinity of the weak scale.

In the event that Weakly Interacting Massive Particles do indeed exist and exhibit stability, it can be inferred that their production occurs in a way that aligns with the relic density necessary for DM. This suggests that particles driven by efforts to comprehend the Planck mass, frequently serve as highly viable candidates for dark matter.

The production of dark matter would occur through a straightforward and predictable process as a result of being a thermal relic originating from the Big Bang [42]. Fig. 2.9 illustrates the temporal variation of the number density of a thermal relic throughout its evolutionary process. In the early stages, the Universe exhibits high density and temperature, with all particles existing in a state of thermal equilibrium.

As the Universe undergoes cooling, it reaches temperatures T that are lower than the mass m_X of the dark matter particle. Consequently, the population of dark matter particles experiences a decrease due to Boltzmann suppression, which follows an exponential decline characterised by $e^{-m_X/T}$. The quantity of dark matter particles would decrease to zero, if not for the fact that, alongside the process of cooling, the Universe was also undergoing expansion.

Consequently, the density of dark matter particles diminishes to such an extent that their

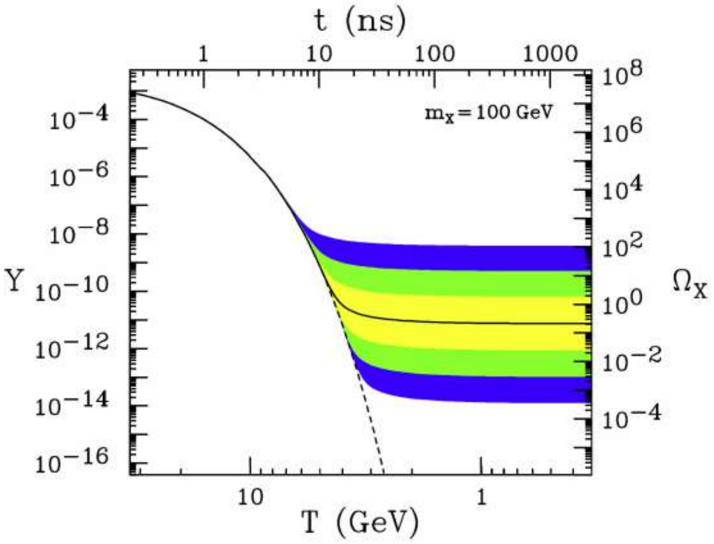

Figure 2.9: The comoving number density for a 100 GeV, DM particle as a function of time t (top) and temperature T (bottom), the consequent thermal relic density (right), and the ratio of number density to entropy density (left). The shaded areas represent cross sections that deviate by 10, 10^2, and 10^3 from the solid contour for an annihilation cross section that produces the desired relic density. The number density of a particle that maintains thermal equilibrium is shown by the dashed contour. *Taken from [41].*

ability to encounter one another and undergo annihilation becomes severely limited. The particles of dark matter subsequently undergo a process known as "freeze out", wherein their quantity gradually approaches a constant value, referred to as their thermal relic density.

The quantitative description of this mechanism is provided by the Boltzmann equation,

$$\frac{dn}{dt} = -3Hn - \langle\sigma_a v\rangle(n^2 - n_{eq}^2), \tag{2.21}$$

where H corresponds to the Hubble parameter, n represents the number density of the dark matter particle X, n_{eq} represents the dark matter number density in thermal equilibrium, and $\langle\sigma_a v\rangle$ denotes the thermally-averaged dark matter annihilation cross section.

Freezeout is defined as the moment when the expansion rate equals the interaction rate, $(n\langle\sigma_a v\rangle = H)$. Presuming freezeout occurs during the radiation-dominated era, we can derive the following expression for the freezeout number density, n_f:

$$n_f \sim (m_X T_f)^{3/2} e^{-m_X/T_f} \sim \frac{T_f^2}{M_{Pl}\langle\sigma_a v\rangle}, \tag{2.22}$$

where the subscript f indicates quantities at freezeout. The exponential function involves the ratio $x_f \equiv m_X/T_f$. It is considered constant and insensitive towards the properties of dark matter, with a value of approximately $x_f \sim 20$. The expression for the thermal relic density, denoted as Ω_X, can be written as follows:

$$\Omega_X = \frac{m_X n_0}{\rho_c} = \frac{m_X T_0^3 n_0}{\rho_c T_0^3} \sim \frac{m_X T_0^3 n_f}{\rho_c T_f^3} \sim \frac{x_f T_0^3}{\rho_c M_{Pl}\langle\sigma_A v\rangle}. \tag{2.23}$$

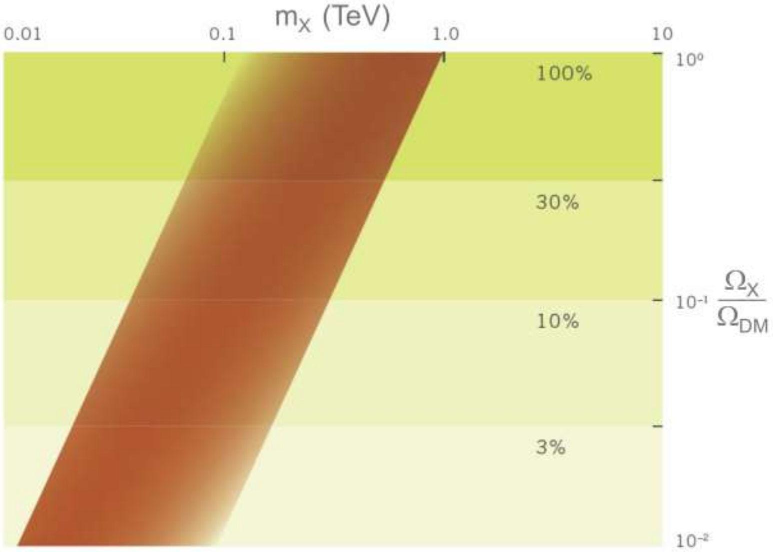

Figure 2.10: Plane for a thermal relic X (m_X, Ω_X/Ω_{DM}), with $\Omega_{DM} \sim 0.23$ the dark matter density expected from Eq. (2.2), shown a band of natural values. *Taken from [41]*

The subscript 0 indicates the present-day values, and it is assumed that the Universe is undergoing adiabatic expansion. The critical density is denoted as ρ_c. It is observed that the thermal relic density exhibits a lack of sensitivity to the mass of dark matter, denoted as m_X, and is inversely proportional to the annihilation cross section, represented as $\langle \sigma_A v \rangle$.

While m_X does not directly participate in Ω_X, it often serves as the sole determinant of the annihilation cross section in various theories. Based on dimensional analysis, the cross section can be expressed as:

$$\sigma_A v = \frac{k g_{weak}^4}{16\pi^2 m_X^2}(v^2 or 1), \tag{2.24}$$

where the factor v^2 is omitted (included) for S-(P-)wave annihilation, and higher-order terms in v have been disregarded. The value of g_{weak} is constant , approximately equal to 0.65, represents the gauge coupling of the weak interaction. The parameter k is used to quantify deviations from this estimated value.

The relic density can be determined as a function of the parameter m_X, given a specific value of k, we can see a band of natural value in Fig. 2.10. It is observed that the mass of a particle constituting the entirety of DM is anticipated to fall within the range of m_X ~100 GeV-1 TeV. Additionally, a particle accounting for 10% of DM is projected to have a mass ranging from m_X ~30-300 GeV. Chapter 5 will discuss with greater details the search for low mass dark matter hence cover the mass range of low mass WIMPs.

Due to the aforementioned reasons, WIMPs are commonly present in numerous BSM physics models. The plethora of models and their respective particles as well as the absence of an indisputable discovery has raised some concern regarding the WIMPs paradigm. Taking a stance on this matter is well above the aim of this Thesis, it can nonetheless be argued that models such as SUSY[7] are able to produce particles (e.g. mixed Higgsino-Bino neutralinos

---

[7] Independently discovered in the context of quantum field theory, with a new type of symmetry of spacetime and fundamental fields, along with emergence of string theory in the 1970s, supersymmetric (SUSY) extensions to the Standard Model has mostly been driven by the presence of the gauge hierarchy

up to 1 TeV) that would solve the muon $g-2$ anomaly[8], the gauge hierarchy problem and escape current limitations.

WIMPs rate and cross-section

Through the processes $XSM \to XSM$, WIMP might be discovered by its scattering off usual matter (see Sec. 2.3.3). For a WIMP velocity $v = 10^3$ and mass m_X around 100 GeV, the deposited recoil energy is 100 keV at most, necessitating the use of very sensitive, low-background detectors buried far under the surface. Very strongly interacting DM, would be halted by earth or in the atmosphere and would be invisible in the underground laboratory.

Nonetheless, extremely strongly interacting dark matter would be detected by space-based investigations, or it would gravitate towards the Earth's center, with other fascinating and strange consequences [43]. As a result of several constraints coming together to rule out huge scattering cross sections for a variety of DM masses, we can now turn our focus on the weak cross section frontier being explored by underground detectors (see Cooley [44]).

The most stringent constraints for WIMP masses of around 100 GeV come from experiments searching for scattering off atomic nuclei. Scattering off electrons, which is now also being intensively explored (e.g. [45]), is especially efficient for light DM candidates with masses around the GeV scale and lower. Dark matter-quark interactions cause dark matter to scatter off of nuclei. The primary interactions for WIMPs are given with the Lagrangian

$$\mathcal{L} = \sum_{q=s,c,b,t,u,d} \left(\alpha_q^{SI} \bar{X} X \bar{q} q + \alpha_q^{SD} \bar{X} \gamma^\mu \gamma^5 X \bar{q} \gamma^\mu \gamma^5 q \right). \tag{2.25}$$

We should take these interactions into account in the non-relativistic limit given the current dark matter velocities. In this limit, the first terms reduce to couplings that are spin independent while the second terms is spin-dependent. Here, we will concentrate on couplings that are independent of spin. Experiments measure the dark matter-nucleus cross sections

$$\sigma_{SI} = \frac{4\mu_N^2}{\pi} \sum_q \alpha_q^{SI} \left[Z \frac{m_p}{m_q} f_{T_q}^p + (A-Z) \frac{m_n}{m_q} f_{T_q}^n \right]^2, \tag{2.26}$$

with the reduced mass

$$\mu_N = \frac{m_N m_X}{m_N + m_X} \tag{2.27}$$

---

problem. Within these models, it is postulated that each Standard Model particle possesses an accompanying particle (that remains unobserved to date).

These partner particles exhibit identical quantum numbers and gauge interactions as their corresponding SM particles, with the exception of a spin difference of 1/2.

[8] Similar to the electron, the muon exhibits magnetic properties. The parameter referred to as the "g factor" quantifies the magnitude of a magnet and its rotational motion when subjected to an externally imposed magnetic field. The discrepancy observed from the value of 2 (referred to as the "anomalous" component) can be attributed to the presence of higher-order contributions originating from quantum field theory.

By conducting a high-precision measurement of g-2 and comparing it to the theoretical prediction, physicists aim to ascertain the level of agreement between the experimental results and the theoretical framework. Any deviation would indicate the presence of subatomic particles that have not yet been observed.

and the fraction of the neutron's mass carried by quark q, (identical expression for protons)

$$f^n_{T_q} = \frac{\langle n|m_q \bar{q} q|n\rangle}{m_n}. \tag{2.28}$$

It can be parameterized by

$$\sigma_A = \frac{\mu_A^2}{M_*^4}[f_p Z + f_n(A - Z)]^2, \tag{2.29}$$

where $f_{p,n}$ are the nucleon level couplings and $A - Z$ and Z, respectively, are the number of neutrons and protons in the nucleus. DM sees the whole nucleus and cannot resolve individual nucleons at the normal energies of WIMP scattering. Results are generally scaled to a single nucleon and given on the assumption that $f_p = f_n$, or $\sigma_A \propto A^2$.

This assumption dramatically increases scatterings off big nuclei. However, f_p and f_n are not always equal, and this crucial qualification applies to all comparisons of scattering off various target nuclei. Of course, experimental and astrophysical information also affects the event rate seen in a detector. In the case of spin-independent detection, the rate is written

$$R = \sigma_A I_A, \tag{2.30}$$

with

$$I_A = N_T n_x \int dE_R \int_{v_{min}}^{v_{esc}} f(v) \frac{F_A^2(E_R)}{2v\mu_A^2} d^3v, \tag{2.31}$$

where n_X is the local dark matter number density, N_T the number of target nuclei, v_{esc} the halo escape velocity, the local DM velocity distribution $f(v)$, E_R is the recoil energy and F_A the nuclear form factor.

During the last several decades sensitivities have been growing by an order of magnitude every few years, indicating that the field of direct detection is quite active.

2.2.6 Hidden Sector

The hidden sector, alternatively referred to as the dark sector, is a theoretical assemblage of hypothetical quantum fields and their associated particles that are yet to be observed.

The interactions between the particles in the hidden sector and those in the SM are characterised by their weak nature, indirect manifestation, and sometimes involve mediation through gravitational forces or other novel particles. As shown in Fig. 2.6 examples particles within this category of hypotheses encompass many possibilities $MeV < m_\chi < 100\ TeV$, such as the dark photon, sterile neutrino, WIMPS, axion.

In numerous instances, dark sectors encompass a novel gauge group that exhibits independence from the known SM one. The existence of hidden sectors is frequently postulated by theoretical frameworks within the domain of string theory. These phenomena have been identified as potentially significant in the context of dark matter, supersymmetry breaking, as well as addressing the muon g-2 anomaly and Beryllium-8 decay anomaly [46, 47].

The dark photon is a theoretical particle inside the hidden sector. It is postulated to serve as a force mediator analogous to the photon in electromagnetism, with potential connections to dark matter. In a simplified context, the introduction of this novel force can be achieved by expanding the gauge group of the SM to include an additional abelian U(1) gauge symmetry. The dark photon, which can be a spin-1 gauge boson, can be associated with the conventional photon through kinetic mixing. This coupling allows for a very weak interaction with electrically charged particles, making it potentially detectable.

The incorporation of dark photons into the Lagrangian of the SM can be achieved in many ways, the potential interactions between the newly introduced field and the particles in the SM are mostly constrained by the imagination of the theorist and the limitations imposed by existing constraints on particular types of couplings. We will introduced some formalism related to Dark Photon in Chapter 4, as it will be used in the inelastic Boosted Dark Matter analysis.

2.3 Dark Matter detection

Considering the diversity of candidates and the colossal mass range (Fig. 2.6) that defines them, it seems very improbable to identify the nature of dark matter without an experimental effort proportional to the task. Physics is above all an experimental discipline, filled with unexplained constants, fine tuning problems and, at first glance, puzzling observations. Physics needs experiments to guide our understanding of nature.

One could take the Standard Model as an example to illustrate the importance of experiment to cement what might be considered as the most robust theory in Physics. For the last three decades a good portion of the effort was put into WIMPs and we are now building ton-scale detectors that should reach the so-called neutrino fog. Unless progress is made regarding directional detection, to distinguish coherent neutrino scattering from dark matter particles, increasing the volume will only scale the sensitivity as $\sqrt{V}$. As recommended by US strategic roadmaps and APPEC [25, 48] there is a critical need to significantly broaden the experimental program in addition to the well established WIMP searches.

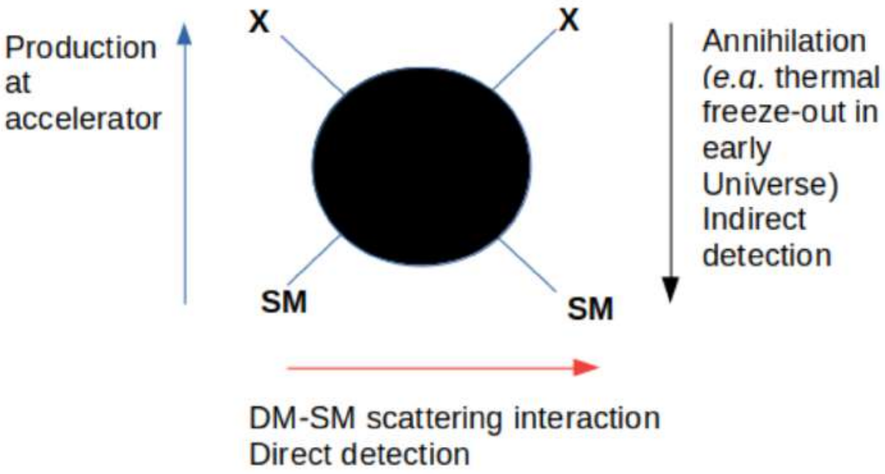

Figure 2.11: WIMP dark matter complementarity. Annihilation of WIMPs to SM particles during the early stages of the Universe is crucial for the occurrence of the WIMP miracle. Consequently, this suggests that there is a high level of effectiveness in the scattering, annihilation, and generation of dark matter. As a result, there are promising rates for direct detection, indirect detection, and collider searches.

2.3.1 Particle accelerators

Historically, particle accelerators were mostly focused on the search for WIMPs when it comes to Dark Matter candidate. We will focus on LHC as it possesses better opportunity to scan higher energy as well as a enhance luminosity to scan higher intensity.

Regrettably, the direct generation of XX pairs is generally not detectable. Therefore, it becomes necessary to search for indications of WIMPs generated alongside other particles. The presence of missing energy and momentum, which is a common indicator in the search for physics beyond the Standard Model, serves as evidence of their existence. This type of analysis can be conducted using fully-defined supersymmetric models or simplified versions, sometimes referred to as "effective models". In effective models, only a limited number of particles, including dark matter, are added, and a small set of defining parameters are considered [49].

In more recent years LHC has greatly diversified its search in the hidden sector (see [50] for a recent presentation made at TAUP 2023). Two frontiers are actively pushed back, the high-intensity frontier aiming at lower interaction strength or coupling to SM and the high energy frontier.

Search related to the intensity frontier occurs in the MeV-GeV range. The small expected coupling (below the weak scale) between the hidden sector and the SM is challenging to detect, but nonetheless points toward relevant and cosmologically allowed interactions. Four main categories of candidates can be investigated,

- fermion, with a possible mediation from heavy neutral lepton that could mix with neutrinos
- vector, mediated for example by a dark vector boson (potentially dark photon) that

mixes with photons

- pseudo-scalar, an ALP could have couplings to gauge bosons or SM fermions
- scalar, with a possible mediation with a new scalar dark Higgs mixing with the Higgs boson, leading to fermion couplings

The energy frontier, in the range GeV-TeV, is facing similar challenges as for previously described search, and rely extensively on model assumption to scan vast parameters space. Those could be simplified models with few relevant parameters (usually choose to define the most sensitive signatures) and a spin-1 or spin-0 mediator between SM and BSM (e.g. Higgs boson). It could be more complete models such as Minimal Supersymmetric Standard Model (MSSM) [51] as well as specific models.

As we saw the search for dark matter signatures at the LHC is a complex and multifaceted endeavor that involves various channels and methods.

- Invisible Signatures: dark matter particles are created as a result of the decay of portal particles or SM particles. Their presence is inferred through missing transverse energy (MET) or transversal momentum (p_T) in the detector. The imbalance in energy and momentum indicates the presence of invisible particles, suggesting the existence of dark matter in the collision events.
- Visible Signatures: Dark mediator can be relatively massive and can decay back into Standard Model particles, especially if they constitute the lightest state in the dark sector. When dark mediators decay into SM particles, these decay products are detectable in the LHC detectors. These visible signatures manifest as unique particle tracks, energy deposits, or decay products that physicists can observe, measure, and analyze.
- Displaced (Long-Lived) Signatures: In some scenarios, dark sector particles can have significant lifetimes, meaning they persist for a relatively long duration before decaying. When these long lived dark sector particles are produced at the LHC, they can travel a measurable distance within the detector before eventually decaying into Standard Model particles. This results in particle trajectories that are displaced from the primary collision point. Detecting such displaced vertices or tracks is a distinctive signature that points to the existence of dark matter or other exotic particles in the dark sector.

The aforementioned energy frontier is mainly investigated by experiments such as ATLAS, CMS, LHCb (with Long Lived Particles searches) whereas the intensity frontier is mostly pushed back by NA64, Belle II, FASER and μBooNE. As for the indirect detection search, analysis are usually strongly model dependent making it a very rich and complex field. This thesis does not aim to extensively explore the different results. Nevertheless we should mention dark photon search as it will be a core component of chapter 4, Fig. 2.12 shows the current and future limits.

2.3.2 Indirect detection

Indirect detection searches aim to identify visible products of dark matter interactions (for recent overviews see [53, 54]). Their searches usually focus on looking for Standard Model particles coming from dark matter annihilation, decays, oscillations, and other mechanisms, as well as the secondary effects of those particles occurring in the Sun, Earth or various others astrophysical sources.

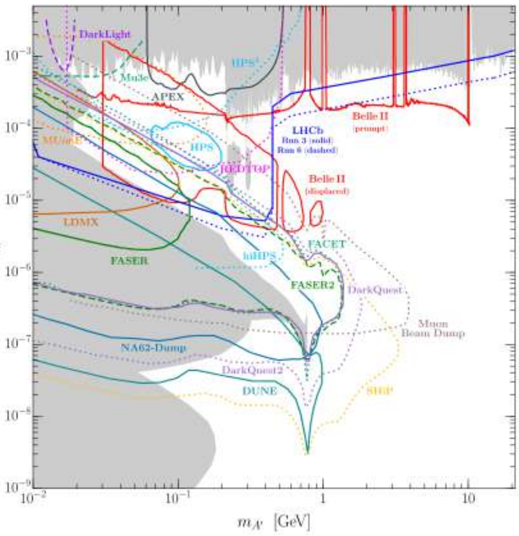

Figure 2.12: Constraints on visible dark photon mass ($m_{A'}$) - kinetic mixing (ϵ) parameter space decays from proton beam dumps, e^+e^- colliders, electron beam dumps, pp collisions, electron on fixed target experiments and meson decays. As well as near-term and future opportunities. *Taken from [52].*

These searches make use of telescopes originally designed for astronomy and astrophysics, which detect various sources of SM particles, in particular photons (Fermi-LAT, CTA), over a wide range of energies as well as Neutrinos (IceCube, Antares/KM3NeT), cosmic ray positrons, cosmic ray antiprotons (AMS) and cosmic ray anti-helium whose observed excess could potentially be due to dark matter.

The methods used in indirect detection searches include analyzing the spatial distribution and energy distribution of particles produced by dark matter interactions, as well as considering the directional information and backgrounds to separate signals from noise. Indirect searches face challenges due to the weak interaction between dark matter and the Standard Model.

This results in a small expected rate of particle production and potential large backgrounds from astrophysical particle production.

Backgrounds vary depending on the particle species and energy. For example, at high-energy gamma rays, backgrounds are essentially non-existent, and the challenge is to collect sufficient statistics. From hot gas and and from various atomic processes there are spectral lines and continuum X-rays. At microwave and radio energies, backgrounds include the cosmic microwave background, thermal emission from interstellar dust and synchrotron radiation from astrophysical sources .

2.3.3 Direct detection

As seen in Fig. 2.6, there is an immense mass range for dark matter candidates to exist.

We gave a brief introduction to wave-like candidate (also called Ultralight Dark Matter, $\lesssim$eV, axion being a prime example, see Sec. 2.2.4). Despite the significance and rapid evolution of this sector, it is beyond the scope of this thesis to provide a description regarding their detection (a review is available in [55]).

We will set our attention toward particle-like candidates, particularly in the range MeV$\lesssim m_\chi \lesssim$ TeV, with a distinction between experiments centering around candidates below and above the GeV scale.

The energy spectrum is the most commonly employed signature. Numerous searches employ detectors that aim to detect the interaction between dark matter particles and the nuclei or electrons of the detector, resulting in nuclear or electronic recoil, respectively.

The identification of the energy that the particle recoil deposited serves as the distinctive characteristic that we are seeking. These studies require meticulous control over the background conditions, which is why they are typically conducted in underground laboratories that are adequately insulated and utilize materials with low radiation levels.

Another approach would be to focus on directionality, if after elastic scattering interactions with nuclei it is possible to retain information regarding the initial direction of the incident particles. A "WIMP wind" arises due to the Sun's rotation within the Galaxy. As a result, it may be inferred that the flux of dark matter would reach Earth aligned with the direction of solar motion.

Consequently, the nuclear recoil would also be expected to occur in the direction of solar motion, specifically, from the direction of the Cygnus constellation [44]. In addition, the diurnal rotation of the Earth results in the detector observing the "WIMP wind" from varying angles during the day at a specific location on Earth [56]. The majority of well-known backgrounds exhibit isotropy, or originate from the Sun. Therefore, the search for angular distribution anisotropy of nuclear recoils would serve as a robust method to distinguish between the anticipated signal and background sources.

Moreover, in the context of searching for WIMPs, it could surpass the limitations imposed by the neutrino fog. The concept of the neutrino fog refers to the threshold cross-section at which Coherent Elastic Neutrino-Nucleus Scattering (CEνNS) occurs.

The term "fog" is now preferred to the previously employed "floor" at it is a better reflection of the complexity and variety of sources and process from which neutrinos could come from. It is nonetheless a serious challenge for direct detection experiment, as it drastically increase the number of dark matter induces events above this indistinguishable background to be able to claim a discovery.

Finally, annual modulation is a very powerful tool, which uses similar assumptions as directionality with possible deviations from the so-called Standard Halo Model (SHM) [57]. While we dedicated an entire chapter 5 to the subject, a proper introduction will be given in the first section.

Direct detection techniques and status

During the past three decades, dark matter direct detection field went through an impressively dynamic and innovative phase. Many technologies, Fig. 2.13, were discovered, refined and utilized to look for and isolate from background, this so hard to detect signal. In this section we will go through some of them:

- Sodium Iodide (NaI). Since the 1990s, detectors with NaI crystal array, equipped with photo-multiplier tubes (PMTs) to detect scintillation light, occupy a central place in the direct detection community. Indeed since 1998, DAMA (and later DAMA/LIBRA with 250 kg cesium iodide (CsI) crystal array) reports a positive dark matter result,

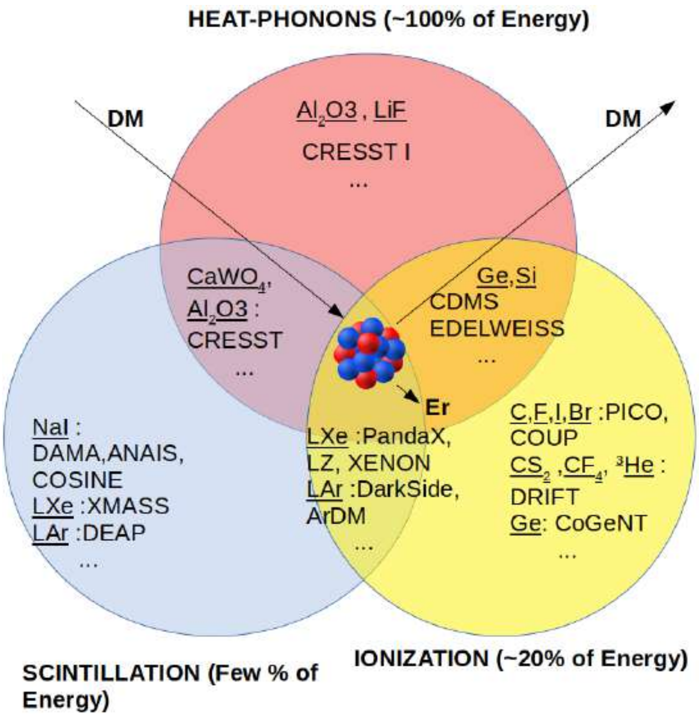

Figure 2.13: Overview of direct detection experiment associated with their target and detection techniques used to look for DM.

finding the expected modulation period and phase for a dark matter interaction [58] (see chapter 5). Early on, this finding was already in tension with other experiments' null results, in the same cross section sensitivity [59]. Collaborations such as ANAIS, COSINE and SABRE have begun to build or run detectors with the same technology as DAMA to find the same modulation signal. Even if the current results are not conclusive, we can note that ANAIS-112, using high purity thallium doped sodium iodide (NaI(Tl)), favor the null-hypothesis with three years of data and is incompatible with DAMA at 3.3σ [60].

- Liquid noble detectors. Two main targets are used: liquid xenon (LXe) and liquid argon (LAr). Calorimeters such as DEAP-3600 and XMASS, with PMTs or other light sensitive device are used to detect scintillation after an interaction; position reconstruction is achieved with 3D hit photon pattern and arrival times. Time projection chamber (TPC) systems employ a dual-phase methodology, involving both liquid and gas phases, in order to expand the number of detectable signals available to them, as they can look at the scintillation as well as the ionization channels. This enhancement provides significant capabilities in terms of background discrimination, particularly for high-mass dark matter candidates, which currently surpasses other methods in the area. Several experiments that employ this methodology include XENON, LZ, DarkSide, and PandaX. Chapter 3 will introduce LAr detectors (which are fairly similar to the LXe-based). Currently noble liquid detectors dominate the "high mass" range for the WIMPs spin-independent cross section Fig. 2.14; LZ published its first results and reaches a 90% exclusion limit at $\sigma_{SI} = 9.2 \times 10^{-48}$ cm^2 for $m_\chi = 36$ GeV$/c^2$ [61]. The future looks bright for liquid noble detectors with DarkSide-20k currently under con-

struction at Laboratori Nazionali del Gran Sasso (LNGS). With 50 t of underground argon and novel photon detection methods (Silicon Photomultipliers, SiPMs) it should reach a 90% exclusion sensitivity for $\sigma_{SI} = 7.4 \times 10^{-48}$ cm^2 at $m_\chi = 1$ TeV/c^2 [62] in case of no detection.
We should also mention, as this is the subject of chapter 5, the so called low-mass WIMP search (1 GeV$\lesssim m_\chi \lesssim$10 GeV) where LAr and LXe TPCs have shown high sensitivity Fig. 2.14 with a dedicated detector such as DarkSide-LowMass [63], a better understanding of low energy events, and a potential presence of the Migdal effect[9]. The potential of LAr detectors to scan a wide region of parameter space is an exciting prospect.
- Cryogenic solid-state detectors, are typically engineered to measure both ionisation and phonon signals resulting from interactions occurring within the detectors. Phonon detectors exhibit superior energy resolution and energy threshold in various materials as compared to ionisation detectors. This allow detectors (CDMS, EDELWEISS, CRESST) using germanium (Ge) and silicon (Si) crystal, as well as calcium tungstate ($CaWO_4$) to reach extremely low energy threshold and to set limits as low as 100 MeV for SuperCDMS, see Fig. 2.15 [64]. Future detector could even reach few tens of MeV [65], a sensitivity achievable for liquid noble detectors only with an experimental confirmation of the Migdal effect.
- Bubble chambers are appealing as dark matter detectors due to their distinctive capability to differentiate between various particle interactions [66]. The thresholds for electron recoiling events are significantly lower in comparison to events that result in nuclear recoils. Therefore, the detectors can be adjusted to activate exclusively in response to nuclear recoil events. The experimental collaborations known as PICASSO and COUPP have merged their efforts to establish a novel collaboration named PICO. The newly formed team aspires to construct and manage a bubble chamber with a capacity of 500 litres in the long run.

Throughout this chapter we emphasised on the complexities present in both the theoretical framework surrounding dark matter as well as in the experimental aspect. At the same time, for brevity, many aspects were omitted, for example we did not discuss spin-dependent cross section [69], as well as Non-Relativistic Effective Field Theory [70] and many others subjects. All the above makes this field especially interesting, with many relevant avenue for discoveries and scientific progress.

---

[9] The interaction between dark matter and a nucleus can result in a low probability of producing detectable ionisation by causing an electron to undergo excitation, which is commonly referred to as the Migdal effect.

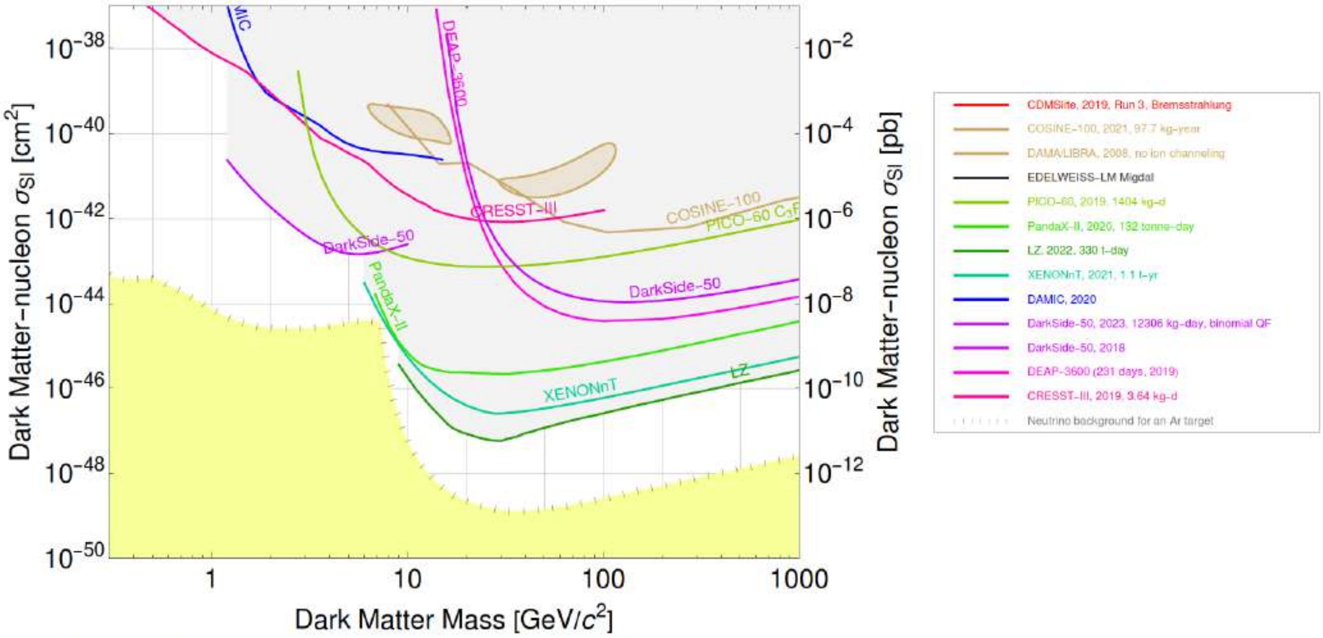

All Nuclear Recoil limits are scaled to a local dark matter density of 0.3 GeV/c^2

Figure 2.14: Current experimental limits in the WIMP mass and cross-section plane. *Made with [67].*

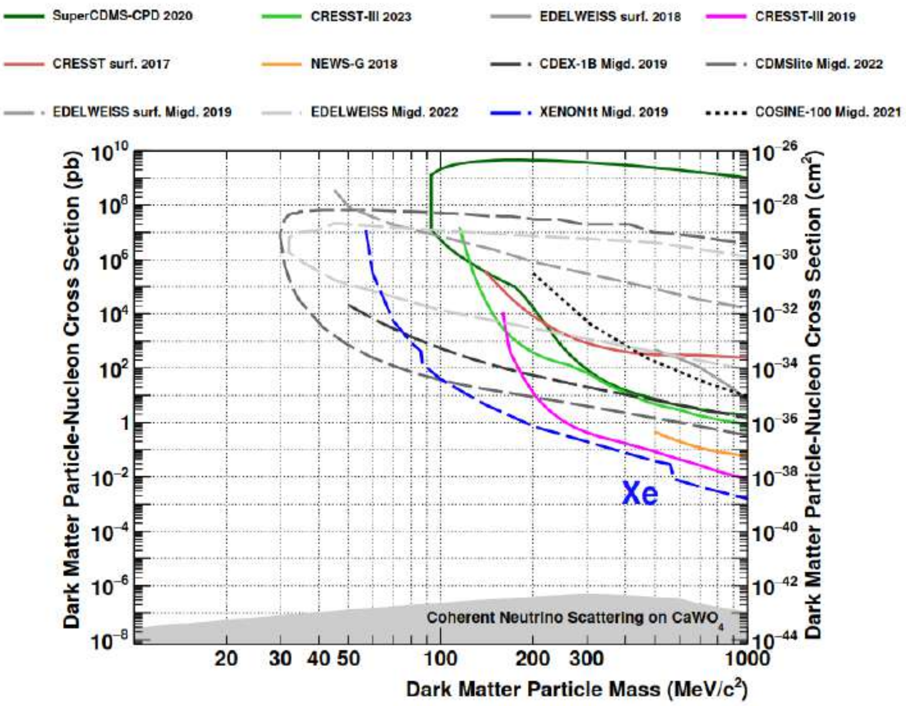

Figure 2.15: Current experimental limits in the WIMP mass and cross-section plane, for low-mass DM, with and without the occurrence of the possible Migdal effect. *Taken from [68].*

Chapter 3

Liquid Argon detectors

Liquid Argon detectors have produced some of the strongest exclusion limits in the WIMP parameter space and are expected to reach the “neutrino fog” within the next generation of experiments.

The detecting characteristics of liquid argon (LAr) are especially helpful for the rejection of background from natural radioactivity thanks to its ability to separate electronic recoils (ER) from nuclear recoils (NR). This is based on crucial findings from experiments such as DEAP-3600, which uses 3200 kg of LAr (Sec. 3.3), and showed a pulse shape discrimination (PSD) power against the electronic recoil background larger than 10^9 [71].

DarkSide-50 experiment (Sec. 3.2) was a dual phase time projection chamber measuring scintillation light and the subsequent electroluminescence light that is caused by the acceleration of drifted electrons in a gaseous region above the liquid. It has demonstrated a remarkable efficiency to provide excellent positional resolution, which is necessary for effective fiducialization, identification of multiple scatters events, and rejection of ER background by PSD and looking at the scintillation-to-ionization ratio [72].

In light of the strong potential that the LAr technology has and building on the success of the previous experiments, the Global Argon Dark Matter Collaboration (GADMC) aspires to integrate all experiments hunting for WIMPs utilizing argon-based detectors, under a uniform approach. The objective is to completely cover the spin-independent coupling WIMP hypothesis from 1 GeV/c^2 to hundreds of TeV/c^2.

Collaborations included within GADMC are DarkSide-50 (Laboratori Nazionali del Gran Sasso (LNGS Italy), ArDM (Laboratorio Subterraneo de Canfranc (LSC), Spain), Mini-CLEAN and DEAP-3600 (SNOLAB, Canada).

Together, they are making preparations for two future detectors. The first of these is called DarkSide-20k, and it is a dual-phase TPC that will replicate the success of the DarkSide-50 design but will have a 50-ton active mass. It is anticipated that its sensitivity will be greater than the previous by a factor of more than 50 at 1 TeV/c^2 and that it will cover a major chunk of the parameter space that is now preferred by supersymmetric models.

1.6 NR events are expected as a consequence of the coherent scattering of atmospheric neutrinos after an exposure time of 100 t-yr. If this were to occur, DarkSide-20k would become one of the very first direct dark matter detection experiment (with LZ [61, 73] and XENONnT [74, 73]) capable of reaching this important threshold.

Towards the end of the next decade, the ultimate goal will be to construct the Argo detector [75] with a fiducial mass of about 300 tons in order to push the detector's sensitivity into the region where the neutrino background becomes not negligible.

3.1 Liquid Argon properties

3.1.1 Scintillation process

When a particle undergoes scattering in a liquid argon medium, it can either experience scattering interactions with the orbiting electrons associated with argon atoms or with the argon nucleus itself (see [76, 77, 78] for a more exhaustive overview of the subject). Most of the nuclear recoils are caused by αs and neutrons whereas electron recoils are usually due to γs, βs, and muons. In either scenario, the atom will remain in an excited state, or either a charged electron or nucleus will be sent recoiling through the liquid argon.

As the charged particle traverses the argon medium, it will experience a constant dissipation of energy. This may occur by the ionization or excitation of argon atoms, or it may occur through the scattering off of more argon nuclei, which will cause those nuclei to recoil as well. In this latter scenario, part of the energy that was originally provided to the argon nuclei will eventually be conveyed to the electrons (either by the recoiling nucleus or in a cascade of recoils originating from the recoiling nucleus), while the remaining energy will eventually be lost as heat.

The transfer of energy from an electron to a nucleus in a single recoil is significantly constrained by kinematic restrictions. When an electron crosses a material, almost all of its kinetic energy is transferred to other electrons. The Lindhard theory [79] describes the energy that is lost directly to electrons as well as the energy that is lost directly to nuclei when a nucleus is travelling through a medium that is homogeneous.

The process of scintillation with liquid argon is shown in Fig. 3.1. An incoming particle scatters off of the nucleus of an argon atom. A subset of the recoiling nuclei may lack sufficient energy to undergo scintillation, leading them to dissipate their kinetic energy as thermal energy. Conversely, certain recoiling nuclei may decelerate and potentially exhibit scintillation by the same mechanism as the initial recoil nucleus. This happens because the recoiling argon nucleus looses some fraction of its energy as it slows to a stop by recoiling off of other argon nuclei. This induces ionization and excitation of surrounding argon atoms, which will result in the formation of N_{ions} ions and αN_{ions} excitons, where α is the ratio between the numbers of excitons and the number of ions.

The exciton has one of the valence electrons that is promoted from the first excited state. The exciton is able to dimerize with a neighboring ground state argon atom because there is a vacancy in the highest orbital. The bonding pairs in the Ar_2 dimer are formed by the valence electron of the ground state argon atom and the excited electron of the exciton. The excimers eventually return to their ground state, at which point a photon is produced.

This phenomenon, which is sometimes referred to as exciton self-trapping, happens on the order of picoseconds and is characterized by the equation

$$\begin{aligned} &Ar^* + Ar \rightarrow Ar_2^* \\ &Ar_2^* \rightarrow Ar_2 + h\nu, \end{aligned} \tag{3.1}$$

where $h\nu$ stands for an ultraviolet photon with a wavelength of 128 nm. Another possibility is for an argon ion to combine with an argon atom in its ground state to produce a dimer in which one of the atom's valence electrons is shared. The charged dimer is then in a position to take possession of a free electron that was previously ionized from an argon atom in the vicinity by the same charged projectile.

Recombination is the name given to the process that separates the dimer into an atom in a doubly excited state and an atom in its ground state. The doubly excited atom will subsequently decay into a single excited state by a process called non-radiative transition, and then it will decay through exciton self-trapping:

$$\begin{aligned} &Ar^+ + Ar \rightarrow Ar_2^+ \\ &Ar_2^+ + e^- \rightarrow Ar^{**} + Ar \\ &Ar^{**} \rightarrow Ar^* + phonons \\ &Ar^* + Ar \rightarrow Ar_2^* \\ &Ar_2^* \rightarrow Ar_2 + h\nu. \end{aligned} \tag{3.2}$$

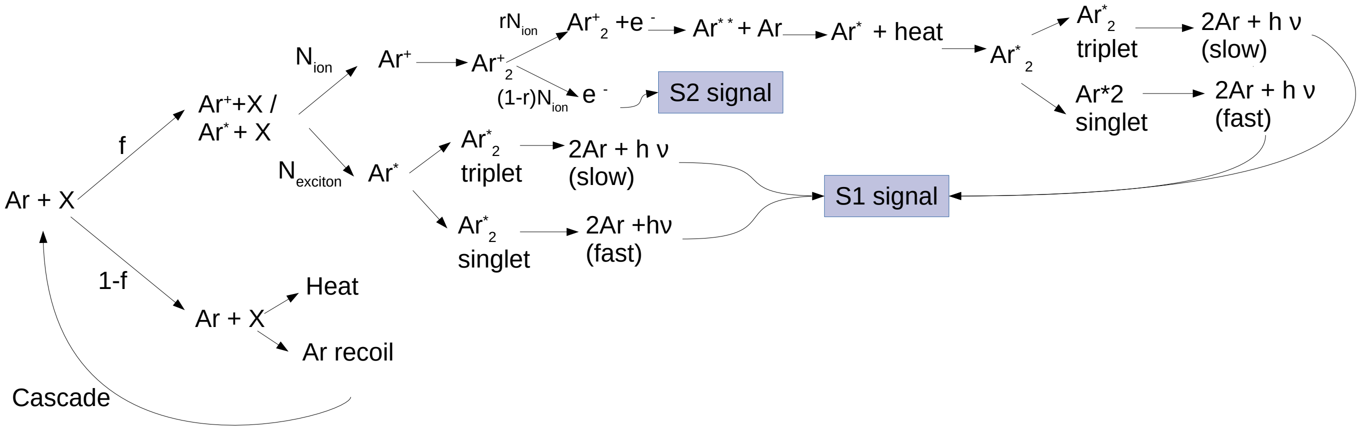

Figure 3.1: Diagram illustrating the scintillation of liquid argon induced by a particle X scattering on an argon nucleus. The energy lost by the recoiling argon nucleus to electrons is measured as f, while the energy lost to other argon nuclei is measured as $(1 - f)$. $N_{exciton}$ and N_{ion} represent the quantity of generated excitons and ions, respectively. The rate at which argon ions seize an ionised electron is denoted as r. In both a single phase liquid argon detector and a double phase liquid argon detector, recombination and the exciton self-trapping processes both contribute to S1. Failure to recombine results in free electrons that may be detected as S2, absorbed by another atom (such as an impurity), or recombine with another ion at a later time.

The density of ions in the LAr has an effect on the recombination probability, which is the likelihood that an electron is captured by a Ar_2^+ dimer [76]. This probability changes depending on the density of the ions in the LAr. In most cases, if there is no electric field present, the likelihood of this happening will be lower than 1. This likelihood, however, decreases when an electric field is present, and it decreases even more as the field strength increases, since a greater number of electrons are displaced before they are able to recombine.

This phenomenon was investigated in [80], and it was shown that a single excited dimer that is created as a result of these activities is in a Rydberg state. This state is characterized by the presence of a bound electron that orbits the Ar_2^+ core. The bound electron and the core possess a spin with a magnitude 1/2; but, since the orientations in which the spins are oriented in relation to one another may change, we find that there are four different potential spin configurations:

$$\begin{aligned} &\text{Singlet State : } \frac{1}{\sqrt{2}}(|\uparrow\downarrow\rangle - |\downarrow\uparrow\rangle) \\ &\text{Triplet State : } \begin{cases} |\uparrow\uparrow\rangle \\ \frac{1}{\sqrt{2}}(|\uparrow\downarrow\rangle + |\downarrow\uparrow\rangle) \\ |\downarrow\downarrow\rangle \end{cases} \end{aligned} \tag{3.3}$$

The two states exhibit spectroscopic equivalence, characterised by an emission peak at 128 nm. However, their temporal decay in liquid argon displays notable dissimilarities.

Due to both the singlet state and the ground state, having a total spins equal to zero, the transition from the singlet state to the ground state is permitted by all selection criteria and therefore takes place on a timeframe of just 6 ns. The decay of the triplet state, on the other hand, is prevented by the conservation of angular momentum since the state has a total spin of 1. As a result, the decay of the triplet state takes place on a significantly slower timeframe of 1.5 μs.

Excitons and ions both form excimers, but they do so through distinct mechanisms. Consequently, it is imperative for the excited electron, arising from the exciton channel, to possess an identical spin to that of the elevated electron. Conversely, the recombination electron will exhibit a spin that is predominantly uncorrelated with the spin of the ionised electron. Furthermore, it is worth noting that both channels exhibit varying probabilities in forming triplets and singlets. The prevailing consensus in the scientific community is that the exciton-to-ion ratio LAr should be below 0.21 for electron recoils and below 1 for nuclear recoils, as supported by [81, 80].

Exciton-to-ion ratios are different for electron recoils and nuclear recoils because the methods through which they lose energy to atomic excitation and ionization are distinct for each kind of recoil. As a result of the fact that the non-unitary recombination probability reduces the number of ions that ultimately create photons, and as the recombination probability rises in tandem with the ionization density, the singlet-to-triplet ratio is also subject to change in accordance with the ionization density of the particle's path. When an electric field is present, this effect becomes stronger, and it has a tendency to make the singlet-to-triplet ratios for nuclear and electron recoils more comparable to one another than they are when there is no electric field present.

It is also possible for competing processes to suppress scintillation light by allowing argon excitons to decay in a way that does not involve radiation. This is possible via a variety of mechanisms, including photo-ionization, biexcitonic collisions, and the Penning process Mei et al. [76]. Since the pace of these processes is related to the exciton density squared, a greater exciton density would, as a result, suppress a greater amount of scintillation. Argon excitons or excimers are able to non-radiatively de-excite using the following three methods, respectively: photo-ionization, biexcitonic quenching, and the Penning process:

$$\begin{aligned} \text{Biexcitonic collisions} &: Ar^* + Ar^* \rightarrow Ar + Ar^+ + e^- \\ \text{Penning process} &: Ar_2^* + Ar_2^* \rightarrow 2Ar + Ar_2^+ + e^- \\ \text{Photo-ionization} &: Ar^* + Ar_2^* \rightarrow Ar + Ar_2^+ + e^-. \end{aligned} \tag{3.4}$$

Because of these effects and the various exciton-to-ion ratios for nuclear and electron recoils, a greater proportion of the scintillation light generated by nuclear recoils will arise from singlet state dimers in comparison to electron recoils. This is because nuclear recoils have larger stopping powers. Because of this disparity, the scintillation pulse that is generated by nuclear recoils will be far quicker than that which is generated by electron recoils. When stopping powers are high, spin-exchange interactions are the primary factor that contribute to this discrepancy.

The temporal profile of the LAr scintillation pulses allows us to differentiate between electron and nuclear recoils. The proportion of the scintillation light that occurred in the first 90 ns of the scintillation pulse is a parametrization that is often used for this. The fact that almost all of the singlet dimers will have decayed by the time 90 ns passes while only a very small percentage of the triplets will have done so justifies the use of this parameter.

The term "Pulse Shape Discrimination," or PSD, is often used to refer to this method. Drift fields in TPCs diminish the total quantity of light generated and decrease the rejection power of PSD. This is because the presence of an electric field may lower the rate at which argon ions recombine, and hence drift fields in TPCs include electric fields. Despite this, tests carried out in DarkSide-50 at a voltage of 200 V/cm revealed that a f90 (3.12) cut with a 90% nuclear recoil acceptance had a rejection power of more than 1.5×10^7 for ^{39}Ar decays that occurred in the range of 8.6–65.6 keV. According to the results of several measurements that were published in [71], the rejection power for electron recoils with energies exceeding 20 keV in the absence of an electric field is estimated to be more than 10^{10}.

The Lindhard's theory provides a broad description of the distribution of the energy that is lost to the nuclei in comparison to the energy that is lost directly to the argon electrons for a charged particle in LAr. The percentage of the projectile's energy that is transferred to the electrons may be calculated using f (fraction of energy that the recoiling argon nucleus loses to electrons) in Fig. 3.1.

The ability of a medium to stop a projectile can be expressed simply as the sum of the nuclear stopping power and the electronic stopping power.

When the energies involved in a collision are low, the amount of energy that is transferred from an ion to electrons is proportional to the amount of momentum that is being transmitted. Because of this, the ability of an electrical system to stop a projectile is often inversely related to the velocity of the projectile. Lindhard and Scharff employ the dimensionless range ρ and energy variables ϵ, defined by Eq. (3.5), in order to normalize their results for the various sets of nuclei that make up the projectile and the target,

$$\begin{aligned}\rho &= r4\pi\eta M_2 a^2 \frac{M_1}{(M_1+M_2)^2} \\ \epsilon &= T\frac{aM_2}{Z_1 Z_2 k q_e^2 (M_1+M_2)},\end{aligned} \tag{3.5}$$

where:

- η is the number density of the target atoms,
- T is the kinetic energy of the projectile ion,
- q_e is the charge of an electron,
- k is Coulomb's constant,
- r is the range of the ion,
- M_1 and M_2 are the masses of the projectile nucleus and the target nucleus, respectively,
- and $a = 0.8853a_0(Z_1^{2/3} + Z_2^{2/3})^{-1/2}$ is the screened potential radius, the Bohr radius is a_0, and the atomic numbers of the projectile and target, Z_1 and Z_2.

The electronic stopping power for low energy ions was subsequently written down by Lindhard [79] as

$$\begin{aligned}S_e &= \kappa\epsilon^{1/2} \\ &\text{with} \\ \kappa &= \xi_e \frac{0.0793 Z_1^{1/2} Z_2^{1/2}(A_1 + A_2^{3/2})}{(Z_1^{2/3} + Z_2^{2/3})^{3/4} A_1^{3/2} A_2^{1/2}}.\end{aligned} \tag{3.6}$$

A_1 and A_2 are the mass numbers of the nuclei of the projectile and target, respectively, and $\xi_e \approx Z_1^{1/6}$. In the low-energy regime, the energy dissipated due to nuclear recoils is commonly described using the concept of hard-sphere scattering. Consequently, a simplified approximation may be made wherein the nuclear stopping power remains constant in relation to the energy of the ion,

$$S_n \approx (\frac{\pi^2}{e})\frac{q_e^2 a_0 Z_1 Z_2 M_1}{(Z_1^{1/3} + Z_2^{1/3})(M_1 + M_2)}. \tag{3.7}$$

The model that was given by Lindhard et al. works well for $\epsilon \geq 0.01$, and as a result, the equations that were published continue to be the most often used.

When discussing the scintillation of noble liquids, it is a common practice to focus on the total amount of energy that is finally lost due to electronic ionisation and excitation. However, a comprehensive explanation of the quantity of scintillation light generated by an ion has to take into consideration the cascade in addition to the parameter f, which in Fig. 3.1 defines the proportion of energy that is transferred directly to these electronic processes.

After taking into consideration the whole cascade, the total proportion of deposited energy that is eventually wasted by electron excitation and ionisation is referred to as the

Lindhard factor, and its abbreviation is f_L. The consequences of the cascade may be calculated using this semi-empirical equation when the projectile and target nuclei are the same (for example, an ^{40}Ar nucleus recoiling in LAr),

$$f_L = \frac{\kappa g(\epsilon)}{1 + kg(\epsilon}, \tag{3.8}$$

with the function $g(\epsilon) = 3\epsilon^{0.15} + 0.7\epsilon^{0.6} + \epsilon$.

However, in cases when the projectile nucleus and the target material are distinct from one another, a simulation has to be carried out in order to account for the whole cascade. To mimic ions' deceleration while moving through a material, Ziegler et al. [82] "Stopping and Range of Ions in Matter" (SRIM) software applies this theory, modifying it so that it takes into consideration the target material's electron density distribution in accordance with the Hartree-Fock theory. This software computes the impacts of the whole cascade and estimates the effect that the projectile ion has on the target material.

The calculations take into account the total amount of energy that is lost as heat as well as the amount of energy that is finally lost due to electron ionisation. Because these calculations are based on a model that is founded on Lindhard theory, and because that theory does not take into consideration the energies at which electrons are bound, the accuracy of these calculations suffers when the projectile's energy is low.

In conclusion, a comprehensive explanation of LAr scintillation has to take into account the light that is lost due to the processes of bi-excitonic quenching. These processes are best represented by Birks's saturation law [83], as its magnitude increases proportionally with the square of the projectile's stopping power,

$$f_B = \frac{1}{1 + kB\frac{dE}{dx}}, \tag{3.9}$$

where kB is Birks' constant, which characterises the consequences of saturation.

The quenching factor is a term that is used to broadly define the non-linearity of the response of a scintillator. In the case of a scintillator that uses noble liquids, the quenching factor is greater than $f_L B = f_l \times f_B$. On the other hand, we often need to represent the quenching in a different way depending on the scintillator.

Since the nonlinearity of a scintillator's response changes depending on the energy and identity of the incident particle, it is usual practise to normalize the scintillator's response to that of an electron. This is done because the nonlinearity of a scintillator's response varies with the energy and identity of the incoming particle.

When talking about the brightness of a scintillation signal, it is a standard practice to refer to it using the units "keV electron equivalent," or keVee for short. These units describe the amount of energy an electron must possess to generate an equivalent quantity of scintillation light. Hence, the ratio between an energy measurement expressed in keV and keVee units usually approximates the quenching factor. This phenomenon occurs due to the inherent tendency of electrons to undergo minimal quenching.

3.1.2 Underground Argon

There is a high concentration of ^{40}Ar in the atmosphere with 0.934% of terrestrial atmosphere being Argon and ^{40}Ar/^{36}Ar $= 298.6$ in air, and its manufacture on a commercial scale is not too costly. ^{40}Ar is not a radioactive isotope. However, there is also a trace amount of cosmologically activated radioactive isotopes of argon, most notably ^{42}Ar, ^{39}Ar and ^{37}Ar. The concentration of ^{39}Ar is only at trace levels in atmospheric argon (AAr) [84], but for the purpose of a DM detector, it presents a number of serious difficulties.

The DarkSide-50 data were dominated by ^{39}Ar decays during the time when the DarkSide-50 TPC was being filled with AAr. The β decays coming from ^{39}Ar were the primary contributor to the trigger rate, and a large number of pile-up events was seen despite a drift time of several hundred of microseconds. This will become a considerably bigger issue when dealing with detectors that are larger. In addition, the abundance of ^{39}Ar events lowers the sensitivity of the WIMP search, considering the leaking of electronic recoil background in the nuclear recoil zone.

The activation of ^{40}Ar by cosmogenic processes results in the production of ^{39}Ar in the atmosphere. Additionally, it may be generated in the subsurface environment by the neutron capture by ^{39}K or alpha emission by Ca. The cosmogenically protected argon found underground has a lower concentration of ^{39}Ar. For the purposes of DarkSide, a facility owned by Kinder Morgan recovered underground argon (UAr) from wells in Western Colorado. Fermilab was the location where the argon was put through the processes of purification and distillation. In April of 2015, the DarkSide-50 TPC was loaded with argon, which has a low radioactivity level, and data collection got underway for more than 3 years.

It was discovered that the activity of ^{39}Ar was $\sim$ 1400 times lower than in the argon present in the atmosphere. For next-generation GADMC detectors, DarkSide-20k and ARGO, it is essential to purchase UAr on a massive scale and purify it. At a production rate of several hundred kilogrammes per day, the Urania project is extracting and purifying argon from CO_2 wells at the Kinder Morgan Doe Canyon Facility in Cortez, Colorado. The argon that is recovered will go through a process of chemical purification as part of the Aria project before it is injected into the LAr TPC. Aria is made up of two cryogenic distillation columns named Seruci-I and Seruci-II, each measuring 350 metres in height and having a processing diameter that is distinct from the other.

These columns are able to separate isotopes. The method will not only lower the concentration of the ^{39}Ar isotopes in the already ^{39}Ar-depleted argon, but it will also reduce the traces of N_2, O_2, and Kr to levels that are suitable for a DM experiments.

3.2 DarkSide-50

DarkSide-50 is a detector placed under Italy's Gran Sasso mountain range, in hall C at LNGS. It is made up of three detectors that are stacked within one another, as illustrated in Fig. 3.2. The detectors are as follows, beginning from the outer shell: a water Cherenkov detector (WCD), a liquid scintillator veto (LSV), and a liquid argon time projection chamber (LAr TPC). The LAr TPC is made out of an active volume of LAr that aims to detect DM and, more precisely, WIMP particles. For neutrons, gamma rays, and cosmogenic events

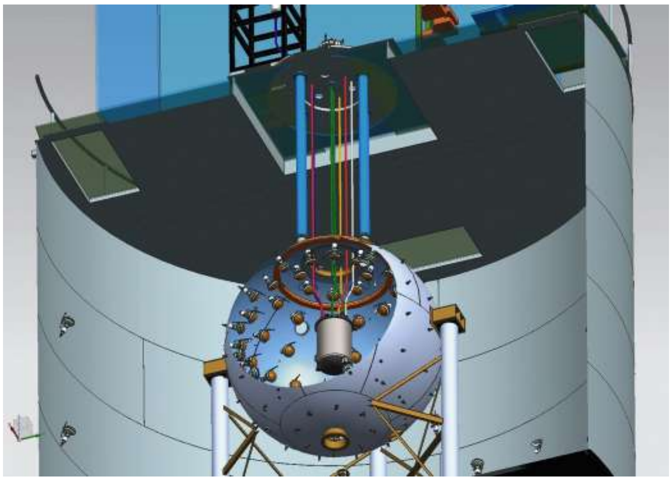

Figure 3.2: DarkSide-50's nested detector system. The WCD is the outermost grey cylinder, the LSV is the sphere, and the LAr TPC cryostat is the grey cylinder in the centre of the sphere.

(such as muons and their follow up events), the LSV serves as a shield. In addition to its role as a shield, the WCD also plays an anti-coincidence veto role for cosmogenic events. A presentation of DarkSide-50 design can be found in [72].

3.2.1 Water Cherenkov Detector (WCD)

The DarkSide-50 WCD is a cylindrical tank with a height of 10 metres and a diameter of 11 metres that contains water of very high purity. The water tank, which was initially a component of the Borexino Counting Test Facility, is now used by the WCD. While travelling through the water, muons and other charged relativistic particles may emit Cherenkov photons, which can be detected by the WCD's 80 ETL 9351 8" PMTs, which are mounted on the side and the bottom of the device. Reflector material composed of Tyvek-polyethylene-Tyvek is used to cover the inside surface of the WCD.

The WCD, acts as a strong protection against the external background radiation, which includes neutrons coming from the walls of the surrounding wall and gamma rays. Additionally, it performs the function of a veto for muon and muon-induced secondary particles. In the WCD, Cherenkov signals are produced either by the muons themselves or by their follows-up. According to the findings of Borexino's observations, the muon flux in the LNGS is equal to $3.41 \pm 0.01 \times 10^{-4}$ $\mathrm{m}^{-2}\mathrm{s}^{-1}$. Every day, there are still around 2000 muons that go through the WCD. The cosmogenic muons have the potential to generate high-energy neutrons, which are able to break through the shielding and deposit energy in the TPC. The WCD performs the function of an active veto in order to identify muons that can be responsible for these neutrons.

3.2.2 Liquid Scintillator Veto (LSV)

The DarkSide-50 LSV is a 4 meter diameter sphere made of stainless steel containing 30 tonnes of boron-loaded liquid scintillator. There are three basic components that make up the boron-loaded liquid scintillator:

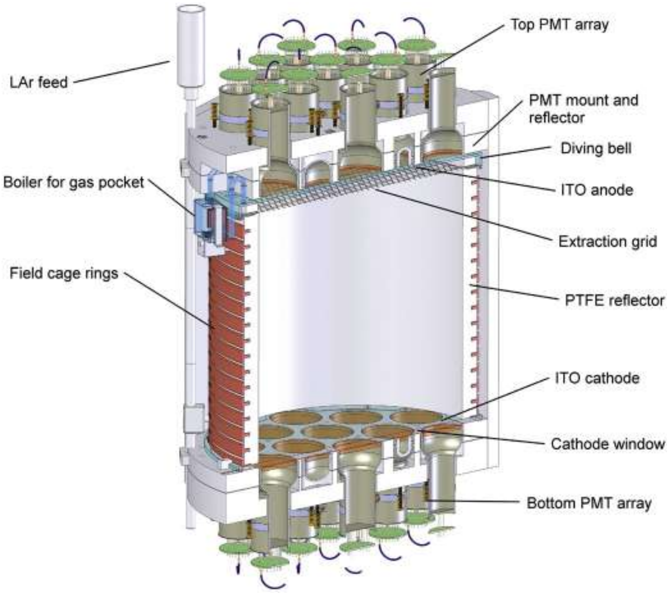

Figure 3.3: Cut-view of DarkSide-50 TPC

- 2,5-diphenyloxazole
- trimethyl borate
- pseudocumene

In the LSV, pseudocumene is the principal scintillator used.

^{10}B makes up 20% of trimethyl borate, it has a significant thermal neutron capture cross-section. Because of this, the LSV functions as an efficient neutron veto. 2,5-diphenyloxazole act as the wavelength-shifter.

For the purpose of detecting scintillation photons, an array consisting of 110 Hamamatsu R5912 LRI 8" PMTs has been installed on the inside surface of the sphere. A prompt thermalization signal and/or a delayed signal after neutron capture inside LSV is left behind by neutrons when they enter the TPC, making it an active shield for neutrons. Boron-loaded scintillators are able to effectively eliminate neutron background thanks to a process known as the neutron capture reaction $^{10}\text{B}(n, \alpha)^{7}\text{Li}$.

The capture of ^{10}B neutrons may take place in any of the following two ways:

1. $^{10}\text{B} + n \rightarrow \alpha(1775\ keV) + {}^{7}\text{Li}(1015\ keV)$ (BR: 6.4%)
2. $^{10}\text{B} + n \rightarrow \alpha(1471\ keV) + {}^{7}\text{Li}^{*}$ (BR: 93.6%), $^{7}\text{Li}^{*} \rightarrow {}^{7}\text{Li}^{*}(839\ keV) + \gamma(478\ keV)$.

It is quite probable that the γ resulting from the decay of $^{7}\text{Li}^{*}$ to ^{7}Li will leave a signal in the LSV that can be detected. Both the γ and the ^{7}Li have very short track lengths, which means that all of their energy is deposited inside the LSV. However, the scintillation output of the two is comparable to an electron with an energy of between 50 and 60 keV because ionisation quenching has a significant suppressing effect on it.

3.2.3 Liquid Argon TPC (LArTPC)

Fig. 3.3 presents a cut-view of the DarkSide-50 TPC. The active LAr volume is a cylindrical section containing 46.4 ± 0.7 kg of liquid argon. It has a height of 36 centimetres and a diameter of 36 centimetres. At the very top of the LAr volume lies a layer of argon gas that is 1 centimetre thick. The PTFE (polytetrafluoroethylene) reflector has a thickness of 2.54 centimetres and makes up the cylindrical wall of the TPC.

Windows made of fused silica may be found at both the bottom and the top of the active volume. Arrays of 38 Hamamatsu R11065 3" PMTs that are submerged in LAr see the active volume via the fused-silica windows. Nineteen of these PMTs are located on each of the top and bottom of the array. Tetraphenyl butadiene (TPB) is used to cover the inside surfaces of the fused-silica windows and the Teflon. TPB is able to transform the 128 nm UV scintillations emanating from LAr into visible photons, which can then be detected by the PMTs.

On both sides of the fused-silica windows, a thin layer of transparent and conductive indium tin oxide is applied as a coating. Because of this, the inner window faces are able to function as a grounded anode at the top, while a high voltage is delivered to the bottom, and the outside surfaces are maintained at the average PMT photocathode potential gradient.

The whole TPC structure is encased in a cryostat made of double-walled stainless steel, and it is kept together by rods that extend from the top of the cryostat and pass through the WCD and LSV. Insulation made of many layers of mylar may be found inside the space that is formed by the cryostat's walls. The cryostat is maintained at a 89 K by use of an external circulation loop of pure liquid argon and the mylar insulation, while the temperature on the exterior of the cryostat is kept at ambient temperature.

Indium tin oxide anode and cathode planes, as well as a grid and a field cage, are the components that make up the electron drift mechanism of the DarkSide-50 TPC. The grid is a hexagonal mesh that has been carved from a stainless steel foil that is 50 micrometres thick and has high optical transparency (at normal incidence, more than 95% transparent). It is positioned 5 millimetres below the liquid-gas contact. Ionisation electrons in the LAr are propelled upwards because of the voltage that is applied between the grid and the cathode. This voltage generates a vertical electric field.

The field cage is made up of copper rings that encircle the Teflon cylinder wall. These copper rings are retained at graded potentials in order to maintain a consistent drift field over the active volume.

Single Phase detectors are just looking at scintillation light and function without the presence of any drift field. Under these circumstances, the likelihood of recombination is very close to 1, which means that almost all of the visible energy is dissipated as the scintillation light (called S1). DEAP-3600 is an example of a LAr single-phase detector, and the following section will provide a more in-depth description of it.

An electroluminescence signal (called S2) will also be accessible in the event that a drift field is applied up to the gas pocket located above the LAr phase. Electrons that are accelerated excite the atoms of argon gas, which then emit light via a process known as electroluminescence. This process is analogous to the exciton-self-trapping mechanism. The S2 signal is proportional to the number of electrons that make it to the gas pocket without recombining in the liquid argon,

$$S_2 = g_2 Y_{s2}(1 - r(E_{rec}))N_{ions}. \tag{3.10}$$

The S_2 gain, g_2, was determined to be 23 ± 1 pe/e^- in DarkSide-50 (more discussions in Chapter 5).

The signal has a duration of around 3.4 microseconds, which is much longer than the scintillation pulse in LAr. Within the framework of the conventional WIMP analysis, the S1 light makes it possible to disregard the electromagnetic background. In 2018, the DarkSide-50 experiment was able to set the strongest WIMP exclusion limit over 20 GeV/c^2 in LAr as a result of this, in addition to the radio-pure level that was attained [72].

On the other hand, due to the strengthening of S2 in comparison to S1, the S1 pulse may not be discernible at extremely low energies. In DarkSide-50, the S1 trigger requires two or more PMTs to detect at least 0.6 PE within one hundred nanoseconds; this trigger may not be triggered below 10 keVnr.

As a result, a search for low-mass WIMPs associated with dark matter was carried out by using the S2 signal as the trigger. Despite the unavailability of the PSD, the achieved remarkably low background level and the exceptional quality of the conducted calibration at low energy facilitated the exploration of WIMPs down to a threshold of 0.6 keVnr, which established the world's strongest exclusion limit in the WIMP mass range of 1.8–10 GeV/c^2 [85].

3.2.4 Slow Control parameters

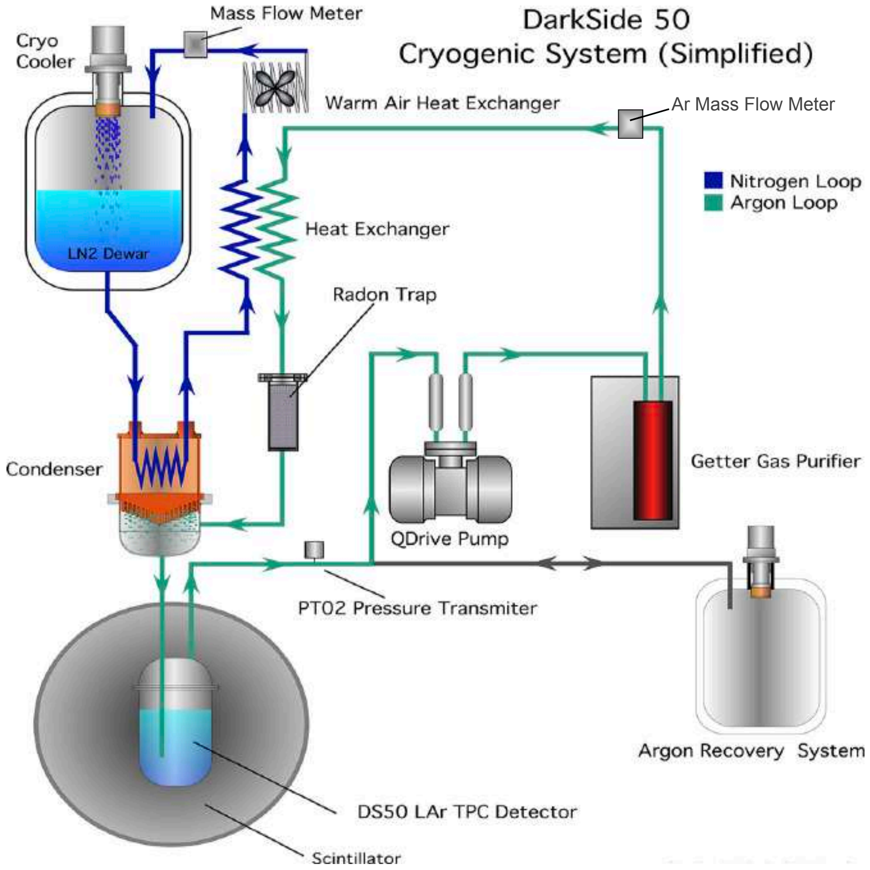

Figure 3.4: Overview of the DarkSide-50 cryogenic system.

The evolution of the cryogenic system was continuously monitored with sensors placed at various locations. The emphasis is put towards four main concerns:

- Thermodynamic, the temperature, pressure and flow of the Argon and Nitrogen loop are monitored in order to asses the condition of the LAr volume
- Radon Trap, as its increase in temperature yields an increase in the background rate
- Getter, to purify Argon from contaminants with an impact on the average detected PE per ionization electron and scintillation photon
- Drift/extraction field, with an impact on the average detected PE per ionization electron

The electron drift system is comprised of several components, including the ITO anode and cathode planes, a field cage, and a grid that serves to separate the extraction and electron drift regions. A vertical electric field is generated by applying voltage between the cathode and grid, which facilitates the upward drift of ionisation electrons. In order to maintain a uniform drift field within the active volume, copper rings at graded potentials are positioned outside the cylindrical PTFE wall.

The generation of the secondary scintillation signal is facilitated by the establishment of an adjustable potential difference between the grid and anode, which in turn generates the necessary electric fields to extract electrons into the gas and subsequently accelerate them. The data presented Chapter 5 were obtained using specific cathode and grid potentials, resulting in electric fields for extraction, drift, and electroluminescence of 2.8 kV/cm, 200 V/cm, and 4.2 kV/cm, respectively.

The cryostat is cooled through the utilization of an external circulation loop. The flow rate of argon gas extracted from the cryostat is 30 std L/min. This gas then exits the detector system and enters the cryogenic and purification system. This system is situated in a clean room that is specifically designed to suppress radon and contains all the necessary equipment that directly interfaces with the detectors.

The gas is routed through an SAES Monotorr PS4-MT50-R-2 getter, which effectively diminishes the presence of contaminants such as O_2 and N_2 to levels below one part per billion. Subsequently, the gaseous argon undergoes pre-cooling within a heat exchanger, followed by going through a radon trap containing cold charcoal.

This trap is maintained within a temperature range of 185 to 190 K. Subsequently, the argon is subjected to liquefaction through the utilization of a heat exchanger that is cooled by liquid nitrogen. The control of loop cooling power is implemented in order to ensure a consistent pressure within the cryostat. The pressure exhibits oscillations within a range approximately centred around the established set point of 1080.0 mbar.

3.3 DEAP-3600

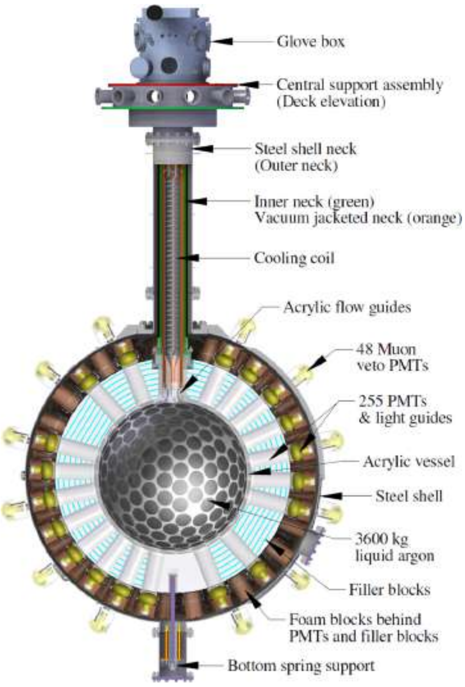

Figure 3.5: The acrylic container, light guides, filler blocks, steel shell, neck, and glove box are all shown. The muon veto water tank and the wavelength-shifting coating covering the acrylic vessel's inside are not visible.

The DEAP-3600 experiment is situated 2 kilometres below ground level at SNOLAB, which is located in Sudbury, Ontario. DEAP has been specifically engineered to detect WIMPs within a mass range of around 30 GeV to 10 TeV.

The DEAP-3600 experiment is situated at a depth of more than 2 kilometres below in order to mitigate the effects of cosmogenically activated isotopes and atmospheric shower particles on the detector. In the absence of the protective shield constituted by the two-kilometer layer of rock, the detector would experience an overwhelming influx of background events, rendering it saturated. However, WIMPs possess a low interaction cross section, which enables them to go unimpeded.

The design and construction of the detector are described in full in [86]. Fig. 3.5 shows that the detector is made up of a sphere of acrylic that is filled with liquid argon and is surrounded by 255 PMTs. A particle's interaction with LAr results in the production of UV scintillation photons that have a wavelength of 128 nanometers. The energy that is deposited in the LAr is used to calculate the number of photons that are created. These photons find their way to the interface between the LAr and the acrylic.

Because acrylic is not transparent to UV light, a layer of TPB, has been placed on the inside surface of the acrylic volume. This layer had a thickness of 3 micrometres. After passing through this layer, the UV photons are converted to visible light, which enables them to travel through the acrylic light guides and arrive to the PMTs that are positioned at the ends of these light guides. When a photon enters a PMT, it sets off an avalanche of electrons, which is then detected by the readout circuitry as a voltage spike.

A coordinate system was established with the intention of using it to pinpoint the exact locations of events that occurred inside the detector, with the center of the sphere that is holding the liquid argon as the origin. The Z-axis extends in a direction that is vertically upward towards the neck.

The diameter of the inside of the acrylic sphere is 85 centimetres. The acrylic sphere is first filled with liquid argon up to a height of 55 centimetres above its center, then the remaining 30 centimetres are filled with gaseous argon. The total mass of argon in liquid form is calculated to be 3279 kg

Thermal insulation and neutron shielding are provided by filler blocks that are made up of alternating layers of high density polyethylene and Styrofoam. These blocks are used to fill the area in between the light guides. Polystyrene is used to fill the voids that are left between the PMTs.

Through a neck that is located at the very top of the sphere, one may fill the primary detector chamber. The temperature of the argon is maintained between 84 K and 87 K by a cooling coil made of stainless steel that is located in the neck. An upward flow of gaseous argon occurs thanks to the acrylic flow guides at the bottom of the neck, into the cooling coils.

Cross-section of the DEAP-3600 detector is shown in Fig. 3.5, with selected components highlighted. A vacuum jacket acts as an insulator around the neck. The detector is completely encased in a steel casing from top to bottom. The detector is protected from neutrons coming from the outside world by a water tank that completely encases the steel casing. The muon veto mechanism relies heavily on the water tank in order to function properly.

On the steel shell, there are 48 PMTs that face outward in order to gather the light created by muons as they go through the WCD. They function using a mode known as self-trigger. They have been split up into six groups of eight for easier management. A group is considered "active" when even a single PMT found inside it is more than the predetermined limit.

When the veto system detects that there are three active groups, a signal is sent to the digital trigger module informing it about the satisfaction of the trigger condition. This causes the PMTs to be read out. As this happens, it is possible to veto all detector events that occurred within a certain length of time following the trigger. This makes it extremely simple to subsequently eliminate such events from the data set. In order to facilitate the DM search, the muon veto time cut was calibrated to reject 95% of all muons that came into contact with the water tank.

Some background in the data-sets is caused by the muon flux that is left over from the showers that are created by cosmic rays. These showers produce a wide variety of different particles, the vast majority of which are halted in their tracks as soon as they reach the surface of the planet. However, owing to the large amount of energy and mass that muons possess, they are able to pass through matter for a considerable distance before being halted. At SNOLAB, the muon flux was measured and found to be below 0.27 muons/m^2/day.

These muons, when they interact with the rock under the surface, may result in the production of neutrons. The muon detector is open to receiving both these muon-induced neutrons as well as the muons themselves. If a muon were to enter, it would be easily rejected. However, the muon has the potential to activate detector components in addition to the LAr itself, which will result in a delayed background that is associated with the muon.

Vetoing events up to one second after the muon veto mechanism has been activated, it is to exclude these backgrounds as much as possible. It is important to keep in mind that muon-activated neutrons reach DEAP even if the original muon has not passed through the water tank.

As previously mentioned, PMTs detect the scintillation photons. After a photon interacts with the photocathode of the PMTs, it induces the emission of an electron through the photoelectric process.

The aforementioned electrons are commonly referred to as photoelectrons (PE). The PE initiate an amplification process in the PMTs, resulting in the generation of a voltage spike that is directly proportional to the quantity of PE released by the incident photons. Hence, the magnitude of the collective voltage surge originating from all PMTs exhibits a direct relationship with the quantity of scintillation light present in the LAr.

Our variable for the total charge will be qPE, it is simply define as,

$$qPE = \sum_{i=1}^{255} \frac{TotalQ_i}{SPE_i} \tag{3.11}$$

with the charge found in the i^{th} denoted as $TotalQ_i$, and a calibration constant SPE_i representing the charge a single PE creates in each PMT. The acquisition window start 2.5μs before the trigger event, and last until 13.5μs after.

The calibration of the SPE constants is performed at regular intervals using an optical fibre and LED-based light injection device. Upon the entry of the LED light into the light guide, it undergoes reflection, with a portion of it being directed onto the PMT. Additionally, approximately 20% of the light is directed towards the interior of the detector, it functions as a diffuse light source for all PMTs located within an approximate angular range of 50 degrees from the light guide.

The obtained values as well as numerous others constants from calibrations are recorded and kept in the DEAP database. These constants encompass readings from slow control systems as well as input values for afterpulsing models. F_{prompt} is the name given to our PSD variable for distinguishing between electron recoils and nuclear recoils,

$$F_{\text{prompt}} = \int_{-28ns}^{60ns} PE(t)dt / \int_{-28ns}^{10\mu s} PE(t)dt, \tag{3.12}$$

with $PE(t)$ following Eq. (3.11) without taking the total charge. According to this given definition, nuclear recoil events characterised by substantial populations of short-lived singlets are expected to exhibit a high F_{prompt}, whereas electron recoil events characterised by significant populations of triplets are expected to have an F_{prompt} lower.

3.3.1 Digitizer and PMT Saturation

This data acquisition system (DAQ) is responsible for extracting the PMT signal, performing necessary processing, converting the analogue voltage signals originating from the PMTs into

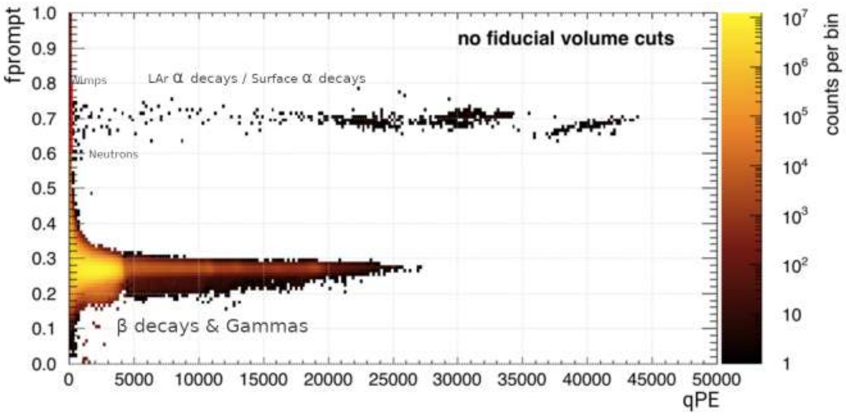

Figure 3.6: Distribution in the F_{prompt} vs qPE plane of LAr scintillation events with a clear separation between ER (lower) and NR (upper) bands

a digital format suitable for storage on a hard drive, and ultimately preserving the data by saving it onto a disc. The CAEN V1720 and V1740 digitizer modules play a crucial role in the acquisition and processing of data. These modules are responsible for capturing and converting analogue signals into digital format. Additionally, they provide the detection and classification of various event types, including the prompt qPE event.

The V1720s possess a sampling rate of 250 MS/s, whereas the V1740s exhibit a sampling rate of 62.5 MS/s. The V1720s are employed in the WIMPs search. The V1740s are designed to handle high-amplitude PMT pulses that would cause saturation in the V1720s. Consequently, the pulses undergo a tenfold reduction in amplitude and experience broadening before to their transmission to the V1740s.

In addition to the phenomenon of digitizer saturation, PMTs demonstrate non-linear characteristics when a large number of PEs are generated.

After a digitizer reaches its saturation point, the signal undergoes a process of truncation or "clipping". When a photomultiplier tube is exposed to a significant amount of light, the linear relationship between the amplitude of the voltage spike produced by the PMT and the intensity of the incident light on the PMT photocathode is broken. Consequently, a reduction in the signal strength of an interaction is observed.

The concentration of light in a few PMTs is observed in events that take place near the interface between the LAr and acrylic vessel. Conversely, events occurring in the centre of the LAr volume exhibit a very uniform distribution of light across the detector. Events that occur in close proximity to the edge would consequently experience a greater impact from digitizer clipping and PMT non-linearity compared to events that take place further away from the edge.

Furthermore, the impact on the high-energy reconstructed events is accompanied by a notable influence on the proportion of total light within the prompt time window, as proportionally less light are detected within the prompt windows due to clipping we observe a reduction of F_{prompt}.

Chapter 4

Sensitivity to inelastic boosted dark matter with DEAP-3600

We investigate a new category of multi-particle dark sectors known as Inelastic Boosted Dark Matter (iBDM) [87] and the potential track they might leave in DEAP-3600. These models are created by combining characteristics of particles generated in annihilation processes in the galactic halo, with a significant Lorentz boost (Boosted Dark Matter) [88] with characteristics of particles that scatter off matter and transition into heavier states (Inelastic Dark Matter) [89].

This combination results in the generation of novel signals that can be detected using standard direct detection techniques. However, the detection of these signals necessitates non-traditional methods, such as searching for high-energy recoil electrons that occur simultaneously with displaced multi-track events.

With a total mass of 3279±96 kg of LAr, DEAP is an optimal detector to scan unexplored parameter space and serves as an excellent proof of efficiency for future LAr detectors such as DarkSide-20k.

In contrast with conventional theoretical approach of constructing realistic models that address physics at the weak-scale and yield dark matter as a result, the attention here is primarily on doing experimental searches, instead of engaging in theoretical model construction. Models for sub-GeV dark matter can initially seem less ambitious and more ad hoc compared to typical WIMPs models.

However, their main purpose is to inspire intriguing and unconventional experimental investigations, leaving "no stone unturned". Furthermore, the assumption of a single dark matter particle, may be an oversimplification, especially when considering the intricate nature of conventional matter. Therefore, it is now highly justifiable to investigate more intricate dark sectors. This research adopts a particular viewpoint and presents original signatures originating from multi-particle dark sectors.

The chapter is structured in the following manner. We will first outline the overall approach behind iBDM models, while in Sec. 4.2, we provide a concise overview of the benchmark DM model used in this search, we analyse important kinematic characteristics of signal events, such as decay lengths and energy spectra of visible particles. Sec. 4.3.2 presents the DEAP-3600 sensitivity to iBDM.

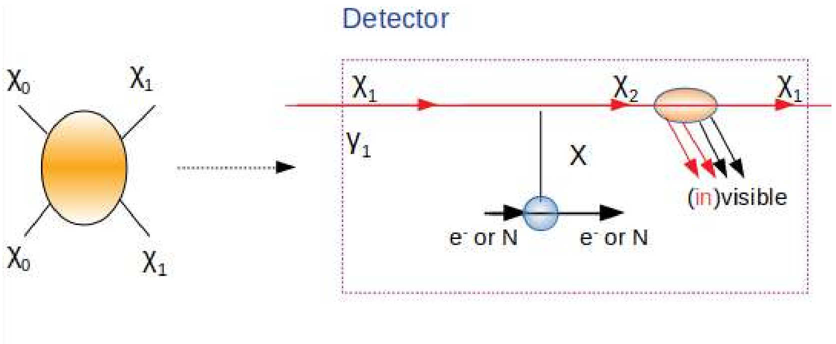

Figure 4.1: iBDM scenarios with the DM-signal processes taking into consideration in this chapter.

4.1 Introduction

The underlying DM model propose the existence of a dark sector consisting of two distinct dark matter particles with a hierarchical mass. The occurrence of boosted dark matter is common in scenarios involving multiple components of DM, as well as in models of single-component DM with non-minimal stabilisation symmetries. In these scenarios, boosted DM can be produced through processes such as DM conversion ($\chi_i\chi_j \to \chi_k\chi_l$), decay transition ($\chi_i \to \chi_j + \phi$), 3 → 2 self-annihilation, or semi-annihilation ($\chi_i\chi_j \to \chi_k\phi$, where ϕ is a non-DM state).

In Giudice et al. [87], the theoretical paper we used to start this analysis, the thermal relic abundance is obtain following the annihilation process,

$$\chi_0\bar{\chi_0} \to \chi_1\bar{\chi_1}. \tag{4.1}$$

To be detected, boosted dark matter must possess a significant cross section for interacting with standard model targets, ensuring scattering occurs. As we aim to maintain the most appealing characteristic of the WIMP paradigm, which is that the thermal relic abundance of χ_0 is solely governed by its annihilation cross section and not affected by other factors, it is necessary for χ_1 to have sufficiently effective interactions with the SM in order to keep χ_0 in thermal equilibrium until the freeze-out process of $\chi_0\bar{\chi_0} \to \chi_1\bar{\chi_1}$ occurs.

These $\chi_1 - SM$ couplings provide a potential means of discovering the dark sector, even if the primary dark matter component χ_0 does not have any direct couplings to the standard model.

As a basic model, we provide a two-component DM model of the aforementioned kind, described by the following Lagragian

$$\mathcal{L} = -\frac{\epsilon}{2}F_{\mu\nu}X^{\mu\nu} + \sum_{i=1,2} g_{ii}\bar{\chi}_i\gamma^{\mu}\chi_i X_{\mu} + (g_{12}\bar{\chi}_2\gamma^{\mu}\chi_1 X_{\mu} + h.c.), \tag{4.2}$$

where χ_0 and χ_1 are now defined as fermions. The initial term refers to the phenomenon of kinetic mixing between SM and dark sector (e.g. [90]), which is quantified by the tiny parameter ϵ. Here, $X_{\mu\nu}$ and $F_{\mu\nu}$ represent the field strength tensors for the dark photons and ordinary one, respectively. The couplings g_{11} and g_{12} quantify the strength of the diagonal and off-diagonal currents.

g_{11} refers to the elastic processes that are typically studied in the phenomenology of boosted dark matter scenarios [88]. The latter results in the inelastic mechanisms examined in this work. The relative magnitude of g_{11} and g_{12} is a matter that is entirely dependent on the specific model being used. We assume that the non-diagonal coupling dominates over the diagonal one, $g_{12} \gg g_{11}$.

The primary dark matter component χ_0 does not have any interactions with the Standard Model at the tree-level, making conventional dark matter searches mostly unresponsive to it. On the other hand, the subdominant DM specie χ_1 has notable interactions with the SM through a dark photon X. The Fig. 4.1 depicts the two procedures associated with the direct or indirect detection of the χ_0 and χ_1 dark sector.

As for Chapter 5, our main dark matter candidate, called χ_0, is a non-relativistic particle in the sub-GeV range, without direct coupling to SM. Instead, it undergoes pair-annihilation to produce two χ_1 particles, which can directly interact with SM particles. Their individual relic abundances are determined by the "assisted" freeze-out mechanism [91] resulting in the heavier component becoming dominant and the lighter sub-dominant in the dark matter composition.

Currently, the boosted χ_1 can be generated by the annihilation of χ_0 in the galactic halo, resulting in a flux,

$$\mathcal{F} = 6.1 \times 1.6 \times 10^{-4}\text{cm}^{-2}\text{s}^{-1} \left(\frac{\langle \sigma v \rangle_{0\to 1}}{5 \times 10^{-26}\text{cm}^3\text{s}^{-1}} \right) \left(\frac{\text{GeV}}{m_{\chi_0}} \right)^2 , \tag{4.3}$$

with the reference value for $\langle \sigma v \rangle_{0\to 1}$, representing the velocity-averaged annihilation cross section of $\chi_0\chi_0 \to \chi_1\chi_1$, chosen to ensure the right thermal relic density for χ_0. It has to be noted that after further calculations and discussion with the Ref. Giudice et al. [87] author, there is a factor of 6.1 missing in the paper, because of a different dark halo model being tested.

For weak-scale mass particles χ_0 (approximately 200 GeV), the incoming flux of lighter dark matter particles χ_1 around the earth is extremely low, on the order of $10^{-8}\text{cm}^{-2}\text{s}^{-1}$. Therefore, neutrino detectors with large volume like Deep Underground Neutrino Experiment, Super and Hyper-Kamiokande, are the most efficient choice for searching for elastic signatures (as mentioned in [88]).

Alternatively, if the main relic component χ_0 has a mass in the sub-GeV range, these neutrino detectors discussed earlier may not be optimal for detecting the interactions of χ_1. This is because these detectors have rather high threshold energies, often ranging from several tens to a hundred MeV.

Furthermore, based on the equation Eq. (4.3), it is observed that the flux of χ_1 is inversely proportional to the square of the mass of χ_0. It is noted that the flux can grow significantly, by 4-6 orders of magnitude, when the χ_0 dark matter has a mass in the sub-GeV/GeV region. Despite this increase, the relic density remains consistent with the present-day measurement.

Therefore, it is logical to focus on detectors with relatively tiny volumes and low threshold energies, such as typical experiments for direct detection of dark matter. We will demonstrate that present direct detection experiments for dark matter, such as DEAP-3600, are likely to have enough sensitivity to detect signals produced by boosted (less massive) dark matter particles with masses in the MeV range.

We focus on inelastic scatterings of boosted dark matter as depicted in Fig. 4.1. The scenario presents the occurrence of an incident DM particle χ_1, which is generated through the pair-annihilation of a heavier DM particle χ_0 (for example, at the Galactic Centre).

This process involves a boost factor $\gamma_1 = m_0/m_1$. The incident DM particle χ_1 then interacts with a target recoil (either an electron or a proton) and scatters off to χ_2, a heavier as well as unstable particle, in the dark sector, through the exchange of a mediator particle X, here a dark photon.

This is what is commonly refer as the primary process. The χ_2 subsequently undergoes decay, resulting in a new χ_1 and several other decay products, which may consist of Standard Model particles. In our case we focus on a production of a pair of electron and positiron. This phenomenon is referred to as the secondary process.

When a portion of the secondary process is detectable within the detector (indicated in Fig. 4.1 with a blue boxes), the correlation between the secondary and primary signatures would serve as a strong tool to identify dark matter events from background events.

In addition, the secondary signal can be significantly displaced from the primary vertex with respect to the position resolution of the detector, depending on the chosen parameters. This displacement can be regarded as clear proof of an inelastic scattering process.

4.2 Boosted Dark Matter models

The dominant process to consider is upscattering of the lighter DM species to the excited state, $\chi_1 T \to \chi_2 T$ (primary process), where we denote the SM target by T, either an electron or proton. This is followed by the decay of the excited state (secondary process),

$$\chi_2 \to \chi_1 X \to \chi_1 e^+ e^-. \tag{4.4}$$

The decay can proceed via the on-shell or off-shell mediator X. Both the scattering and decay processes can generate a visible signal. As a first approximation we should consider both these visible signals together, i.e. our signature would be the total visible energy given by,

$$E_{vis} = E_T + E_{e^+} + E_{e^-} \tag{4.5}$$

The relevant differential scattering cross sections and decay width can be found Eq. (4.7) and Sec. 4.3.1. We should note that in the case of elastic scattering, additional contribution to the DM signal can come from fully coherent scatterings of nuclei, $\chi_1 Z \to \chi_2 Z$ that have been studied by Trojanowski [92] and briefly introduced in Appendix C.

This contribution is Z^2-enhanced, which is better than the scattering of protons or electrons (Sec. 4.2.1) that are only Z-enhanced.

On the other hand, for growing momentum-exchange, it becomes quickly suppressed by the relevant form factors. In practice then, it remains important in the limit of low mediator mass, e.g., $m_X \sim \mathcal{O}(10 \text{ MeV})$. When we consider coherent scatterings, the visible energy is again a small recoil energy of the entire nuclei and the e^+e^- energy from the subsequent decay.

The regime with $g_{11} \gg g_{12}$ is dominated by the scattering of $\chi_1 T \to \chi_1 T$, rendering it an identical scenario to the elastic scattering case, with $E_{vis} = E_T$.

From the assumptions detailed above, and Eq. (4.1), we have $E_{\chi_1} = m_{\chi_0}$. In this chapter we will focus our attention on the inelastic scattering case, Eq. (4.4), as it offers an interesting scenario rendering our region of interest (RoI) free from background expectation. On the other hand, the briefly introduced subsequent scenarios offer enhanced expected sensitivity, as demonstrated in [92, 93].

Table 4.1: Table presenting our iBDM model reference points, as detailed in the text. All masses are in MeV and $g12$ is set to unity.

	m_{χ_1}	m_{χ_2}	m_X	γ_1	ϵ
ref1 (red)	2	5.5	5	20	4.5×10^{-5}
ref2 (green)	3	8.5	7	50	6×10^{-5}
ref3 (blue)	20	35	11	50	7×10^{-4}
ref4 (orange)	20	40	15	100	6×10^{-4}

As already mentioned this chapter is based off Giudice et al. [87], hence we utilize their reference points in order to have a direct comparison. Table 4.1 present our iBDM model reference points with their relevant parameters (masses of DM species and dark photon and the coupling constant). A clear distinction between ref1 & 2 and ref3 & 4 has to be established, as they differ regarding the dark photon decay: the first two being off-shell and the others on-shell, leading to 3-body and 2-body decays considerations, respectively.

First, we examine the desired range of mass to achieve a significant flux of χ_1: χ_0 is selected to be within the sub-GeV/GeV range, χ_1 and χ_2 are within the MeV range for sufficient flux and boost factor. If the difference $\delta m = m_{\chi_2} - m_{\chi_1}$ is less than m_X, the decay of χ_2 occurs by an off-shell dark photon, if the difference is larger it occurs with an on-shell one.

There is a maximum of δm that is allowed, for a specific combination of incoming χ_1 with $E_{\chi_1} = \gamma_1 m_{\chi_1}$ and mass of the target, here m_{e^-}, given by

$$\delta m \leq \sqrt{(m_{\chi_1} + m_{e^-})^2 + 2(\gamma_1 - 1) m_{\chi_1} m_{e^-}} - (m_{\chi_1} + m_{e^-}) \tag{4.6}$$

Consequently, the range of possible values for the on-shell dark photon scenario is somewhat restricted. The inequality $\delta m > m_X$ is more readily fulfilled when E_{χ_1} is larger hence an enhanced boost factor. This necessitates a heavier χ_0 and hence a lower flux of χ_1.

In the off-shell as well as in the on-shell scenarios, we observed an primary electron recoil followed by an electron-positron pair production. From [87] we observe that the scattering of electrons can rival the scattering of protons when $m_{e^-} \ll m_X \ll m_p$, and when γ_1 is sufficiently large. This considerations are relevant to maximize the range of parameters we expect to scan as we implement the necessary equations.

4.2.1 Upscattering off electrons

Primary process

We start with the primary process: $\chi_1 e^- \rightarrow \chi_2 e^-$. In order to obtain the distribution of the recoil energies, we calculated with Gaussian quadrature the integral of the differential cross section in the laboratory frame,

$$\frac{d\sigma}{dE_T} = \frac{m_T}{8\pi\lambda^2(s, m_T^2, m_{\chi_1}^2)}|\overline{M}|^2 \tag{4.7}$$

with the matrix element squared,

$$\begin{aligned} |\overline{M}|^2 = & \frac{8m_T(\epsilon e g_{12})^2}{[2m_T(E_{\chi_2} - E_{\chi_1}) - m_X^2]^2} \\ & \times \left[M_0(F_1 + \kappa F_2)^2 + M_1 \left[-(F_1 + \kappa F_2)\kappa F_2 + (\kappa F_2)^2 \frac{E_{\chi_1} - E_{\chi_2} + 2m_T}{4m_T} \right] \right] . \end{aligned} \tag{4.8}$$

M_0 and M_1 are:

$$M_0 = \left[m_T(E_{\chi_1}^2 + E_{\chi_2}^2) + (\delta m)^2 \tfrac{E_{\chi_2} - E_{\chi_1} + m_T}{2} + m_T^2(E_{\chi_1} + E_{\chi_2}) + m_{\chi_1}^2 E_{\chi_2} - m_{\chi_2}^2 E_{\chi_1} \right] \tag{4.9}$$

$$M_1 = m_T \left[\left(E_{\chi_1} + E_{\chi_2} - \tfrac{m_{\chi_2}^2 - m_{\chi_1}^2}{2m_T} \right) + (E_{\chi_1} - E_{\chi_2} + 2m_T) \left(E_{\chi_2} - E_{\chi_1} - \tfrac{\delta m^2}{2m_T} \right) \right], \tag{4.10}$$

where $\kappa = 1.79 = 1 - \mu_p$, the proton anomalous magnetic moment and the phase space function $\lambda(x, y, z) = \sqrt{(x - y - z)^2 - 4yz}$. For the upscattering off electrons this expression is simplified as F1 = 1 and F2 = 0.

Additional kinematics conditions based on PDG (kinematics) [94, Eq. (47.35) therein] are implemented to always have $t0 > t1$,

$$t_0(t_1) = \left[\frac{m_{\chi_1}^2 - m_{T,inc}^2 - m_{\chi_2}^2 + m_{T,out}^2}{2\sqrt{s}} \right]^2 - (p_{1cm} \mp p_{3cm})^2; \tag{4.11}$$

with

$$p_{icm} = \sqrt{E_{icm}^2 - m_i^2}, \tag{4.12}$$

and

$$E_{1cm} = \tfrac{s + m_{\chi_1}^2 - m_T^2}{2\sqrt{s}}, \tag{4.13}$$

$$E_{2cm} = \tfrac{s - m_{\chi_1}^2 + m_T^2}{2\sqrt{s}}, \tag{4.14}$$

with the center-of-mass energy of the $\chi_1 e$ collision,

$$s = m_T^2 + 2E_{\chi_1} m_T + m_{\chi_1}^2. \tag{4.15}$$

For the total cross section the integral is performed from $E_T = 1$ MeV to 700 MeV with a step of $(E_{Tmax} - E_{Tmin})/10000$:

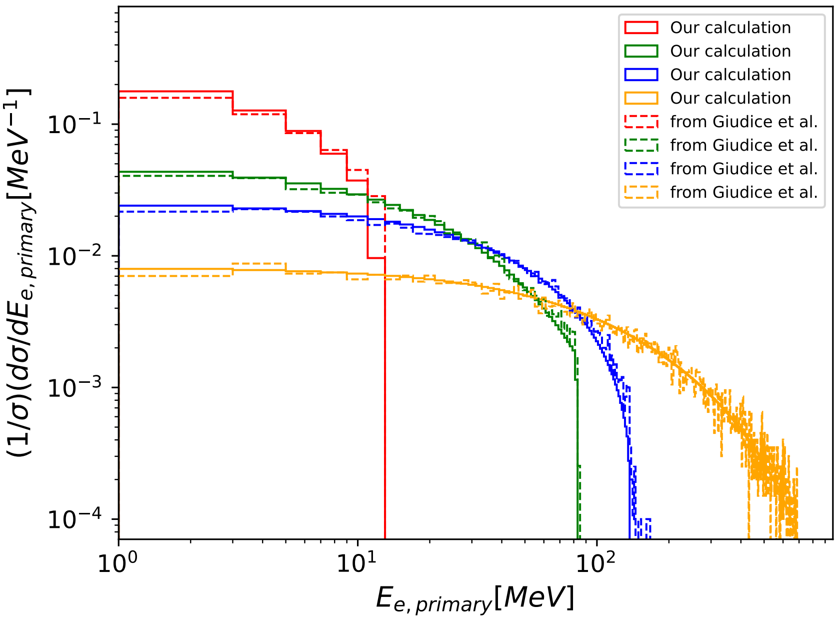

Figure 4.2: Juxtaposition of our result for the calculation of the primary spectrum and the one from Giudice et al. [87]. We respected the color code depicted in Table 4.1, ref1 (red), ref2 (green), ref3 (blue) and ref4 (orange)

$$E_{Tmax} = \frac{s + m_T^2 - m_{\chi 2}^2}{2s}(E_{\chi 1} + m_T) + \sqrt{\lambda(s, m_T^2, m_{\chi_2}^2)}\frac{\sqrt{E_{\chi_1}^2 - m_{\chi_1}^2}}{2s} \tag{4.16}$$

$$E_{Tmin} = \frac{s + m_T^2 - m_{\chi 2}^2}{2s}(E_{\chi 1} + m_T) - \sqrt{\lambda(s, m_T^2, m_{\chi_2}^2))}\frac{\sqrt{E_{\chi_1}^2 - m_{\chi_1}^2}}{2s} \tag{4.17}$$

To produce the primary spectrum Fig. 4.2, the cross section is then calculated for each 2 MeV bins and normalized to unity. We compare our results with MadGraph5_amc@NLO [95] files shared by the author of [87], respecting the color code, resulting in quasi-identical spectrum. As can be seen, in the ref3 and ref4 cases the primary electron spectrum extends towards a few hundred MeV (the indicent χ_1 energy is equal to 1 GeV), which is well above the energy threshold of 10 MeV that we are considering for this analysis.

Hence, most of the scattering events in these scenarios will result in the visible energy deposition above the threshold and even taking E_T alone would be sufficient to estimate the expected sensitivity reach (although we take into account both in Sec. 4.3.2).

On the other hand, we also show in Fig. 4.2 the result for the red benchmark case, in which most of the energy deposition of the primary electron falls below the energy threshold. This is also the case of secondary electrons. In this case, the visibility criteria above the threshold can be satisfied typically thanks to a combination of both E_T and $E_{e^+e\_}$ (secondary process energy). Nonetheless our interest in the inelastic scenario is not only the possibility of high energy threshold but also the distinct kinematic feature it presents in order to have a RoI free from background expectation.

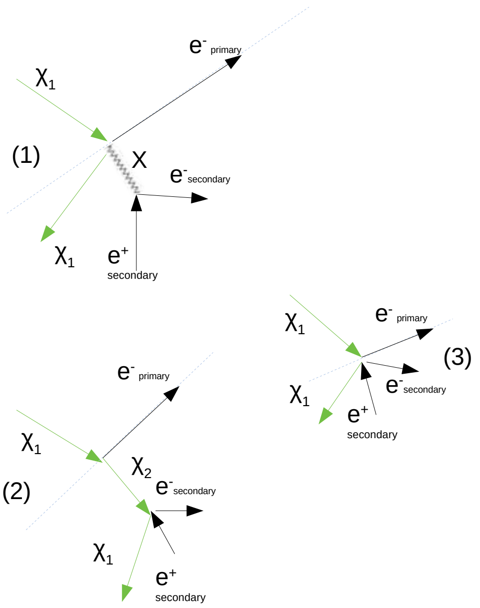

Figure 4.3: Different events shapes for iBDM signals taking into consideration in this analysis, the green solid arrow represent particles that doesn't leave visible tracks, the black solid arrows are used for recoiling e$^-$ and the pair of e$^-$ e$^+$ visible tracks.

Secondary process

We consider three different event shapes for signal events. Fig. 4.3 (3) shows the possibility that the primary scattering and secondary decay occur swiftly, it is anticipated that all three electron tracks will originate from a single vertex point. (1) represents the scenario where χ_2 decays immediately but the dark photon X has a lengthy lifespan, we call it the two-body process (on shell decay of Dark Photon, ref 3 and 4, $\delta m = m_{\chi_2} - m_{\chi_1} > m_X$). Finally (2) shows when χ_2 has a long lifespan, it undergoes decay into χ_1 and an e$^-$ e$^+$ pair by three-body decays (off shell decay of Dark Photon, ref 1 and 2, $\delta m = m_{\chi_2} - m_{\chi_1} < m_X$).

For the secondary spectrum a Monte-Carlo approach has been implemented, using the relevant Lorentz transformation and kinematic equations we found in [20, 87, 96, 92].

For the off shell decay, the simulation goes as follows:

- First we select a random s_2 between s_2^+ and s_2^-, Eq. (4.21), to calculate the decay width integral Eq. (4.18) , if the ratio between this integral and the total decay width integral (calculated with s_2^+ and s_2^-), is below R (random number between 0 and 1) we reiterate this step.

$$\Gamma_2 = \frac{g_{12}^2\epsilon^2\alpha}{64\pi^2 m_{\chi_2}^3}\int_{s_2^-}^{s_2^+} ds_2 \int_{s_1^-}^{s_1^+} ds_2 1\frac{|\overline{A}|^2}{[m_{\chi_1}^2+m_{\chi_2}^2+2m_{e^-}^2-s_1+s_2-m_X^2]^2+m_X^2\Gamma_X^2}, \tag{4.18}$$

the integration limits are:

$$s_1^{\pm} = m_{\chi_1}^2 + m_{e^-}^2 + \frac{1}{2s_2}[(m_{\chi_2}^2 - m_{e^-}^2 - s_2)(m_{\chi_1}^2 - m_{e^-}^2 + s_2) \\ \pm \lambda(s_2, m_{\chi_2}^2, m_{e^-}^2)\lambda(s_2, m_{\chi_1}^2, m_{e^-}^2)], \tag{4.19}$$

$$s_2^- = (m_{\chi_1} + m_{e^-})^2, \tag{4.20}$$

$$s_2^+ = (m_{\chi_2} - m_{e^-})^2, \tag{4.21}$$

with The spin-averaged amplitude squared for fermions:

$$|\overline{A}|^2 = 4\{(s_1 + s_2)[(m_{\chi_1} + m_{\chi_2})^2 + 4m_{e^-}^2] - (s_1^2 + s_2^2) \\ - 2m_{\chi_1}m_{\chi_2}(m_{\chi_1}^2 + m_{\chi_2}^2 + m_{\chi_1}m_{\chi_2}) \\ - 2m_{e^-}^2(m_{\chi_1}^2 + m_{\chi_2}^2 + 4m_{\chi_1}m_{\chi_2} + 3m_{e^-}^2)\}, \tag{4.22}$$

and the dark photon decay width:

$$\Gamma_X = \frac{\epsilon^2 \alpha m_X}{3}\left(1 + \frac{m_{e^-}^2}{m_X^2}\right)\sqrt{1 - \frac{4m_{e^-}^2}{m_X^2}} \tag{4.23}$$

- Else we take a random $\cos(\theta)$,
- Calculate the energy of the electron in the χ_2 rest frame,

$$E_{e^-,\chi_2 r.f.} = \frac{m_{\chi_2}^2 + m_{e^-}^2 - s_2}{2m_{\chi_2}} \tag{4.24}$$

- The energy of the positron in the χ_2 rest frame,

$$E_{e^+,\chi_2 r.f.} = \frac{m_{\chi_2}^2 + m_{e^-}^2 - s_1}{2m_{\chi_2}} \tag{4.25}$$

- The energy of χ_1 in the χ_2 rest frame,

$$E_{\chi_1,\chi_2 r.f.} = m_{\chi_2} - E_{e^+,\chi_2 r.f.} - E_{e^-,\chi_2 r.f.} \tag{4.26}$$

- The momentum of χ_1 in the χ_2 rest frame,

$$P_{\chi_1,\chi_2 r.f.} = \sqrt{E_{\chi_1,\chi_2 r.f.}^2 - m_{\chi_1}^2} \tag{4.27}$$

- The momentum of χ_1 along the z axis,

$$P_{\chi_1,\chi_2 r.f.,z} = P_{\chi_1,\chi_2 r.f.}\cos(\theta) \tag{4.28}$$

- The energy of χ_1 in the lab frame,

$$E_{\chi_2} = \gamma_1 m_{\chi_1} + m_{e^-} - E_{e^-,p} \tag{4.29}$$

$$E_{\chi_1,lab} = \frac{E_{\chi_2}}{m_{\chi_2}}E_{\chi_1,\chi_2 r.f.} + \sqrt{\frac{\gamma_1^2 - 1}{\gamma_1^2}}P_{\chi_1,\chi_2 r.f.,z} \tag{4.30}$$

- And finally the visible energy for e$^-$ and e$^+$, for e$^+$ we take $-\cos(\theta)$,

$$E_{e^{-/+},s(off-shell)} = \frac{E_{\chi 2,rest}}{m_{\chi_2}} E_{e^{-/+},rest} + \sqrt{\left(\frac{E_{\chi 2,rest}}{m_{\chi_2}}\right)^2 - 1} \times P_{e^{-/+}} \cos(\theta), \tag{4.31}$$

with

$$P_{e^-,rest} = \sqrt{E_{e^-}^2 - m_{e^-}^2}, \tag{4.32}$$
$$P_{e^+,rest} = \sqrt{E_{e^+}^2 - m_{e^-}^2}. \tag{4.33}$$

For the on shell decay:
- We take a random $\cos(\theta)$
- Calculate the momentum along the z axis of the Dark Photon in the χ_2 rest frame

$$E_{X,\chi_2 r.f.} = \frac{m_{\chi_2}^2 + m_X^2 - m_{\chi_1}^2}{2m_{\chi_2}} \tag{4.34}$$

$$P_{X,\chi_2 r.f.} = \sqrt{E_{X,\chi_2 r.f.}^2 - m_X^2} \tag{4.35}$$

$$P_{X,\chi_2 r.f.,z} = P_{X,\chi_2 r.f.} \cos(\theta) \tag{4.36}$$

- The energy of the Dark Photon in the lab frame

$$E_{X,lab} = \frac{E_{\chi_2}}{m_{\chi_2}} E_{X,\chi_2 r.f.} + \frac{E_{\chi_2}}{m_{\chi_2}} P_{X,\chi_2 r.f.,z} \tag{4.37}$$

- Take a second random $\cos(\theta_2)$
- Calculate the energy for the secondary spectrum

$$E_{e^-,(on-shell)} = \frac{E_{X,lab}}{2} + \frac{E_{X,lab}}{m_X} \sqrt{\left(\frac{m_X}{2}\right)^2 - m_{e^-}^2} \times \cos(\theta_2) \tag{4.38}$$

$$E_{e^+,s(on-shell)} = E_{e^-,(on-shell)} - E_{X,lab} \tag{4.39}$$

Our simulation returns 10 000 events for each reference point, distributed as shown in Fig. 4.4. It yield a similar spectrum as the one obtained by [87]. We should mention that we are only showing the spectrum for the e$^-$, the e$^+$ gives an identical spectrum, hence most events would have a far greater energy than the 10 MeV threshold once we add the primary, e$^-$ and e$^+$ spectrum. Only ref1 would loose some acceptance due to this cut.

4.3 Inelastic Boosted Dark Matter in DEAP-3600

Now equipped with simulations able to produce the energy spectrum, we will turn our attention toward others relevant parameter of interest such as the decay length. They will help us build the expected signature and assess DEAP-3600 sensitivity to the different scenarios.

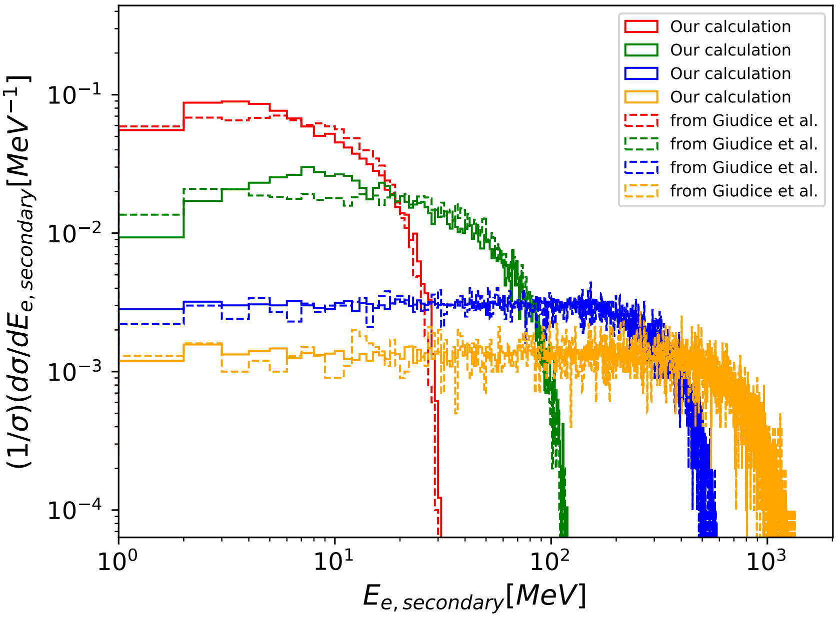

Figure 4.4: Juxtaposition of the secondary spectrum from our calculation and the one from Giudice et al. [87]. We respected the color code depicted in Table 4.1, ref1 (red), ref2 (green), ref3 (blue) and ref4 (orange)

4.3.1 Models considerations for DEAP-3600

One of the most important parameter to construct the signature model for our different iBDM signals is the decay length of either χ_2 or X. We showed in Fig. 4.3 that only scenario (3) would have the two e^- and the e^+ originating from the same vertex point. Whereas (2) and (1), the three body and two body decay cases, emphasize the importance of the χ_2 and X decay lengths, as our visible tracks coming from primary e^- and the e^+ e^- pair would have a noticeable displacement.

We introduced in Sec. 4.2.1 Eq. (4.18) for Γ_2, for which [87] offers a simplification in the regime $m_{e^-} \ll \delta m \ll m_X \ll m_{\chi_2}$,

$$\Gamma_2 \approx \frac{\alpha \epsilon^2 g_{12}^2}{15\pi^2 m_X^4}(\delta m)^5, \tag{4.40}$$

with α the electromagnetic fine structure constant. In the three body case, we would have a sizeable χ_2 decay length $\sim \mathcal{O}$(cm-m).

We obtain the laboratory-frame mean decay length with:

$$\ell_{2,lab} = \frac{c\gamma_2}{\Gamma_2} \sim 16\text{cm}\left(\frac{10^{-3}}{\epsilon g_{12}}\right)^2\left(\frac{m_X}{30\text{ MeV}}\right)^4\left(\frac{10\text{ MeV}}{\delta m}\right)^5\frac{\gamma_2}{10}. \tag{4.41}$$

Fig. 4.5 shows a contour plot of $\ell_{2,lab}$ where the full line represents the displacement between primary and secondary processes in unit of cm. The dashed lines represents, for $E_{\chi_1} = 150$ MeV and three different values of m_{χ_1}, the maximum allowed value δm can take,

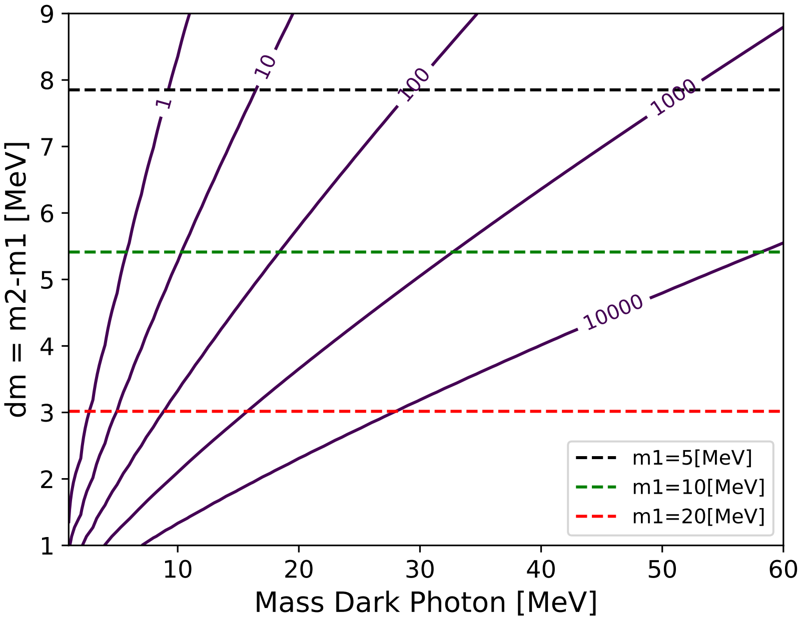

Figure 4.5: $m_X - \delta m$ plane, showing χ_2 decay length in the laboratory frame in cm, with $g_{12} = 1$, $\epsilon = 10^{-3}$, $\gamma_2 = 20$.

following Eq. (4.6). With Eq. (4.41) one could easily obtain an estimation of χ_2 decay length for others parameters than the benchmark scenario one. We compare Fig. 4.5 with [87, Fig. 3 therein], showing identical feature once we change $\gamma_2 = 10$ to $\gamma_2 = 20$, which turned out to be a mistake in the aforementioned paper.

When it comes to the two body decay scenario, the displacement would be caused by the dark photon decay, as χ_2 decays into an on shell X. The dark photon decay width is obtained by Γ_X with Eq. (4.23), resulting in the mean decay length :

$$\ell_{X,lab} = \frac{c\gamma_X}{\Gamma_X} \sim 0.4\text{cm} \left(\frac{10^{-4}}{\epsilon}\right)^2 \left(\frac{20\ \text{MeV}}{m_X}\right) \frac{\gamma_X}{10}. \tag{4.42}$$

Eq. (4.42) results in significantly lower displaced vertex in $\mathcal{O}$(mm), hence we should consider the primary and secondary interaction as one event.

The decay length is of particular importance when it comes the acceptance A_{lab}, which is as a first approximation, 1 when both processes occur in the fiducial volume and 0 otherwise (in Sec. 4.3.2 we will discuss in more details A). Eq. (4.41) returns a maximum value $>$2000cm for ref1 & 2, hence completely outside DEAP-3600. Nonetheless when E_T (recoil energy from primary process) augment $s_{1/2}$ augment, increasing the value of Γ_2 hence $\ell_{2,lab}$ is reduced to $\mathcal{O}$(cm). We calculated A_{lab} to be around 0.34 for ref2 within our simulation. But a dedicated analysis will be necessary to confirm this number taking into consideration DEAP-3600 detector response, geometry etc.

We should mention that as E_{χ_1} decreases the flux increases, making ref1 and ref2 viable options to look for iBDM, within DEAP-3600 reach with 1 year of data, even looking at events with the two processes inside the fiducial volume.

	ref 1		ref 2		ref 3		ref 4	
	A_{tot}	A_{pr}	A_{tot}	A_{pr}	A_{tot}	A_{pr}	A_{tot}	A_{pr}
1 year	48.38	3.69	23.60	15.76	12.63	10.20	3.73	3.47
3 years	145.16	11.18	70.80	47.22	37.94	30.65	11.19	10.41

Table 4.2: Number of events each benchmark model would produce in DEAP-3600, with 1 and 3 years of data, considering an energy threshold at 10 MeV on the total energy deposition (A_{tot}) or on the primary interaction (A_{pr}).

4.3.2 Sensitivity of DEAP-3600

We begin our sensitivity study with a focus on the reference points given in Table 4.1, we calculated the number of expected events in the following manner:

- We first calculate the flux Eq. (4.3) for each reference point,
- Then the expected number of χ_1,

$$N_{\chi_1} = \mathcal{F} t_{exp} S \tag{4.43}$$

- We simplify the interaction length calculation, using an effective surface for DEAP, with $S = a^2 = 2\pi r^2$, hence $V_{DEAP} = a^2 b = \frac{4\pi}{3} r^3$ giving $b = \frac{4r}{3}$
- Allowing us to calculate the probability of χ_1 interaction in DEAP,

$$P_{\chi_1} = \int_0^b dx \frac{1 - e^{x/\ell_{2(X),lab}}}{L_{int}} \tag{4.44}$$

- with,

$$L_{int} = \frac{1}{\rho_{LAr} \mathcal{N}_A \frac{Z}{A} \sigma} \tag{4.45}$$

- Which then gives the expected number of event :

$$N_{ev} = P_{\chi_1} \times N_{\chi_1} \tag{4.46}$$

Our results can be found in Table 4.2, for 1 and 3 years of data. A_{tot} is the acceptance after applying a cut at 10 MeV on the total deposited energy, so $E_T + E_{e^+ + e^-}$, whereas A_{pr} is the same threshold but apply on the primary interaction. We used this threshold as extreme cases to encompass the variety of energy deposition that could occur. Our numbers have to be considered as upper limits due to the poor treatment of A_{lab}, that necessitates a proper simulation in RAT [97] to account for all potential effect related to DEAP-3600. Such simulation is in progress (see Sec. 4.3.3), our toy MC and analytic model allows to validate it.

We can nonetheless confirm that DEAP-3600 is an excellent candidate to observe these scenario as most points are well above the 2.3 signal events corresponding to 90%C. L. upper limit, assuming a null observation over a background free RoI under Poisson statistics.

$A_{tot/pr}$ are calculated thanks to the 2D spectrum depicted in Fig. 4.6 for ref3, as an example. The threshold at 61000 PE (photoelectrons), which corresponds to approximately 10 MeV, is applied on A_{tot}.

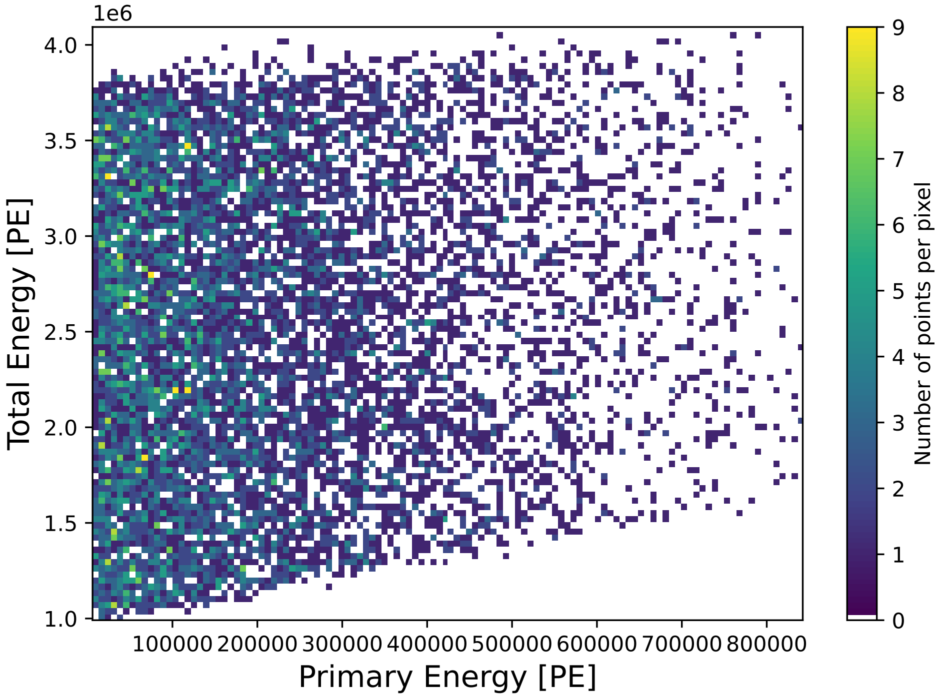

Figure 4.6: Total energy $E_T + E_{e^+ + e^-}$ versus primary energy for ref3 after applying Gaussian smearing to our energy spectrum.

To obtain the energy spectrum in PE, we applied the DEAP-3600 response function, relating the energy deposited to the number of detected PE (see [98]). We define μ and σ, the mean and variance of our Gaussian response:

$$\mu = \langle N_{DN} \rangle + Y_{PE}.E \tag{4.47}$$

$$\sigma^2 = \sigma^2_{PE}.\mu + \sigma^2_{rel,LY}.\mu^2, \tag{4.48}$$

with Y_{PE} the detector light yield, (6.1 ± 0.4) PE/keV$_{ee}$, $\langle N_{DN} \rangle$ the average number of PEs resulting from uncorrelated photons and dark noise in the PE integration window, (1.1 ± 0.2) PE, $\sigma^2_{rel,LY}$ take into consideration variance of the light yield relative to its mean value, $0.0004^{+0.0010}_{-0.0004}$, and σ^2_{PE} a resolution scaling factor that consider the effects such as PE counting noise and the Fano factor, (1.4 ± 0.1) PE.

Our resulting spectrum can be found in Fig. 4.7 and shows the energy in PE assuming the primary and secondary processes both happened within DEAP-3600 LAr bulk, and fully deposited their energy.

An intermediate case in Fig. 4.8, considers only $E_T + E_{e^-}$, where the secondary interaction would occur near the detector wall and the gammas from e$^+$ annihilation would escape (completely similar results, though, if e$^-$ escapes). Considering that an electron with energy around 1000 MeV would travel $\sim$ 40 cm before stopping in LAr [99], we could very well have only a partial energy deposition from e$^+$ or e$^-$.

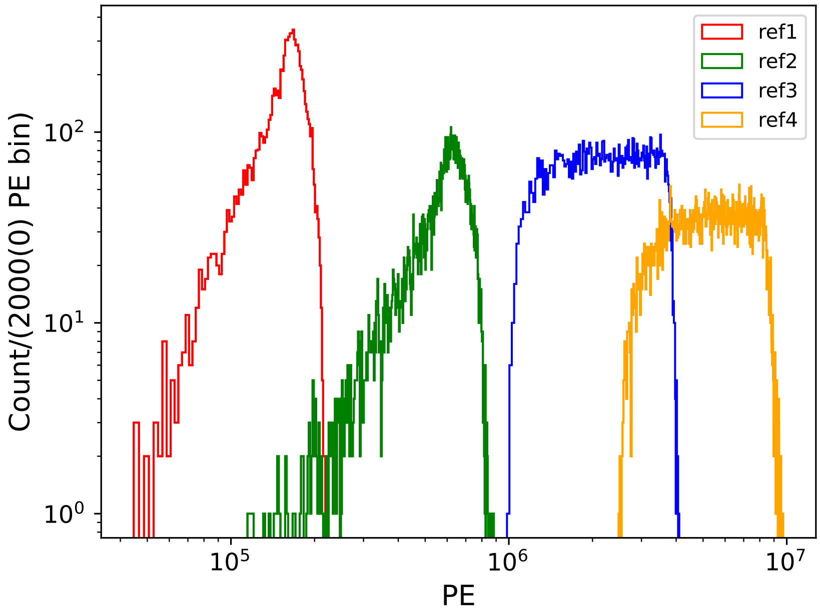

Figure 4.7: Energy spectrum of our 4 reference points, adding the primary and secondary energies. We utilized a binning of 2000 PE for ref1 & 2 and 20000 PE for ref3 & 4.

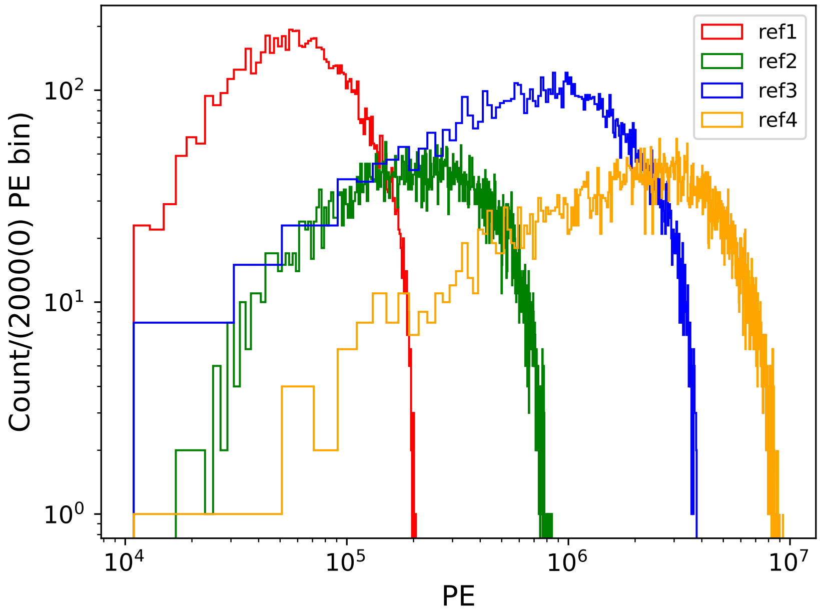

Figure 4.8: Energy spectrum of our 4 reference points, adding the primary and the secondary e^- only energies. We utilized a binning of 2000 PE for ref1 & 2 and 20000 PE for ref3 & 4.

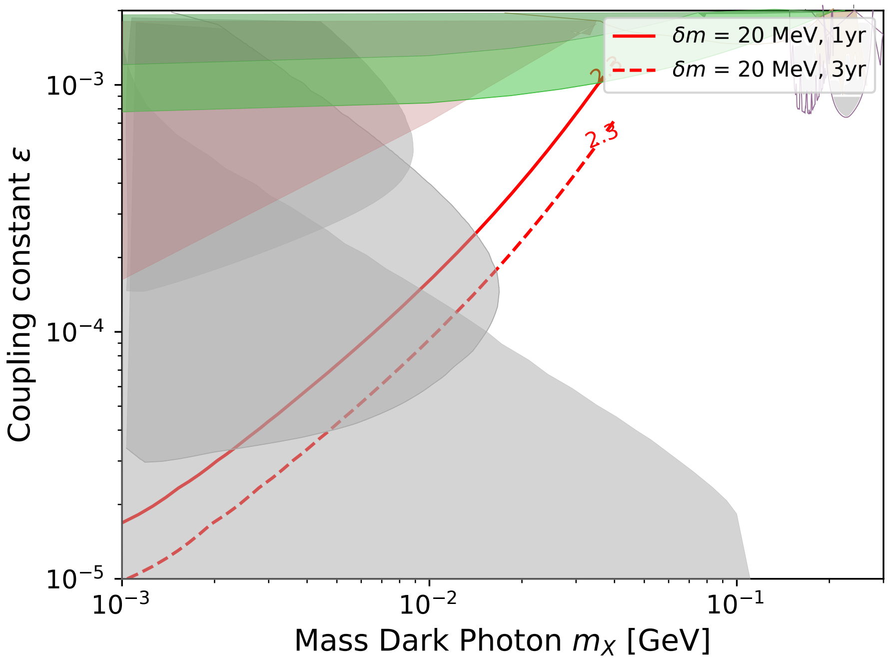

Figure 4.9: DEAP experimental reach in the $m_X - \epsilon$ plane for the visible decay of the dark photon. We used $m_{\chi_1} = 20$ MeV, $\gamma_1 = 100$ and $m_{\chi_2} = 40$ MeV for comparison with [87] . The colored areas are the excluded parameter space from [100].

Finally we turn our attention toward model-independent search, to assess the parameter space DEAP-3600 could cover. Our experimental sensitivity is determined by

$$\sigma \mathcal{F} > \frac{2.3}{A(\ell_{lab}) t_{exp} N_e}, \tag{4.49}$$

where σ is the cross section for the primary process Eq. (4.7), the right hand side is determined by the experimental characteristics and on ℓ_{lab}, which differ from event to event, whereas the left hand side is model dependent, to reproduce [87, Fig.6 therein] we fix E_{χ_1} and δm but let m_X and ϵ vary in σ calculation Eq. (4.7). This allows us to compare our results to other dark photon phenomenology, shown in the $m_X - \epsilon$ plane.

We selected some scenarios to produce our sensitivity plots. Fig. 4.9 presents DEAP-3600 sensitivity for 1 and 3 years of data for the visible decay of the dark photon. We took the same value as in ref4 for m_{χ_1}, m_{χ_2} and γ_1, to allow direct comparison with [87]. In this scenario the A has been set to 1, with $\mathcal{O}$(mm) we do not expect the energy deposition to be bellow 10 MeV even if the secondary e^- or e^+ leave DEAP-3600 without leaving a track. We nonetheless expect the acceptance to be reduce after further limitations on the detector response are considered; Sec. 4.3.3 will introduce the preliminary work effectuated.

Fig. 4.10 shows the case for invisible decay, with parameters, m_{χ_1}, m_{χ_2} and γ_1 from ref1. A is set with the 10 MeV cut applied on E_T (see Fig. 4.6 and discussions), leading to a value of 0.08. This value is a lower limit considering we expect few % of events to also have the

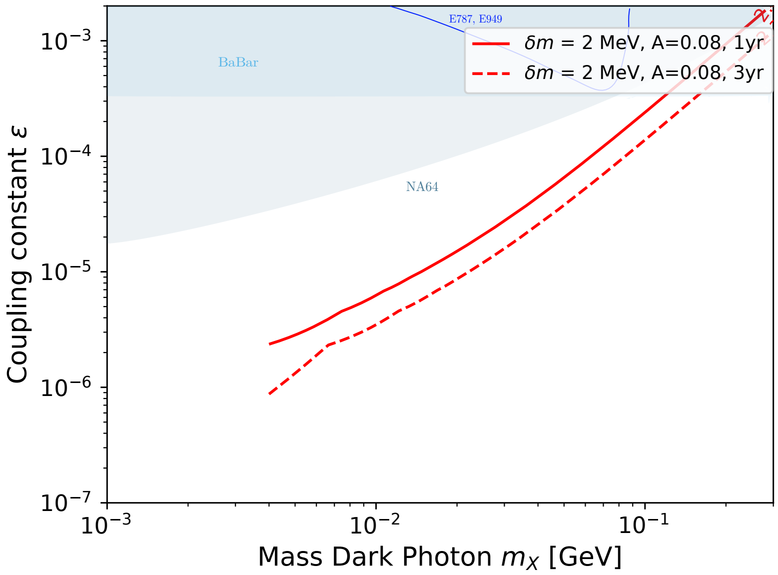

Figure 4.10: DEAP experimental reach in the $m_X - \epsilon$ plane for the invisible decay of the dark photon. We used $m_{\chi_1} = 2$ MeV, $\gamma_1 = 20$ and $m_{\chi_2} = 4$ MeV for comparison with [87] . The colored areas are the excluded parameter space from [101].

secondary process occurring in DEAP-3600. Nonetheless it already shows the DEAP-3600 sensitivity to the considered parameter space, thanks to the higher expected $\mathcal{F}$.

Finally we compared in Fig. 4.11 our sensitivity varying A. We focus on the invisible decay of the dark photon using m_{χ_1}, m_{χ_2} and γ_1 from ref2. Hence our nominal case is with the acceptance calculated for ref2, $A_{pr} = 0.6$ (green curves), we compare it with $A_{lab} = 0.3$ (red curves) in the case where both primary and secondary interaction are forced to happen inside the DEAP-3600 detector.

As we demonstrated in the three sensitivity plots, DEAP-3600 is highly suitable to scan a large part of parameter space unexplored by other experiments. Considering a background free RoI, the required 2.3 events signal statistics is well within the detection capabilities. We should nonetheless mention, that a dedicated analysis on DEAP-3600 detector's response to very high energy inelastic scattering is necessary to efficiently estimate the acceptance. We briefly introduced the subject in Sec. 3.3.1, it will be the topic of our last section.

Lastly, our 10 MeV threshold is motivated by the consideration of background candidates coming from the solar neutrino absorption, in particular ^{8}B neutrinos, and atmospheric one. The latter flux is considered too small to be observed, even with 3 year of data. But ^{8}B solar neutrinos, within a $\sim 1 - 15$ MeV range, have a total flux of $\sim 10^6 cm^{-2} s^{-1}$ [102]. SNO measured the ^{8}B neutrinos flux to be $\phi_{SNO} = 1.76^{+0.14}_{-0.14} \times 10^6$ cm^{-2}s^{-1} [103] at SNOLAB. It is consequently a background worth considering, fortunately for us, this topic is the subject of an on-going analysis within the DEAP-3600 Collaboration. We will make use of their conclusion to improve our analysis. Muon events and their follow-up, cosmogenic events, are also a potential source of background. They are studied in other analysis and will be considered in the final iBDM analysis appropriately.

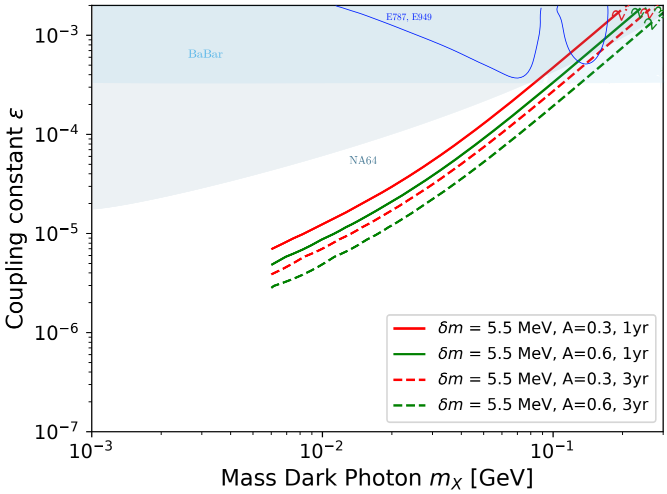

Figure 4.11: DEAP experimental reach in the $m_X - \epsilon$ plane for the invisible decay of the dark photon. We used $m_{\chi_1} = 3$ MeV, $\gamma_1 = 50$ and $m_{\chi_2} = 7.5$ MeV and vary the acceptance A_{pr} to show the impact. The colored areas are the excluded parameter space from [101].

To conclude our section, we will mention some interesting scenario that could be considered in this analysis. The upscattering off electrons could occur in the water Cherenkov tank, leaving a ∼MeV energy deposition in the WCD. Far below the expected energy from muon interactions, and a secondary process within LAr, with expected energy similar to ref1 or ref2 as we are considering off-shell decay of dark photon. If feasible, this scenario would allow higher $\ell_{2,lab}$, hence a higher acceptance. A very similar scenario would have the primary process outside of the detector and only consider the secondary as our expected signature. A challenge arise to discriminate elastic from inelastic scattering, but if achieved, the pair production of e^+e^- alone would be sufficient to detect three body decay scenarios of iBDM. The same considerations could be applied to the upscattering off protons and the coherent scattering with nuclei, with a primary process occurring in LAr, WCD or outside. This processes have been studied in [92], and introduced in Appendix C.

4.3.3 Simulation of the iBDM expected signal in DEAP-3600

We conducted an exploratory analysis of the detector high energy response to understand its behavior and the effectiveness of different cuts to erase pile-up and others instrumental backgrounds we may encounter. Fig. 4.12 shows 80 days of data without the use of any cut, to presents our RoI, with a cut at 10 MeV instead of 2 MeV. The number of events shown can be explained by the lack of data cleaning cuts, much of the future work will be dedicated to have a background free RoI, keeping the acceptance as high as high possible.

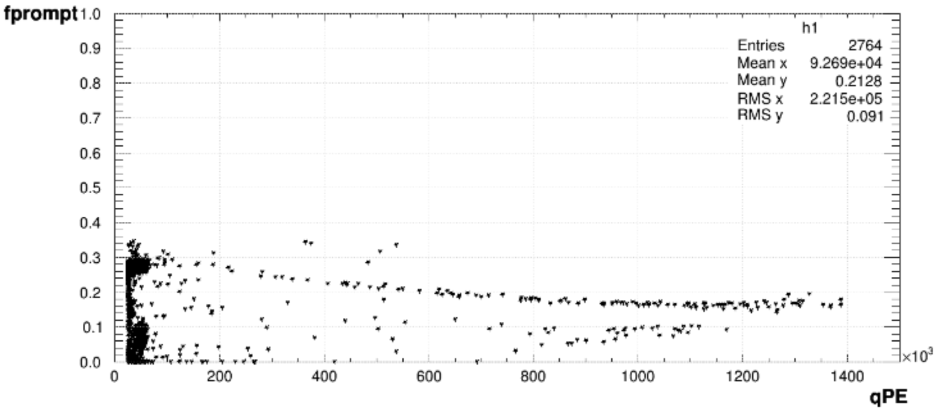

Figure 4.12: F_{prompt} vs qPE plot, showing the population of events with a cut on $F_{\text{prompt}} < 0.35$ (Electronic recoil band) and qPE>20k (>2 MeV), for an 80 days dataset.

We produced a Monte Carlo simulation of high energy electron recoil events, this simulation is comparable to a simplified elastic scattering scenario. We simulated 23 runs with 1000 events at a given energy, from 1 MeV to 50 MeV. The goal of this analysis was to understand: What is the fraction of events lost Fig. 4.13 due to (1) partial energy deposition, (2) DAQ splitting one physics into multiple data events, (3) fraction of good events lost due to data cleaning analysis cuts?

We obtained Fig. 4.13 by integrating the peak at the desired energy and divide it by the total number of simulated events.

The main effect influencing the detector response in this analysis is partial energy deposition, DAQ splitting one real event into multiple ones does not significantly lower the value in qPE and the data cleaning cuts does not seem to erase a lot of good events (order of 0.3%).

At low qPE we observed events that have been split by the DAQ, these events disappear with data cleaning cuts, such as cut on event time, number of early pulses and fraction of the total event charge (in units of PE) which appears in the PMT with the most charge in the event. We also observed events that do not have the nominal energy deposition. This is related to the location of the events, as depicted in Fig. 4.14, energy deposition versus R is shown with a clear relation established between the two. We expect this effect to occur as events situated close to the wall have a greater chance to experience digitizer clipping hence a lower detected energy.

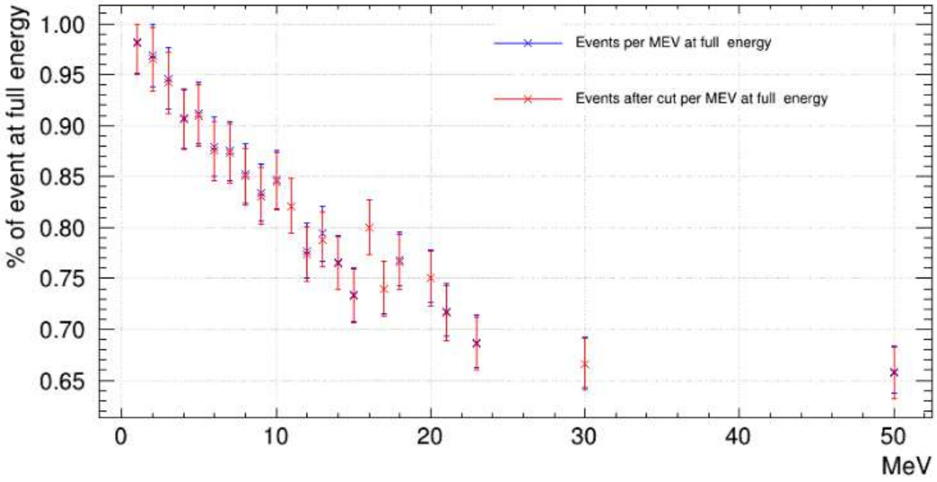

Figure 4.13: Graph representing the fraction of events at the full energy peak (with and without cuts).

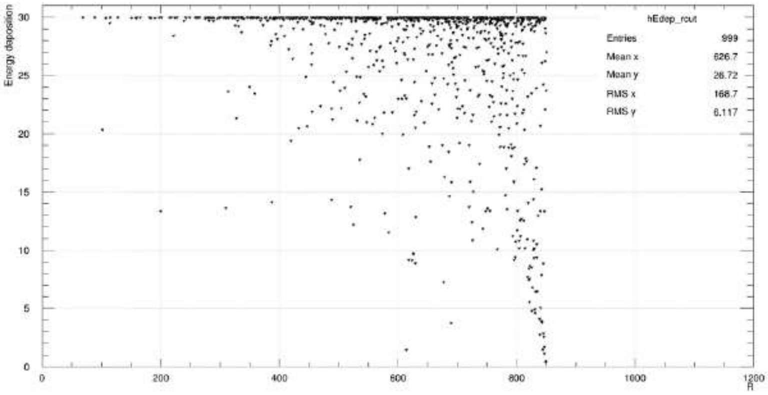

Figure 4.14: Truth MC variable, energy deposition, versus DEAP radius, R, for 1000 simulated electrons recoils at 30 MeV.

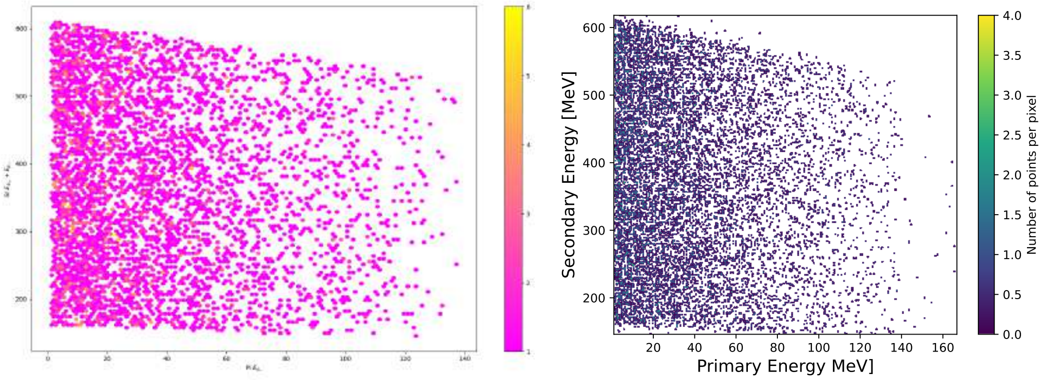

Figure 4.15: Comparison of E_T versus $E_{e^+e^-}$ between the simulated event in RAT and the implementation discussed above.

We started the simulation of iBDM with the RAT framework, lead by the effort of Dr. Michał Olszewski. We begin with the ref3 benchmark model, after implementing further kinematic considerations, we are able to compare the theoretical predictions and the results from MC simulations. Fig. 4.15 serves as a validation plot for the RAT/Geant4 simulations (which create a full realistic model of the detector geometry), recreating our results discussed above.

This is also confirmed by Fig. 4.16, where the red spectrum is $E_T + E_{e^+e^-}$, identical to the one shown in Fig. 4.7 before smearing with the detector energy resolution. E_e (the blue spectrum) shows the scintillation energy spectrum resulting from the RAT/Geant4 simulation. It demonstrates a clear displacement between the expected energy and the detected one, with a peak around 200 MeV, the minimum energy in the theoretical spectrum.

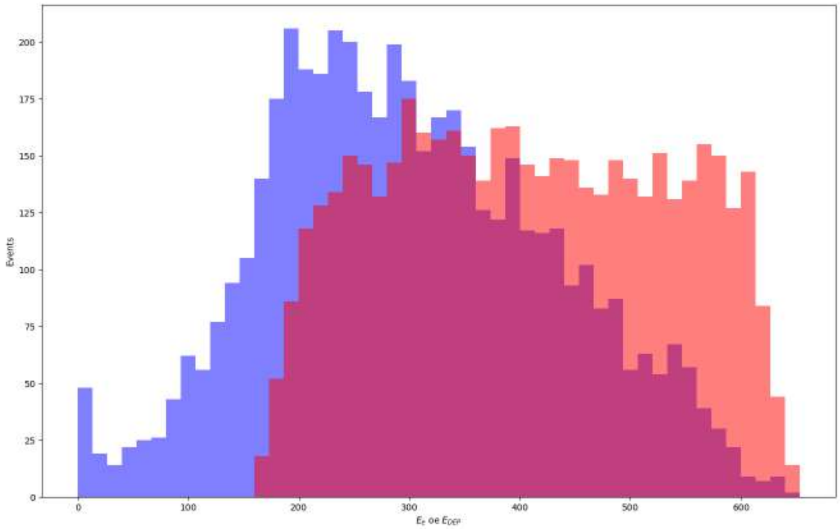

Figure 4.16: Energy spectrum of the theoretical prediction for the total energy deposited by ref3 (red), and the detected scintillation energy (blue) resulting from it. *Taken from [104].*

Fig. 4.17 presents the $\mathrm{F}_{\mathrm{prompt}}$ vs. PE spectrum we obtained. As expected most events lays in the electronic recoil band ($0.2 < F_{\text{prompt}} < 0.35$), but a noticeable lower band with $\mathrm{F}_{\text{prompt}}<0.2$ is visible. This band is populated by events subject to strong digitizer clipping, leading to proportionally less light in the prompt window, hence a decreased $\mathrm{F}_{\text{prompt}}$.

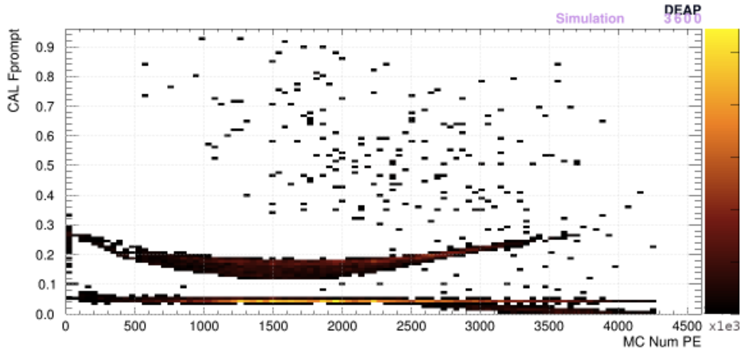

Figure 4.17: $\mathrm{F}_{\text{prompt}}$ versus qPE, from RAT/Geant4 simulation, without the use of data cleaning cut. *Taken from [104].*

4.4 Conclusion

This chapter introduced a novel class of dark matter candidates, called inelastic Boosted Dark Matter, resulting in a distinct signals that may be examined in DEAP-3600.

The iBDM signal is distinguished by the presence of high energy recoil electrons and additional visible particles (e^+e^-) that exhibit displacements vertex. The distinctive nature of the signal enables searches to be conducted in a background free environment.

We implemented the relevant kinematic calculations to reproduce the work done in [87], and considered the relevant scenario DEAP would be most sensitive to.

Our research indicates that DEAP-3600 is sensitive enough to scan a large part of unexplored dark photon parameter space, the considered mediator of iBDM. With only a year of data, DEAP-3600 could achieve a world leading limit for $10^{-6} < \epsilon < 10^{-5}$, $10^{-2} < m_X < 10^{-1}$.

Using a custom software called RAT, we were able to validate our finding and progressed toward a complete model simulation, which is an essential task needed to accurately evaluate the acceptance achievable by DEAP-3600 for the different iBDM scenarios.

The continuation of this research will be a background estimation, with the relevant data cleaning cuts, to minimize instrumental and physics backgrounds.

Chapter 5

Search for dark matter annual modulation with DarkSide-50

Search for event rate modulation has been conducted using the ionization signal from DarkSide-50 underground argon campaign, demonstrating the efficiency Liquid Argon TPC can achieve. The analysis is based on the previous S2-only study that utilized the spectrum of the detected number of electrons, N_{e^-}; we will refer to this past analysis as the spectrum analysis.

We implemented a blind analysis approach by concealing a specific region of interest in the time series of the event rate. It is important to note that the data used in this study has been previously utilized in other research, however it is not the case for the time-series. The blind region was defined as spanning from 4–170 e^- with a time differential $dT > 20$ ms following the prior triggered event, and extended between 3–4 e^- for a simultaneous Likelihood fit, described in Appendix B. The data was unblinded at the DarkSide collaboration meeting in November 2022, after the agreement was reached by the collaboration.

One notable source of concern for this investigation is originating from the long-term stability of the detector, discussed in Sec. 5.4. In this study, we examine the stability of detector parameters, namely the S2 gain, denoted as g_2, as well as the slow-control variables.

In comparison to the spectrum analysis, we proceed to augment the overall level of exposure by incorporating data from the initial phase of the campaign, during which the cosmogenic radioactive isotope ^{37}Ar persists. This results in a 20% increase in overall exposure and, significantly, extends the duration by an additional four months.

We present analysis that encompasses model-independent approaches, specifically by establishing an upper limit on dark matter amplitude signal with a Lomb-Scargle analysis Sec. 5.5. The obtained results are juxtaposed with those reported in the existing literature, which notably includes the discovery claim by the DAMA/LIBRA experiment.

By leveraging the temporal information, the model-independent analysis achieves a lower energy threshold of 3 e^-, as opposed to the 4 e^- threshold employed in the spectrum analysis, achieving the lowest ever energy threshold of 0.04 keV for an annual modulation analysis.

5.1 Reasons and characteristics of an annual modulated signal

5.1.1 Model-independent analysis

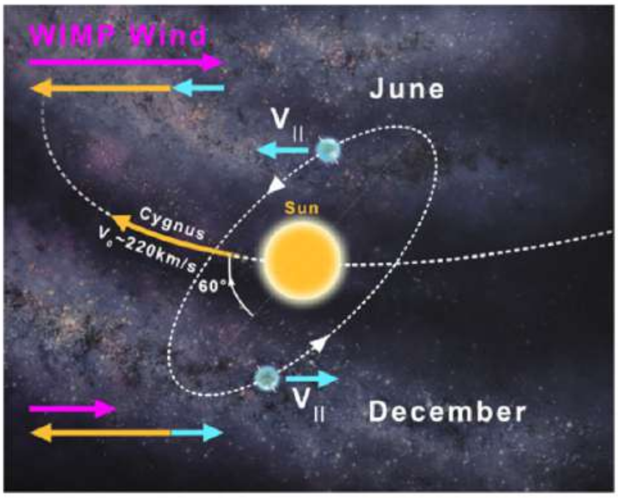

Figure 5.1: The rotation of the Earth around the Sun can induce an annual modulation of the event rate. Such a modulation on the event rate would peak on June 1st. *Taken from [105].*

In the context of a stationary halo, the Sun's revolution around the galactic centre produces a persistent apparent flow of dark matter, referred to as a "wind" (see [105] for a thorough presentation). The wind strength on Earth experiences fluctuations as a result of its annual revolution around the Sun. The aforementioned phenomenon, as depicted in Fig. 5.1, leads to a yearly fluctuation in the event rate in our detector. The differential scattering rate can be expressed as a Fourier series due to the fixed duration of one year,

$$\frac{dR}{dE}(v_{min}, t) = A_0 + \sum_{n=1}^{\infty} A_n(v_{min}) \cos(n\omega(t - \phi)) + \sum_{n=1}^{\infty} B_n(v_{min}) \sin(n\omega(t - \phi)). \tag{5.1}$$

The approximation of an isotropic and smooth halo component can be represented by

$$\frac{dR}{dE}(E, t) \approx S_0(E) + S_m(E) \cos(\omega(t - \phi)). \tag{5.2}$$

In this equation, $\omega = 2\pi/year$, and ϕ represents the phase of the modulation. The modulation is projected to reach its highest point on June 1 [106], with a modulated amplitude, S_m, anticipated to be only a fraction of the constant one, S_0. The specific amplitude will vary based on the halo model [107]. The modulating effect is somewhat limited as a result of a 60 degree inclination between the ecliptic and the Galactic plane.

The approximation in Eq. (5.2) may also be too simplistic. There exists a possibility that the dark matter present in the local region consists of several dark matter components. In such a scenario, the assumption of a fixed phase or sinusoidal form for the modulation may not accurately represent the phenomenon [57, 108].

In addition, there is a hypothetical possibility that the trajectory of dark matter particles may be altered by the gravitational potential of the Sun, leading to a concentration of the dark matter wind. This concentration has the potential to cause a notable change in the modulation phase [108]. Nonetheless our analysis is performed to look upon a large range of possible periods and independent from any assumption on the phase (as discussed in Sec. 5.5 and shown in Fig. 5.35). In addition to the annual modulation, there exists a diurnal variation resulting from the Earth's rotation on its own axis. Nevertheless, due to the Earth's rotation velocity being considerably lower (about 0.5 km/s at the equator) compared to its orbital velocity (30 km/s), the amplitude of a daily modulation signal is expected to be far smaller than that of the annual modulation signal. Consequently, detecting such a diurnal modulation signal poses a greater challenge.

Therefore, the parameters of interest are the amplitude A^s, period T^s, and phase ϕ^s of the signal $S(t)$;

$$S(t) = A^s \cos\left(2\pi \frac{t - \phi^s}{T^s}\right) + C^s. \tag{5.3}$$

This analysis allows direct comparison to other experiments such as DAMA/LIBRA [109], COSINE-100 [110], XENON100 [111], XMASS [112], LUX [113], and so on.

5.1.2 Standard WIMP model

As demonstrated in [45], there is a variety of dark matter candidates that might be investigated utilizing the DarkSide-50 ionization signal. DAMA/LIBRA positive result also yields a plethora of candidates [114, 115, 116]. We nonetheless put an emphasis on the standard WIMP dark matter model which scatters off argon nuclei elastically, keeping a open mind in case a slight deviation in the observed period or phase was found. The recoil energy spectrum from $3\,\mathrm{GeV}/c^2$ and $10\,\mathrm{GeV}/c^2$ WIMPs for June (where the velocity distribution takes the highest value) and December (lowest) are shown in Fig. 5.2 for the two extreme NR fluctuation models (with (QF) and without (NQ) quenching fluctuation more details in Sec. 3). The expected event rate for $3\,\mathrm{GeV}/c^2$ ($10\,\mathrm{GeV}/c^2$) WIMP in 4–29 e^- (29–49 e^-) as a function of time is shown in left (right) panel of Fig. 5.3.

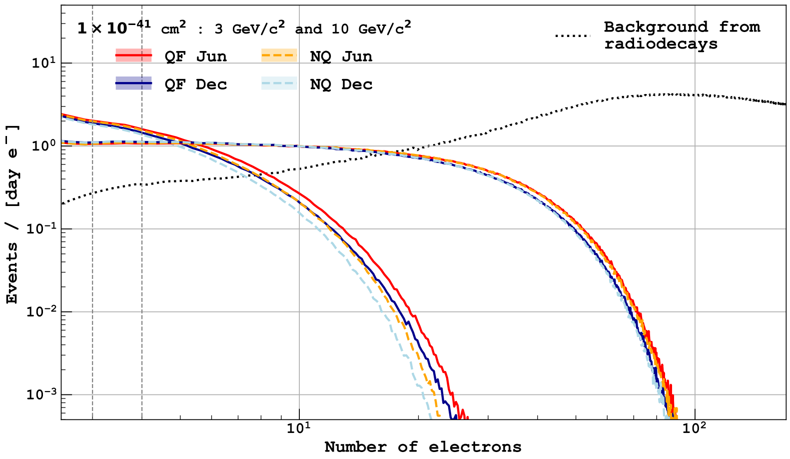

Figure 5.2: Expected N_{e^-} spectra from $3\,\mathrm{GeV}/c^2$ and $10\,\mathrm{GeV}/c^2$ WIMP at June and December. Two extreme cases of NR fluctuation, with (QF) and without (NQ) quenching fluctuation, are considered as was done in the spectrum analysis. The band for each line corresponds to the uncertainty from NR calibration. The dotted line represents the sum of the radioactive background expectations at 600 d from the reference day (2015-04-01). *Taken from [117].*

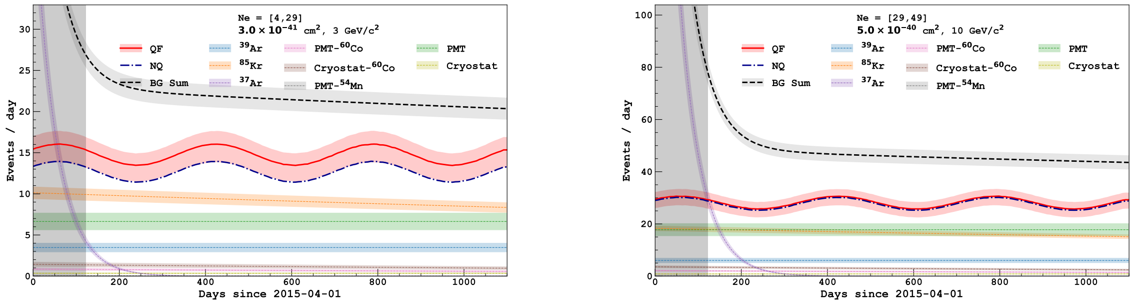

Figure 5.3: Time series of the expected event rate from $3\,\mathrm{GeV}/c^2$ (left) and $10\,\mathrm{GeV}/c^2$ (right) WIMPs in 4–18 e^- and 24–29 e^-, respectively. Also shown are the expected backgrounds from each radioactive isotope. The band represents the corresponding uncertainty. *Taken from [117].*

5.2 DarkSide-50 low-mass analysis strategy

The dataset used in this work spans from August 2nd, 2015 to February 24th, 2018. Note that here we use about 4.5 months more data than the spectrum analysis which uses data only after December 12th 2015. The UAr run started in April 2015, however, the earlier period is used for the ionization yield calibration with higher ^{37}Ar activity [118] and thus we exclude it. The stable data taking was terminated on Feb 25th, 2018, due a severe power outage at the whole LNGS underground laboratory, resulting in poor data quality for unclear reasons. The runs with trigger rate outside the 1.2–1.8 Hz range are skipped as was done in the spectrum analysis. The total livetime is 693.3 days as shown in Fig. 5.4.

The event reconstruction and selection follow the same routine as that of the spectrum analysis.

Due to the low detection efficiency of S1 photons, 0.16 ± 0.01 [119], it is observed that not all low energy events are accompanied by an S1 pulse. Consequently, the chosen events are categorised into two distinct groups based on the presence of either one or two pulses (S2-only or S1 and S2). The sole deviation occurs when "echoes" are present, specifically referring to electrons that are emitted by 128 nm photons by the photoelectric effect from the cathode.

Events that exhibit echoes can be effectively detected by examining the temporal alignment between the two, which is equivalent to the maximum drift time of 376 μs [120].

The efficiency of the position reconstruction algorithm at the keV scale, in the plane perpendicular to the electric field is sub-optimal, which is the specific range of concern for this analysis. The position of the event is defined in this study as the position of the top-array PMT that detects the highest proportion of S2 photons. Events that are chosen by the outermost ring of photomultiplier tubes are eliminated because they occur in the region that is most susceptible to external radioactive background, mostly αs and γs. The observed signal acceptance is 41.9% of the total volume for this cut, and it has been determined to be unaffected by the magnitude of the S2 pulse by Monte Carlo simulations [85].

The S2 yield, which refers to the average number of photoelectrons produced per ionisation electron extracted into the gas pocket, was estimated to be 23 ± 1 pe/e^- for events that were localised beneath the central PMT [85]. The energy observable utilized in this analysis refers to the quantity of electrons observed, denoted as N_{e^-}. It is defined as the quotient of the corrected number of S2 photoelectrons with the S2 yield.

The trigger efficiency is predicted to be close to 100% across the entire range of interest. The selection of the lower bound of the RoI, 3 or 4 to 170 N_{e^-}, is motivated by the need to prevent interference from spurious ionisation electrons that may become caught by small amounts of contaminants and then released, as will be elaborated upon in Sec. 5.2.3.

The process of data selection involves the implementation of two categories of cuts: selection cuts, which aim to eliminate alpha-induced events, spurious electrons, and events with an abnormal start time and quality cuts, which are designed to eliminate pulse pile-ups. Acceptances and cut efficiencies are assessed using analysis on the AAr sample or with Monte Carlo. The former is primarily characterised by the presence of ^{39}Ar, which exhibits an activity level that is three orders of magnitude more than the event rate observed during the underground argon campaign. ^{39}Ar is considered an ideal calibration sample due to its characteristics. Specifically, the detection of ^{39}Ar β-decays occurs through single-sited interactions uniformly distributed in liquid argon, which closely resembles the anticipated signal of dark matter interactions.

It is required that no triggers occurs for 20 ms before good events, in order to suppress the spurious electron (SE) event (see Sec. 5.2.3 for more detail).

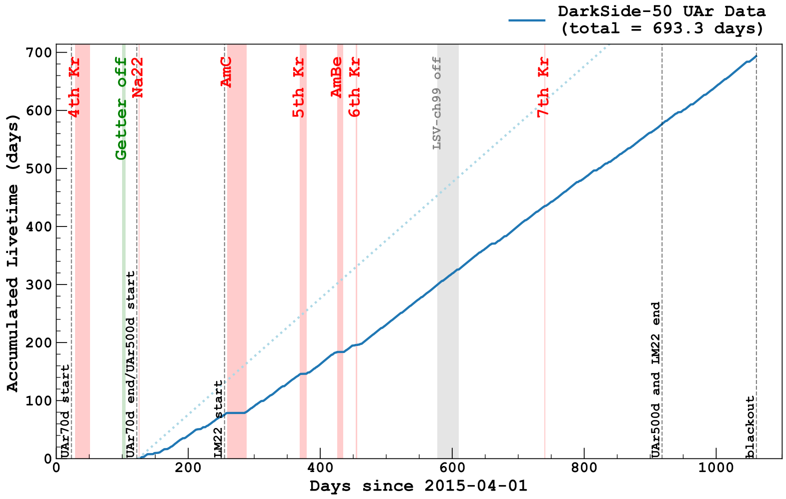

Figure 5.4: History of the dataset used in this analysis. The red hatched regions represent calibration campaigns with radioactive sources. The vertical black dashed lines show the start and end time of each dataset. The data from gray hatched region was not used in high mass analysis but used in low mass analysis because the latter does not use LSV information. *Taken from [117].*

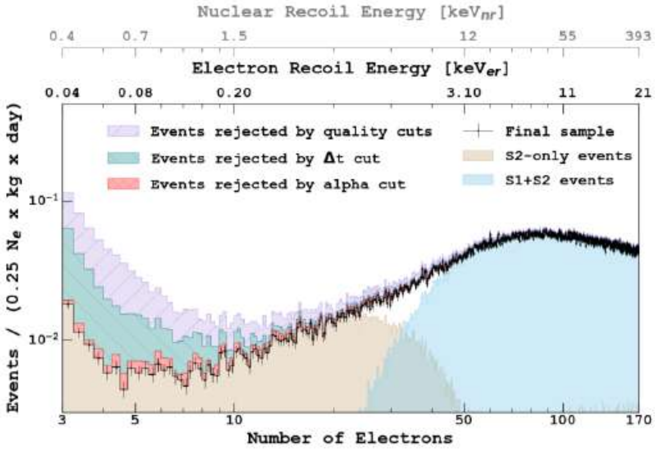

Figure 5.5: Energy spectra with the inclusion of different steps of the data selection, such as after rejection of events outside the fiducial volume and with multiple interactions. *Taken from [85].*

5.2.1 Long-lived isotopes

According to the spectrum analysis, the primary sources of the background budget in our RoI are the decays of ^{39}Ar and ^{85}Kr in LAr bulk, as well as the emission of γ- and x-rays from the PMTs and stainless steel cryostat.

We consider the set of sources, ^{60}Co ($t_{1/2}$=5.27 yr), ^{85}Kr ($t_{1/2}$=10.8 yr) and ^{54}Mn ($t_{1/2}$=312.2 d), as their decays occur within time intervals that are sufficiently brief to result in noticeable fluctuations in the rate of events during the period of data collection, as depicted in Fig. 5.3. Given that the energy spectra of all radioactive isotopes in both the PMT and cryostat components exhibit a high degree of similarity, as depicted in Fig. 5.6, they are combined and averaged over time in the spectrum analysis procedure.

In this investigation, the isotopes ^{54}Mn and ^{60}Co are isolated in order to examine the uncertainties associated with these specific isotopes. Table 5.1 presents an overview of the individual contributions from various sources, together with the corresponding shape and overall systematic uncertainty.

The event rate of ^{85}Kr is represented by an exponential decay model, with the initial activity being calculated during the spectrum analysis. The G4DS simulation results indicate that the contribution fraction from ^{60}Co remains relatively constant within the RoI for both the PMTs and cryostat. This observation is depicted in the lower panels of Fig. 5.6. Therefore, we approximate the change in event rate from ^{60}Co for the purpose of simplifying calculations,

$$\begin{aligned} N_{\text{pmt,cryo}}(t) &= N^{\text{all}}_{\text{pmt,cryo}}(t_0) - N^{\text{Co60}}_{\text{pmt,cryo}}(t_0)\left(1-\exp\left(-\frac{t-t_0}{\tau_{\text{Co60}}}\right)\right) \\ &= N^{\text{all}}_{\text{pmt,cryo}}(t_0)\left(1-\frac{N^{\text{Co60}}_{\text{pmt,cryo}}(t_0)}{N^{\text{all}}_{\text{pmt,cryo}}(t_0)}\left(1-\exp\left(-\frac{t-t_0}{\tau_{\text{Co60}}}\right)\right)\right), \end{aligned} \tag{5.4}$$

with $\frac{N^{\text{Co60}}_{\text{pmt,cryo}}(t_0)}{N^{\text{all}}_{\text{pmt,cryo}}(t_0)}$ the fraction of event rate coming from ^{60}Co (0.78 and 0.07 for cryostat and PMTs, respectively) and $N^{\text{all}}_{\text{pmt,cryo}}(t_0)$ the total event rate of cryostat or PMTs component without the decays

The anticipated spectra for each source are depicted in Fig. 5.7, together with their associated uncertainties, including those arising from activity, ionisation yield for ER, and the calculation of the β-ray-spectrum.

Table 5.1: Background components and event rate in the RoI (4–170 e^-) from the bulk, PMTs, and cryostat. The event rate is as of the reference day (2015-04-01). The uncertainty on the event rate accounts for the shape systematics, while the right column for the normalization systematics.

Location and source			Event rate [Hz]	Overall uncertainty	
				Modulation ana.	Spectrum ana.
LAr		^{39}Ar	$(6.5 \pm 0.9) \times 10^{-4}$	14.0%	14.0%
		^{85}Kr	$(2.0 \pm 0.1) \times 10^{-3}$	4.7%	4.7%
		^{37}Ar	$(7.6 \pm 0.0) \times 10^{-3}$	6.5%	N/A
PMT	Ceramic and Stems	^{232}Th, ^{238}U, ^{235}U, ^{40}K	$(3.3 \pm 0.2) \times 10^{-3}$	12.6%	12.6%
	Stems	^{54}Mn	$(3.5 \pm 0.1) \times 10^{-5}$	40.0%	
	Body	^{60}Co	$(3.1 \pm 0.4) \times 10^{-4}$	12.6%	
Cryo.		^{232}Th, ^{238}U, ^{235}U, ^{40}K	$(1.2 \pm 0.2) \times 10^{-4}$	10.0%	6.60%
		^{60}Co	$(4.8 \pm 0.3) \times 10^{-4}$	7.6%	

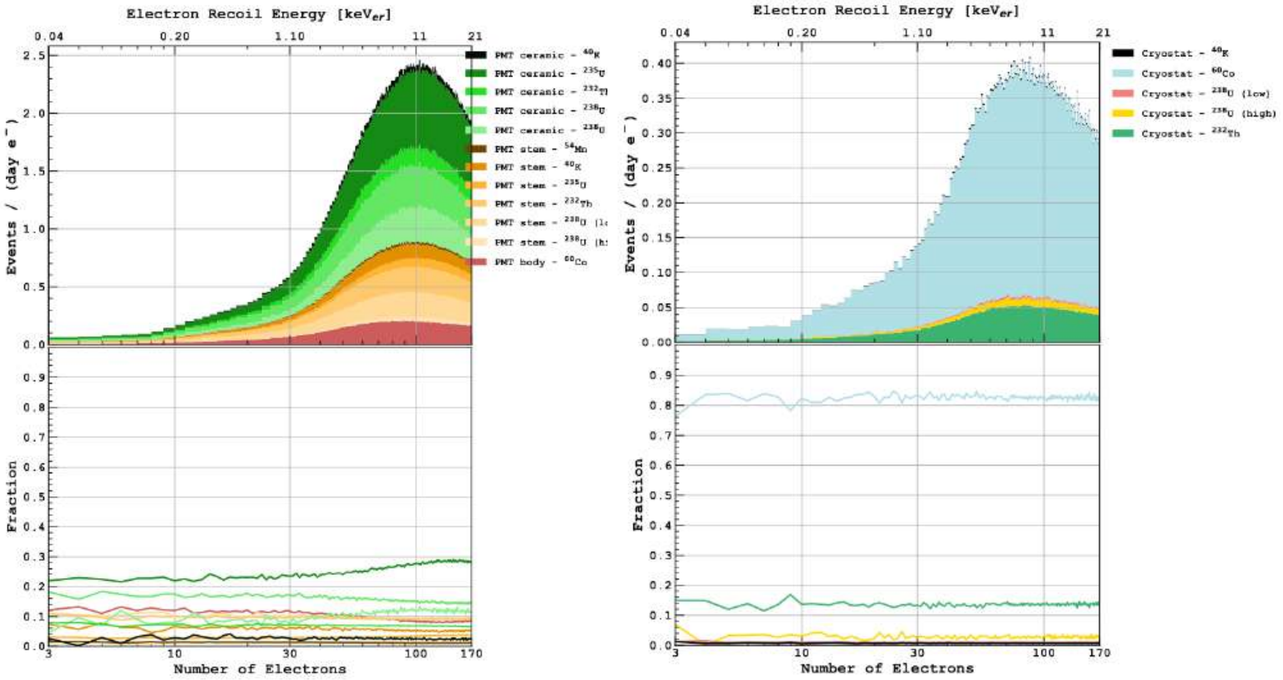

Figure 5.6: Top: breakdown of the background component from PMT (left) and the cryostat (right), evaluated by G4DS. Bottom: fraction of each component. That of ^{60}Co, which decays short enough, is almost flat for both PMT and cryostat. These plots are normalized at the reference day (2015-04-01). *Taken from [117].*

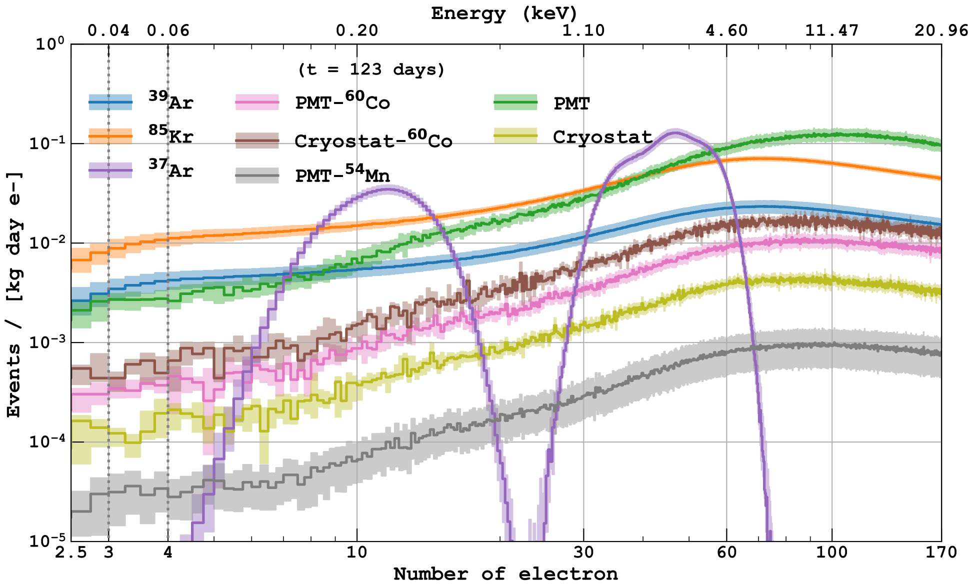

Figure 5.7: Background model of each component with their total uncertainties including both shape and amplitude systematics. The amplitude of each component shown here is normalized at 123 d passed since the reference day. *Taken from [85].*

5.2.2 Short-lived isotope (^{37}Ar)

The inclusion of the cosmogenic radioactive isotope ^{37}Ar is considered in order to augment the dataset prior to its complete decay. The anticipated spectra resulting from the decay of ^{37}Ar through its L1-shell 0.28 keV and K-shell 2.83 keV decay lines were generated following the methodology outlined in the calibration paper [118].

The total activity and branching ratio are subject to constraints based on the initial 70-day dataset. The event selection method mentioned in Section 5.2 is initially applied to the dataset covering the first 70 days.

Next, the event rate in energy windows is computed for each run that has an integrated livetime above 0.1 days. The energy windows have been established to encompass 99.9% of the event originating from the two lines. These energy windows are determined based on the anticipated spectrum, which ranges from 5.50–19.25 e^- and 29.75–68.75 e^- for L1- and K-shells.

Fig. 5.8 displays the temporal dependence of the event rate. The data was fitted using the following function.

$$f(t) = \frac{A_{\mathrm{Ar}}^{L1,K}}{\tau_{\mathrm{Ar}}} \exp\left(-\frac{t}{\tau_{\mathrm{Ar}}}\right) + C \tag{5.5}$$

$$A_{\mathrm{Ar}}^{L1} = \frac{R}{1+R} A_{\mathrm{Ar}}, \quad A_{\mathrm{Ar}}^{K} = \frac{1}{1+R} A_{\mathrm{Ar}} \tag{5.6}$$

where τ_{Ar} is the lifetime of ^{37}Ar.

The fitting procedure is conducted concurrently for the two peaks, utilising a predetermined ratio of $R = 0.093$ derived from the theoretical prediction provided by `BetaShape`. The fit yields the total activity of ^{37}Ar at the reference day as (7.4 ± 0.3) mBq. Corresponding to (0.42 ± 0.03) mBq/kg by considering both the cut efficiency and the branching ratio to the M-shell decay.

The overall level of activity exhibits a consistency of around one standard deviation with the anticipated values derived from the argon activation investigation utilising nuclear data libraries, using `FLUKA` simulation [121]. Additionally, the branching ratio found with the fit aligns with the predicted value of approximately 0.093 from `BetaShape` and other measurements (see [118] and references cited therein).

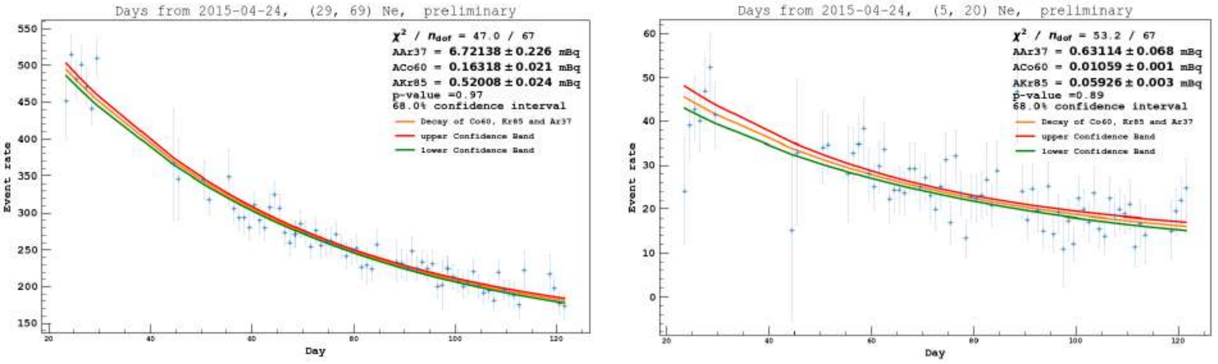

Figure 5.8: Event rate of each run in the energy windows covering the two lines from ^{37}Ar, together with the fit.

Table 5.2: Expected activity of ^{37}Ar from the cosmogenic activation based on the transportation history of UAr and nuclear data libraries at the reference day of 2015-04-01.

Transportation from US to Italy	Amount [kg]	Activity [mBq/kg]
Flight	16	$2.07^{+0.46}_{-0.49}$
Oversea	142	$0.32^{+0.11}_{-0.11}$
Total	158	$0.50^{+0.11}_{-0.11}$

5.2.3 Spurious electrons

The spectrum of N_{e^-} below $4\,e^-$ is affected by the presence of spurious electrons (SE) that are not directly generated by energy depositions.

The spectra of SE are widely recognised as nearly identical to that of a WIMPs with a mass of a few GeV/c^2. The absence of limitations on both the rate of SE and their spectrum hinder the inclusion of this background in the spectrum analysis that relies on well understood background models.

However, the inclusion of temporal information would allow us to use events with energies over $3\,e^-$ with a data-driven calculation of the contamination caused by the SE background.

The top side of Fig. 5.9 illustrates the distributions of dT across several ranges of N_{e^-}. The presence of a temporal correlation between previous events and low N_{e^-} events is readily apparent. The correlations under investigation has been extensively examined in previous studies within the DarkSide collaboration.

Our findings indicate that around 33% of the observed SE events exhibit a correlation within the range of 10^0 to 10^2 milliseconds. Of particular significance to this work is the observation that the rate of the correlated component diminishes over time. Conversely, the rate of the uncorrelated component remains rather stable. The time evolution of the time-correlated SE component is derived from the aforementioned study, as depicted in Fig. 5.9 (bottom).

In this study, the rate of the correlated component is determined with a time bin of 7 d in 0–3 e^-.

The studies previously mentioned provide a foundation for incorporating the SE background into a bin $N_{e^-} = [3,4]$. The rate of SE events in a specific bin, denoted as $\mathcal{R}_{\text{se}}^{3\text{-}4}(t)$, can be described by the following equation:

$$\mathcal{R}_{\text{se}}^{3\text{-}4}(t) = \eta \mathcal{R}_{\text{t-corr}}(t) + \xi, \tag{5.7}$$

with η and ξ are parameters being constant in t.

The absence of comprehensive understanding regarding the characteristics of SE necessitates the absence of prior estimations for the parameters η and ξ, resulting in their determination solely through the utilization of actual data.

Due to the presence of inherent uncertainty, the utilization of this particular bin is limited to the model-independent analysis outlined in Appendix B.

However, the enhanced sensitivity in the extremely low energy range obtained by this methodology provides a novel perspective on dark matter, particularly due to the unprecedentedly low energy threshold attained for an annual modulation analysis.

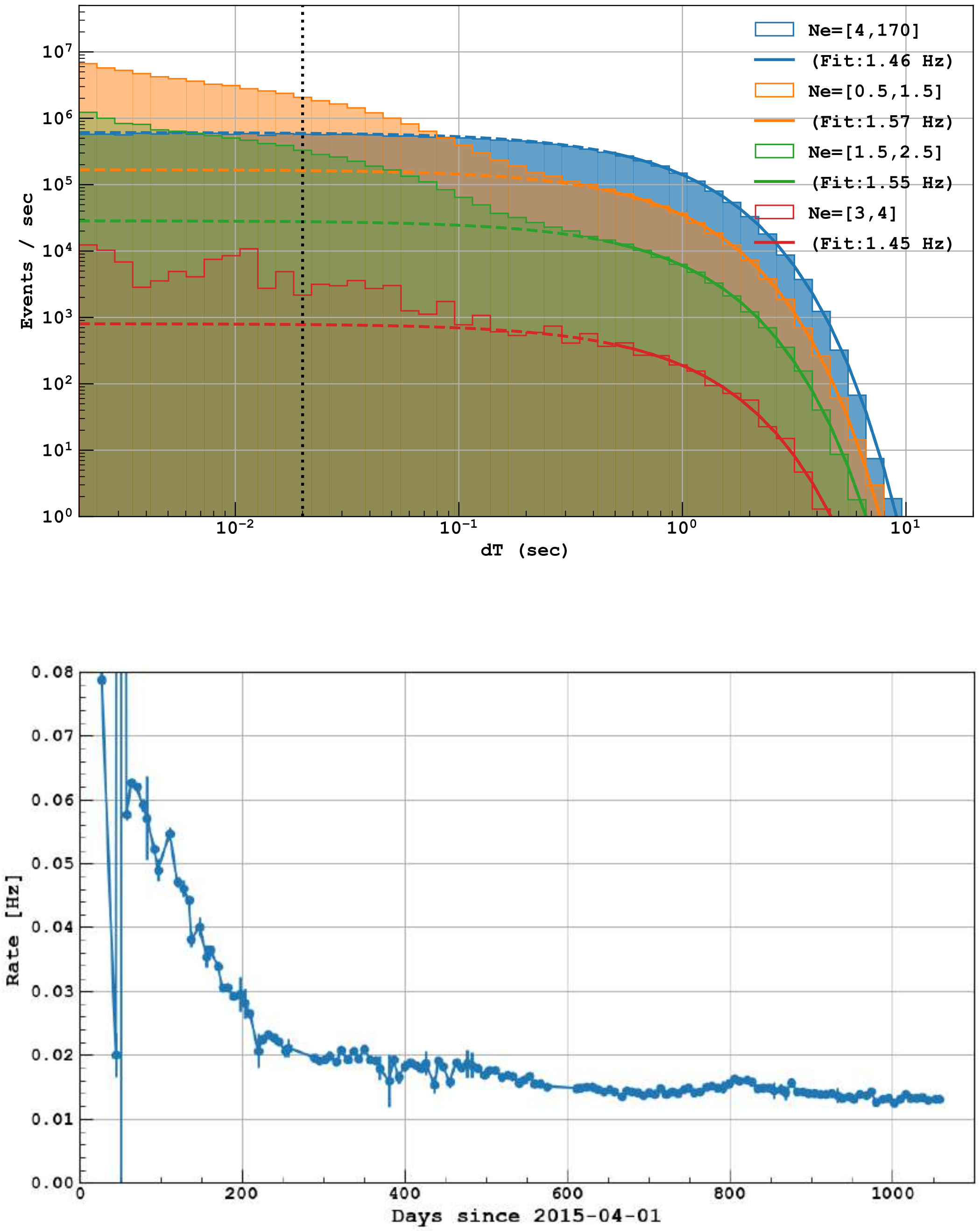

Figure 5.9: Top: distributions of dT, time difference between the preceding event, for each N_{e^-} window. The fit for each histogram is performed by $dT \geq 0.5$ s and its extrapolation is shown by dashed line. The region below the black vertical dotted line is defined as the SE-rich window. Excesses above the extrapolation of small N_{e^-} samples indicate the contamination from SE. Bottom: observed temporal evolution of the time-correlated SE rates. *Taken from [117].*

5.2.4 Time series

We have now described event and run selection as well as the overall structure of the low-mass dark matter search, with the intention of doing an annual modulation search, only a few more pieces of information are needed. We are summing the selected runs in time bins of one day or seven days and the selected events in energy bins: 3–170 e^-, 4–41 e^-, 41–68 e^-, 68–170 e^-, 170–300 e^- depending on the analysis. We are only extracting two necessary variables, the livetime, lt, as well as the number of events, nev, present in each of the time bins.

Our variable of interest is the event rate, simply obtained with $rate = nev/lt$, as we are considering a Poisson process:

- The occurrence of one event does not affect the probability for another event to take place,
- The average rate is constant,
- Events cannot take place at the same time.

We define the standard error as $rate_{error} = \sqrt{nev}/lt$. It has to be noted that this definition holds above a certain value of nev. If we have a count below 5, this standard error becomes inaccurate. Hence our choice to use a seven days times bin to circumvent this issue. We nonetheless perform an analysis with a one day time bin, to confirm our results found with the seven days binning. As we can see from Fig. 5.10, we do not observe a significant variation between both binnings, only a small difference regarding the False Alarm Level $1, 2, 3\sigma$ lines that will be introduced in Sec. 5.3. As we scan higher frequency, we expect peak to appear due to structure windows effect and statistical fluctuation, as also observed in simulation (Sec. 5.5.2), these peaks have an impact on False Alarm Probability calculation. Nevertheless the low variation is negligible in this case.

In order to have an error bar for the low event count in the one day binning case, we used the relationship between the chi-squared distributions and the cumulative distribution functions of the Poisson. The confidence interval for the Poisson distribution mean can be expressed as follows,

$$\frac{1}{2}\chi^2(\alpha/2; 2k) \leq \mu \leq \frac{1}{2}\chi^2(1-\alpha/2; 2k+2), \tag{5.8}$$

where μ is the mean of the Poisson distribution, χ^2 is is the quantile function of the chi-squared distribution, $1-\alpha$ is the confidence level, and k the observed nev.

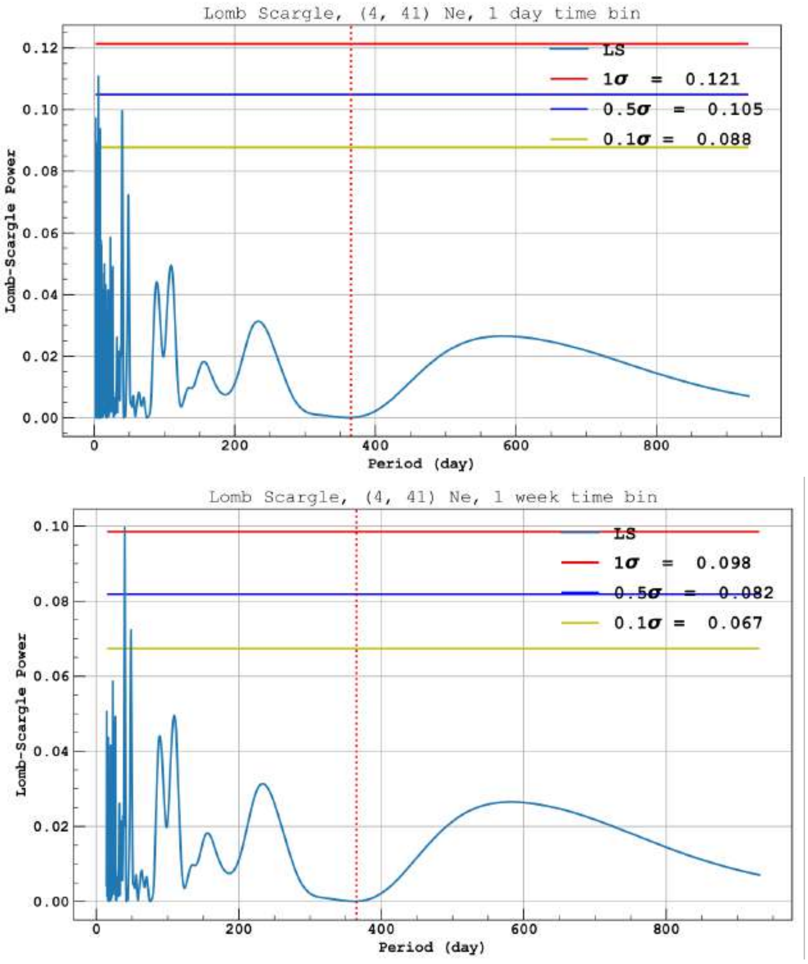

Figure 5.10: Upper plot shows a Lomb-Scargle periodogram calculated on the residual of the time-series between 0.06–2 keV with a one day time bin. Lower plot shows a Lomb-Scargle periodogram within the same energy range with a seven day time bin, showing unnoticeable variation.

Once the error is defined, we perform a chi-square fit,

$$\chi^2 = \sum_{i=1}^{n} \frac{(O_i - E_i)^2}{\sigma_i^2}, \tag{5.9}$$

with O_i as the observed count in the bin i, σ_i^2 the variance and E_i the expected count in the bin i. The expected count are obtained with,

$$f(t) = A_{\mathrm{Ar}} e^{-t/\tau_{\mathrm{Ar}}} + A_{\mathrm{Kr}} e^{-t/\tau_{\mathrm{Kr}}} + A_{\mathrm{Co}} e^{-t/\tau_{\mathrm{Co}}} + C. \tag{5.10}$$

As described in Sec. 5.2.2, we are considering three short lived isotopes in this analysis. ^{60}Co, ^{85}Kr and ^{37}Ar decay on time scale short enough to have a noticeable impact on the time series event rate. Our background-only fit considers exponential decay of these isotopes with their activities and lifetimes, as well as a constant C representing a flat term in the time series dominated by ^{39}Ar. We add a constraint term on the activities in the least square fit with

$$\chi^2 = \sum_{i=1}^{n} \frac{(O_i - E_i)^2}{\sigma_i^2} + \sum_{i=Co,Kr,Ar} \frac{(A_i - A_{i,nom})^2}{\sigma^2_{A_{i,nom}}}, \tag{5.11}$$

where $A_{i,nom}$, $\sigma_{A_{i,nom}}$ are the activities and uncertainties shown in Table 5.1. The activities are obtained after integration of the spectrum, presented in Fig. 5.7, in the relevant RoI. For 170–300 e^- we first perform a linear extrapolation in 100–300 e^- for ^{60}Co and ^{85}Kr before integration. To minimize χ^2 and find the parameters values we use the the iminuit package [122]. We then perform the error propagation by first calculating the confidence band (see Wolberg [123]) around our fit function Eq. (5.47),

$$CB = \hat{y} \pm t_{\alpha/2,\nu} \sqrt{\chi^2_\nu \sum_{j=0}^{n} \sum_{k=0}^{n} \frac{\partial f}{\partial p_j} \frac{\partial f}{\partial p_k} C_{jk}}, \tag{5.12}$$

where χ^2_ν the reduced chi square is one. There is no need to rescale the covariance matrix as we are not using relative weighting. ν is the degrees of freedom, C the covariance matrix and p the best-fit parameters from the iminuit minimization. $\hat{y} = f(p, x)$, where f is our model from Eq. (5.47) and $t_{\alpha/2,\nu}$ is the scale factor, where t is the upper $\alpha/2$ critical value for the t-distribution with N-n degrees of freedom, in our case we are interested in 1σ confidence band.

Finally, we define the error band on the residuals after subtracting the fit function from our event rate with

$$\sigma_f = \sqrt{\sigma_A^2 + \sigma_B^2 - 2\rho_{AB}\sigma_A\sigma_B}, \tag{5.13}$$

where σ_A is the $rate_{error}$ introduced above, σ_B is the second term of Eq. (5.12) and ρ_{AB} is the correlation between the two using Pearson method Eq. (5.39).

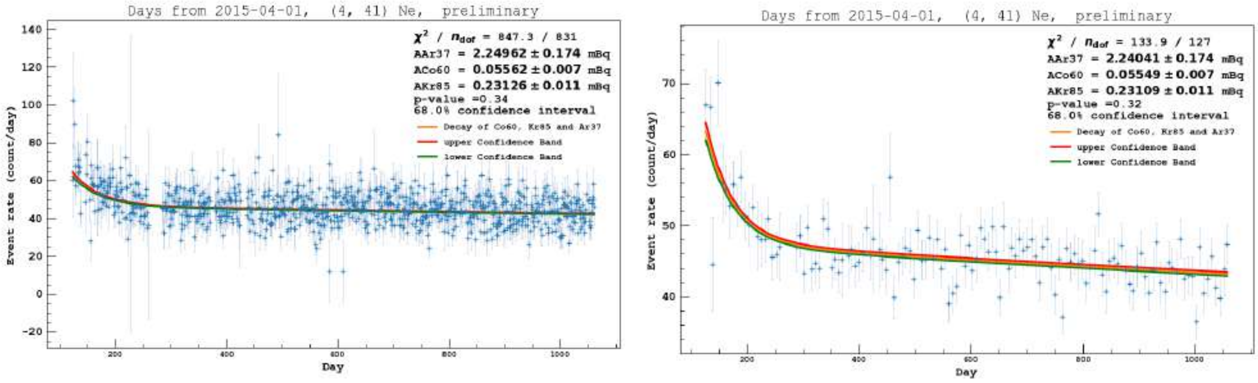

Figure 5.11: Comparison between one day and seven days binning in 4–41 e^-, showing good stability in the methodology employed.

Fig. 5.11 shows a comparison between one day and seven days binning in 4–41 e^-, the resulting activities found with Eq. (5.11) are stable within 0.5%, $\chi^2_\nu s$ are between 1.02 and 1.05 and the p-value are found with

$$\mathrm{p-value} = 1 - F(x; k), \tag{5.14}$$

where $F(x;k)$ is the cumulative distribution function,

$$F(x;k) = \frac{\gamma(\frac{k}{2}, \frac{x}{2})}{\Gamma(\frac{k}{2})}, \tag{5.15}$$

with x the cost function value at the minimum, k the degrees of freedom in our case numbers of data points minus the number of fit parameters, $\gamma(x,k)$ is the lower incomplete gamma function and $\Gamma(k)$ the gamma function, which has closed-form values for integer k:

$$\gamma(s,x) = \int_0^x t^{s-1}\, e^{-t}\, dt, \tag{5.16}$$

$$\Gamma(z) = \int_0^\infty t^{z-1} e^{-t}\ \mathrm{d}t, \qquad \mathrm{Re}(z) > 0. \tag{5.17}$$

Further discussions on fit results and Lomb-Scargle periodogram will take place in Sec. 5.5

5.3 Lomb-Scargle periodogram

The Lomb–Scargle periodogram is a method to estimate a frequency spectrum, which uses a least squares fit of sinusoids. Alike Fourier analysis it has been particularly used within the astronomy community. It was first proposed by Lomb [124] and then expanded by Scargle [125] to find, and test, with uneven temporal sampling, the significance of weak periodic signals.

Usually, the standard Lomb–Scargle periodogram, before calculating the periodogram, is approximated by subtracting the mean of the data, this is valid for a model with zero mean. Nonetheless, this assumption is inaccurate if the fitted sinusoids mean is not zero. This is explicitly solved with the generalized Lomb–Scargle periodogram. The fitted function is

$$y(t; f, \overrightarrow{\theta}) = \theta_0 + \sum_{n=1}^{n_{terms}} [\theta_{2n-1} \sin(2\pi n f t) + \theta_{2n} \cos(2\pi n f t)] \tag{5.18}$$

here $\overrightarrow{\theta}$ is the array of the best-fit model parameters at a given frequency, θ_0 being the offset of the model (the weighted mean of the y values).

For each frequency sine and cosine functions are evaluated, and dot products of the sinusoid vectors with the data vector are done and normalized. Before the dot product, to orthogonalize the sine and cosine components, a time shift is calculated for each frequency. Finally, power is computed from those two amplitude components.

Normalizations

Several normalizations of the Lomb-Scargle periodogram can be found in the literature, for this work we use the "Standard Normalization" (more details here [126] and [127]).

As shown in [128], we can obtain an analytic solution for the generalized Lomb-Scargle periodogram as follows. With t_i the time, y_i is the N measurements of a time series, and σ_i

the errors at given frequency ω. To fit the full sine function Eq. (5.18) we need to minimize the squared difference between the model function $y(t)$ and the data y_i:

$$\chi^2 = \sum_{i=1}^{N} \frac{[y_i - y(t_i)]^2}{\sigma_i^2} = W \sum w_i [y_i - y(t_i)]^2, \tag{5.19}$$

where

$$w_i = \frac{1}{W} \frac{1}{\sigma_i^2}, \tag{5.20}$$

$$W = \sum \frac{1}{\sigma_i^2}, \tag{5.21}$$

$$\sum w_i = 1, \tag{5.22}$$

w_i are the normalized weights. The ability to establish a connection between the least-squares interpretation and the Fourier interpretation of the Lomb-Scargle periodogram presents intriguing and valuable opportunities such as using measurement uncertainties. The Lomb-Scargle power can then be found with,

$$p(\omega) = 1 - \frac{\hat{\chi}^2(\omega)}{\hat{\chi}_0^2}, \tag{5.23}$$

with $\hat{\chi}^2(\omega)$ the minimize χ^2 at each frequency and $\hat{\chi}_0^2$ the χ^2 for the weighted mean. With previously introduced notation, Eq. (5.19) it becomes,

$$p(\omega) = \frac{1}{YY \cdot D} \left[SS \cdot YC^2 + CC \cdot YS^2 - 2CS \cdot YC \cdot YS \right], \tag{5.24}$$

with:

$$D(\omega) = CC \cdot SS - CS^2, \tag{5.25}$$

and the following abbreviations for the sums:

$$Y = \sum w_i y_i \tag{5.26}$$

$$C = \sum w_i \cos \omega t_i \tag{5.27}$$

$$S = \sum w_i \sin \omega t_i \tag{5.28}$$

as seen in [128].

False-alarm probability

The measurement of the peak's height is a significant parameter for indicating the level of uncertainty in the periodogram, particularly in relation to the parasitic background peaks that manifest inside the periodogram. The property in question is contingent upon two factors: the quantity of observations and their signal-to-noise ratio. In situations when the signal-to-noise ratio is low, the spurious peaks present in the background become comparable in magnitude to the real peak. The Lomb-Scargle periodogram was developed as a result of the need to have a quantitative and analytical understanding of the association between significance and peak height.

The conventional method for determining the significance of a peak is through the utilization of the False-alarm Probability (FAP). This metric assesses the likelihood that a collection of data, devoid of any signal except for a coincidental alignment of random errors, would result in a peak of comparable magnitude. This assessment is made under the assumption that the data comprises of Gaussian noise without any periodic element.

Baluev Baluev method derived an analytic result using the extreme value theory. Baluev [129] demonstrated that, even in the case of highly structured window functions (i.e. observation patterns Sec. 5.3.1), for the standard periodogram, the following formula for the false-alarm probability provides a close upper limit:

$$FAP(z) \approx 1 - P_{single}(z)e^{-\tau(z)}, \tag{5.29}$$

with $P_{single}(z)$ denoting the cumulative distribution function of z our periodogram. For the normalized periodogram,

$$\tau(z) \approx W(1-z)^{(N-4)/2}\sqrt{z}, \tag{5.30}$$

and $W = f_{max}\sqrt{4\pi\,\delta(t)}$ is a rescaled frequency bandwidth ($W = f_{max}T_{eff}$ and $T_{eff} = \sqrt{4\pi\,\delta(t)}$ is the effective time series length (further explanation in [129]).

This should be considered an upper limit for alias-free periodograms and not an exact measure of the false alarm probability.

Boostrap In the absence of an exact analytical answer for the false-alarm probability, one often resort to employing computational techniques, such as the Bootstrap approach [130]. The statistical measure is iteratively calculated on numerous random samples of the data in order to estimate the underlying distribution. Temporal coordinates are recorded for each resampling iteration. During resampling, observations are randomly selected, with replacement, from the observed values.

Subsequently, the maximum value is calculated for the resulting periodogram. In scenarios where periodic signals are absent and a sufficient number of resamplings are conducted, the distribution of these maxima will serve as an approximation of the genuine distribution. The bootstrap method is considered to be the most robust estimate of the false-alarm probability due to its minimal reliance on assumptions on the distribution's shape and its comprehensive consideration of survey window effects. The bootstrap approach incurs significant computing costs. In order to determine the level that corresponds to a given false alarm probability, P_{false}, it is necessary to compute approximately $n_{boot} \approx 10/P_{false}$ individual periodograms for the dataset.

False-alarm probability is a useful concept, but one should remember that it is the answer to a very precise question:

"What is the probability that a peak of this magnitude will be present in a signal without periodicity?"

To be specific, it does not answer the much more relevant question:

"What is the probability that this is a periodic data set given these observations?"

Validation Plots

A model-independent analysis using the Lomb-Scargle method has been done on a set of simulated data. The simplified simulated dataset consists of a signal model and RMS noise set at 0.04, with A^s the amplitude of the signal, t in days, ϕ denoting the phase, and T the period:

$$S(t) = A^s \cos\left(2\pi \frac{t-\phi}{T}\right). \tag{5.31}$$

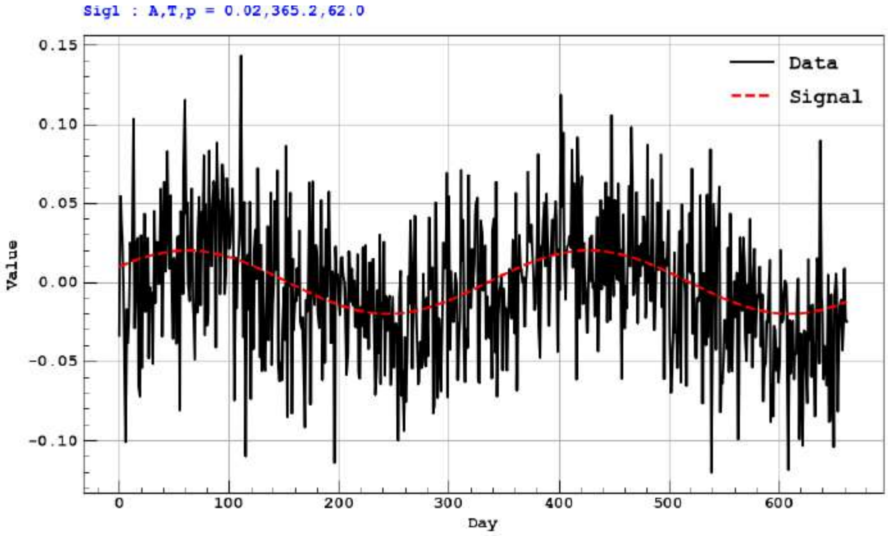

Figure 5.12: Fake data study using the signal model (with an amplitude of 0.02) discuss earlier in addition to noise (rms=0.04).

A convenient tool provided by Astropy [126] is the so-called False Alarm Level. Given a specified FAP for the largest peak, it returns an estimate of the corresponding periodogram power level. It is important to underline that, as for the False Alarm Probability, it assumes a null hypothesis of non-varying data with Gaussian noise.

In this analysis, the area of the tails α outside $\pm\delta$ from the mean of a Gaussian distribution has been set to 0.3173, 4.55×10^{-2} and 2.7×10^{-3} the corresponding value for 1σ, 2σ and 3σ.

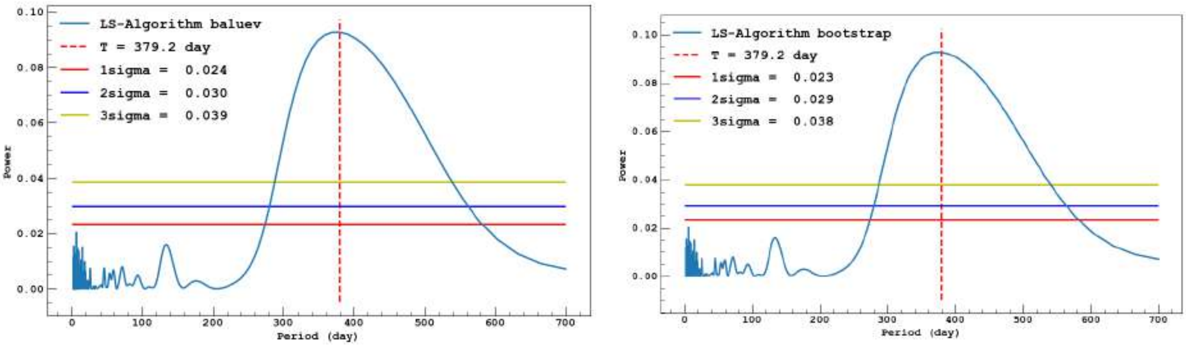

Figure 5.13: Result of the Least-squares spectral analysis with the Lomb-Scargle method, 1, 2 and 3 σ are the false alarm level computed with the Baluev method and Bootstrap method.

5.3.1 Pseudo-Nyquist limit

The Nyquist limit arises as a consequence of the inherent symmetry present in the Dirac comb window function, which is used to describe evenly sampled data. Deviations from this symmetry, such as uneven sampling, disrupt the underlying formulation of the Nyquist limit. However, the notion of the "Nyquist frequency" appears to have become ingrained in the scientific mindset. The methodology for determining the optimal maximum frequency for the Lomb-Scargle analysis is explained in [131].

The maximum frequency is far from the periodicity we are interested in, and it was found that a variation in the maximum frequency does not affect the features in the periodogram that are relevant for this analysis. But the algorithm used to assess the significance of these features, meaning the FAP calculation, is heavily impacted. The more we "zoom in" on the feature, by reducing the maximum frequency, the lower False Alarm Probability it returns (more details in [129]).

The Nyquist frequency is define as:

$$\nu_{Ny} = \frac{1}{2p}, \tag{5.32}$$

where p is the largest value so that $\forall t_i, t_i = t_1 + n_i p, n_i \in \mathbb{N}$, and p may be determined by extending the Euclid greatest common divisor method to include more than two integers. In practice, however, the values of t_k are not known with infinite accuracy, and the Euclid method is numerically unstable for non-integer quantities. So, a feasible option may be to terminate the calculation when the lowest number is less than some threshold.

Apart from that, the spectral window is likely the most effective method for locating p, which is the inverse of the least ν for which $G_N(\nu)$ is bigger than some value below one,

$$G_N(\nu) = \frac{\mid \sum_{k=1}^{N} e^{i2\pi\nu t_k} \mid^2}{N^2}. \tag{5.33}$$

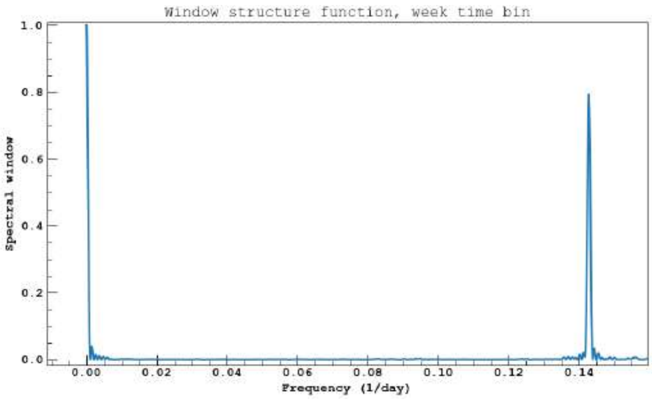

Figure 5.14: Spectral window G_N for the search dataset with a 7 day binning.

It returns a value for $\nu_{N_y} = \frac{1}{2\times\frac{1}{0.14277}}$ so a minimum period of around 14 days.

The same work has been repeated for the analysis using a 1 day binning which is not presented here but done to confirm consistency between both binning choices.

5.3.2 White noise

One notable constraint of the fundamental Lomb-Scargle formula is that its statistical assurances are applicable solely in cases when the observations consist of uncorrelated white noise. However, when dealing with data that exhibits more intricate noise characteristics, additional caution must be exercised [132].

White noise distribution is, in brief, any distribution that possesses: zero mean, constant standard deviation and no autocorrelation, r_k, at all lags, calculated using:

$$r_k = \frac{\sum_{t=k+1}^{T}(y_T - \overline{y})(y_{t-k} - \overline{y})}{\sum_{t=1}^{T}(y_T - \overline{y})^2}. \tag{5.34}$$

The autocorrelation formula is comparable (but not identical) to the correlation formula. The numerator is comparable to the covariance between the current and lagged versions of the time series. A closer look at the two components of the numerator reveals that the mean of the original time series, $\overline{y}$, is subtracted from them, and not $\overline{y_T}$ and $\overline{y_{t-k}}$, respectively. Hence, the numerator of the expression differs somewhat from covariance. The denominator resembles the square of the standard deviation of the original time series (but does not include 'N-1').

Fig. 5.15 shows the autocorrelation plot for the residuals of the event rate in the range $[4{,}29]N_{e^-}$, the dash and full gray line are 95% and 99% confidence levels. A few spikes are above the 99% line for some of the 1 day time bins, which should be considered as a statistical fluctuation. Here no data point shows a spike above 95% confidence level. The histogram of the residuals shown in Fig. 5.16 shows a bell-curve shape, which indicates that no noise whitening procedure is needed before applying the Lomb-Scargle algorithm.

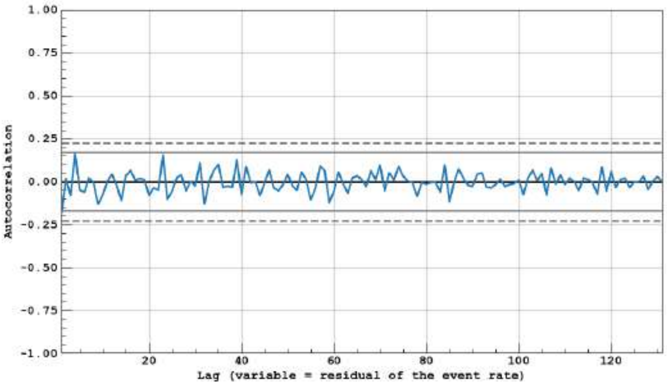

Figure 5.15: Autocorrelation plot for the event rate in the range [4,29]N_{e^-} with a binning of 7 days.

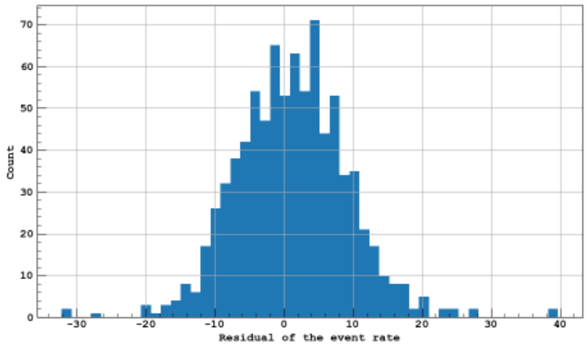

Figure 5.16: Histogram of the event rate residuals in the range [4,41]N_{e^-} with a binning of 1 day.

5.4 DarkSide-50 stability

The long-term stability of the detector performance is a critical factor in this analysis. It is assessed through monitoring of numerous sensors integrated into the cryogenic system, as well as the examination of recorded events from the TPC. The alteration of any parameters within the experimental system has the potential to modify the response of the detector. Consequently, this can lead to inaccuracies in its calibration or the introduction of a spurious modulation in the event rate. Based on the quantifiable radioactive contamination present in the system and the cumulative level of exposure, it is anticipated that DarkSide-50 possesses the capability to detect and respond to a modulation amplitude of approximately 1% of the recorded event rate. Hence, it is intended that the detector remains stable at around that level.

5.4.1 TPC parameters

Among the various parameters, the detector response is characterised by three specific parameters. The electric field of the fiducial volume, denoted as F_d, has a linear impact on the scintillation and ionisation yields at the nominal value of 200 V/cm, which is the designated value for the detector, as stated by [77].

The remaining two parameters are denoted as g_1 representing the average number of detected photoelectrons (PE) per scintillation photon and g_2 the average number of PE per ionization electron. g_1 is for particular importance for the energy reconstruction in high-mass dark matter search [133]. On the other hand, g_2 plays a significant role in the analysis focused solely on the ionization signal.

A study utilizing toy Monte Carlo simulation [117] has indicated that a 1% change in the parameter g_2 has the ability to generate a spurious signal in the ionization spectrum throughout the energy range of around 1 keV.

Response of the Photomultiplier Tubes (PMT)

The characterisation of the PMTs is conducted at regular intervals of approximately every 12 hours by subjecting the TPC to pulses from a blue laser. All PMTs exhibit a consistent pattern over time, their gain decreases gradually and uniformly by around 5% during the duration of data collection. Meanwhile, the single photoelectron resolution stays unchanged. The measurement of both the gain and resolution instabilities yields a value of approximately 1%.

A Monte Carlo simulation [117] was performed to assess the effects of temporal variation and instability on the analysis, with particular emphasis on the alterations in trigger and event selection efficiency, no discernable impact were observed.

Electric Fields

The stability of F_d is measured in-situ, and determined by the drift time of events occurring at the lowermost region of the TPC, denoted as t_d^{full}.

The instability of the system is quantified as $\mathcal{O}(0.01\%)$, as depicted in Fig. 5.18. This value is considered negligible and does not significantly impact the response of the detector.

The voltage measured at the power supplier, which is responsible for supplying the correct potential to each electrode, exhibits negligible variance, not exceeding 0.01%. In contrast, the current at the power supply experiences a gradual variation of approximately 10%.

The reason of this variability remains uncertain; nonetheless, a lack of significant association with the observed event rates (correlation coefficient below 0.05) has been identified. Hence, we assert that the modulation search is not susceptible to the influence of this variation.

The electroluminescence field, denoted as F_g, is influenced by two factors: the potential difference existing between the gate grid and the anode, as well as the height of the gas pocket. Fig. 5.18 illustrates the relevant parameters. The potential difference controlled by supplied high voltage, remains consistently stable during the duration of data collection.

The power supply responsible for operating the boiler, needed in order to maintain the gas pocket, experiences fluctuations of around ±1%. However, it is important to note that the height of the gas pocket, and consequently the value of F_g, is not solely governed by the boiler's output. This observation provides evidence that the inputs for the field F_g exhibit stability.

Scintillation light yield

The temporal fluctuation of g_1 can be observed by the presence of mono-energetic peaks originating from the background γ-ray. The figure presented in (c) of Fig. 5.18 displays the peak positions of gamma rays with energies of 352 keV emitted by the ^{214}Pb and 609 keV emitted by the ^{214}Bi. The fluctuations of g_1 over the duration of data collection are assessed to be 0.3%.

A calibration campaign was conducted to independently test the stability of g_1. This was achieved by introducing a dispersed radioactive source of ^{83m}Kr into the TPC. The variation seen among the three campaigns conducted during the duration of the study is approximately $\sim 0.4\%$ [133].

Electroluminescence yield

As previously stated, the stability of g_2 is of special significance due to its direct correlation with the observed ionisation spectrum. The monitoring of background β-ray events, which have energy above the RoI for our dark matter investigations, is accomplished by observing the S2/S1 ratio denoted as R.

The variable being monitored in this study is $R_{\text{scaled}} = R_{\text{obs.}} \times \frac{\bar{R}(200\ \text{PE})}{\bar{R}(\text{S1})}$. This choice of variable is made to eliminate the influence of energy on R, as previously demonstrated in the work of DarkSide [117]. Here, $R_{\text{obs.}}$ represents the observed R value for each event, while $\bar{R}(\text{S1})$ is an empirical function that assess the mean value of R.

The parameter R is additionally adjusted by the electron lifetime τ_e as determined in Section 5.4.1. Fig. 5.18(b) illustrates the temporal progression of the variable R, demonstrating a volatility of around 0.4%. Considering the variability of g_1, the assessment of g_2 indicates a maximum deviation of 0.5%.

A supplementary examination is conducted to track the S2 spectrum originating from argon events that occurred within the UAr.

Mean S2 yields of ^{222}Rn and ^{218}Po events are obtained for each 30-day period, with the observed S1 yield being utilized to select these events. This selection is based on the clear separation of peaks in terms of S1 [133]. There is no observable temporal fluctuation over 0.5%.

The stability of the system is within 1.5% as depicted in Fig. 5.18(b). It is worth noting that the sensitivity of the system is constrained by the statistical uncertainty.

The relationship between electroluminescence yield and the electric field is positively linear, while the relationship between electroluminescence yield and the number density of argon atoms is negatively linear. To validate our results, we conduct a comparative analysis using the findings presented in [134]. We perform a straightforward evaluation by examining the observed variations in temperature and pressure within the TPC. The evaluations conducted above demonstrate a lack of significant variation in the value of g_2. The aforementioned observation is in agreement with the prediction of a minimal fluctuation in g_2.

Drift field In order to make sure that scintillation and ionization yields is constant over the data taking period, the relative change of the drift filed is examined from the background data. Two pulses ER event is selected by `npulses==2 | (npulses==3 &`

`s3_start_time>376)` and `0.1<s1_f90<0.5`. The drift time distribution around the edge is fitted by a model with error function,

$$f(t) = (p_0 + p_1(t - t_{\text{full}})) \times \text{erfc}(\frac{t - t_{\text{full}}}{\sqrt{2}\sigma}) + p_2. \tag{5.35}$$

Fig. 5.17 shows the typical distribution and its fit (left) and temporal evolution of the full TPC drift time t_{full} (right).

The drift time is stable within 0.01%, which in turn means that drift field is stable within almost same magnitude. Such variation does not result in any visible impact.

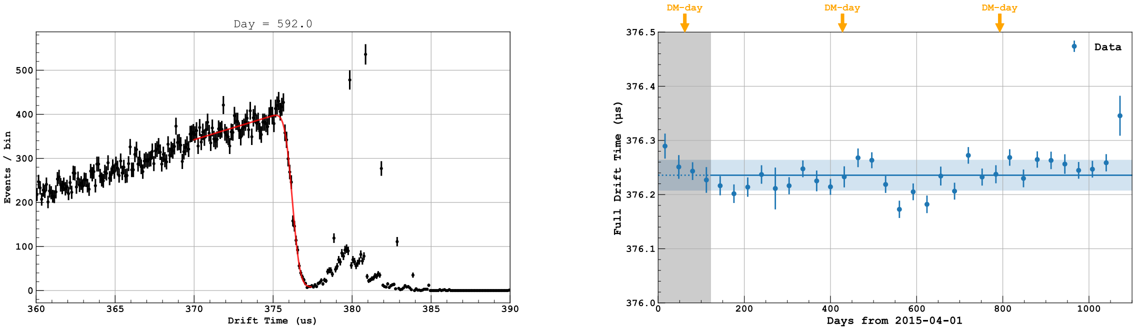

Figure 5.17: Left: Drift time distribution around the TPC full drift time, together with a fit with the error function model. Right: temporal evolution of the full TPC drift time from the fit for every one month. *Taken from [117].*

Purity

The presence of contaminants within liquid argon has the potential to negatively impact the performance of the detector. Specifically, electronegative impurities, such as oxygen (O2), water (H2O), and methane (CH4), have the ability to capture drifting electrons as they transition into the gaseous phase. This process results in the suppression of further electrons originating from events that occur at deeper places. The lifetime τ_e is determined using the same methodology as R, but with a focus on its positional variation. Fig. 5.18 (d) illustrates the temporal progression of τ_e, which exhibits a rise from 5 ms (equivalent to a O_2 concentration of 60 ppt [135]) to a value exceeding 20 ms (15 ppt), with a fluctuation of approximately 1 ms. It is noteworthy that the value of τ_e is approximately ten times greater than the TPC full drift time of 376 µs. It is expected that the observed event rate will not be significantly affected by the tiny fluctuation in drift time, given the lengthy lifetime. This expectation is validated by a Monte Carlo [117] simulation.

5.4.2 Slow control variable (SLC)

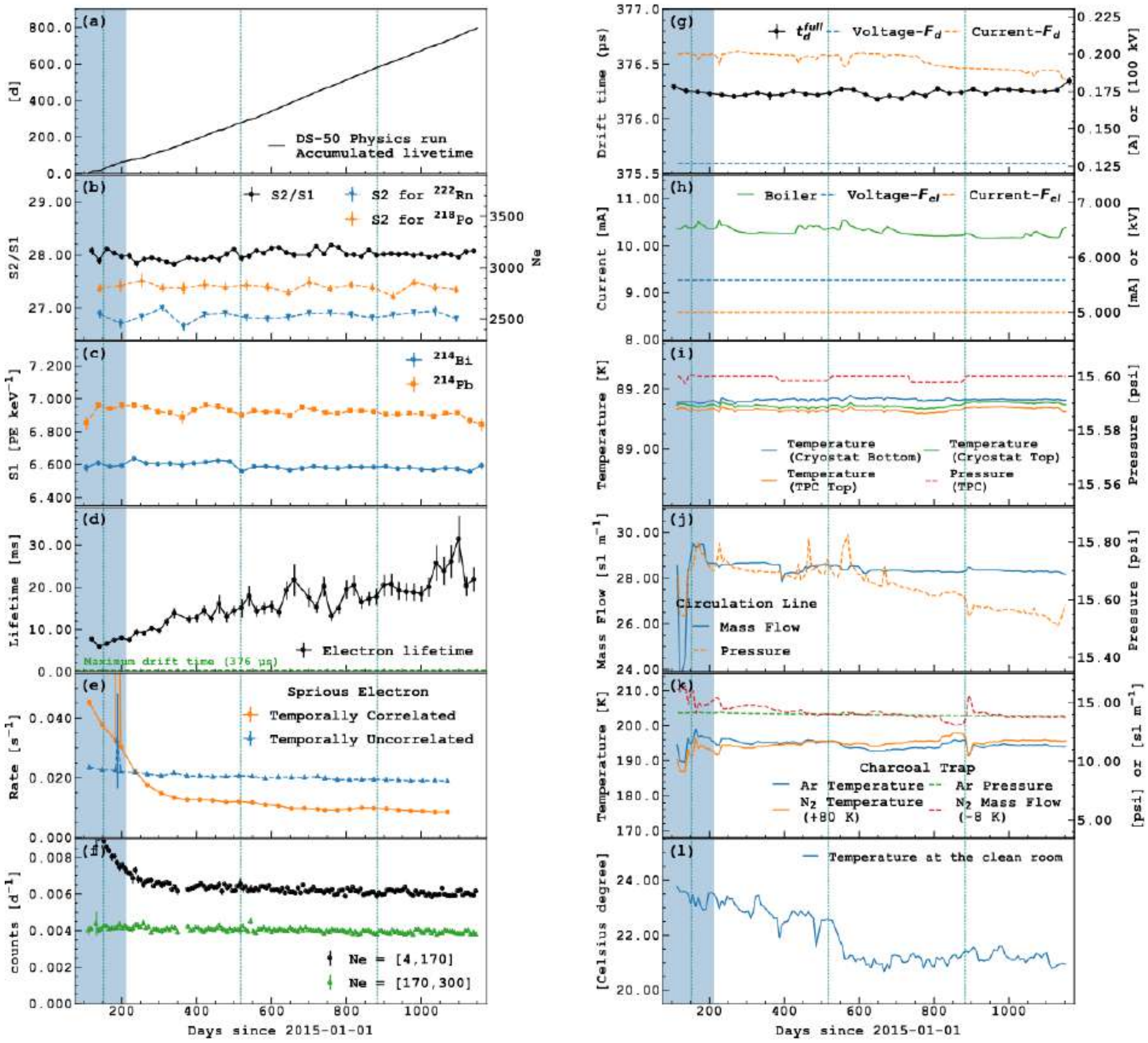

Figure 5.18: Temporal evolution of the detector parameters of interest for this analysis. b–d: the parameters measured by β-ray/γ-rayevents from the TPC such as the S2/S1 ratio, S1 detection efficiency, and electron lifetime. e: temporally correlated and uncorrelated SE rates. f: the observed event rates of both the RoI and higher energy region. g: full drift time of the TPC measured by the event from the bottom edge and the measured current at the voltage supplier. h–l: the parameters monitored by sensors inside the system such as temperatures, pressures, and gas flow rate. The blue-shaded period represents the period devoted to the ^{37}Ar calibration. The vertical dashed lines represent June 2nd of each year when the dark matter induced event rate is expected to be maximum. *Taken from [117].*

There is generally no anticipated underlying mechanism for most parameters to induce a fluctuation in the event rate. However, a comprehensive analysis was conducted on all sensors in order to evaluate any potential seasonal variations and significant impacts they might have.

Fig. 5.18 shows the history of selected variables. Among all the available parameters, several of them show continuous or periodic change during the data taking period. We first assess the potential impact of them on the event rate from the absolute variance of each parameter. In addition, we apply the Lomb-Scargle periodogram to the temporal evaluation of each parameter so that we quantitatively assess the correlation between these changes and the event rate.

Simplified assessment for parameters exhibiting temporal fluctuations

Temperature and pressure of gaseous argon inside TPC. The temperatures and pressure exhibit variations within a range of ±0.02 K and <0.005 psi, respectively.

- They can impact g_2. However, the stability of g_2 is evaluated in Section 5.4.1, revealing a stability level of 0.5%. Furthermore, when examining the formalism for electroluminescence yield, denoted as $\frac{Y}{N}$ $[10^{-17}\text{ph/e}^{-}\ \text{cm}^2/\text{atom}] = 0.081\frac{E}{N} - 0.190$, $\frac{E}{N}$ is expressed in $[10^{-17}\text{Vcm}^2\text{atom}^{-1}]$, according to [136], hence the observed effect is indeed minimal.

Temperature near TPC. The temperature fluctuations within the cryostat range from ±0.02 K.

- The dark count[1] (DC) rate seen in DarkSide-50 is approximately 4 Hz per PMT, resulting in a total rate of 150 Hz. The standard duration of the S2 window is 20 µs, resulting in a probability on the order $\mathcal{O}(10^{-3})$ for a DC to occur within this time frame. As a result, DC are unable to produce discernible trace inside our dataset, leading us to disregard their presence.
- The quantum efficiency[2] (QE) of R11410, which possesses an identical structure to our PMT (R11065) but is use with liquid xenon [137] , exhibits a temperature dependency of 0.03 %/K[138]. Given a fixed value for R11065, the variation of QE is negligible (6×10^{-6}) compared to the QE value of approximately 0.3, hence it can be disregarded.
- After-pulsing [3] (AP) probability associated with our PMT is 0.02%. This indicates that a small fraction, approximately 1-10%, of the events are affected by contamination from the PMT. No measurement of the temperature dependency of AP has been found. Nevertheless, when taking into account common sources of AP such as residual gas within the PMT and contaminants on the dynodes, it becomes very challenging to anticipate any discernible alteration in the event rate modulation due to a deviation of 0.02 K.

Circulation line condition. Parameters involving the circulation line have moderate fluctuations.

- There appears to be a link between the temperature at the radon-trap and the rate of SE. The aforementioned SE model Sec. 5.2.3 takes into consideration this aspect.
- The electron lifetime shows a constant increase. A continual purification of LAr was

---

[1] It refers to the mean rate at which counts are recorded in the absence of incident light. This criterion establishes the threshold count rate at which the signal is primarily attributed to genuine photons.

[2] The measure of the efficacy of a PMT in our case, in converting incident photons into electrons.

[3] The generation of a pulse, subsequent to a specific event, as a result of feedback in a photon detector.

carried out to remove electro-negative contaminants. The potential consequences arising from variations in electron lifetime are evaluated in Sec. 5.4.1.

- There may be other detector parameters affected by the circulation line condition, such as argon purity in terms of electro-neutral impurities. However, we do not notice any potential parameters to cause event rate change at any level.

As introduced in Sec. 3.2.4 there is 71 SLC monitoring DS-50 and its cryogenic system. With three years of data, some false values with unreasonable reading of the sensors occasionally occur, which we will call outliers from now on. These outliers can increase the correlation coefficient and impact the Lomb-Scargle algorithm. To clean all SLC time-series we employed the method described below. We employed the interquantile rule to all SLC values, as opposed to solely focusing on those with a high correlation coefficient.

The first quartile of each time-series, denoted as Q1, is calculated using the quantile function with a parameter value of 0.25. The third quartile, denoted as Q3, is calculated by determining the 75th percentile. The interquartile range (IQR) is calculated by subtracting the first quartile from the third quartile

$$\text{Upperbound}: \quad Q3 + 1.5 \times IQR \tag{5.36}$$

$$\text{Lowerbound}: \quad Q1 - 1.5 \times IQR \tag{5.37}$$

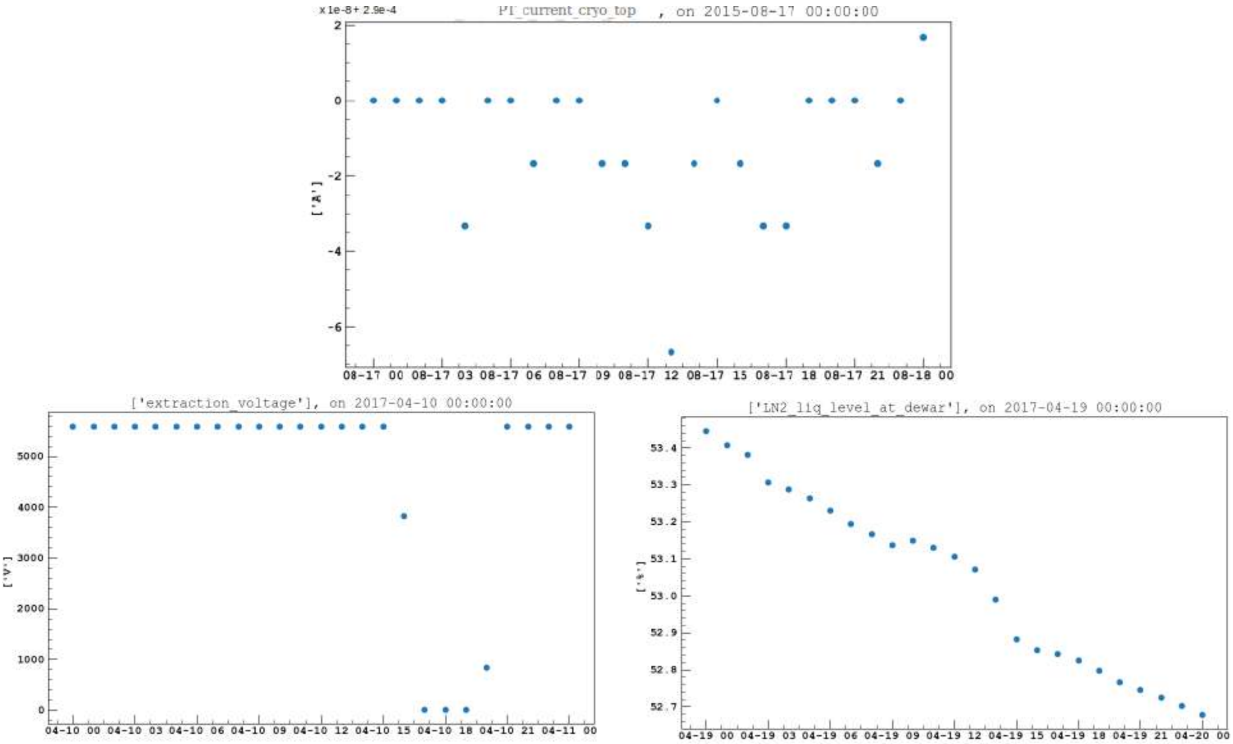

Figure 5.19: Example of hourly bin time series, showing pressure sensor at the top of cryostat (a), the extraction field voltage (b), the nitrogen liquid level at the dewar (c)

We utilize this methodology across all SLCs, employing a time bin of 1 day, in order to identify outliers. The analysis yields a total of 2220 outliers. Next step consisted in examining the hour bin file and identify any outliers that need to be deleted. The primary objective was to determine the number of malfunctioning sensors among the identified outliers. To understand if outliers are caused by malfunctioning sensors, we look at the z-score,

$$z = \frac{x - \mu}{\sigma}, \tag{5.38}$$

with x the value being evaluated, μ the mean, σ the standard deviation. And calculate the derivative between each data-point, simply using threshold on the z-score was deemed insufficient as it returned too many outliers that are within reasonable variation as seen in Fig. 5.19 (c). On the other hand selecting the date where more than 6 derivatives of the z-score are ≤ 0.01, yield a stronger separation. This method resulted in ~ 350 outliers, most of them needing to be erased from the analysis Fig. 5.19 (b), but some Fig. 5.19 (a) are misidentified. This is due to the fixed quantification of the observed value for specific sensors. Thanks to the e-log of the cryogenic system and manually looking through each dates to assess the need to erase them or not, we were left with ~ 280 outliers that got erased. With the help of DS-50 experts a dozens of other dates were erased as they possesses values far from the main distribution, they had a significant impact on the correlation coefficients and some entries in the e-log showed expectations of misbehavior.

Finally we opted to use one day time bin for the calculation of correlation coefficient as increasing the number of data-point from ~ 130 to ~ 900 significantly reduces the impact that one outlier can have [139]. This effect has been observed, with Fig. 5.20 (a) results in $r_p = -0.14$ and (b) $r_p = -0.06$.

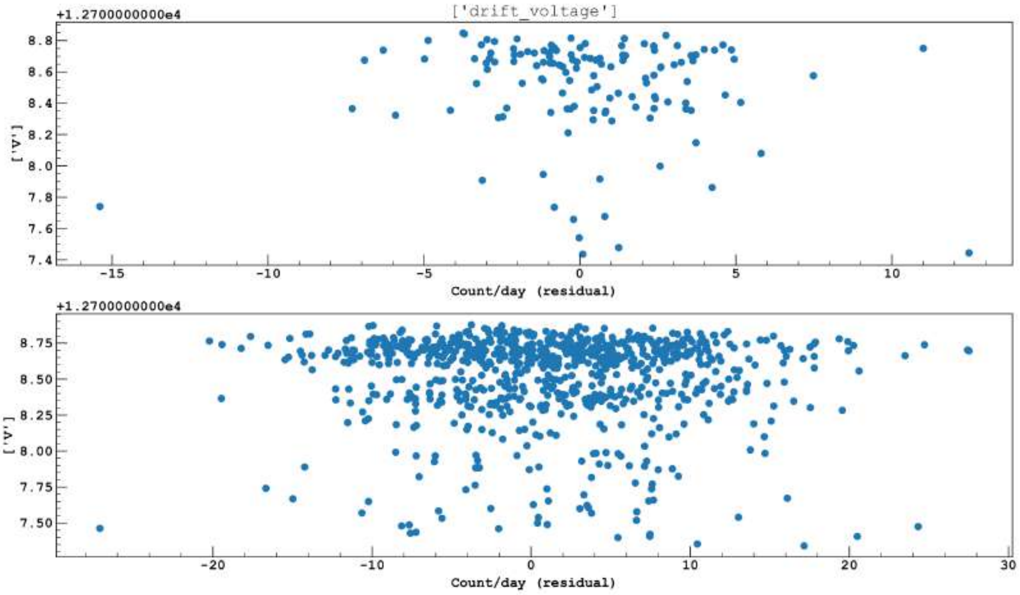

Figure 5.20: Scatter plots between drift voltage and residual of the event rate in 4–41 e^-. Upper plot (a) use a binning of 7day, while the lower plot (b) use a 1 day bin.

5.4.3 Correlation coefficient between SLC and data

A significant portion of research in the field of investigative sciences is dedicated to the identification and exploration of crucial links between datasets. The aim is not only to identify the presence of an association, but also to measure the extent of it. Bivariate correlational procedures assess the extent of the relationship between two variables.

The Pearson [140] correlation coefficient is considered one of the oldest and most commonly used measures of association in academic research,

$$r_p = \frac{\sum (x_i - \bar{x})(y_i - \bar{y})}{\sqrt{\sum (x_i - \bar{x})^2 \sum (y_i - \bar{y})^2}}, \tag{5.39}$$

with y_i values of the y-variable, $\bar{y}$ mean value of the y-variable, x_i values of the x-variable, $\bar{x}$ mean value of the x-variable. It is widely recognised as the most frequently employed measure of correlation. The utilization of the correlation coefficient is contingent upon the assumptions made regarding the variables under investigation and the population from which the sample is derived. In case of Pearson correlation, the typical assumptions is that both variables are normally distributed and the connection between these variables is linear. Given these assumptions, the degree of the population correlation, the sufficiency of the sample size, and the consistency of the sample data are determining factors for reliability of the estimate

The association between variables is an essential component of correlational research, however, the degree of significance of this association is dependent on the specific practical context. A stronger correlation coefficient indicates a more effective predictor, although the magnitude of the correlation coefficient does not necessarily have to be large to offer valuable insights.

The interpretation of this magnitude also exhibits variation across different studies. The determination of whether a correlation is considered moderate or high lacks a universally agreed-upon and rigid definition. The correlation coefficient is measured on an ordinal scale, which means that the values are relative rather than absolute. The classification of a correlation coefficient of 0.5 as low, moderate, or large might vary depending on the specific application and interpretation. Typically, a moderate correlation is defined as a coefficient value about around 0.5.

In a similar way, Hopkins [141] suggests that a correlation coefficient of approximately 0.8 can be considered a high correlation.

All SLC parameters have continuous variables, they can be categorized as ratio or interval variables.

- Interval variables are quantitatively measured on a continuous scale, represented by numerical values, such as temperature in Celsius.
- Ratio variables can be classified as interval variables, with the additional requirement that the zero point on the measurement scale signifies the absence of the variable being measured, such as voltage.

Conditions to apply the Pearson methods are as follow: heteroscedasticity[4], continuous variables, linearity and normality, the first two are respected for all SLC parameters, but linear relationship and normality is not expected for most. Hence the utilization of two others

---

[4] If all of the random variables in a sequence does not have an homogeneous variance, they are said to be heteroscedastic, as opposed to homoscedastic when all random variable have the same finite variance.

methods that do not possess these requirements. The Spearman's [142] and Kendall [143] rank correlation coefficient use similar methods, they determine how similar two rankings are to one another. They can be derived from a more general correlation coefficient formalism [144]. They can be used on a monotonic[5] relationship. Spearman is equal to the Pearson coefficient between the rank values of the variables,

$$r_s = \rho_{\mathrm{R}(X),\mathrm{R}(Y)} = \frac{\mathrm{cov}(\mathrm{R}(X), \mathrm{R}(Y))}{\sigma_{\mathrm{R}(X)}\sigma_{\mathrm{R}(Y)}}, \tag{5.40}$$

where X_i,Y_i are converted to ranks $\mathrm{R}(X_i), \mathrm{R}(Y_i)$,

$\sigma_{\mathrm{R}(X)}$ and $\sigma_{\mathrm{R}(Y)}$ are the standard deviations $\mathrm{cov}(\mathrm{R}(X), \mathrm{R}(Y))$ is the covariance. If all n ranks are distinct integers it becomes,

$$r_s = 1 - \frac{6\sum d_i^2}{n(n^2-1)}, \tag{5.41}$$

with d_i difference for each observation, between the two ranks, n being number of observations. Regarding Kendall's coefficient, it can be observed that the coefficient exhibits a direct relationship with the count of inversions of pairs of objects necessary to transform one rank order into another. In order to accomplish this task, it is necessary to express each rank order by utilising the set that consists of all pairs of objects,

$$r_\tau = 1 - \frac{2[d\Delta(P_1, P_2)]}{N(N-1)}, \tag{5.42}$$

with N number of datapoint , and $d\Delta(P_1, P_2)$ represent the symmetric difference distance between two sets of ordered pairs, denoted as P_1 and P_2. What is the proper interpretation of the Kendall coefficient? The meaning of r_τ can be comprehended within a probabilistic context, as it is obtained by enumerating the quantity of unique pairs between two ordered sets. Within the framework of randomly selecting a pair of objects,

$$r_\tau = P(same) - P(different), \tag{5.43}$$

with $P(same)$ and $P(different)$ the probabilities for these objects to be in a same/different order.

The results from these methods applied on the residual[6] of the data, can be found in Table 5.3 , as well as a short description of all 71 SLC. We do not observe any correlation method yielding a results above 0.11 in the energy range 4–170 e^-. A more complete analysis, separating all energy ranges (4–41 e^-, 41–68 e^-, 68–170 e^-, 170–300 e^- covering the regions of interest as well as above), resulted in low coefficients with the highest acquire with the Spearman methods between LN2 level at dewar and 41–68 e^- at 0.11. Table 5.3 presents our results taking the highest coefficient from the three methods for all N_{e^-} ranges, column 8 and 9 show p-value related to the correlation coefficient, column 8 was obtained using the Scipy methods described in Appendix A. The latest columns shows again p-values but compared

---

[5] We do not expect the increase of a sensor value to induce both an augmentation and diminution of the TPC event rate

[6] Our method to obtain the residual is fully explained in Sec. 5.2.4

to null-hypothesis distributions coming from toy Monte-Carlo simulations that are detailed in Sec. 5.5.2.

Correlation coefficients are calculated on all 5000 pseudo-datasets, the resulting distributions is shown in Fig. 5.21, where the dotted line represents r found in the data. Under the assumption that the distribution of the statistical test under the null hypothesis H_0 exhibits symmetry around 0, the p-value for a two-sided test is computed using the cumulative density function as,

$$p = 2P(T_S|t_s||H_0 \text{is true}) = 2(1 - CDF(|t_s|)), \tag{5.44}$$

with, P representing the probability, T_S denoting the test statistic, t_s representing the observed value of the test statistic, and $CDF()$ symbolising the cumulative distribution function of the test statistic under the null hypothesis. The lowest observed p-value is for the mass flow at circulation line, with $r_s = 0.10$.

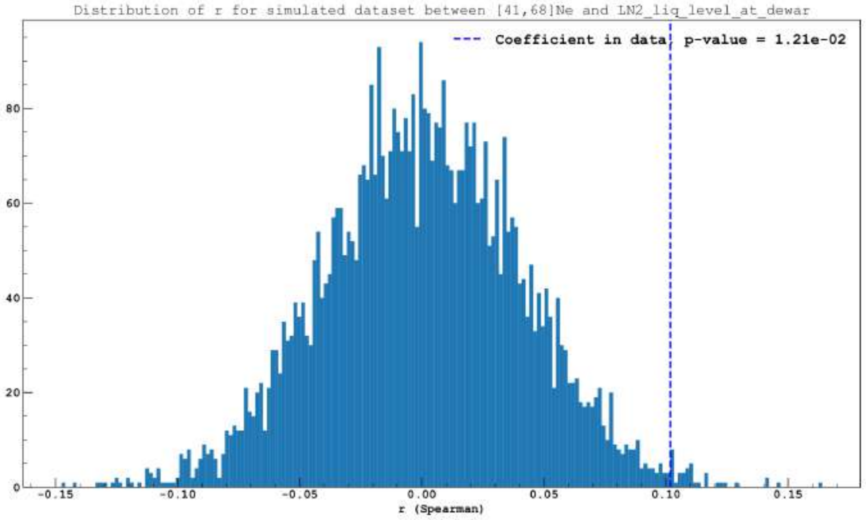

Figure 5.21: r_s distribution calculated on pseudo-dataset in order to find a p-value related to the r_s found in the data. Calculated between residual in 41–68 e^- and LN_2 level at dewar.

The hypothesis emitted to calculate the correlation coefficient on the residual instead of the original time-series was that the overall shape coming from the time-series from SLC evolution might coincide with the radioactive decay of short lived isotopes. Hence inflating the value of the correlation coefficient without any real causality. To confirm it, we employed the same simulations framework stated above, without applying the final steps regarding the Least-square fit and error propagation. The correlation coefficient found in the data are significantly higher with $r_{p,max} = 0.49$, $r_{p,min} = -0.45$, $r_{s,max} = 0.46$, $r_{s,min} = -0.43$.

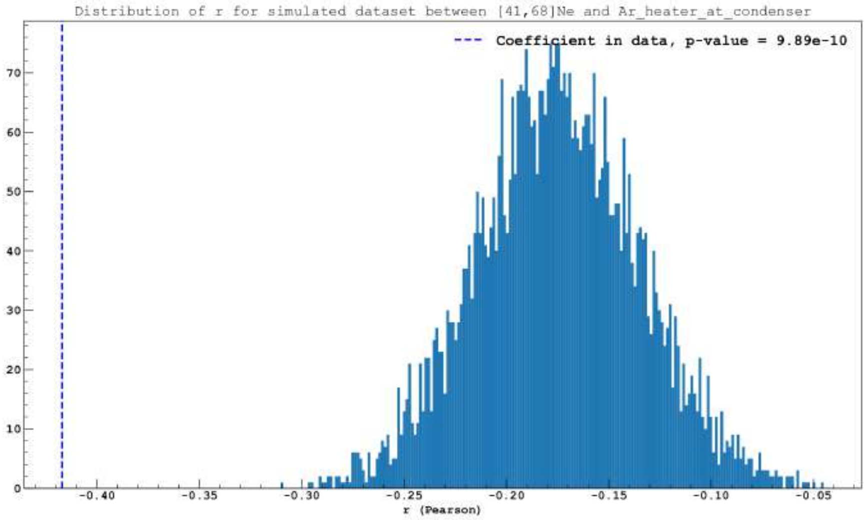

Figure 5.22: r_p distribution calculated on pseudo-dataset in order to find a p-value related to the r_p found in the data. Calculated between raw event rate in 41–68 e^- and Ar heater at the condenser.

As seen in Fig. 5.22, the distribution is not center around 0 hinting at non causal correlation. Nonetheless the r_p found is distant from the background only distribution and yield an especially low p-value. Many others SLC have p-value $\approx 10^{-5}$, and even as low as $\sim 10^{-10}$ as shown in Fig. 5.22. To improve our understanding, we analysed all of these correlation coefficient by identifying event rate values that could render more extreme the correlation coefficient, we looked at scatter plots used to calculate them. We employed different color code to differentiate between three periods (red for $123 < d < 480$, blue for $481 < d < 766$ and black for $767 < d < 1060$) to assess if a distribution from one of this period could present an unexpected behaviour, this is not the case in Fig. 5.24 as they exhibit a typical positive correlation distributions. For example in Fig. 5.24, we erased data points below 450 and above 650 counts/day. It resulted in a reduction of ~ 0.05 for r_p and r_s, and $\mathcal{O}(10^2)$ lower p-value (as we are interested in causality and not simply correlation, here p-value refers to the one calculated with MC simulation from Sec. 5.5.2 and not the one from scipy). We noticed similar variation for all correlation coefficient and associated p-value, as we can see from Fig. 5.22 and Fig. 5.23 where employing a similar method result in a p-value $\mathcal{O}(10^3)$ lower.

Our simulations are not able to perfectly predict the correlation coefficient in data, $\sim 15\%$ of p-value are $> 10^{-5}$, we nonetheless decided to present our results with the correlation coefficient calculated on the residual for the following reason:

- The data was fitted using activities that were constrained based on external analysis. This approach did not incorporate temporal evolution, which could be influenced by variations in the cryogenic system. In our Least square fit we do not observe a 'pull' from the nominal values to compensate from an external effect. Hence the disappearance of a causal correlation after the subtraction of the radioactive decays is unlikely
- A shift in the distribution of r is present with the background only simulations, showing the presence of non causal correlation due to the shape of both time series. This shift explains most of the distributions as it follows the coefficients found in data, and is

enhance after erasing maximum and minimum value from the event rate. Only $r > 0.35$ yield low p-value.

- $r \sim 0.5$ is in most case not consider as a strong correlation coefficient, and the inconsistency between the N_{e^-} ranges make it difficult to believe a variation in a SLC could impact in a different manner 4–41 e^- , 41–68 e^- and 68–170 e^-.
- Lastly we present a delay analysis in Sec. 5.4.4, the un-subtracted event rate exhibit a flat evolution after implementing a delay as long as eight weeks between the sensor reading and the event. It strengthens again the idea that this correlation is mostly due to the shape and slope of both time-series, as it seems difficult to explain why a variation of a parameter in the cryogenic system would have a continuous effect during eight weeks.

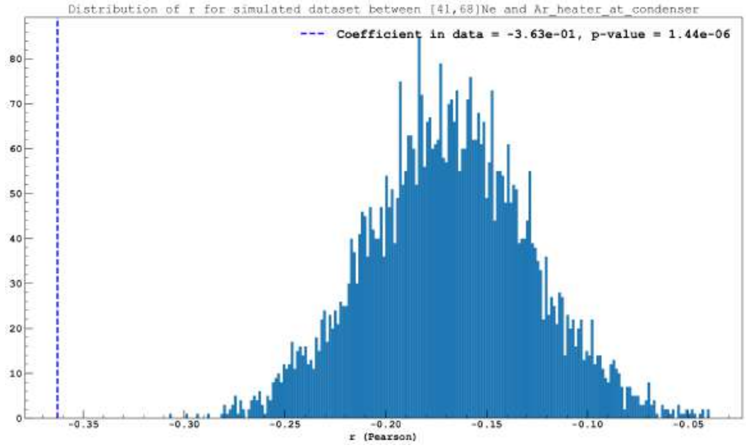

Figure 5.23: Identical plot as Fig. 5.22 but with extreme values of the event rate in data erased to test the impact they have.

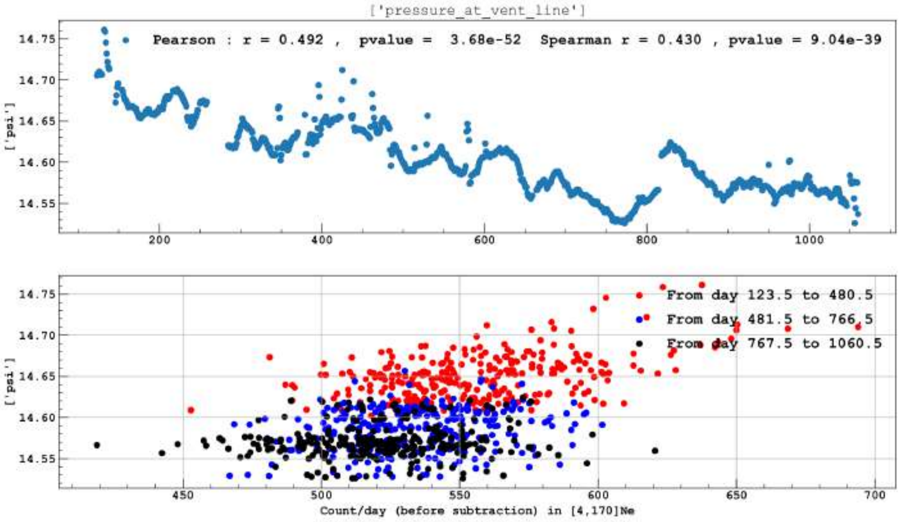

Figure 5.24: Time-series of the pressure at the vent line (upper plot), scatter plot between the pressure at the vent line and the event rate in 4–170 e^- (bottom plot)

Table 5.3: Table summarizing the Slow Control variables and their units, with their correlation coefficient with the residual of the data in the RoI 4–170 e^-. The last 2 columns are the p-value related to the most extreme of the four correlation coefficient.

Slow control parameter	Desription	units	Correlation Coefficients				p-value	
			4–41 e^-	41–68 e^-	68–170 e^-	4–170 e^-	Scipy	MC
ArHTR-1	Ar heater at condenser	%	0.0072	-0.0465	0.0173	0.0186	0.181	0.227
TE N2-1	N2 temp at condenser in	K	-0.0203	0.0719	-0.0371	-0.0279	0.0386	0.064
TE N2-2	N2 temp at condenser out	K	0.0183	-0.0678	0.0483	0.043	0.0515	0.095
TE Ar3	Ar temp at condenser 3	K	0.033	-0.0535	0.0113	0.0225	0.124	0.216
TE Ar4	Ar temp at condenser 4	K	-0.0099	0.0754	-0.0494	-0.0332	0.0304	0.063
MFC-20	mass flow control N2 Loop	sl/min	-0.0379	0.066	-0.0436	-0.0416	0.0575	0.145
MFM-02	mass flow at circulation line	sl/min	-0.0202	0.0943	-0.0507	-0.0311	0.00665	0.018
N2-HTR	N2 heater	W	0.023	0.0106	-0.026	-0.0051	0.454	0.135
TE N2-4	N2 temp at LN2 dewar	K	-0.0146	-0.0193	-0.0327	-0.0237	0.347	0.445
PT-1	pressure at vent line	psi	0.0163	0.0681	0.0141	0.027	0.0501	0.349
PT-2	pressure at TPC out	psi	-0.0285	0.031	-0.0142	-0.012	0.373	0.176
PT-21	pressure at RnTrap out	psi	-0.0084	0.0515	-0.0106	-0.009	0.138	0.208
PT-22	pressure at RnTrap out He	psi	-0.0072	0.048	-0.0105	-0.0113	0.168	0.120
PT-23	pressure at RnTrap in	psi	-0.0118	0.0574	-0.0023	0.0133	0.0985	0.120
TE N2-3	N2 temp at RnTrap	K	0.0353	-0.0539	0.0388	0.0347	0.121	0.283
TE Ar1	Ar temp at RnTrap	K	0.0261	-0.0363	0.0298	0.0137	0.297	0.336
TE Ar2	TE Ar2	K	-0.0176	0.0529	-0.021	-0.0262	0.128	0.241
MFC-Ar	mass flow control Ar supply	sl/min	0.0209	-0.0695	0.0497	-0.0405	0.242	0.170
PT-GV2	outer vacuum TPC	mbar	0.0314	-0.0339	-0.0524	-0.0575	0.0993	0.133
PT-GV3	outer vacuum Condenser	mbar	0.0137	0.0537	-0.0118	0.0259	0.122	0.119
PT-N2	pressure at LN2 supply	psi	0.0037	-0.059	0.0121	-0.0036	0.0895	0.161
PT-50	pressure at recovery tank	psi	0.0491	-0.0137	0.0177	0.041	0.163	0.215
LT-50	liq level recovery tank	%	0.0498	0.0473	-0.0495	-0.0223	0.18	0.273
PT-N2serv	PT N2serv	psi	0.0174	0.0165	-0.0652	-0.071	0.0405	0.070
TT-R1	temp at recovery tank	K	-0.0433	0.0279	0.0387	0.0277	0.212	0.329
PW-R1	heater at recovery tank	W	0.0406	0.0186	-0.0074	-0.0048	0.242	0.293
MFC-R1	mass flow control N2 recovery	sl/min	0.0098	-0.0253	0.0403	0.0364	0.293	0.315
LN2level	LN2 liq level at dewar	%	-0.0186	0.1018	-0.0485	-0.0075	0.166	0.212
CRH-temp	temp at CRH	C	-0.0083	0.0608	-0.0326	-0.0347	0.0801	0.145
MFC20-SP	mass flow control N2 condenser	sl/min	-0.0327	0.0619	-0.0302	-0.0304	0.0751	0.171
R1-I	PT current at cryo bottom	A	-0.0171	0.0325	-0.0153	-0.0226	0.351	0.385
R2-4-I	boiler loop current	A	-0.0083	0.0331	-0.0249	-0.0278	0.342	0.275
R3-I	boiler current lower	A	-0.0184	0.0333	-0.0112	-0.0173	0.34	0.353
R5-I	boiler current upper	A	-0.0063	0.0354	-0.0224	-0.0251	0.309	0.309
R6-I	PT current at TPC Top	A	-0.0139	0.0391	-0.0272	-0.0318	0.261	0.285
R7-I	PT current at cryo Top	A	-0.0084	0.0412	-0.026	-0.0265	0.238	0.263
R1-power	PT power at cryo bottom	W	-0.0187	0.0293	-0.019	-0.0153	0.4	0.439
R2-4-power	boiler loop power	W	-0.0164	0.0273	-0.0304	-0.024	0.434	0.428
R3-power	boiler power lower	W	-0.0161	0.0271	-0.014	0.016	0.437	0.462
R5-power	boiler power upper	W	-0.0144	0.0288	-0.0277	-0.0212	0.409	0.400

R6-power	PT power at TPC Top	W	-0.0193	0.03	-0.0294	-0.0255	0.389	0.406
R7-power	PT power at cryo Top	W	-0.0192	0.0373	-0.0284	-0.0207	0.285	0.312
R1-Temp	temp at cryo bottom	K	-0.0486	0.0763	-0.032	-0.0171	0.0283	0.133
R3-Temp	temp at boiler lower	K	0.0518	0.0106	-0.008	0.0096	0.136	0.213
R5-Temp	temp at boiler upper	K	0.0528	0.021	0.0145	0.0215	0.129	0.183
R6-Temp	temp at TPC top	K	-0.0318	0.0544	-0.0142	0.0066	0.36	0.557
R7-Temp	temp at cryo top	K	-0.0156	0.0456	-0.0085	0.015	0.654	0.368
R1-raw	raw at cryo bottom	TBD	-0.0463	0.0756	-0.0283	-0.0133	0.0294	0.135
R3-raw	raw at boiler lower	TBD	-0.0158	0.0493	0.0286	0.0412	0.159	0.203
R5-raw	raw at boiler upper	TBD	0.0602	-0.011	0.0176	0.0341	0.0835	0.087
R6-raw	raw at TPC top	TBD	-0.0321	0.0544	-0.0142	0.0066	0.355	0.551
R7-raw	raw at cryo top	TBD	-0.0159	0.0457	-0.0085	0.015	0.646	0.370
Extraction V	extraction voltage	V	-0.0146	0.0417	-0.0368	-0.0218	0.233	0.287
Drift V	drift voltage	V	-0.0508	-0.0341	-0.0192	-0.0272	1.46e-01	0.156
Extraction I	extraction current	A	-0.006	0.054	-0.0201	0.0124	0.126	0.249
Drift I	drift current	A	0.0199	0.0374	-0.0372	-0.0221	0.282	0.201
UTI-lev	uti level	%	-0.0208	0.0445	0.0076	0.0338	0.216	0.284
UTI-cap	uti capacitance	F	-0.0231	0.044	0.0099	0.0349	0.221	0.295
C1-He-Temp	c1 He temp	K	-0.0605	-0.0578	0.0051	-0.0327	0.0979	0.173
C1-InH20-Temp	c1 H2O temp in	K	0.0149	0.0323	-0.0345	-0.0261	0.353	0.462
C1-OutH20-Temp	c1 H2O temp out	K	0.0419	0.0221	-0.0285	0.0164	0.17	0.265
C1-Oil-Temp	c1 oil temp	K	0.0581	0.0347	-0.0345	-0.006	0.127	0.212
C1-High-Press	c1 high press	psi	0.0075	0.0482	-0.0356	-0.0257	0.166	0.230
C1-Low-Press	c1 low press	psi	0.0133	0.0098	-0.0173	-0.0227	0.513	0.515
C1-Current	c1 current	A	-0.043	0.019	-0.0637	-0.0676	0.0514	0.084
C2-He-Temp	c2 He temp	K	-0.0743	0.0289	0.0178	-0.0141	0.0326	0.087
C2-InH20-Temp	c2 H2O temp in	K	0.0145	0.0223	-0.0421	-0.036	0.225	0.211
C2-OutH20-Temp	c2 H2O temp out	K	0.0477	-0.0127	-0.0372	-0.0148	0.283	0.356
C2-Oil-Temp	c2 oil temp	K	0.053	0.017	-0.0361	-0.0114	0.127	0.212
C2-High-Press	c2 high press	psi	0.0261	-0.0367	0.0113	-0.0105	0.452	0.466
C2-Low-Press	c2 low press	psi	-0.0237	0.0578	-0.0188	0.0123	0.495	0.459

5.4.4 Delay correlation

In order to catch non trivial correlation between SLC and data, we performed a delay analysis consisting in correlations calculations with the aforementioned methods with an implemented time variation of $0-8$ weeks between the sensor reading and the TPC event rate time-series. This delay effect could occur from contamination or weak variation that would result in a noticeable consequence only weeks after it took place in the cryogenic system. As seen in Fig. 5.25 no correlation coefficient above the one mention in Table 5.3 are found.

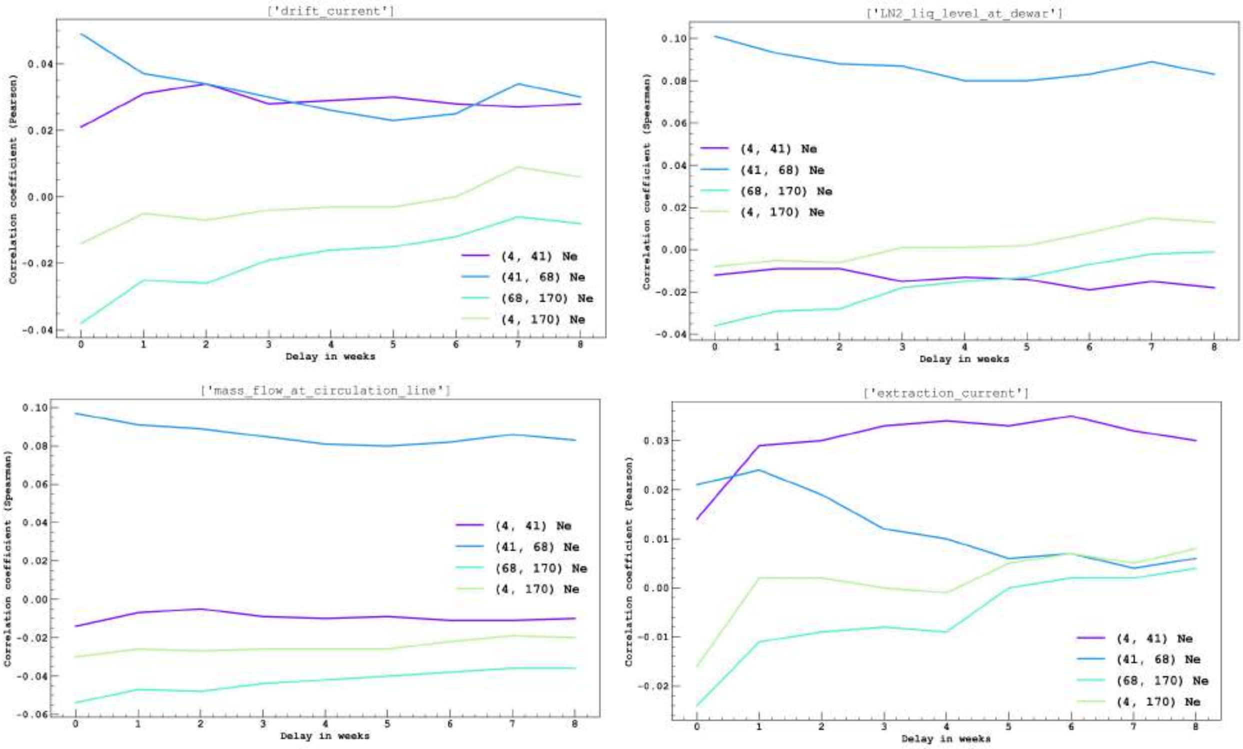

Figure 5.25: Delay coincidence calculated with correlation coefficient with an implemented delay as long as 8 weeks. The correlation coefficient are calculated with Pearson or Spearman methods between SLC and residual of the data. Top-left: drift current; Top-right: LN_2 level at dewar; Bottom left: mass flow circulation line; Bottom right: extraction current

As previously mention we also performed this analysis on the raw event rate to confirm the validity of our assumption to work with the residual. This analysis confirm the correlation due to similar slope for both time-series as it propagates with an implemented time-delay.

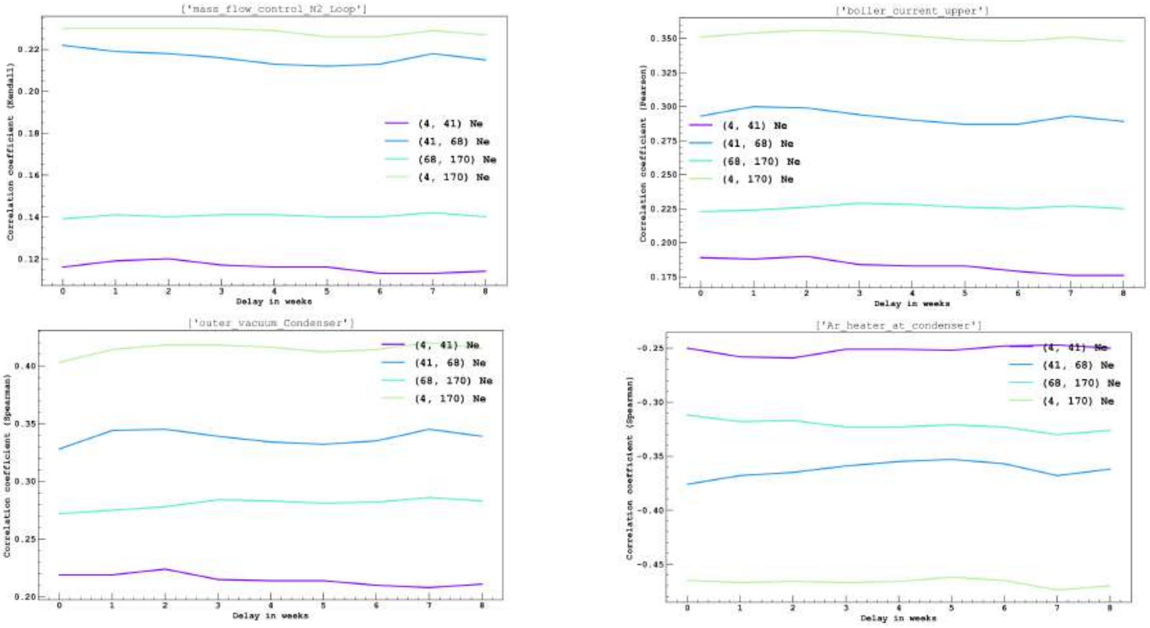

Figure 5.26: Delay coincidence calculated with correlation coefficient with an implemented delay as long as 8 weeks. The correlation coefficient are calculated with Pearson, Kendall or Spearman methods between SLC and raw event rate of the data. Top-left: mass flow control at N_2 Loop; Top-right: Boiler current; Bottom left: Outer vacuum condenser; Bottom right: Ar heater at condenser.

Lomb-Scargle periodogram with Slow control parameter

The Lomb-Scargle periodogram is used to look for any possible periodical change of the slow control variables, we are using a seven days binning to define error bar using the standard deviation calculated after resampling,

$$\sigma = \sqrt{\frac{\sum(x_i - \mu)^2}{N}} \tag{5.45}$$

with N the size of the population, x_i value from the population and μ the population mean. The algorithm returns the power spectrum as a function of the frequency[7]. We evaluate the significance of the power spectrum by the False Alarm Probability calculated by Bootstrap method.

---

[7] Basic study of the LS periodogram is summarized in (5.3), where the capability of the LS periodogram is shown with a simple toy sample.

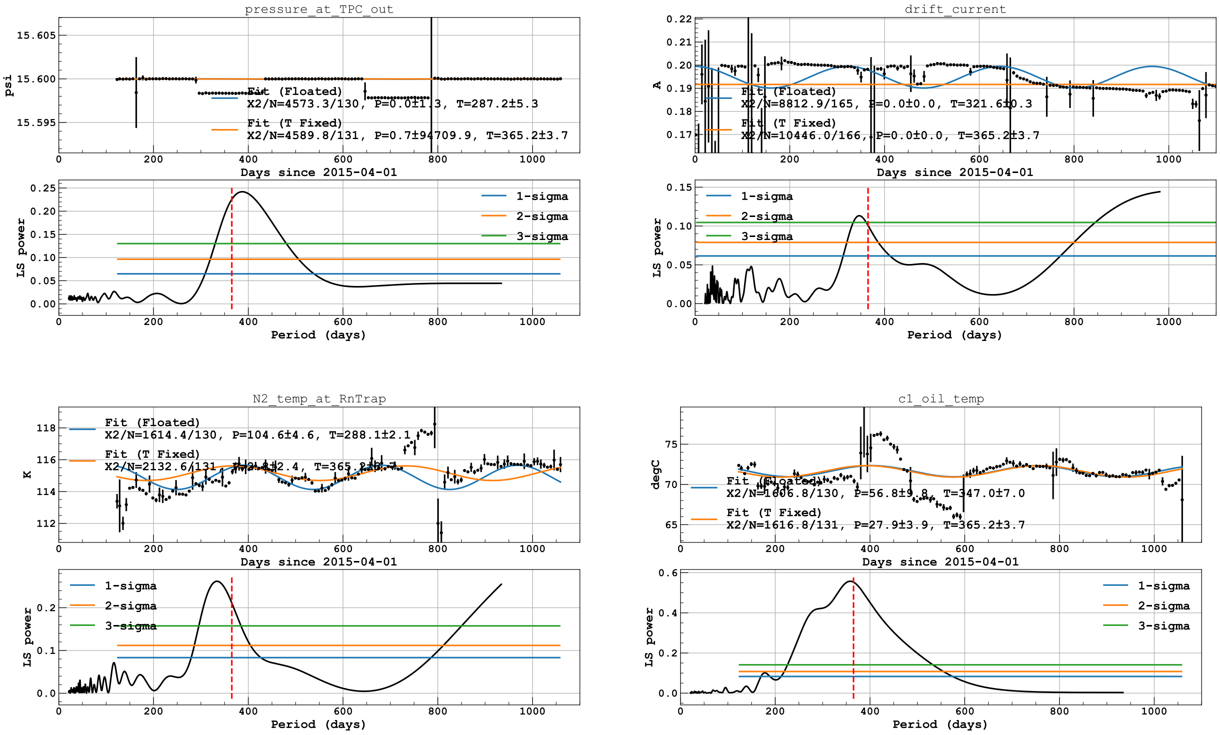

Figure 5.27: History and the power spectrum from the LS periodgram of parameters having a peak around 1 yr. The blue and orange lines are the fit with a cosine plus constant function, with (orange) and without (blue) fixing the period to be 1 yr. Top left: pressure measured at the TPC. Top right: current measured at the drift field supplier. Bottom left: temperature of nitrogen just before the argon pre-cooling (at the Rn-trap). Bottom right: temperature at a pump.

It is found that most parameters do not have any significant peak on the power spectrum, however, several parameters do have a peak around the periodicity of 1 yr. Fig. 5.27 shows the temporal evolution and its power spectrum of such parameters. After detailed check of these parameters, we consider that negligible impact from the variation of these parameters on the TPC is expected because of the following reasons. First of all, these parameters do not have any sinusoidal variations. This is obvious if one tries to fit the variation with a cosine function, as shown with blue and orange lines in Fig. 5.27. Furthermore as discussed in Sec. 5.3 the algorithm has to be applied on data with Gaussian noise which is not the case for all SLC values. Some returned periodogram are clearly malfunctioning with high significant periodicity for the entire scanned frequency range. We also examine the correlations between the parameters and TPC event rates by introducing an arbitrary time shift (from ±7 d to ±2 mo), so that any time-delayed effect may be caught. It is found that no correlation larger than 0.1 is observed. Moreover, we do not find any reasonable explanations how most parameters can affect the condition of the TPC.

Therefore, we do not anticipate any artificial signal from the variance of the detector conditions.

5.4.5 Lomb-Scargle in $N_{e^-} = [170, 300]$

Periodicity in the event rate above the region of interest, in the range 170–300 e^- has been look upon with Lomb-Scargle algorithm apply to the residuals of the data. The same event selection described in Sec. 5.2.4 is used. A Least Square fit is first applied on the data constraining the activity of ^{85}Kr and ^{60}Co (evaluated with G4DS Fig. 5.7, we are above ^{37}Ar energy range). The returned fit function Eq. (5.46) is then subtracted from the event rate and after proper error propagation the Lomb-Scargle is calculated (further discussion on Lomb-Scargle details in Sec. 5.3).

$$f(t) = A_{\mathrm{Kr}} e^{-t/\tau_{\mathrm{Kr}}} + A_{\mathrm{Co}} e^{-t/\tau_{\mathrm{Co}}} + C \tag{5.46}$$

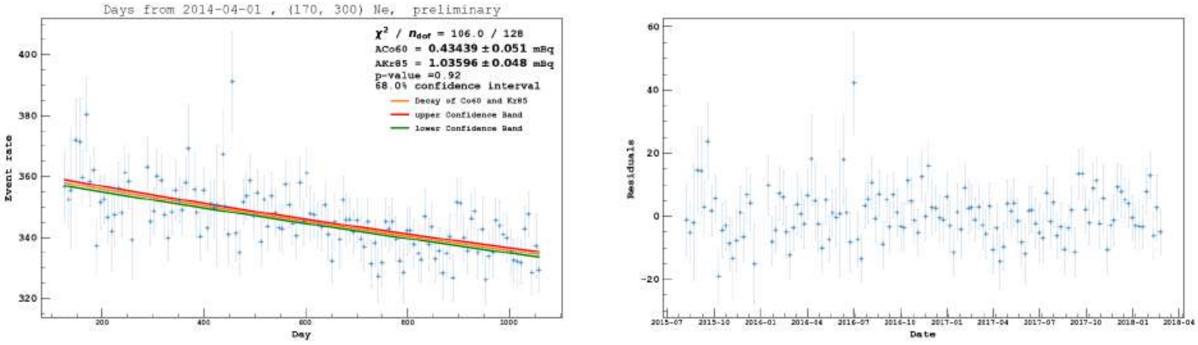

Figure 5.28: Time series event rate in $N_{e^-} = [170, 300]$

A bin width of 7 days is used for consistency with other N_{e^-} ranges, some of them can have data point with less than 3 events per day posing problem for both the Poissonian standard deviation and Least Square fit calculation. Thorough investigation on the effect of the time binning is done, looking at χ^2_ν, p-value, stability of the returned activity for the short lived isotope and stability of the Lomb-Scargle periodogram. No effect greater than 10% is found for all energy ranges. The fit is consistent with the null hypothesis, the decays of ^{60}Co and ^{85}Kr are sufficient to characterize the event rate evolution. The residuals are compatible with Gaussian noise only.

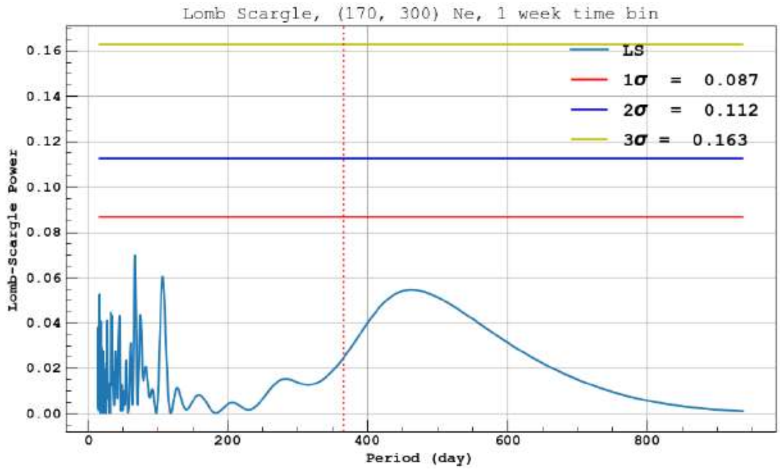

Figure 5.29: Lomb-scargle periodogram in $N_{e^-} = [170, 300]$ with the 1,2 and 3 σ line, the so called false alarm level estimated using the bootstrap method.

The resulting Lomb-Scargle doesn't show any period with a significance around 1 σ showing the stability of the detector.

5.5 Annual modulation analysis with DarkSide-50

5.5.1 Lomb-Scargle results

As discussed in Sec. 5.4.5, Lomb-Scargle is applied on the residuals of the data, after subtraction of Eq. (5.47) taking into account the activity of ^{37}Ar, ^{85}Kr and ^{60}Co as constrained parameter in the Least Square fit. A particular attention is put on the activity of ^{37}Ar as it can induce a strong periodicity in the Lomb-Scargle periodogram (as shown here Fig. 5.33).

This activity is constrained from a side-band analysis Sec. 5.2.2, a cross check analysis using the Least Square fit with Eq. (5.47) on the energy range [4,170] Ne is done on the side band region, as well as the combination of the search region and the sideband, the returned activities are all within 1σ. For these fit only activity of ^{85}Kr and ^{60}Co is constrained as well as the lifetime, the returned value for the activity of ^{37}Ar is (7.23 ± 0.37) mBq for the sideband (almost identical as the one in Sec. 5.2.2), (8.10 ± 0.68) mBq for the combination of the two showing good agreement with the expected value. To assure the well behaviour of the method used to get the residual, the method has been used letting the activity of ^{37}Ar free, and changing the time bin throughout the different energy region. The resulting χ^2_ν, p-value and ^{37}Ar activity are stable within 10%.

$$f(t) = A_{\mathrm{Ar}} \exp\left(-\frac{t}{\tau_{\mathrm{Ar}}}\right) + A_{\mathrm{Kr}} \exp\left(-\frac{t}{\tau_{\mathrm{Kr}}}\right) + A_{\mathrm{Co}} \exp\left(-\frac{t}{\tau_{\mathrm{Co}}}\right) + C \tag{5.47}$$

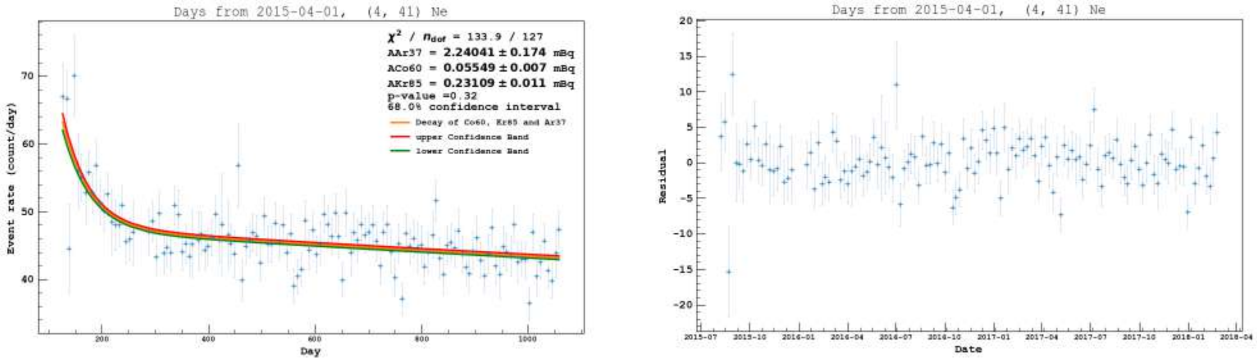

Figure 5.30: Right: Event rate in $N_{e^-} = [4, 41]$ with a binning of 7 day from 2015-04-01. Left: Residuals after subtraction

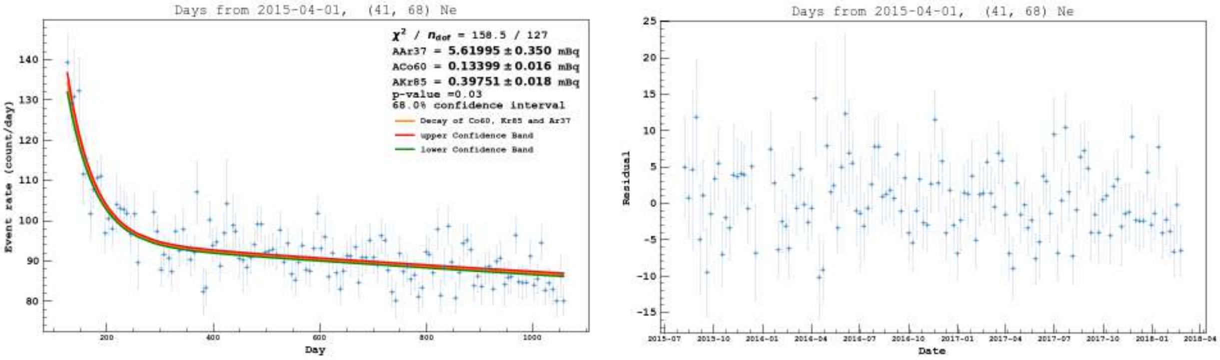

Figure 5.31: Right: Event rate in $N_{e^-} = [41, 68]$ with a binning of 7 day from 2015-04-01. Left: Residuals after subtraction

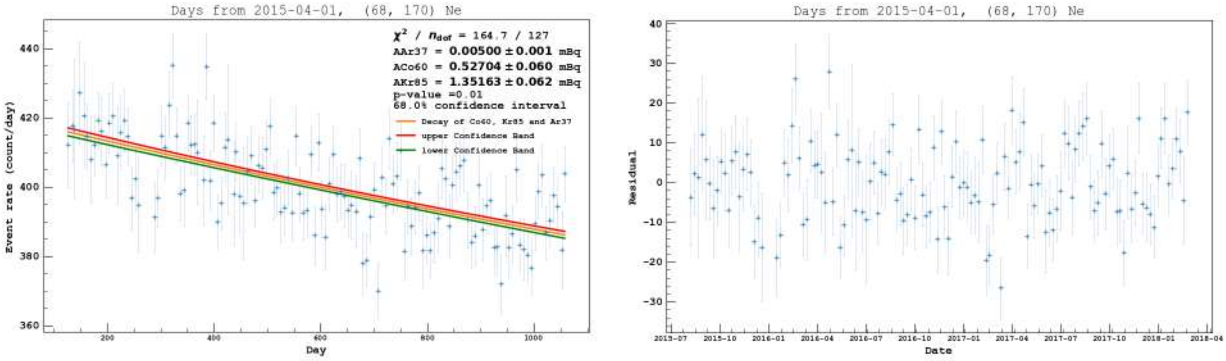

Figure 5.32: Right: Event rate in $N_{e^-} = [68, 170]$ with a binning of 7 day from 2015-04-01. Left: Residuals after subtraction

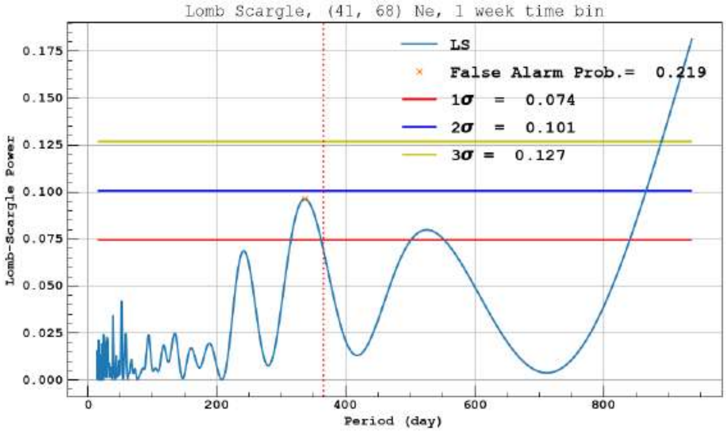

Figure 5.33: Lomb-scargle periodogram in $N_{e^-} = [41, 68]$ with the 1,2 and 3 σ line, the so called false alarm level estimated using the Baluev method. Here the Lomb-Scargle algorithm is applied before subtraction of the short live isotope activity, showing the impact they can have.

The data-set is split between 3 energy ranges, [4,41] Fig. 5.30 [41,68] Fig. 5.31 and [68,170] N_{e^-} Fig. 5.32 to compare with others experiments results. Discussions regarding the pseudo-Nyquist limit, the Gaussian noise and the normalization for Lomb-Scargle are present in Sec. 5.3 following recommendation from [127]. The result from the Lomb-Scargle analysis is show here Fig. 5.34, no periodicity is found with a power above the 1σ line. These lines represents the False Alarm Level calculated using the Bootstrap method.

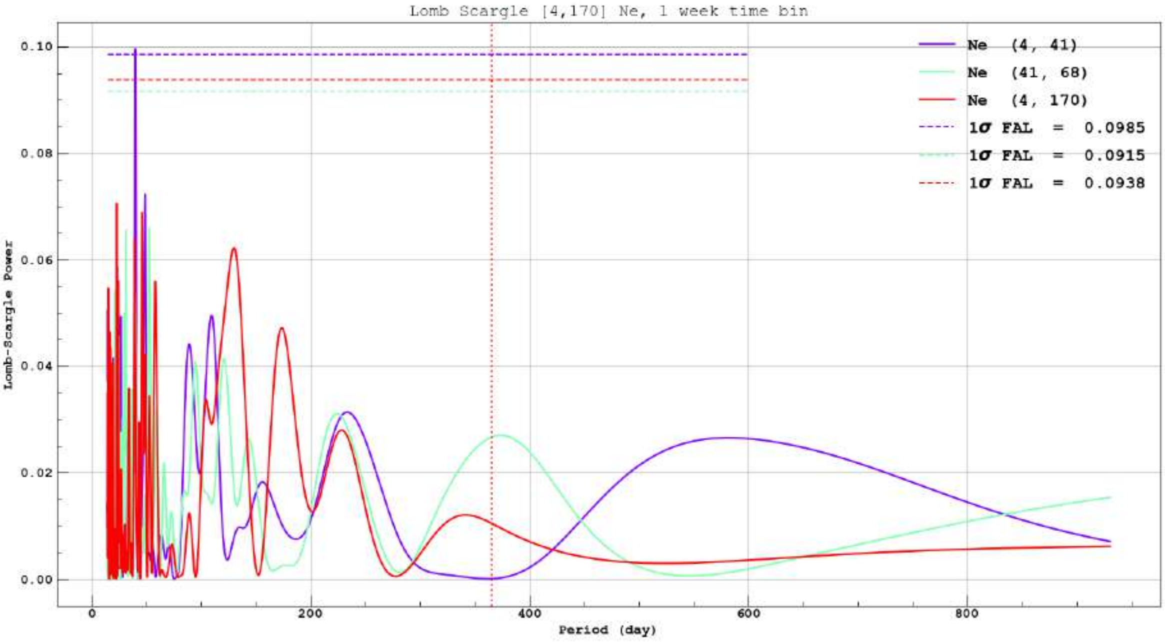

Figure 5.34: Lomb-scargle periodogram in $N_{e^-} = [4, 170]$ with the 1,2 and 3 σ line, the so-called false alarm level estimated using the Bootstrap method.

5.5.2 Monte-Carlo simulations

As previously discussed we performed toy Monte-Carlo simulations to assess the significance of the correlation coefficient found between SLC and data event rate, as well as the results found with the Lomb-Scargle analysis mentioned above. We are interested in:

- The significance of the correlation coefficient and how well the background only hypothesis is able to reproduces these coefficients
- The significance and the well founded hypothesis behind the Lomb-Scargle periodogram and the overall analysis applied to the time series Sec. 5.2.4
- A quantitative analysis on the impact a dark matter signal would have in the time series event rate

Regarding the correlation coefficient calculations it is important to have a date to date comparison, as for the Lomb-Scargle, windows structure effect (described in Sec. 5.3), can create aliases of peaks, and impact the significance. For the purpose of achieving the best comparison to data possible, the first step is to copy the time-series structure. Meaning the date as well as *lt* are the same between data and the simulation data-set. With the date fix, the *nev* is drawn from a Poisson distribution,

$$f(k;\lambda) = \Pr(X{=}k) = \frac{\lambda^k e^{-\lambda}}{k!}, \tag{5.48}$$

with k is the number of occurrences and λ is the expected value of X as well as its variance.

For each date our expected value is governed by,

$$f(t) = A_{\mathrm{Kr}}e^{-t/\tau_{\mathrm{Kr}}} + A_{\mathrm{Co}}e^{-t/\tau_{\mathrm{Co}}} + A_{\mathrm{Ar}}e^{-t/\tau_{\mathrm{Ar}}} + A^s\cos\left(2\pi\frac{t-\phi^s}{T^s}\right) + C, \tag{5.49}$$

with the sums of short lived isotopes (already discussed in Sec. 5.2.4), the cosine term representing dark matter annual modulation, with A^s its amplitude, T^s its period and ϕ^s its phase (further discussion in Sec. 5.1) and the constant term C encapsulating all flat components such as decay of long lived isotopes (e.g. ^{39}Ar) and the possible majority of events occurring from a dark matter interaction.

ϕ^s is set to reach a maximum of the modulation on June 2^{nd} and a minimum on the 2^{nd} of December. Since no modulations were observed, we did not put an emphasis on the phase, nevertheless we should mention that in the case of a strong modulation we could easily establish ϕ^s as shown in Fig. 5.35. It was obtained with a simulation adding $A^s = 0.05$ counts/d/kg/KeV, we then phase the data residuals and plot the Lomb-Scargle model fit found at one year with Eq. (5.18). As expected the best fit model returns a maximum at 0.17, which is 62 days after the first of April so June 2^{nd}.

A^s is expressed in counts/d/kg/keV to simplify comparison with other experiments, hence 4–41 e^- becomes 0.06–2 keV, 41–68 $e^- \rightarrow$ 2–6 keV and 68–170 $e^- \rightarrow$ 6–21 keV. We also need to take into account the fiducial mass, which is 18.63 kg (more details Sec. 5.2).

C is not a parameter of importance in this analysis, for straightforward comparison with the data time-series we took a random value in the distributions that follow the value and covariance matrix found with the Least-square fit Eq. (5.11) (more details about how we obtained these distributions in the next paragraphs).

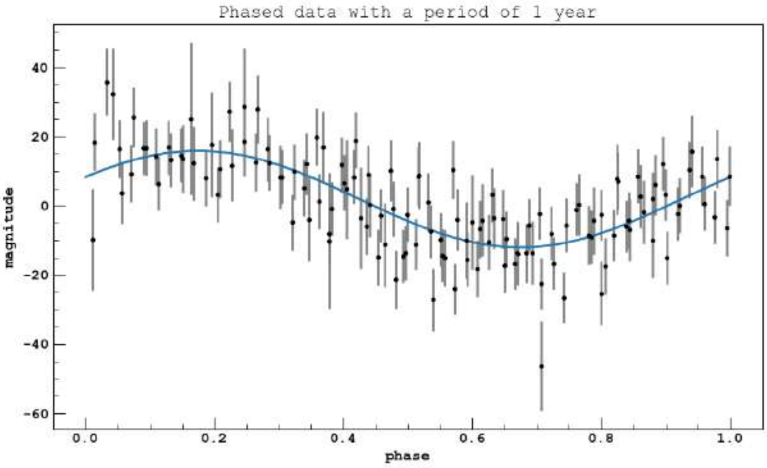

Figure 5.35: Simulated phased data, with the addition of an annually modulated signal of 0.05 events/(keV d kg), the blue line is the best fit model obtain with the Lomb-Scargle algorithm.

Finally we placed a particular interest for the short lived isotope activities, at first we simply used the value from Table 5.1, but it was deemed insufficient to account for the uncertainty related to some of its components, in particular ^{37}Ar (as discussed in Sec. 5.2.2).

To generate data with a sample covariance matrix $\hat{\Sigma}$ that matches a given covariance matrix Σ_S, coming from the Least square fit (Eq. (5.11)) we followed this procedure.

In a broader context, we usually want to produce data from a probability density function $f(x|\theta)$, where x represents the data and θ represents a parameter vector. As a consequence, a representative subset is obtained, from which we can then get an estimated value θ. The focus of our attention lies in the inverse problem, which involves generating a sample x such that $\hat{\theta} = \theta_S$.

For multivariate normal distributions, it is necessary to initially standardise the random normal variables by removing any random fluctuations from the zero mean and identity covariance, I_n. This involves adjusting the sample mean to zero and the sample covariance to I_n, before continuing with the subsequent steps.

This procedure involves the subtraction of the sample mean of z,

$$z^* = z - \bar{z} \tag{5.50}$$

and the subsequent calculation of the Cholesky decomposition of z^*. If L^* represents the left Cholesky factor, then the equation,

$$z^{(0)} = (L^*)^{-1} z^* \tag{5.51}$$

implies that the sample mean of $z^{(0)}$ should be 0 and its sample covariance should be an identity matrix. One can subsequently compute the value of our parameter y by adding the initial value to the parameter , resulting in a sample that possesses the desired sample moments,

$$y = L z^{(0)} + \mu \tag{5.52}$$

Subsequently, it is feasible to impose the desired covariance matrix and mean by applying appropriate transformations. If Σ and μ represent the covariance and population mean that are required, and z represents independent and identically distributed standard normal variables, the calculation of

$$y = Lz + \mu \tag{5.53}$$

can be performed for L where,

$$LL' = \Sigma. \tag{5.54}$$

Here, L is a matrix created using Cholesky decomposition, so that y has the desired population characteristics.

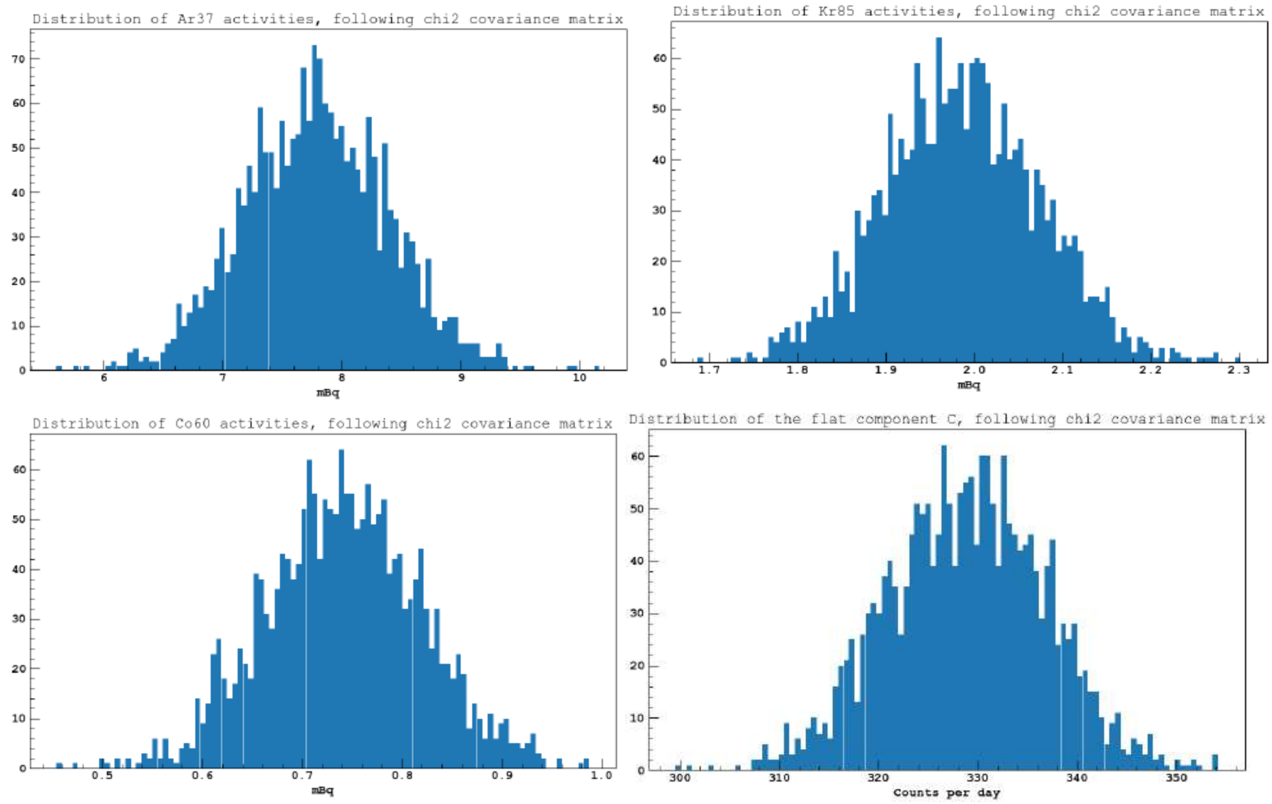

Figure 5.36: Distribution of activities and C for the Monte-Carlo simulations in the full energy range 0.06–21 keV, following Eq. (5.52), a random value from this distributions is taken before each iteration of the algorithm.

Fig. 5.36 shows the distribution used to simulate the Monte-Carlo data-set used for the calculation of p-value in Sec. 5.4.3, as well as Brazilian band around the time-series and the Lomb-Scargle periodogram shown in Sec. 5.5.3. We simply draw random value from these distributions before each iteration of the algorithm. Simulations differ from that point onward as the needed output vary. For the correlation coefficient, we are interested in simulation generating the residuals of the time series for a one day or seven days binning. Consequently we applied the Least square fit and error propagation (discussed in Sec. 5.2.4). Additionally we applied the Lomb-Scargle to obtain both the full periodogram and the power

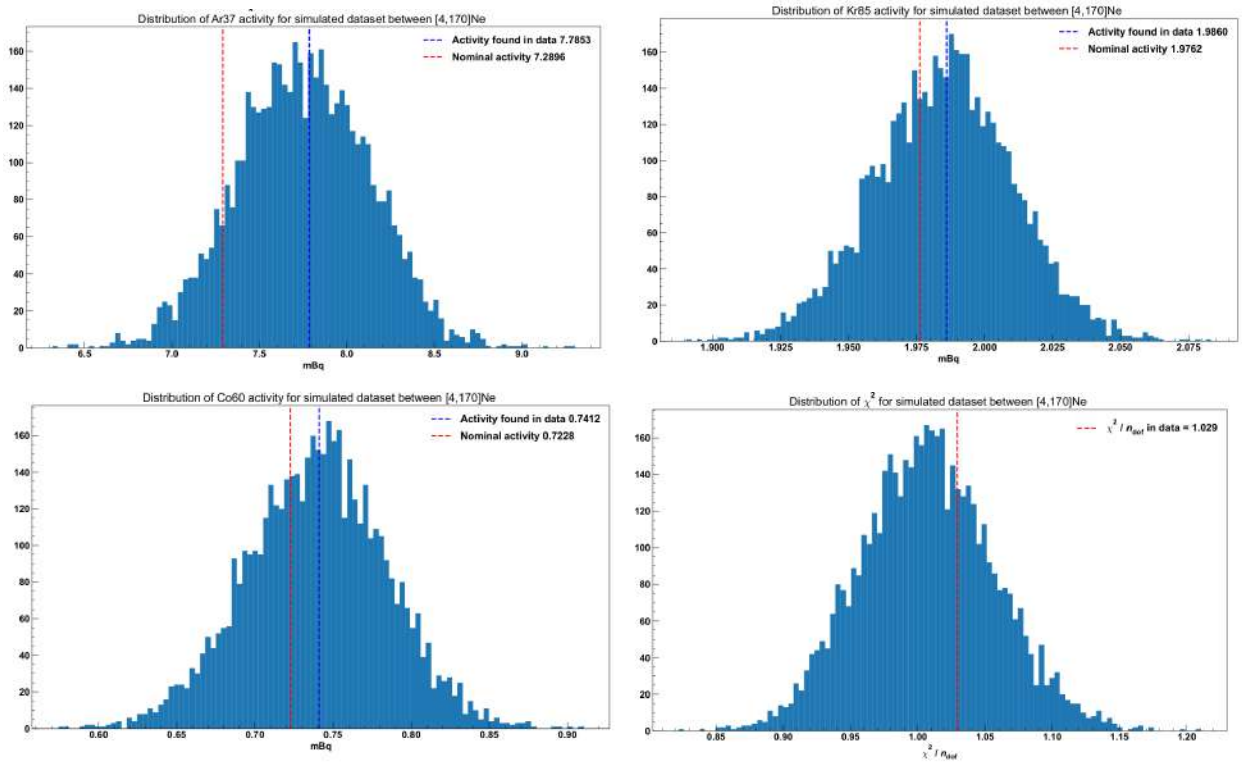

Figure 5.37: Distribution of activities and χ^2_ν found with the χ^2 fit on the Monte-Carlo simulations data-set in the full energy range 0.06–21 keV.

at one year. Finally to confirm some hypothesis presented in Sec. 5.4.3 we looked at some raw time series before subtraction.

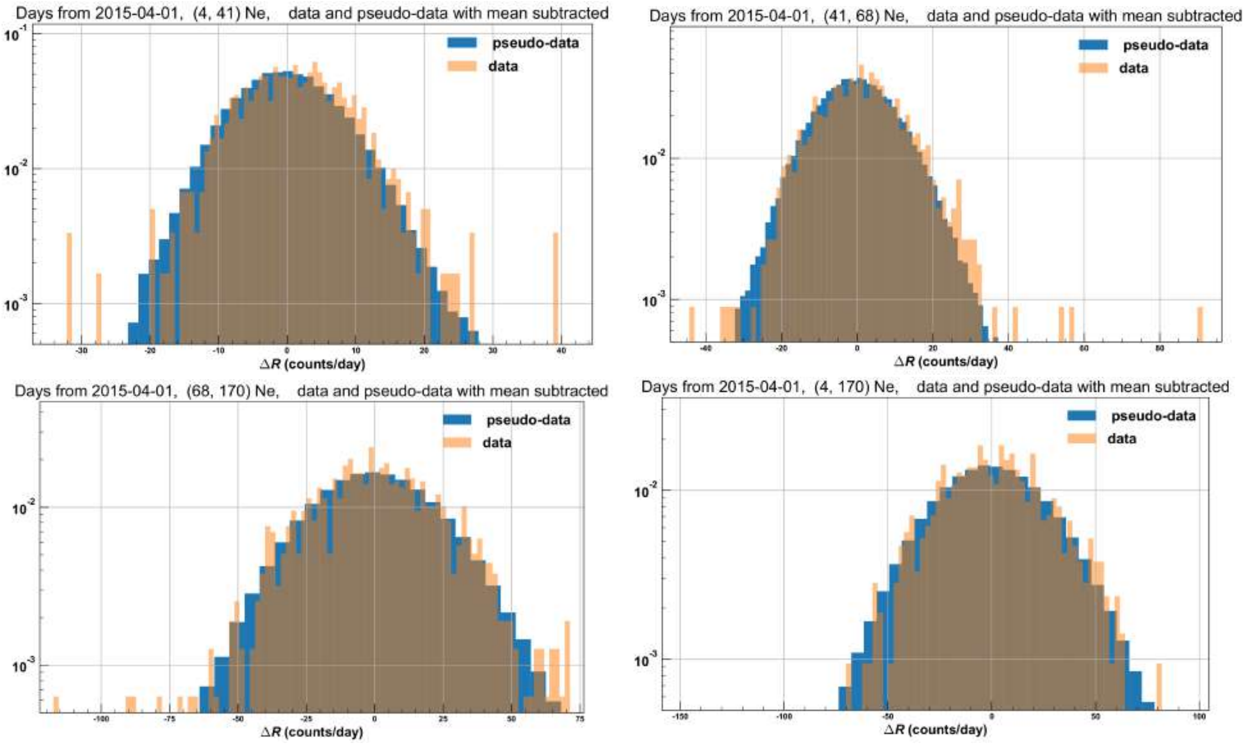

Figure 5.38: Distribution of $\Delta R = R - \bar{R}$, with R event rate at each date and $\bar{R}$ the mean value for both data and Monte-Carlo pseudo data-set. y-axis is normalized to facilitate comparison between the two

Fig. 5.37 shows the relevant distribution found with the χ^2 fit on the Monte-Carlo simulations data-set in 0.06–21 keV, as well as the results from data and the nominal value in Table 5.1. Also shown, the χ^2_ν distribution, serving as a strong argument for the properly realized simulation and it's aptitude to describe the data. Finally Fig. 5.38 presents the distribution of mean subtracted event rate, showing good agreement between data and Monte-Carlo pseudo data-set. The discrepancies could be explain by the statistical difference between the two distributions, as the pseudo data-sets have more than four millions data points whereas the data have ~ 830.

5.5.3 Setting upper limits

From the aforementioned simulations we are able to obtain comparisons between the null-hypothesis, data results and background plus signal hypothesis.

We first looked at time-series of the event rate Fig. 5.39, from the upper plots in 4–41 e^- and 41–68 e^-we obtain a good agreement between time-series data and the distribution from Monte-Carlo simulations shown with the Brazilian, 1σ and 2σ standard deviation, band for the one day and seven days binning.

The lower plots show the impact a dark matter signal added to the background would have, the impact is particularly significant in the 68–170 e^- as the event rate is very stable with no ^{37}Ar decay. 0.015 events/(keV d kg) would already create a noticeable aftermath, for lower energy range such as 2–6 keV, a higher amplitude would be necessary, here

0.04 events/(keV d kg) is exhibited.

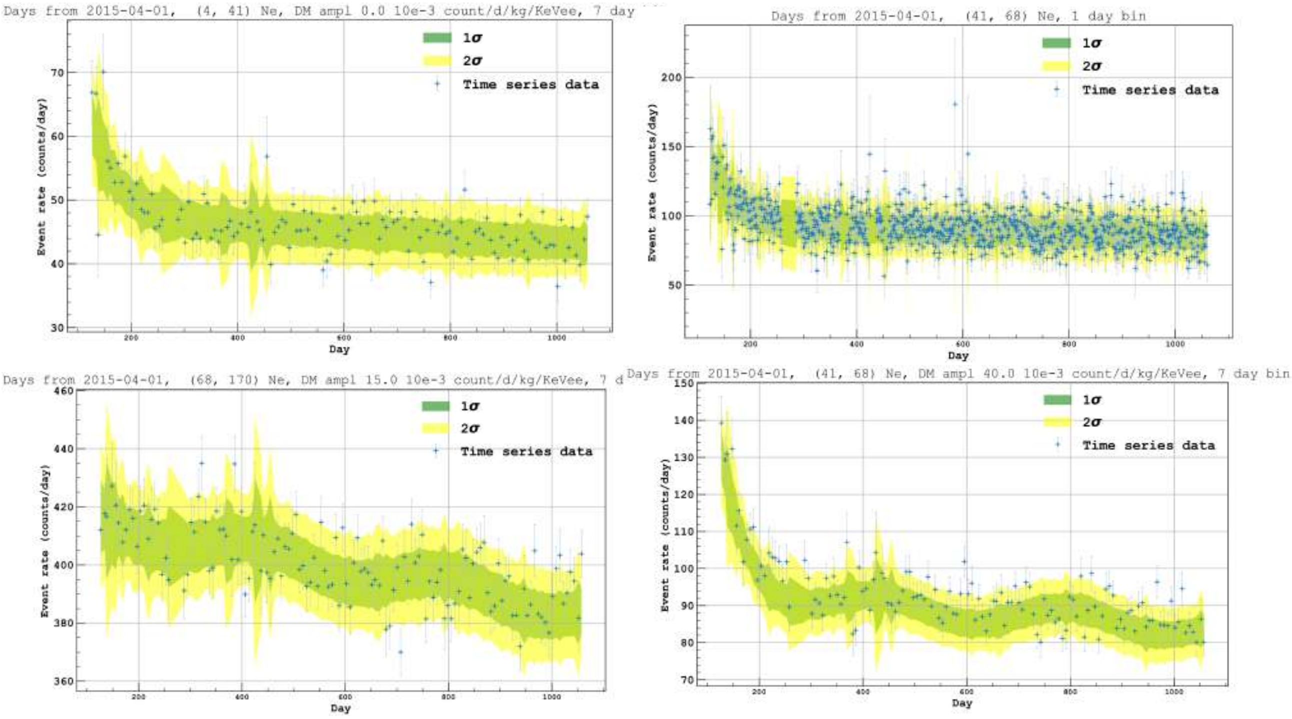

Figure 5.39: Time-series of the event rate with Brazilian band showing 1σ and 2σ standard deviation from Monte-Carlo simulations means with background only for top plots and a binning of one day and seven days. As well as the addition of dark matter signal for lower plots.

As the principal element of our analysis we carried on a similar visual comparison with the Lomb-Scargle periodogram. Fig. 5.40 summarize our finding, once again the background only simulations, upper right plot, offer a good agreement with data. As we increased the strength of the signal a more significant peak appears at one year, yielding a stronger separation with data. After normalization of the Lomb-Scargle power by 1σ false alarm probability for all pseudo data-set, we assessed that a median of 1σ significance is obtained with the addition of 0.035 events/(keV d kg) in 0.06–2 keV, 0.025 events/(keV d kg) in 2–6 keV and 0.015 events/(keV d kg) in 6–21 keV.

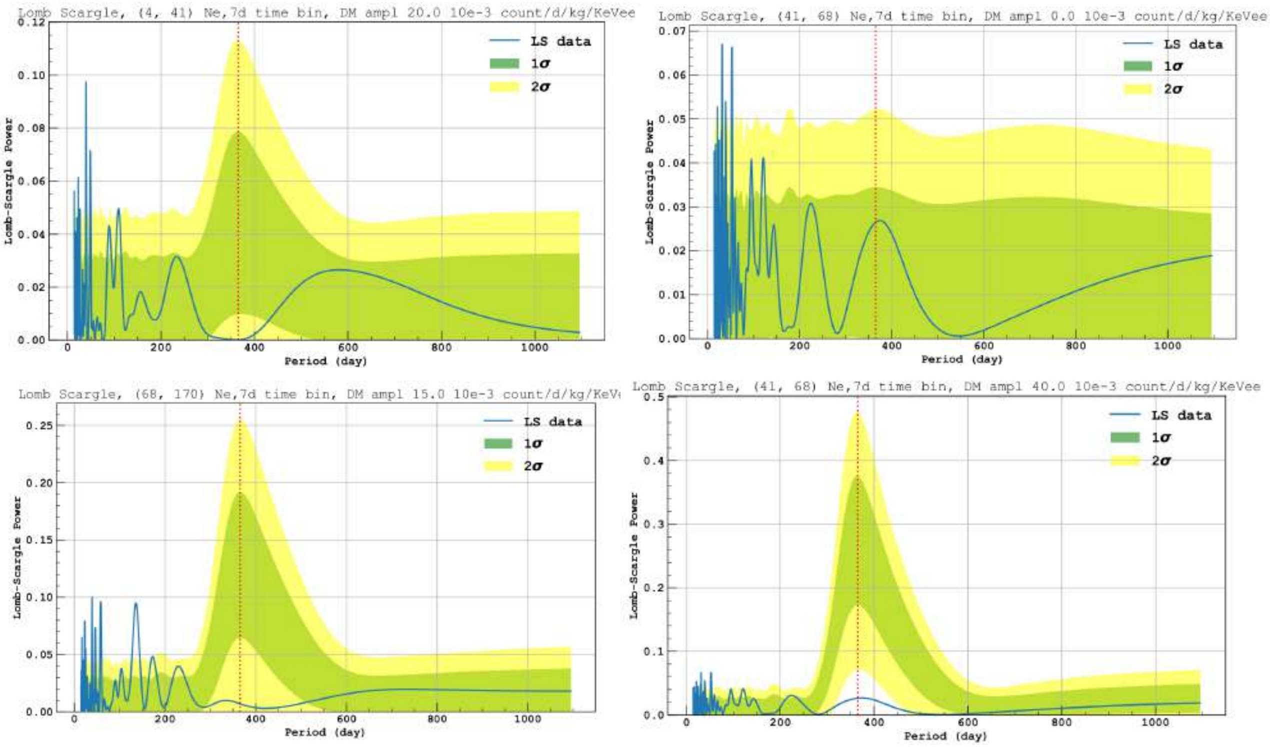

Figure 5.40: Lomb-Scargle periodogram with Brazilian band showing 1σ and 2σ standard deviation from Monte-Carlo simulations means with background only for top left plot. As well as the addition of dark matter signal for the three others plots.

It should be noted that the Lomb-Scargle false alarm probability method was not conceived to exclude the presence of a signal in our data but for assessing the probability that a Gaussian noise only data-set would produce a peak with the same magnitude as we observed. As a consequence we opted to use the CL_S method to set an upper limit on the dark matter amplitude.

From Bin [145], we define CL_S as,

$$CL_S^{(\mu)} = \frac{CL_{S+B}^{(\mu)}}{CL_B^{(\mu)}} \tag{5.55}$$

with μ the strength of our signal, the dark matter amplitude (0 being the background only case),

$$CL_{S+B}^{(\mu)} = \int_{q_\mu^{obs/exp}}^{\infty} f(q_\mu/\mu)dq_\mu \tag{5.56}$$

$$CL_B^{(\mu)} = \int_{q_\mu^{obs/exp}}^{\infty} f(q_\mu/0)dq_\mu \tag{5.57}$$

q is the test statistic results, in our case it is either the expected value, define by the median of the background only distribution or the observed in data Lomb-Scargle power at one year. As the distributions have increasing values we integrate from 0 to $q_\mu^{obs/exp}$

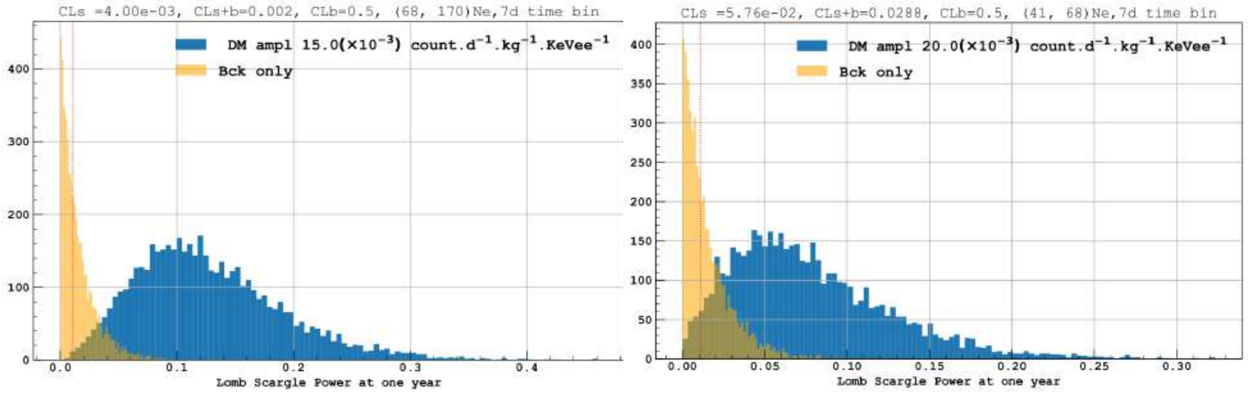

Figure 5.41: Null hypothesis and background plus signal distributions of the Lomb-Scargle power at one year in 68–170 e^- and 41–68 e^- with $\mu = 0.015$ events/(keV d kg) and $\mu = 0.020$ events/(keV d kg), the dash line is the median of the background only distribution.

instead of $q_\mu^{obs/exp}$ to ∞. Fig. 5.41 shows the null hypothesis and background plus signal distributions of the Lomb-Scargle power at one year in 68–170 e^- and 41–68 e^- with $\mu = 0.015$ events/(keV d kg) and $\mu = 0.020$ events/(keV d kg)

Fig. 5.42 demonstrates our expected exclusions limits for all RoI, the 95% CL_S threshold is crossed at ∼0.030 events/(keV d kg) in 0.06–2 keV, ∼0.020 events/(keV d kg) in 2–6 keV and ∼0.012 events/(keV d kg) in 6–21 keV. We should mention that CL_S drop to 0 at 0.045 events/(keV d kg) in 0.06–2 keV, 0.030 events/(keV d kg) in 2–6 keV and 0.015 events/(keV d kg) in 6–21 keV due to statistical fluctuations in the Monte-Carlo simulations that the histogram method is susceptible to. Even with 5000 simulations as the dark matter amplitude augment we are left with not a single simulation possessing a Lomb-Scargle power at one year as low as the one in the data, something that we can get around with the use of probability density function.

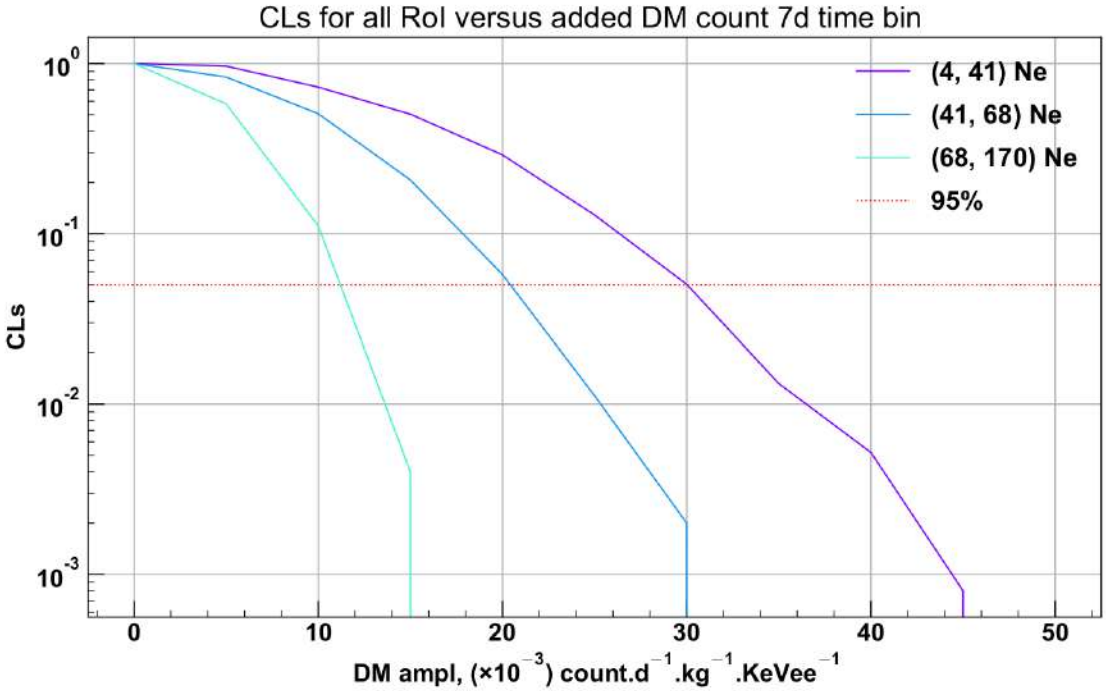

Figure 5.42: Expected exclusion limits for all region of interest.

Lastly we turned our attention toward the observed exclusion limits, as the observed Lomb-Scargle power at one year is notably low in 0.06–2 keV, we could not simply work with the histograms showed in Fig. 5.41 as it returned a value of 0 for CL_S. We had to work with probability density functions instead, obtained through Kernel Density estimation using the Gaussian method [146],

$$\hat{f}_h(x) = \frac{1}{n}\sum_{i=1}^{n} K_h(x - x_i) = \frac{1}{nh}\sum_{i=1}^{n} K\left(\frac{x - x_i}{h}\right), \tag{5.58}$$

where K is the kernel and $h > 0$ is a smoothing parameter called the bandwidth,

$$K(u) = \frac{1}{\sqrt{2\pi}} e^{-\frac{1}{2}u^2}. \tag{5.59}$$

Fig. 5.43 illustrates the probability density functions acquired with this method, the dash line is the Lomb-Scargle power at one year in data. For consistency we compare the CL_S derived with the previously employed method with the aforementioned one Eq. (5.58), yielding identical outcomes.

Our observed exclusion limits are shown in Fig. 5.44, the CL_S evolution is comparable for 0.06–2 keV and 6–21 keV with a slight difference in 2–6 keV due to small increase regarding the Lomb-Scargle power found in the data. As seen in Fig. 5.40 this value is well within the 1σ band, it nonetheless leads to an slight increase regarding the 95% CL_S threshold, achieve at ∼0.025 events/(keV d kg).

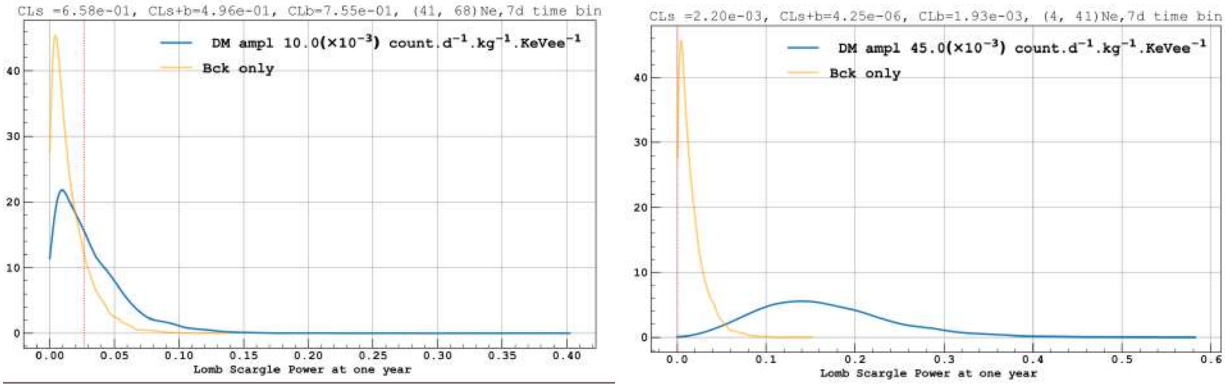

Figure 5.43: Null hypothesis and background plus signal distributions of the Lomb-Scargle power at one year obtained with Kernel density estimates in 4–41 e^- and 41–68 e^- with $\mu = 0.010\,\mathrm{events/(keV\,d\,kg)}$ and $\mu = 0.045\,\mathrm{events/(keV\,d\,kg)}$, the dashed line is the Lomb-Scargle power at one year in the data.

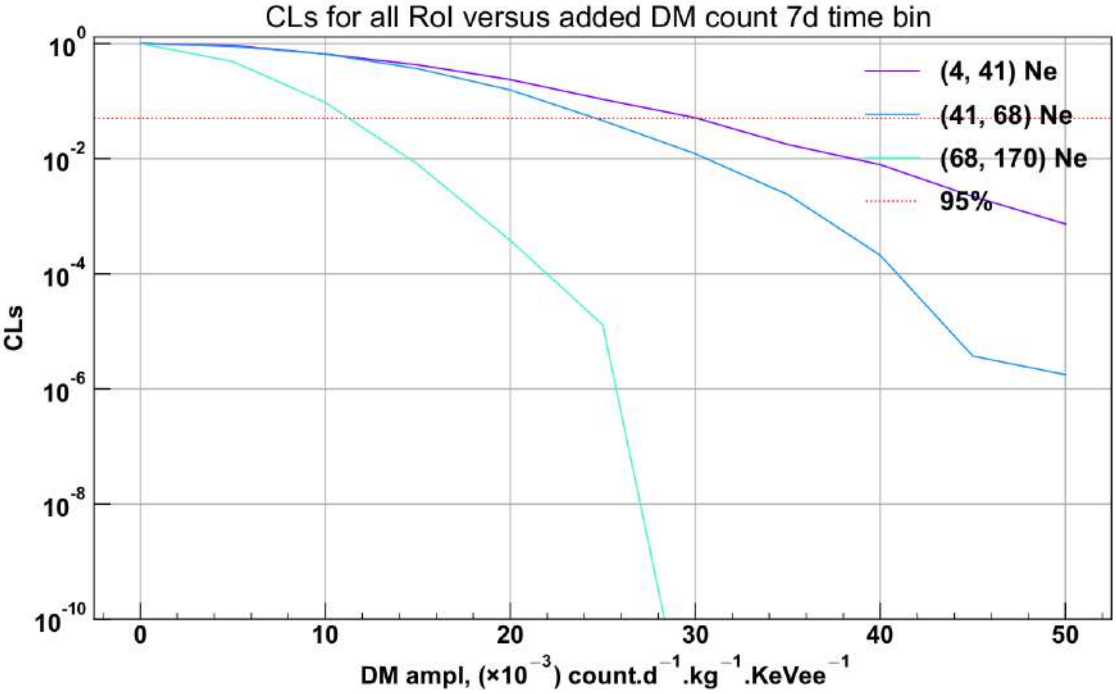

Figure 5.44: Observed exclusion limits for all region of interest.

5.6 Conclusion

For almost three years the DarkSide-50 dark matter experiment ran an underground argon campaign on the hunt for ∼keV interaction unexplained by known standard model processes.

In this chapter we presented two intricated analysis. The first one presented the stability of the detector performance by utilising both the Time Projection Chamber data and a range of sensors integrated inside the system.

The stability of the electroluminescence detection efficiency g_2 has been verified to remain within fluctuations of no greater than 0.5% due to the effective management of the cryogenic system. We were able to assess both quantitatively and qualitatively the stability of the cryogenic system showing no correlation with DarkSide-50 event rate. This analysis will be the subject of a future paper currently under review by the collaboration [2].

As a result of its stability, it was demonstrated that the temporal progression of the observed event rate can be effectively elucidated through the decay of radioactive isotopes. Subsequently, we proceed to illustrate the potential use of both the energy and temporal attributes of individual events in the hunt for dark matter.

A binned likelihood analysis was also performed, Fig. 5.45 and Appendix B, yielding a similar result to the Lomb-Scargle. It allows direct comparison to other experiments, and resulted in a WIMPs observed 90% C.L. upper limit, shown in Fig. 5.46, it is derived by the CLs technique [147] via the `RooStat` framework.

Because of the lack of knowledge on the width of the ionization distribution of nuclear recoils, we show the limits assuming two extreme models, as in Ref. [148, 85]; one allowing for fluctuations in energy quenching, ionization yield, and recombination processes obtained with binomial distributions (quenching fluctuation; QF), and another where the fluctuation in the energy quenching is set to zero (without quenching fluctuation, NQ). Comparing the result with that from the spectrum analysis, we obtain a small gain in terms of sensitivity. This is because our data is background limited and well described by the background model. Nevertheless, this is the first WIMP search utilizing both time and energy information for LAr TPC, working as an additional test of the presence of WIMPs.

In summary, our investigation focused on examining the event rate modulation within the DarkSide-50 dataset, specifically within the energy range of 2.0 to 6.0 keV_{ee}. This analysis was prompted by the observation made by DAMA/LIBRA, which reported a yearly modulated signal that is consistent with the presence of dark matter. In addition, we have successfully explored the energy range down to a record-breaking threshold of 0.04 keV_{ee} in our annual search for dark matter modulation, marking the first instance of such investigation at this level. No modulation signal was identified in any of the analysed intervals. The level of significance associated with this outcome is inadequate for either confirming or refuting the DAMA/LIBRA observation, nevertheless our analysis lead to a publication [1].

The competitiveness of the dual-phase LAr-TPC technology in the search for modulation signals is demonstrated by the stability of the DarkSide-50 detector over its nearly three years of operation, the accuracy of the background model, and the attainment of a low-energy threshold.

Hence, the obtained outcome exhibits promise with regards to forthcoming extensive dual-phase liquid argon experiments [63, 149, 150], which are anticipated to achieve significantly

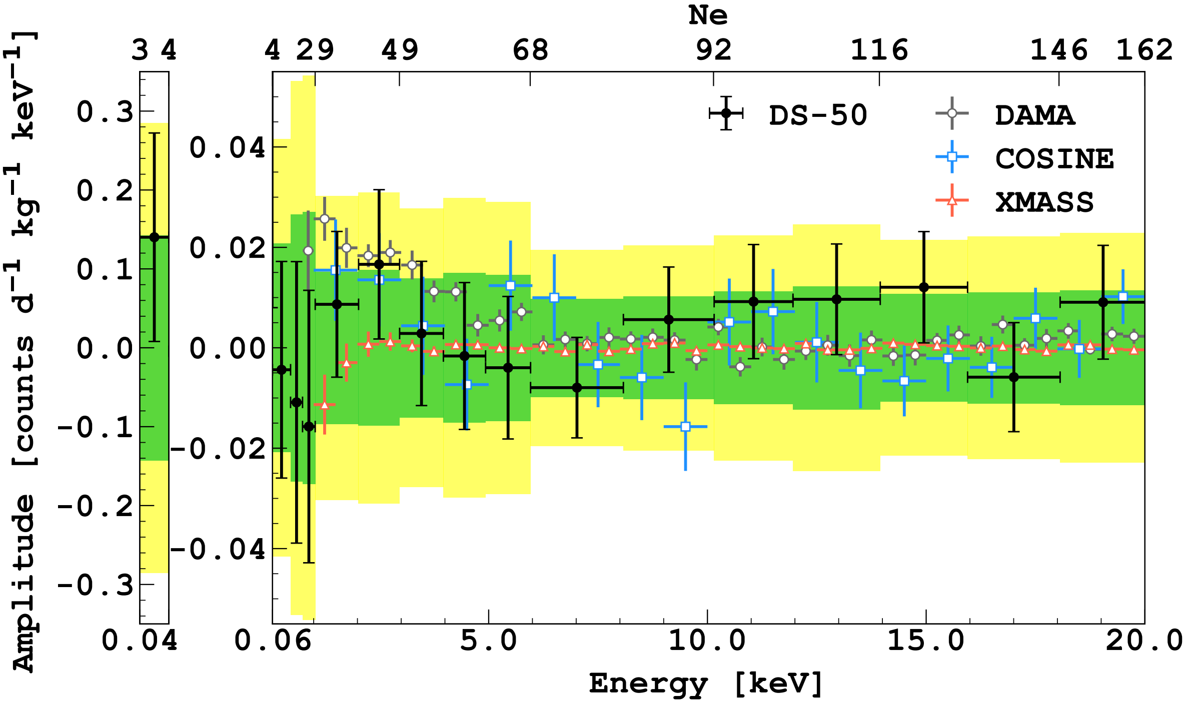

Figure 5.45: Best fit amplitude of the modulation signal as a function of N_{e^-}. The green and yellow bands represent the expected 1σ and 2σ statistical fluctuations derived by background-only Monte Carlo samples. Also shown are the results from DAMA/LIBRA [151], COSINE-100 [110], and XMASS [152]. *Taken from [117].*

higher levels of exposure and even lower levels of background interference.

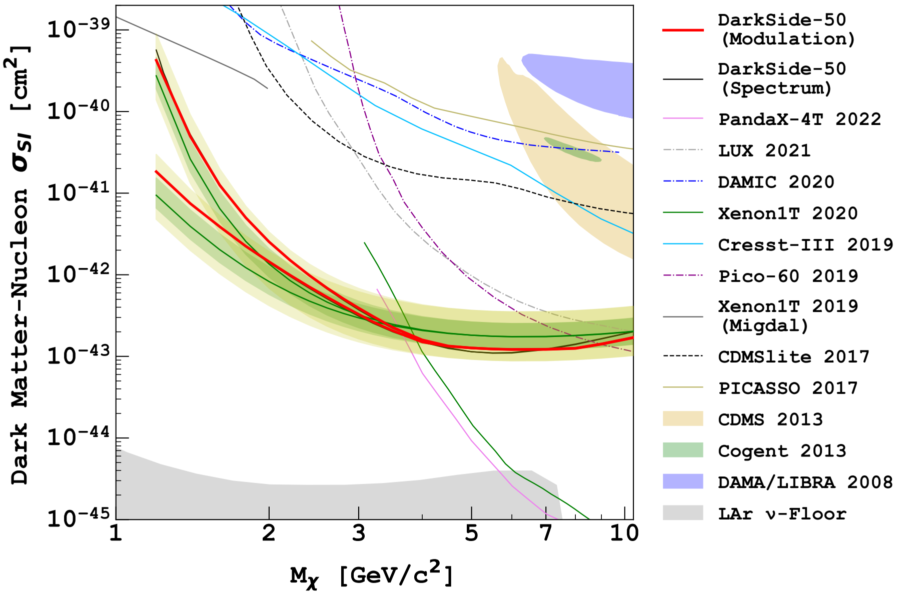

Figure 5.46: Observed 90% C.L. upper limit for the WIMP search (green solid line). The time and N_{e^-} binnings used are 7 d and 1 e^-, respectively. Observed limit from the spectrum analysis, as well as that from other experiments, are also shown. *Taken from [117].*

Chapter 6

Conclusions

In the realm of particle physics and cosmology, the search for dark matter stands as one of the most pressing and profound quests of our time. This thesis has embarked on an exploratory journey through the intricate landscape of dark matter, focusing on the innovative use of liquid Argon detectors and culminating in the search for dark matter via its annual modulation signature.

We first delved into the foundational aspects of dark matter, starting with an exploration of cosmological and astrophysical observations. Diverse candidates for dark matter were presented, from theories of new gravity to MACHOs, primordial black holes, sterile neutrinos, axions, and the Weakly Interacting Massive Particles. The prospects for detecting dark matter were discussed, encompassing particle accelerators, indirect detection methods, and direct detection experiments. Particular focus was dedicated to liquid argon detectors, shedding light on their unique properties and the critical role they play in the quest for dark matter. The scintillation process within liquid argon as well as the utilization of underground argon were discussed. The architecture and components of DarkSide-50 and DEAP-3600, two prominent liquid argon detectors, were examined in details.

Chapter 4 has provided a comprehensive exploration of the intriguing phenomenon of Boosted Dark Matter, which offers a unique avenue for the detection of previously unexplored dark matter interactions.

We investigated specific iBDM models, including upscattering off electrons and protons, which shed light on the diverse mechanisms by which bDM particles may interact with ordinary matter. These models open up exciting possibilities for identifying the elusive dark matter particles within DEAP-3600.

We discussed the sensitivity of DEAP-3600 to iBDM signals, presenting detailed sensitivity plots and an exploration of the expected signal of bDM particles within the detector. This analysis allows to understand DEAP-3600's potential to unveil the presence of iBDM in our Universe.

The culmination of this journey unfolded in Chapter 5, where the concept of annual modulation analysis took center stage. The significance of annual modulation, both as a model-independent approach and within the context of the standard WIMP model, was established. After discussing DarkSide-50 Lowmass analysis strategy, focusing on mitigating the impact of long-lived and short-lived isotopes, was described. Advanced statistical tools, including the Lomb-Scargle periodogram, were applied to investigate the stability of DarkSide-50. The correlation between Slow Control variables and data, as well as delay correlations, were examined in detail. The dark matter search was carried with a Lomb-Scargle analysis on the residuals of the background only fit, yielding no modulation detected in all analyzed energy ranges. I employed Monte Carlo simulations to validate and refine the analysis methodology. The determination of upper limits on dark matter interactions allowed me to put 95% CL_S at ∼0.030 events/(keV d kg) in 0.06–2 keV, ∼0.020 events/(keV d kg) in 2–6 keV and ∼0.012 events/(keV d kg) in 6–21 keV, providing a general model-independent cross-check and complementing the binned likelihood analysis published in Ref. [1]. We presented the first annual modulation search with liquid argon achieving the lowest ever energy threshold of 0.04 keV used in this type of searches. The results cannot confirm nor reject DAMA/LIBRA claims but represent a significant milestone and demonstrate the efficiency liquid argon detector can achieve with the proper stability and exposure.

In conclusion, this thesis has embarked on a multifaceted exploration of dark matter with a particular emphasis on $\sim$GeV/c^2 candidates. Many experiments are currently under construction such as DarkSide-20k. Over a span of ten years, DarkSide-20k anticipates being capable of detecting cross-sections of 6.3×10^{-48} cm^2 with a 90% confidence level for exclusion, and 2.1×10^{-47} cm^2 for a 5σ discovery, specifically for WIMPs with a mass of 1 TeV/c^2. The quest for dark matter remains vibrant, promising a rich future for potential discoveries and technological progress.

Appendix A

P-value for correlation coefficient

As descibed in Sec. 5.4.3, we utilize two methods for the calculation of correlation coefficient, one using MC pseudo data-set explained in details, one with scipy build in method to assess the probability that data with independent distribution would lead to a value as high as the correlation coefficient found.

A.1 Pearson

Assuming x and y are sampled from independent normal distributions, where the population correlation coefficient is 0, the probability density function of the sample correlation coefficient r_p can be described as stated in references [153]

$$f(r) = \frac{(1 - r^2)^{n/2-2}}{B(1/2, n/2 - 1)}, \tag{A.1}$$

with n representing the quantity of samples, and B denotes the beta function. The distribution being considered is a beta distribution, which is defined on the interval [-1, 1]. It has equal shape parameters, denoted as a and b, which are both equal to n/2 - 1.

The p-value produced by the pearson scipy function is a two-sided p-value by default. In the context of a particular sample, the p-value is the likelihood that the absolute value of the correlation coefficient of a randomly selected sample from a population with no correlation would be equal to or greater than the absolute value of the observed correlation coefficient.

A.2 Kendall & Spearman

The examination is conducted by comparing the observed value of the statistic with the null distribution, which represents the distribution of statistic values obtained assuming the null hypothesis, assuming that the measurements are independent.

In the context of this examination, it is possible to apply a transformation to the statistic, resulting in a null distribution that follows Student's t distribution with a degree of freedom equal to the length of the sample minus two.

The quantification of the comparison is determined by the p-value, which is the proportion of values in the null distribution that are as extreme or more extreme than the observed value of the statistic.

If the p-value is deemed to be statistically significant, indicating a low probability of obtaining the observed statistic from independent distributions, it can be interpreted as evidence contradicting the null hypothesis and supporting the alternative hypothesis that the distribution are not independent. It should be noted that:

- The converse of this statement does not hold true; specifically, the test is not employed to furnish support for the null hypothesis.
- The determination of the threshold for values that are deemed "small" is a decision that need to be taken prior to doing data analysis. This decision should take into account the potential dangers associated with both false positives (erroneously rejecting the null hypothesis) and false negatives (failing to reject a false null hypothesis).
- Low p-values do not indicate a substantial effect; instead, they solely offer support for a "significant" effect, implying that they are improbable under the null hypothesis.

It should be noted that the t-distribution offers an asymptotic approximation of the null distribution, and its accuracy is contingent upon the presence of a large number of observations in the sample. In the case of small sample sizes, it may be better suitable to do a permutation test. Assuming the null hypothesis of independence between x and y, it may be inferred that each measurement of y has an equal probability of being observed alongside any observation of x. Hence, it is possible to establish a precise null distribution by computing the statistic for every conceivable combination of elements between the variables x and y.

Appendix B

Likelihood modulation analysis

Sinusoid amplitude as a function of energy

This appendix describes the analysis done in [1] to achieve the Fig. B.2, taken from Kimura et al. [117]. A binned likelihood fit is done to assess the statistical significance of a hypothetical modulation signature. We model the signal and backgrounds with

$$f(t) = A_\chi \cos\left(\frac{t-\phi}{T/2\pi}\right) + \sum_i \frac{A_i}{\tau_i} e^{-t/\tau_i} + C \tag{B.1}$$

where A_χ is the amplitude of the signal, ϕ the phase, and T the period fixed to 1 yr. C is the sum of the non-modulated signal component and long-lived backgrounds. τ_i and A_i, for $i = \{^{37}\text{Ar}, ^{85}\text{Kr}, ^{54}\text{Mn}, ^{60}\text{Co}\}$, correspond to the decay times and amplitudes, of short-lived isotopes. The likelihood $\mathcal{L}$ is built as,

$$\mathcal{L} = \prod_{i\,\in\,\text{bins}} \mathcal{P}\left(n_i|m_i(A_\chi, \phi, \Theta)\right) \times \prod_{\theta_k\,\in\,\Theta} \mathcal{G}(\theta_k|\theta_i^0, \Delta\theta_k). \tag{B.2}$$

The first term represents the Poisson probability of observing n_i events in the i^{th}-bin with respect to $m_i(A_\chi, \phi, \Theta)$, the expected ones evaluated with Eq. (B.1). Θ is the set of nuisance parameters, constrained by Gaussian penalty terms in the last factor of Eq. (B.2), where θ_k^0 and $\Delta\theta_k$ are the nominal central values and uncertainties, respectively.

These are obtained from the combination of the uncertainty on the measured rate (14%, 4.7%, 40%, 12% for ^{37}Ar, ^{85}Kr, ^{54}Mn, ^{60}Co, respectively), with the uncertainty arising from the definition of the energy range due to ionization response. In addition, the uncertainty on the ^{85}Kr activity is combined with spectral uncertainties from the β-decay Q-value and atomic exchange and screening effects, as discussed in Ref. [85].

The observed event rates for three N_e bins are fitted independently by fixing the period T^i to 1 yr but floating the amplitude A_χ and phase ϕ.

Further constrain on the modulation amplitude is obtained by extending $\mathcal{L}^i$ in Eq. (B.2) to accommodate all N_e bins be fitted simultaneously;

$$\begin{aligned}
\mathcal{L} &= \mathcal{P}(N_{\mathrm{obs}}|M(A,\phi,T,C,\Theta)) && \text{(B.3)}\\
&\times \prod_{i\,\epsilon\,N_e\text{-bin}}\prod_{j\,\epsilon\,t\text{-bin}}\left(\frac{m_j^i}{M}\right)^{(n_{\mathrm{obs}})_j^i} \times \prod_{\theta_k\,\epsilon\,\Theta}\mathcal{G}(\theta_k^0|\theta,\Delta\theta_k), && \text{(B.4)}\\
N_{\mathrm{obs}} &= \sum_{i\,\epsilon\,N_e\text{-bin}}\sum_{j\,\epsilon\,t\text{-bin}}(n_{\mathrm{obs}})_j^i, && \text{(B.5)}\\
M(A,\phi,T,C,\Theta) &= \sum_{i\,\epsilon\,N_e\text{-bin}}\sum_{j\,\epsilon\,t\text{-bin}} m_j^i(A^i,\phi^i,T^i,C^i,\Theta), && \text{(B.6)}\\
&\equiv \sum_{i\,\epsilon\,N_e\text{-bin}}\sum_{j\,\epsilon\,t\text{-bin}} \varepsilon^i E_j f^i(t_j;A^i,\phi^i,T^i,C^i,\Theta). && \text{(B.7)}
\end{aligned}$$

Here, A^i is independent from each j-th bin, while Θ are common for all bins. We fix ϕ^i and T^i to that expected from the standard halo model. Benefiting from the correlations between N_e bins, we use a narrower binning having approximately 0.25 keV (below 1 keV), 1 keV (from 1 to 6 keV), or 2 keV (above 6 keV) width in terms of electron recoil energy. Fig. B.1 shows the observed event rate and the fit result with the time bin width of 7 days. Fig. B.2 shows the best fit amplitude A^s of the observed data as a function of electron equivalent energy, together with the expected sensitivity bands obtained by repeating the fit to many pseudo datasets and making the distributions of the best fit amplitude.

Analysis below $4\,e^-$

Based on the discussion in Sec. 5.2.3, the RoI is expanded by incorporating the bin of 3–4 e^-. In this analysis, the background model in Eq. (B.3) is rewritten as,

$$\mathcal{L} = \prod_{i,j\,\in\,\mathrm{bins}} \mathcal{P}\left(n_i|m_i(A_\chi^j,\tilde{\Theta})\right) \times \prod_{\tilde{\theta}_k\,\in\,\tilde{\Theta}} \mathcal{G}(\tilde{\theta}_k|\tilde{\theta}_k^0,\Delta\tilde{\theta}_k), \tag{B.8}$$

which is the product of Poisson probabilities in each of the ij-bins defined by the event time (i) and number of electrons (j). The bin width along the time axis corresponds to 7 d and it is along the energy axis 0.02 keV below 0.06 keV, 0.25 keV below 1 keV, 1 keV up to 6 keV, and 2 keV elsewhere, starting from 0.04 keV ($3\,e^-$).

The expected sensitivity is assessed upon an assumption that the excess event in the 3–4 e^- bin with respect to the background only fit above $4\,e^-$ is fully owed to the SE event. We first perform the background only fit for the N_e spectrum above $4\,e^-$, then determine the total number of SE event ($N_{\mathrm{se}}^{\mathrm{tot}}$) as to be the residual between the observed data and the fitted model. We assume that $N_{\mathrm{se}}^{\mathrm{tot}}$ is distributed based on Fig. 5.9 (right), i.e., $N_{\mathrm{se}}^{\mathrm{tot}}$ is the sum of temporally-correlated and -uncorrelated components and each component is distributed in time according to the observed functions.

The simultaneous fit is performed as is done in the preceding section. Fig. B.3 (left) shows the observed event rate and the fit result of the 3–4 e^- bin where the best fit SE model is shown together. The best fit amplitude of the lowest bin is (0.14 ± 0.13) events/(keV d kg), as shown in Fig. B.3 (right).

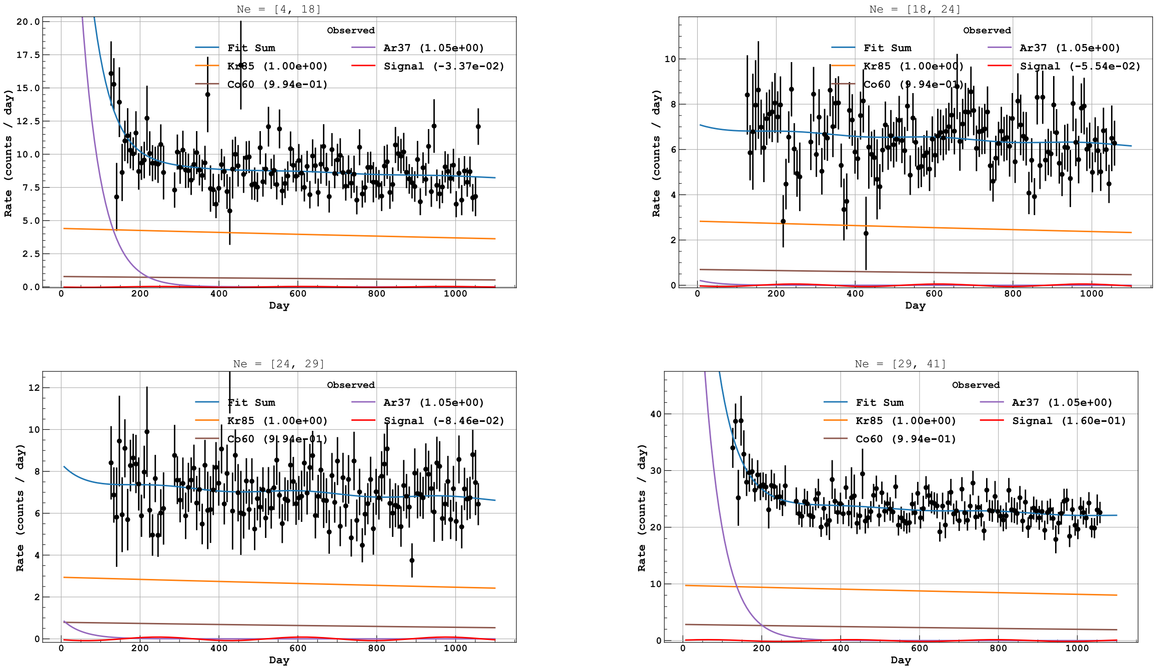

Figure B.1: Observed event rate of the four lowest bins for every 7 days (from left to right and top to bottom, 4–18 e^-, 18–24 e^-, 24–29 e^-, and 29–41 e^-. Also shown with the solid lines is the result of the simultaneous fit.

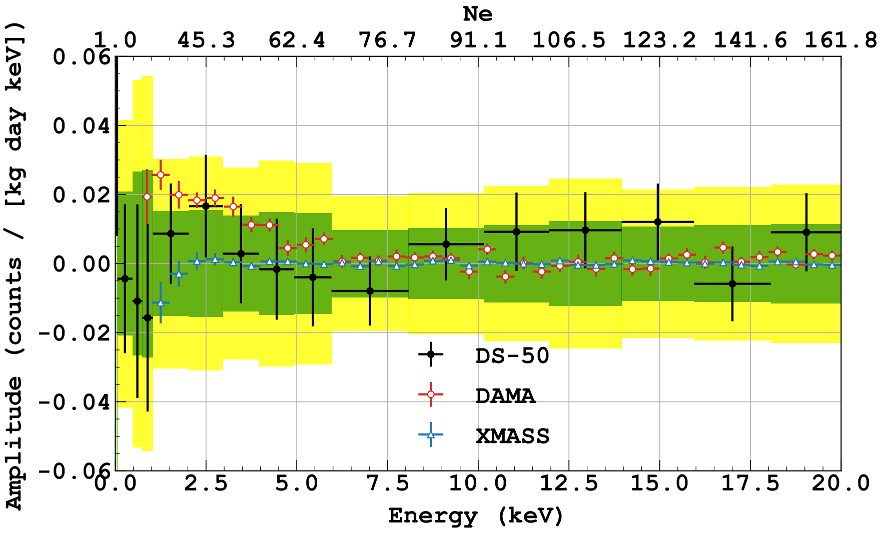

Figure B.2: The best fit amplitude (black point) obtained from the fit shown in Fig. B.1 as a function of electron equivalent energy. The green and yellow bands correspond to 1σ and 2σ expected bands obtained by background-only pseudo dataset. Also shown are the results from DAMA/LIBRA, XMASS, and XENON100.

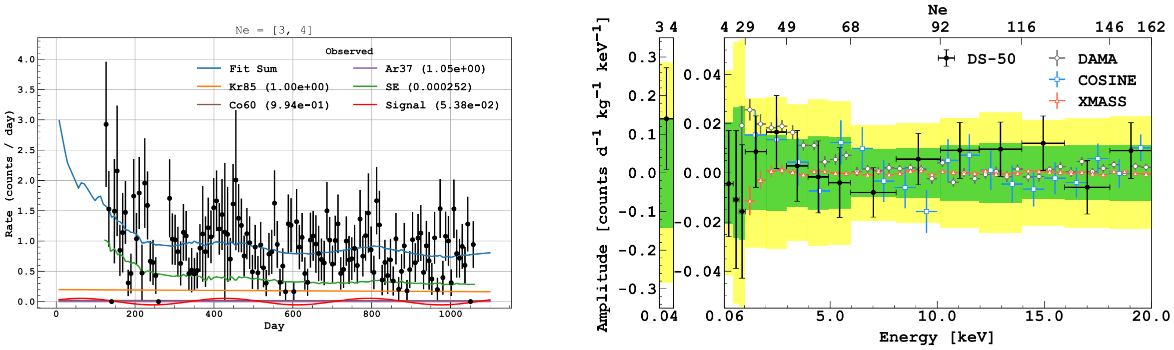

Figure B.3: Left: Observed event rate of 3–4 e^- and its fit with the SE model. The time bin width keeps 7 days. Right: result with with the SE model. Since we do not have enough knowledge on the SE contamination, projected sensitivity below 4 e^- cannot not be calculated.

Appendix C

Upscattering off protons

In this section, we present a material useful for future extensions of the iBDM analysis, I include calculations by Dr Sebastian Trojanowski [92], whom I frequently consulted about the theoretical aspects. Dr Trojanowski worked on extending the Giudice et al. [87] results to scattering off protons and coherent scattering, which can potentially extend the DEAP-3600 sensitivity by considering events only with the secondary electron-recoil interaction (the χ_2 decay track).

We implemented the equivalent of the cross section calculation for the scattering off electrons but for protons (although not yet coherent scattering), following Dr Trojanowski's guideance and rewriting the form factor:

$$G_1 \equiv \tau(F_1 + F_2)^2 = \tau F_M^2 \simeq \tau \mu_p^2 G_E^2 \tag{C.1}$$

$$G_2 \simeq G_E^2[1 + \tau(\mu_p^2 - 1)], \tag{C.2}$$

with the electric Sachs form factors

$$G_E = \frac{1}{1/(1 + Q^2/0.71GeV^2)^2}, \tag{C.3}$$

where the muon magnetic moment is:

$$\mu_p = 1 + \kappa = 2.79 \tag{C.4}$$

$$\tau = \tfrac{Q^2}{4m_p^2} = \tfrac{E_{\chi 1} - E_{\chi 2}}{2m_p}. \tag{C.5}$$

We can now rewrite the amplitude:

$$|\overline{M}|^2 = \frac{8m_P(\epsilon e g_{12})^2}{[2m_p(E_{\chi_2} - E_{\chi_1}) - m_X^2]^2} \times \left[M_0 \frac{G_1}{\tau} + \frac{1}{2} M_1 \left(G_2 - \frac{G_1}{\tau}\right)\right] \tag{C.6}$$

Naive sensitivity projections including proton scattering effects and ignoring the instrumental detector effects, are shown in Fig. C.1.

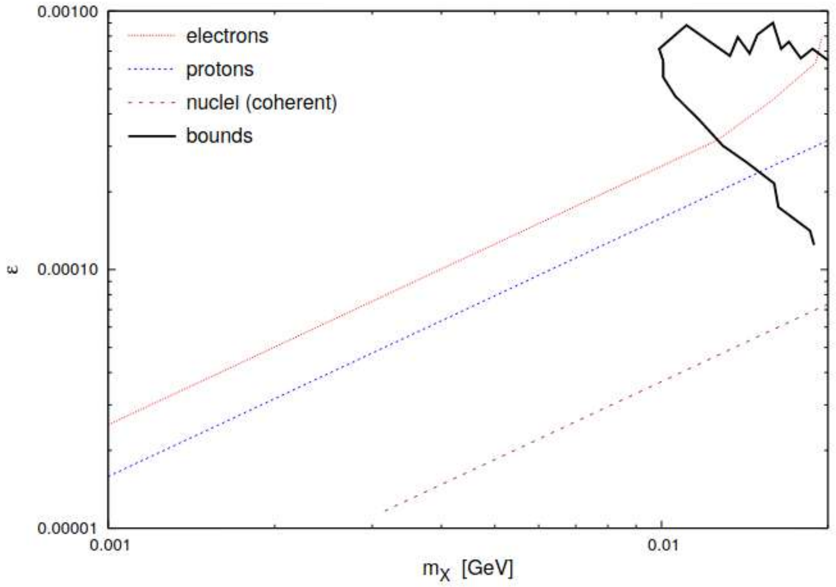

Figure C.1: New sensitivity limit plot from Dr. Trojanowski, assuming looking only at the cascade two-body decays, $\chi_2 \to \chi_1 A$ followed by $A \to e^+e^-$

Bibliography

[1] DarkSide-50, *Search for dark matter annual modulation with DarkSide-50* (2023), `2307.07249`.

[2] DarkSide-50, *Long-term operation of DarkSide-50 to search for dark-matter induced event rate modulation* (2023), to be published.

[3] A. Green, *Dark matter in astrophysics/cosmology*, SciPost Physics Lecture Notes (2022).

[4] *NASA website after Planck update*, `https://wwwmpa.mpa-garching.mpg.de/aquarius/`, accessed: 2023-09-30.

[5] L. Perivolaropoulos and F. Skara, *Challenges for ΛCDM: An update*, New Astronomy Reviews **95**, 101659 (2022).

[6] J. S. Bullock and M. Boylan-Kolchin, *Small-Scale Challenges to the ΛCDM Paradigm*, Annual Review of Astronomy and Astrophysics **55**, 343 (2017).

[7] V. C. Rubin and J. Ford, W. Kent, *Rotation of the Andromeda Nebula from a Spectroscopic Survey of Emission Regions*, ApJ **159**, 379 (1970).

[8] W. J. G. de Blok, F. Walter, E. Brinks, C. Trachternach, S.-H. Oh and R. C. Kennicutt, *High-resolution rotation curves and galaxy mass models from things*, The Astronomical Journal **136**, 2648 (2008).

[9] *Galaxy Formation Group, Max Planck Institut*, `https://map.gsfc.nasa.gov/media/080998/index.html`, accessed: 2023-09-30.

[10] S. M. Faber and R. E. Jackson, *Velocity dispersions and mass-to-light ratios for elliptical galaxies.*, ApJ **204**, 668 (1976).

[11] A. Doroshkevich, V. Lukash, and E. Mikheeva, *A solution to the problems of cusps and rotation curves in dark matter halos in the cosmological standard model*, Physics-uspekhi - PHYS-USP **55** (2012).

[12] F. Zwicky, *Die Rotverschiebung von extragalaktischen Nebeln*, Helvetica Physica Acta **6**, 110 (1933).

[13] B. Ryden, *Introduction to Cosmology* Cambridge University Press (2016), 2nd ed.

[14] A. H. Gonzalez, S. Sivanandam, A. I. Zabludoff, and D. Zaritsky, *Galaxy cluster baryon fractions revisited**, The Astrophysical Journal **778**, 14 (2013).

[15] T. Treu, *Strong lensing by galaxies*, Annual Review of Astronomy and Astrophysics **48**, 87 (2010).

[16] B. Paczynski, *Gravitational Microlensing by the Galactic Halo*, ApJ **304**, 1 (1986).

[17] M. Kilbinger, *Cosmology with cosmic shear observations: a review*, Reports on Progress in Physics **78**, 086901 (2015).

[18] D. Clowe, M. Bradač, A. H. Gonzalez, M. Markevitch, S. W. Randall, C. Jones and D. Zaritsky, *A direct empirical proof of the existence of dark matter*, The Astrophysical Journal **648**, L109 (2006).

[19] S. Tulin and H.-B. Yu, *Dark matter self-interactions and small scale structure*, Physics Reports **730**, 1 (2018).

[20] P. Zyla et al., *Review of particle physics*, Progress of Theoretical and Experimental Physics **2020** (2020).

[21] E. D. Valentino, C. Gustavino, J. Lesgourgues, G. Mangano, A. Melchiorri, G. Miele and O. Pisanti, *Probing nuclear rates with planck and BICEP2*, Physical Review D **90** (2014).

[22] D. J. Fixsen, *The temperature of the cosmic microwave background*, The Astrophysical Journal **707**, 916 (2009).

[23] G. Hinshaw et al., *Nine-year Wilkinson Microwave Anisotropy Probe (WMAP) observations: Cosmological parameter results*, The Astrophysical Journal Supplement Series **208**, 19 (2013).

[24] N. Aghanim et al., *Planck 2018 results*, Astronomy & Astrophysics **641**, A6 (2020).

[25] M. Battaglieri et al., *US Cosmic Visions: New Ideas in Dark Matter 2017: Community Report* (2017), `1707.04591`.

[26] M. Milgrom, *A modification of the Newtonian dynamics as a possible alternative to the hidden mass hypothesis.*, ApJ **270**, 365 (1983).

[27] C. Burrage, *A brief introduction to extended gravity and connections to dark energy: Illustrated with scalar field examples*, SciPost Phys. Lect. Notes p. 41 (2022).

[28] T. Clifton, P. G. Ferreira, A. Padilla, and C. Skordis, *Modified gravity and cosmology*, Physics Reports **513**, 1 (2012).

[29] R. Laureijs, *Euclid Assessment Study Report for the ESA Cosmic Visions* (2009), `0912.0914`.

[30] F. Aharonian et al., *Pathway to the Square Kilometre Array - The German White Paper* (2013), `1301.4124`.

[31] C. Alcock et al., *EROS and MACHO Combined Limits on Planetary-Mass Dark Matter in the Galactic Halo*, ApJ **499**, L9 (1998).

[32] G. Franciolini, *Primordial black holes: from theory to gravitational wave observations* (2021), `2110.06815`.

[33] B. Carr and F. Kühnel, *Primordial black holes as dark matter candidates*, SciPost Physics Lecture Notes (2022).

[34] S. W. Hawking, *Black hole explosions?*, Nature **248**, 30 (1974).

[35] S. Dodelson and L. M. Widrow, *Sterile neutrinos as dark matter*, Physical Review Letters **72**, 17 (1994).

[36] E. Bulbul, M. Markevitch, A. Foster, R. K. Smith, M. Loewenstein and S. W. Randall, *Detection of an unidentified emission line in the stacked x-ray spectrum of galaxy clusters*, The Astrophysical Journal **789**, 13 (2014).

[37] J. Kopp, *Sterile neutrinos as dark matter candidates*, SciPost Physics Lecture Notes (2022).

[38] I. G. Irastorza, *An introduction to axions and their detection*, SciPost Physics Lecture Notes (2022).

[39] A. Arvanitaki, S. Dimopoulos, S. Dubovsky, N. Kaloper and J. March-Russell, *String axiverse*, Phys. Rev. D **81**, 123530 (2010).

[40] I. G. Irastorza and J. Redondo, *New experimental approaches in the search for axion-like particles*, Progress in Particle and Nuclear Physics **102**, 89 (2018).

[41] J. L. Feng, *The WIMP paradigm: Theme and variations*, SciPost Physics Lecture Notes (2023).

[42] Y. ZELDOVICH, presentation at 1965), edited by Z. KOPAL, vol. 3 of *Advances in Astronomy and Astrophysics*, pp. 241–379.

[43] G. D. Mack, J. F. Beacom, and G. Bertone, *Towards closing the window on strongly interacting dark matter: Far-reaching constraints from Earth's heat flow, journal = Physical Review D*, **76** (2007).

[44] J. Cooley, *Dark matter direct detection of classical WIMPs*, SciPost Physics Lecture Notes (2022).

[45] DarkSide Collaboration, *Search for Dark Matter Particle Interactions with Electron Final States with DarkSide-50*, Phys. Rev. Lett. **130**, 101002 (2023).

[46] J. L. Feng, B. Fornal, I. Galon, S. Gardner, J. Smolinsky, T. M. P. Tait and P. Tanedo, *Protophobic fifth-force interpretation of the observed anomaly in* ^{8}Be *nuclear transitions*, Phys. Rev. Lett. **117**, 071803 (2016).

[47] J. Feng, *The beryllium anomaly and new physics*, Conference Lecture (2017), URL `https://indico.cern.ch/event/580599/contributions/2473747/attachments/1416113/2168171/1702cern.pdf`.

[48] J. Billard et al., *Direct detection of dark matter–APPEC committee report*, Reports on Progress in Physics **85**, 056201 (2022).

[49] M. Cirelli, N. Fornengo, and A. Strumia, *Minimal dark matter*, Nuclear Physics B **753**, 178 (2006).

[50] D. Pinna, *Dark matter searches at accelerators*, Conference Lecture (2023), URL `https://indico.cern.ch/event/1199289/contributions/5262813/attachments/2704748/4696111/DarkMatter_TAUP_DP.pdf`.

[51] C. Csáki, *The Minimal Supersymmetric Standard Model*, Modern Physics Letters A **11**, 599 (1996).

[52] B. Batell, N. Blinov, C. Hearty, and R. McGehee, *Exploring dark sector portals with high intensity experiments* (2022), `2207.06905`.

[53] N. Bell, *Dark matter searches with astrophysics*, Conference Lecture (2023), URL `https://indico.cern.ch/event/1199289/contributions/5262820/attachments/2705207/4696161/TAUP_2023_Bell.pdf`.

[54] T. Slatyer, *Les Houches Lectures on Indirect Detection of Dark Matter*, SciPost Physics Lecture Notes (2022).

[55] S. Rajendran, *New directions in the search for dark matter* (2022), `2204.03085`.

[56] F.-S. Ling, P. Sikivie, and S. Wick, *Diurnal and annual modulation of cold dark matter signals*, Phys. Rev. D **70**, 123503 (2004).

[57] N. W. Evans, C. A. J. O'Hare, and C. McCabe, *SHM^{++}: A Refinement of the Standard Halo Model for Dark Matter Searches in Light of the Gaia Sausage* (2018), `1810.11468`.

[58] R. Bernabei et al., *First model independent results from DAMA/LIBRA-phase2*, Nuclear Physics and Atomic Energy **19**, 307 (2018).

[59] J. Angle et al., *First results from the XENON10 dark matter experiment at the gran sasso national laboratory*, Physical Review Letters **100** (2008).

[60] J. Amaré et al., *Annual modulation results from three-year exposure of ANAIS-112*, Physical Review D **103** (2021).

[61] J. Aalbers et al., *First dark matter search results from the LUX-ZEPLIN (LZ) experiment*, Physical Review Letters **131** (2023).

[62] C. E. Aalseth et al., *DarkSide-20k: A 20 tonne two-phase LAr TPC for direct dark matter detection at LNGS*, The European Physical Journal Plus **133** (2018).

[63] Global Argon Dark Matter Collaboration, *Sensitivity projections for a dual-phase argon TPC optimized for light dark matter searches through the ionization channel*, Phys. Rev. D **107**, 112006 (2023).

[64] M. Albakry et al., *Search for low-mass dark matter via bremsstrahlung radiation and the migdal effect in SuperCDMS*, Physical Review D **107** (2023).

[65] S. Collaboration et al., *A Strategy for Low-Mass Dark Matter Searches with Cryogenic Detectors in the SuperCDMS SNOLAB Facility* (2023), `2203.08463`.

[66] E. Adams et al., *Search for inelastic dark matter-nucleus scattering with the PICO-60* CF_3I *and* C_3F_8 *bubble chambers* (2023), `2301.08993`.

[67] *Dark matter limit plotter* (2023), URL `https://supercdms.slac.stanford.edu/science-results/dark-matter-limit-plotter`.

[68] K. Schäffner, *Direct dark matter detection of light particles at the GeV-scale and below*, Conference Lecture (2023), URL `https://indico.cern.ch/event/1199289/contributions/5262810/attachments/2705103/4696339/TAUP_low_mass_schaeffner.pdf`.

[69] V. Barger, W.-Y. Keung, and G. Shaughnessy, *Spin dependence of dark matter scattering*, Physical Review D **78** (2008).

[70] J. Fan, M. Reece, and L.-T. Wang, *Non-relativistic effective theory of dark matter direct detection*, Journal of Cosmology and Astroparticle Physics **2010**, 042 (2010).

[71] P. Adhikari et al., *Pulse-shape discrimination against low-energy Ar-39 beta decays in liquid argon with 4.5 tonne-years of DEAP-3600 data*, The European Physical Journal C **81** (2021).

[72] P. Agnes et al., *First results from the darkside-50 dark matter experiment at laboratori nazionali del gran sasso*, Physics Letters B **743**, 456 (2015).

[73] D. S. Akerib et al., *Snowmass2021 cosmic frontier dark matter direct detection to the neutrino fog* (2022), `2203.08084`.

[74] E. Aprile et al., *Projected WIMP sensitivity of the XENONnT dark matter experiment*, Journal of Cosmology and Astroparticle Physics **2020**, 031 (2020).

[75] C. G. The Global Argon Dark Matter Collaboration, *Future dark matter searches with low-radioactivity argon* (2018), URL `https://indico.cern.ch/event/765096/contributions/3295671/attachments/1785196/2906164/DarkSide-Argo_ESPP_Dec_17_2017.pdf`.

[76] D.-M. Mei, Z.-B. Yin, L. Stonehill, and A. Hime, *A model of nuclear recoil scintillation efficiency in noble liquids*, Astroparticle Physics **30**, 12 (2008).

[77] T. Doke, A. Hitachi, J. Kikuchi, K. Masuda, H. Okada and E. Shibamura, *Absolute Scintillation Yields in Liquid Argon and Xenon for Various Particles*, Jap. J. Appl. Phys. **41**, 1538 (2002).

[78] *A study of nuclear recoil backgrounds in dark matter detectors* (2016), URL `http://arks.princeton.edu/ark:/88435/dsp01hx11xh73n`.

[79] J. Lindhard, V. Nielsen, M. Scharff, and P. V. Thomsen, *Integral equations governing radiation effects. (notes on atomic collisions, iii)*, Kgl. Danske Videnskab., Selskab. Mat. Fys. Medd., **Vol: 33: No. 10** (1963).

[80] SCENE Collaboration, *Measurement of scintillation and ionization yield and scintillation pulse shape from nuclear recoils in liquid argon*, Phys. Rev. D **91**, 092007 (2015).

[81] A. Hitachi, T. Doke, and A. Mozumder, *Luminescence quenching in liquid argon under charged-particle impact: Relative scintillation yield at different linear energy transfers*, Phys. Rev. B **46**, 11463 (1992).

[82] J. F. Ziegler, M. Ziegler, and J. Biersack, *Srim – the stopping and range of ions in matter (2010)*, Nuclear Instruments and Methods in Physics Research Section B: Beam Interactions with Materials and Atoms **268**, 1818 (2010).

[83] J. B. Birks and F. A. Black, *Deterioration of Anthracene under a-Particle Irradiation*, Proceedings of the Physical Society. Section A **64**, 511 (1951).

[84] H. Loosli and H. Oeschger, *Detection of 39ar in atmospheric argon*, Earth and Planetary Science Letters **5**, 191 (1968).

[85] DarkSide-50, *Search for low-mass dark matter WIMPs with 12 ton-day exposure of DarkSide-50*, :2207.11966 (2022).

[86] P.-A. Amaudruz et al., *Design and construction of the DEAP-3600 dark matter detector*, Astroparticle Physics **108**, 1 (2019).

[87] G. F. Giudice, D. Kim, J.-C. Park, and S. Shin, *Inelastic boosted dark matter at direct detection experiments*, Physics Letters B **780**, 543 (2018).

[88] K. Agashe, Y. Cui, L. Necib, and J. Thaler, *(in)direct detection of boosted dark matter*, Journal of Physics: Conference Series **718**, 042041 (2016).

[89] D. Tucker-Smith and N. Weiner, *Inelastic dark matter*, Phys. Rev. D **64**, 043502 (2001).

[90] G. Bélanger, A. Goudelis, J.-C. Park, and A. Pukhov, *Isospin-violating dark matter from a double portal*, Journal of Cosmology and Astroparticle Physics **2014**, 020 (2014).

[91] G. Bélanger and J.-C. Park, *Assisted freeze-out*, Journal of Cosmology and Astroparticle Physics **2012** (2011).

[92] S. Trojanowski, *Notes about the search for boosted DM in DEAP*, internal note.

[93] D. Kim, P. A. Machado, J.-C. Park, and S. Shin, *Optimizing energetic light dark matter searches in dark matter and neutrino experiments*, Journal of High Energy Physics **2020** (2020).

[94] Particle Data Group, *Review of Particle Physics*, PTEP **2022**, 083C01 (2022).

[95] J. Alwall, R. Frederix, S. Frixione, V. Hirschi, F. Maltoni, O. Mattelaer, H.-S. Shao, T. Stelzer, P. Torrielli and M. Zaro, *The automated computation of tree-level and next-to-leading order differential cross sections, and their matching to parton shower simulations*, Journal of High Energy Physics **2014** (2014).

[96] W. von Schlippe, *Relativistic kinematics of particle interactions*, URL `https://web.physics.utah.edu/~jui/5110/hw/kin_rel.pdf`.

[97] S. Seibert, *Rat (an analysis tool)*, URL `https://rat.readthedocs.io/en/latest/overview.html`.

[98] DEAP, *Search for dark matter with a 231-day exposure of liquid argon using DEAP-3600 at SNOLAB*, Phys. Rev. D **100**, 022004 (2019).

[99] *Estar (database)*, URL `https://physics.nist.gov/PhysRefData/Star/Text/ESTAR.html`.

[100] R. Essig et al., *Dark sectors and new, light, weakly-coupled particles* (2013), `1311.0029`.

[101] D. Banerjee et al., *Search for vector mediator of dark matter production in invisible decay mode*, Physical Review D **97** (2018).

[102] J. Billard, E. Figueroa-Feliciano, and L. Strigari, *Implication of neutrino backgrounds on the reach of next generation dark matter direct detection experiments*, Physical Review D **89** (2014).

[103] SNO Collaboration, *Determination of the ν_e and total ^{8}B solar neutrino fluxes using the Sudbury Neutrino Observatory Phase I data set*, Phys. Rev. C **75**, 045502 (2007).

[104] M. Olszewski, *Internal note on ibdm simulation in deap-3600.*

[105] F. Froborg and A. R. Duffy, *Annual modulation in direct dark matter searches*, Journal of Physics G: Nuclear and Particle Physics **47**, 094002 (2020).

[106] K. Freese, M. Lisanti, and C. Savage, *Colloquium: Annual modulation of dark matter*, Rev. Mod. Phys. **85**, 1561 (2013).

[107] A. K. Drukier, K. Freese, and D. N. Spergel, *Detecting cold dark-matter candidates*, Phys. Rev. D **33**, 3495 (1986).

[108] S. K. Lee, M. Lisanti, A. H. G. Peter, and B. R. Safdi, *Effect of gravitational focusing on annual modulation in dark-matter direct-detection experiments*, Phys. Rev. Lett. **112**, 011301 (2014).

[109] R. Bernabei et al., *First model independent results from DAMA/LIBRA-phase2*, Universe **4**, 116 (2018).

[110] COSINE-100, *Three-year annual modulation search with COSINE-100*, :2111.08863 (2021).

[111] XENON, *Search for Electronic Recoil Event Rate Modulation with 4 Years of XENON100 Data*, Phys. Rev. Lett. **118**, 101101 (2017).

[112] XMASS, *Direct dark matter search by annual modulation with 2.7 years of XMASS-I data*, Phys. Rev. D **97**, 102006 (2018).

[113] LUX, *Search for annual and diurnal rate modulations in the LUX experiment*, Phys. Rev. D **98**, 062005 (2018).

[114] P. Gondolo and G. Gelmini, *Compatibility of DAMA dark matter detection with other searches*, Physical Review D **71** (2005).

[115] R. Foot, *Mirror dark matter and the new DAMA/LIBRA results: A simple explanation for a beautiful experiment*, Physical Review D **78** (2008).

[116] A. Zhitnitsky, *DAMA/LIBRA annual modulation and axion quark nugget dark matter model*, Physical Review D **101** (2020).

[117] M. Kimura, T. Hugues, D. Franco, M. Ku and M. Wada, *Analysis note on search for event rate modulation using ionization signal from DarkSide-50*, internal analysis note.

[118] DarkSide, *Calibration of the liquid argon ionization response to low energy electronic and nuclear recoils with DarkSide-50*, Phys. Rev. D **104**, 082005 (2021).

[119] P. Agnes et al., *Simulation of argon response and light detection in the DarkSide-50 dual phase TPC*, Journal of Instrumentation **12**, P10015 (2017).

[120] P. Agnes et al., *A study of events with photoelectric emission in the DarkSide-50 liquid argon time projection chamber* (2021), `2107.08015`.

[121] T. V. John and I. Ahmad, *Cosmogenic activation calculation of darkside. determining the rate for 37Ar in DarkSide-50 experiment*, internal note.

[122] H. Dembinski and P. O. et al., *scikit-hep/iminuit*, (2020).

[123] J. Wolberg, *Data analysis using the method of least squares: Extracting the most information from experiments*, pp. 1–250 (2006).

[124] N. R. Lomb, *Least-Squares Frequency Analysis of Unequally Spaced Data*, Ap&SS **39**, 447 (1976).

[125] J. Scargle, *Studies in astronomical time series analysis. II - Statistical aspects of spectral analysis of unevenly spaced data*, The Astrophysical Journal **263** (1983).

[126] A. Developers, *LombScargle Periodograms* (2022), URL `https://docs.astropy.org/en/stable/timeseries/lombscargle.html`.

[127] J. T. VanderPlas, *Understanding the Lomb-Scargle Periodogram*, The Astrophysical Journal Supplement Series **236**, 16 (2018).

[128] M. Zechmeister and M. Kürster, *The generalised Lomb-Scargle periodogram*, Astronomy &amp Astrophysics **496**, 577 (2009).

[129] R. Baluev, *Assessing the statistical significance of periodogram peaks*, MNRAS **385**, 1279 (2008).

[130] Željko Ivezić, A. J. Connolly, J. T. VanderPlas, and A. Gray, *Statistics, Data Mining, and Machine Learning in Astronomy: A Practical Python Guide for the Analysis of Survey Data*, Princeton University Press (2014), stu - student edition ed., ISBN 9780691151687.

[131] Eyer, L. and Bartholdi, P., *Variable stars: Which nyquist frequency?*, Astron. Astrophys. Suppl. Ser. **135**, 1 (1999).

[132] Vio, R., Andreani, P., and Biggs, A., *Unevenly-sampled signals: a general formalism for the Lomb-Scargle periodogram*, A&A **519**, A85 (2010).

[133] DarkSide, *DarkSide-50 532-day Dark Matter Search with Low-Radioactivity Argon*, Phys. Rev. D **98**, 102006 (2018).

[134] C. Monteiro, J. Lopes, J. Veloso, and J. dos Santos, *Secondary scintillation yield in pure argon*, Physics Letters B **668**, 167 (2008).

[135] WArP, *Oxygen contamination in liquid Argon: Combined effects on ionization electron charge and scintillation light*, JINST **5**, P05003 (2010).

[136] C. M. B. Monteiro, J. A. M. Lopes, J. F. C. A. Veloso, and J. M. F. dos Santos, *Secondary scintillation yield in pure argon*, Phys. Lett. B **668**, 167 (2008).

[137] G. Bakale, U. Sowada, and W. F. Schmidt, *Effect of an electric field on electron attachment to sulfur hexafluoride, nitrous oxide, and molecular oxygen in liquid argon and xenon*, The Journal of Physical Chemistry **80**, 2556 (1976).

[138] A. Lyashenko, T. Nguyen, A. Snyder, H. Wang and K. Arisaka, *Measurement of the absolute Quantum Efficiency of Hamamatsu model R11410-10 photomultiplier tubes at low temperatures down to liquid xenon boiling point*, JINST **9**, P11021 (2014).

[139] M. A. Suchowski, *An analysis of the impact of an outlier on correlation coefficients across small sample data where rho is non-zero*, URL `https://scholarworks.wmich.edu/dissertations/1348`.

[140] E. S. PEARSON, *SOME NOTES ON SAMPLING TESTS WITH TWO VARIABLES*, Biometrika **21**, 337 (1929).

[141] K. D. Hopkins, *Educational and psychological measurement and evaluation* ERIC (1998).

[142] *Spearman Rank Correlation Coefficient* Springer New York (New York, NY (2008), pp. 502–505, ISBN 978-0-387-32833-1, URL `https://doi.org/10.1007/978-0-387-32833-1_379`.

[143] M. Kendall and J. D. Gibbons, *Rank Correlation Methods* A Charles Griffin Title (1990), 5th ed.

[144] *Kendall Rank Correlation Coefficient* Springer New York (New York, NY (2008), pp. 278–281, ISBN 978-0-387-32833-1, URL `https://doi.org/10.1007/978-0-387-32833-1_211`.

[145] *Data analysis in particle physics*, lecture note on the Experimental Elementary Particle Physics lectures, URL `https://www.roma1.infn.it/~bini/StatEPP_new.pdf`.

[146] E. Parzen, *On Estimation of a Probability Density Function and Mode*, The Annals of Mathematical Statistics **33**, 1065 (1962).

[147] A. L. Read, *Presentation of search results: The CL(s) technique*, J. Phys. G **28**, 2693 (2002).

[148] DarkSide, *Low-Mass Dark Matter Search with the DarkSide-50 Experiment*, Phys. Rev. Lett. **121**, 081307 (2018).

[149] DarkSide-20k, *DarkSide-20k: A 20 tonne two-phase LAr TPC for direct dark matter detection at LNGS*, Eur. Phys. J. Plus **133**, 131 (2018).

[150] D. Franco et al., *Solar neutrino detection in a large volume double-phase liquid argon experiment*, JCAP **08**, 017 (2016).

[151] R. Bernabei et al., *The dark matter: DAMA/LIBRA and its perspectives* (2021), `2110.04734`.

[152] XMASS Collaboration, *Direct dark matter searches with the full data set of XMASS-I*, Phys. Rev. D **108**, 083022 (2023).

[153] STUDENT, *PROBABLE ERROR OF A CORRELATION COEFFICIENT*, Biometrika **6**, 302 (1908).

List of Figures

List of Tables